SEISMIC RESPONSE OF LITTLE RED HILL

–

TOWARDS AN UNDERSTANDING OF TOPOGRAPHIC EFFECTS ON GROUND MOTION AND ROCK SLOPE FAILURE

A thesis submitted in partial fulfilment of the requirements

for the degree of

Doctor of Philosophy in Engineering Geology

at the University of Canterbury

by

Florian Büch

Department of Geological Sciences

University of Canterbury, Christchurch, New Zealand

March 2008

ABSTRACT

A field experiment was conducted at near Lake Coleridge in the Southern Alps of New Zealand, focusing on the kinematic response of bedrock-dominated mountain edifices to seismic shaking. The role of topographic amplification of seismic waves causing degradation and possible failure of rock masses was examined. To study site effects of topography on seismic ground motion in a field situation, a small, elongated, and bedrock-dominated mountain ridge (Little Red Hill) was chosen and equipped with a seismic array. In total seven EARSS instruments (Mark L-4-3D seismometers) were installed on the crest, the flank and the base of the 210 m high, 500 m wide, and 800 m long mountain edifice from February to July 2006. Seismic records of local and regional earthquakes, as well as seismic signals generated by an explosive source nearby, were recorded and are used to provide information on the modes of vibration as well as amplification and deamplification effects on different parts of the edifice. The ground motion records were analyzed using three different methods: comparisons of peak ground accelerations (PGA), power spectral density analysis (PSD), and standard spectral ratio analysis (SSR). Time and frequency domain analyses show that site amplification is concentrated along the elongated crest of the edifice where amplifications of up to 1100 % were measured relative to the motion at the flat base. Theoretical calculations and frequency analyses of field data indicate a maximum response along the ridge crest of Little Red Hill for frequencies of about 5 Hz, which correlate to wavelengths approximately equal to the half-width or height of the edifice (~240 m). The consequence of amplification effects on the stability and degradation of rock masses can be seen: areas showing high amplification effects overlap with the spatial distribution of seismogenic block fields at Little Red Hill. Additionally, a laboratory-scale (1:1,000) physical model was constructed to investigate the effect of topographic amplification of ground motion across a mountain edifice by simulating the situation of the Little Red Hill field experiment in a small-scale laboratory environment. The laboratory results show the maximum response of the model correlates to the fundamental mode of vibration of Little Red Hill at approximately 2.2 Hz.

It is concluded that topography, geometry and distance to the seismic source, play a key role causing amplification effects of seismic ground motion and degradation of rock mass across bedrock-dominated mountain edifices.

ACKNOWLEDGMENTS

This research project was only achievable due to the contribution of many helping hands. I am especially grateful for the invitation to study in New Zealand from my principal supervisor Tim Davies, allowing me to become a part of the big family of the Geological Sciences Department at University of Canterbury.

Jarg Pettinga, thanks for your supervision, some nice conversations and good ideas, without them the project would not have reached this standard.

John Berrill, thanks a lot for your advice and brilliant input. Our meetings, even quite rare ☺, were the most helpful discussions I had.

Mike Finnemore, the electronic and applied brain in the background of the project, I am grateful for the time you spent with me drilling and helping me to set up the foundations of the project.

Tim O'Neill (GNS), thank you very much for showing me all the tricks using and setting up the EARSS seismographs. It was a pleasure to work with you. Thanks for the effort, the spontaneity and the work you put into my project.

Brian and Judy Kirk, the owners of Lake Coleridge station: Cheers, for giving me permission to conduct the field experiment on your land and giving me an understanding of Kiwi-mentality.

A massive thank you to my field slaves Andrea & Jesse, Rose, Stefan, Uwe, and Verne.

A big cheers to the geophysics group of Euan Smith at Victoria University in Wellington for the excellent cooperation regarding the field data processing. A hug in particular for Michelle Salmon for her patience and help!

Thanks also to: Mark Staiger, Elijah VanHouten (both Mechanical Engineering Dept.), Misko Cubrinowski (Civil Engineering Dept.), Warwick Hill (Lincoln University), Alan Wood (Electrical Engineering Dept.), and Nick Key (Geography).

To the “working bees” at the department: Anekant, I very much appreciate your Swiss precision during the construction process of the laboratory model. Also thanks to Pat & Janet, Kerry, Rob, John, Kathy and Vanessa.

More than just thank you, Rose, for your fantastic support over the last couple of years and especially during that crazy writing up period.

The study was supported by a University of Canterbury Doctoral Scholarship. The research project received important external funding from GNS & EQC (Project Uni/528 & Uni/529) --- Thanks a lot!

TABLE OF CONTENTS

LIST OF FIGURES

LIST OF TABLES

1 INTRODUCTION

1.1 PROJECT BACKGROUND

Earthquakes often cause extensive rock slope failures and various types of mass movement in mountainous areas (Havenith et al., 2003b; Jibson et al., 2006; Sepúlveda et al., 2005a; Sepúlveda et al., 2005b). Catastrophic seismically-induced landslides are among the Earth's most powerful geomorphic events, causing sudden and dramatic changes to the landscape, representing high risks of this type to both infrastructure and life, and reputedly causing large economic losses. A well-known devastating event was the Nevado Huascaran rock and debris avalanche triggered by a magnitude M = 7.7 earthquake in Peru, 1970, destroying two townships and causing about 20,000 fatalities (Cluff, 1971; Keefer, 2002; Plafker et al., 1971). Large rock avalanches were also triggered by the magnitude M = 7.9 earthquake in Alaska, 2002 (Jibson et al., 2006) and the magnitude M = 7.7 Kashmir earthquake in Pakistan, 2005 (Schneider, 2006).

Seismic waves interacting with topography lead to amplification and deamplification of the resulting ground motion. Topographic amplification of ground motion can be an important factor in exceeding the shearing resistance of the rock mass, and in triggering deep-seated failure of rock slopes which are stable under aseismic conditions. Besides source motion characteristics and path effects, local geological, structural, hydrological, and local topographic conditions have a strong influence on ground response during earthquakes (Fig. 1.1).

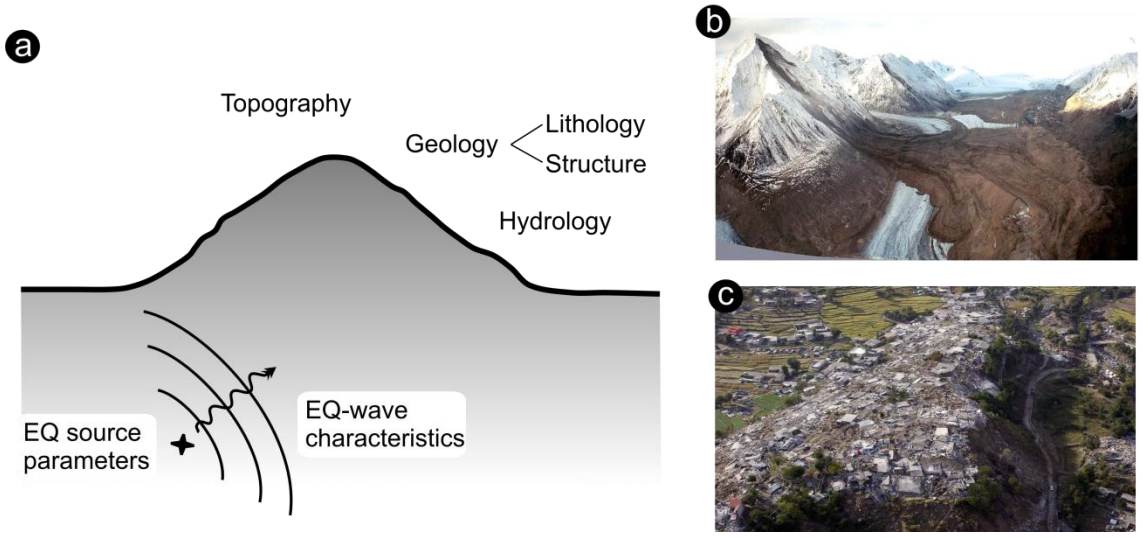

Figure 1.1:Pictures showing a) main factors influencing ground response during earthquakes, b) topographic amplification of seismic waves contributing to the initiation of earthquake triggered rock slope failures (Black Rapids Glacier rock avalanches, Alaska; photo taken by Jibson et al., 2004) and c) topographic amplification of seismic waves causing structural damage on top of an elevated mountain ridge in the city of Balakot, Pakistan (Photo taken by REUTERS after the Kashmir/Pakistan earthquake in 2005)

Indications of amplification effects of seismic ground motions by topography includes seismogenic blockfields on ridge crests (represented by churned ground and overturned boulders,(Boore, 1972), and increased structural damage during earthquakes on elevated topography (Fig. 1.1 c).

Experimental field studies (LeBrun et al., 1999; Montalvo-Arrieta et al., 2003; Spudich et al., 1996) and analytical studies (Bouchon et al., 1996; Sánches-Sesma and Campillo, 1993) on the seismic response of hill sites have shown that:

- Amplification of the ground motion at the top of the hill occurs relative to the base of the edifice. The amplification is frequency dependent and has its maximum at the resonant frequency of the edifice;
- Amplifications for motions perpendicular to the direction of elongation of the edifice are larger than parallel, and amplifications are higher for the horizontal components than for the vertical component;
- Observations show significantly higher amplitude of amplification (up to greater than 10) than numerical simulations predict;

- Next to the pure topographic effect, amplified ground motions at the top of an edifice can also be related to the presence of deeply weathered rock mass on the surface, acting as a low-velocity layer on top of intact bedrock (Havenith et al., 2003c).

1.2 PURPOSE & OBJECTIVES

Much of the populated mountainous terrain around the world is located in areas of high seismicity and prone to seismic landslide hazard. Increasing the understanding of earthquake-triggered, deep-seated landslide initiation is a complex task on the way to possible prediction of seismically-induced landslides. The seismic wave field interacting with mountain edifices and their local geological and geotechnical settings will determine the specific seismic landslide potential.

The tectonically active Southern Alps of New Zealand are recognised as one of the places where seismically-triggered rock slope failures occur frequently The seismically active Craigieburn area (Chamberlain, 1996; Whitehouse, 1983; Whitehouse and Griffiths, 1983) was chosen as a location to conduct a field study, in combination with a laboratory-scaled physical model, to investigate topographic effects on seismic ground motions of a bedrock-dominated mountain edifice. The impact of earthquake waves on Little Red Hill (LRH) and in particular topographic effects on seismic ground motion within the structure are key factors addressed in this research project.

The objectives for this study were defined as follows:

- Conduct geological & geotechnical investigations of the Little Red Hill test site and identify areas of rock mass degradation;
- Determine the response of LRH to seismic waves including
    - Identification of areas of amplification / deamplification
    - Identification of frequency response;
- Determine how the response of LRH is affected by earthquake source parameters, such as magnitude, epicentral distance, and azimuth;
- On the basis of the given results, determine the areas of LRH that are prone to rock mass degradation and compare the findings with the geological & geotechnical investigation;

- Develop a laboratory-scale physical model to investigate topographic effects on seismic ground motion in a small-scale environment;
- Determine the response of the laboratory-scale model to seismic waves and compare the findings with the results gained by the LRH field study.

1.3 THESIS ORGANISATION

Chapter one provides a brief introduction to the background of the study. The purpose and objectives of the research project are presented and its organization introduced.

Chapter two provides theoretical background information of topographic effects on seismic ground motion. Field observations of topographic effects on seismic ground motions and seismically-induced rock avalanches are presented. Previous seismic field experiments, numerical modeling approaches, mathematical models, and physical modeling studies on topographic effects on seismic ground motion are discussed.

Chapter three outlines the results from the seismic field study that was conducted at Little Red Hill. A geographic overview as well as information on the geological and geotechnical setting of the test site is given, data acquisition and processing techniques are introduced, and an overview of results is presented. Based on these results further analysis is presented and overall findings are discussed.

Chapter four introduces a laboratory-scale (1:1,000) physical model study, based on the Little Red Hill field experiment, to evaluate the role of topographic effects on ground motion and rock slope failure. Dimensional analysis techniques to establish the scaling laws between the model and the prototype are presented. A description of the development and the technical setup of the physical laboratory model are given, and results from the seismic response test of the model edifice are presented. The results of the laboratory model approach are compared with the prototype response of Little Red Hill, further interpretation provided, and the basic results are discussed and combined into a broader context of interaction of topography and seismic waves and its effect on deep-seated rock slope failure

Chapter five provides the final conclusions of the project, taking into account the theoretical background on topographic effect on seismic ground motion, as well as the findings from the Little Red Hill field experiment, and the laboratory-scale physical modeling approach. Recommendations for further research are presented at the end of this final chapter.

2 TOPOGRAPHIC EFFECTS ON GROUND MOTION – THEORETICAL BACKGROUND

Topographic effects on seismic ground motion have been recognized and discussed in the literature within various areas of research using different approaches. The following literature review focuses on topographic effects on ground motion and their potential to increase (amplify) ground motion and cause rock slope failure. The review incorporates field observations of earthquake-triggered rock avalanches and topographic effects on ground motion, as well as summarizing seismic field experiments, numerical modeling approaches, mathematical models, and physical laboratory modeling studies.

2.1 TOPOGRAPHIC EFFECTS ON GROUND MOTION – FIELD OBSERVATIONS

Boore (1972) made observations of churned ground and overturned boulders (indicative of accelerations > 1g) only on ridge crests and other topographically high features.

Further descriptions of ground fissures and broken tree tops along ridge crests following earthquakes events were made by e.g. Plafker (1967), Morton et al. (1989), Ponti and Wells (1991).

Hancox et al. (2003) conducted a reconnaissance study of landslides and other ground damage after the M_w 7.2 earthquake of 22 August 2003 in Fiordland, New Zealand. They described larger regolith failures that were apparently initiated by point failures at ridge-top level or at the tops of very steep slopes.

Sepúlveda et al. (2005a) studied seismically-induced rock slope failures which occurred after the 1994 Northridge earthquake (M_w = 6.7) in Pacoima Canyon, California. Peak accelerations of up to 1.6 g were recorded at a ridge compared to PGAs of less than 0.5 g at the bottom of the canyon. They concluded, after comparing geotechnical observations with slope stability back-analysis that the high density of landslides at Pacoima Canyon was a result of stronger ground shaking as a consequence of local topographic amplification. These findings confirmed results from an earlier study by Harp and Jibson (2002).

Khazai and Sitar (2003) evaluated factors controlling earthquake-induced landslides caused by the Chi-Chi earthquake in Taiwan in comparison with the Northridge and Loma Prieta earthquakes. The investigation of deep-seated landslides exposed the fact that the rock mass failure occurred mostly sub parallel to bedding and/or foliation. Most of the slope failures were triggered at slopes (slope angle >45°) subjected to ground motions with peak vertical accelerations larger than 0.2 g and mean horizontal peak ground accelerations in the range of 0.35-0.45 g.

Topographic amplification of ground motions during earthquakes have been observed resulting in disrupted ground on mountain tops and causing seismically triggered landslides (i.e. Chigira et al., 2003; Dai et al., 2005; Harp and Jibson, 2002; Havenith et al., 2003b; Jibson and Crone, 2001; Konagai et al., 2002; Schneider, 2006; Sepúlveda et al., 2005b; Tibaldi et al., 1995). A common observation in populated areas is the occurrence of increased structural damage or even collapse of buildings that are located on an elevated or convex topography (Fig. 2.1, (Bouckovalas and Kouretzis, 2001; Carver and Hartzell, 1996; Dowrick, 1985; Gao et al., 1996)).

Figure 2.1: Pictures taken by Reuters in the city of Balakot after the magnitude 7.6 Kashmir/Pakistan earthquake in October 2005 showing the effects of topographic amplification of ground motion and the impact on buildings on top of an elevated topography. Near total destruction of houses can be observed on top of the Kunar river terrace, whereas buildings on the flat surface adjacent to it have not collapsed.

2.1.1 SEISMICALLY TRIGGERED ROCK AVALANCHES

Several studies have been conducted on rock avalanches that were triggered by earthquakes or where the cause of failure could have only been explained by strong ground motion as a triggering mechanism. Databases of earthquake-induced mass movements have been developed by several authors (Bommer and Rodriguez, 2002; Keefer, 1984a; Keefer, 1984b; Prestinzini and Romeo, 2000; Rodriguez et al., 1999). Data from 76 historical earthquakes world-wide from 1811-1997 were analyzed by Rodriguez and co-authors (1999) to evaluate different relationships between earthquake source parameters and landslide distribution (e.g. magnitude and area affected by landslides, magnitude and maximum distance of landslides from epicenter and fault rupture). The landslide types were categorized, based on the terminology of Varnes (1978), and their characteristics separately discussed. In the case of coseismic rock avalanches Keefer (1984a; 1984b) concluded that most slopes were intensely fractured, with the rock mass being broken by several intersecting sets of fractures spaced a few centimeters to a few decimeters apart. He summarized that such slopes are usually steeper than 25°, more than 150 m high, and exhibit at least one of the following additional signs of low strength or potential instability:

a) Conspicuous planes of weakness (faults, master joints, bedding planes, or foliation surfaces) dipping out of the slope
b) Significant weathering of the rock mass
c) Weak cementation of the rock mass
d) Geologic or historic evidence of previous landsliding.

Badger & Watters (2004) investigated three large landslide source areas (cubic kilometers in volume) in the Summer Lake basin (Basin and Range province, Oregon). Geotechnical rock-mass characterization and slope stability analyses confirm that strong shaking was required to trigger landsliding and generate numerous kilometer-long failure surfaces. They concluded that the large volume, degree of fragmentation, and long run-out distances imply that the landslides occurred very rapidly and developed into rock avalanches. A nearby fault is capable of producing M_w 7 earthquakes with near-field flat-ground maximum horizontal accelerations approaching 1g.

After the Arthur's Pass earthquake of 9th March 1929 (South Island, New Zealand), Speight (1933) made an excursion in areas that were likely to be affected and observed several large slips that originated from the top of mountain ridges and shattered crests of mountains.

Pearce & O'Loughlin (1985) analyzed the influence of geology and topography on landsliding after the M 7.7 Murchinson earthquake in 1929 (South Island, New Zealand). They documented a case where a 650 m high ridge collapsed at its crest and a whole mountain side failed and buried the valley floor.

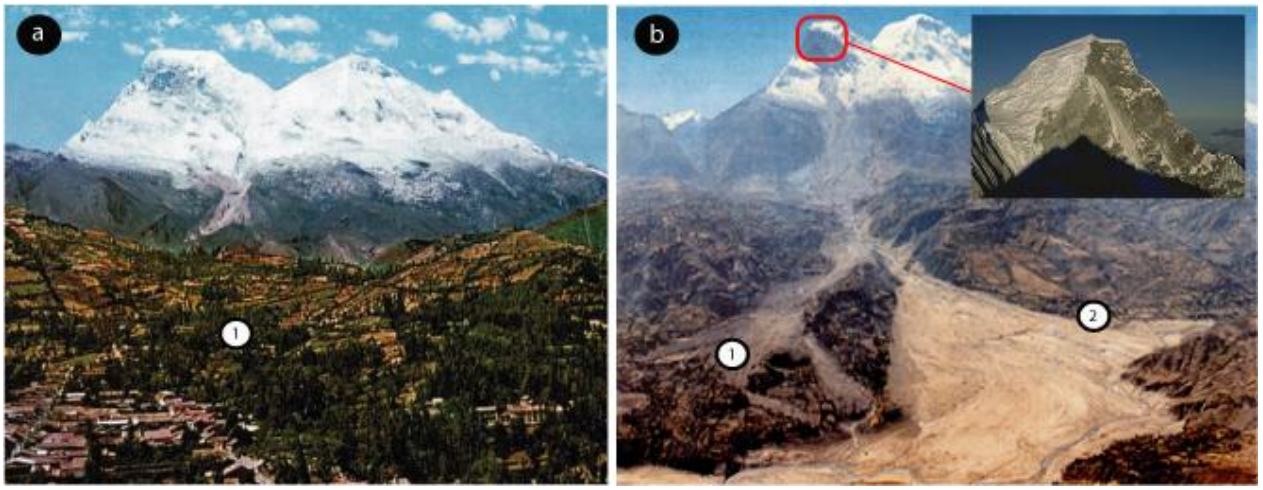

Figure 2.2: Before and after – a) Photograph of the village of Yungay (1) before the 1970 Peru earthquake and b) photograph after the debris avalanche buried the villages Yungay (1) and Ranrahirca (2). Red square indicates the source area which is shown in the upper right corner (modified after Cluff, 1971).

On May 31, 1970, a magnitude M 7.9 earthquake occurred off the coast of Peru and triggered a rock and ice avalanche (volume: about 50-100 x 10^6 m^3) that originated from the west face of the north peak of Nevado Huascaran (6676 m, Fig. 2.2). It dropped 1 km vertically, then slid over a glacier for a slope distance of 2.4 km and reached a maximum velocity of up to 335 km/h. It travelled about 11 km horizontally in about 4 minutes and buried the towns of Yungay and Ranrahirca. The death toll for both villages was about 20,000 (Cluff, 1971; Keefer, 1984a; Keefer, 1984b; Keefer, 1994; Keefer, 2002; Plafker et al., 1971).

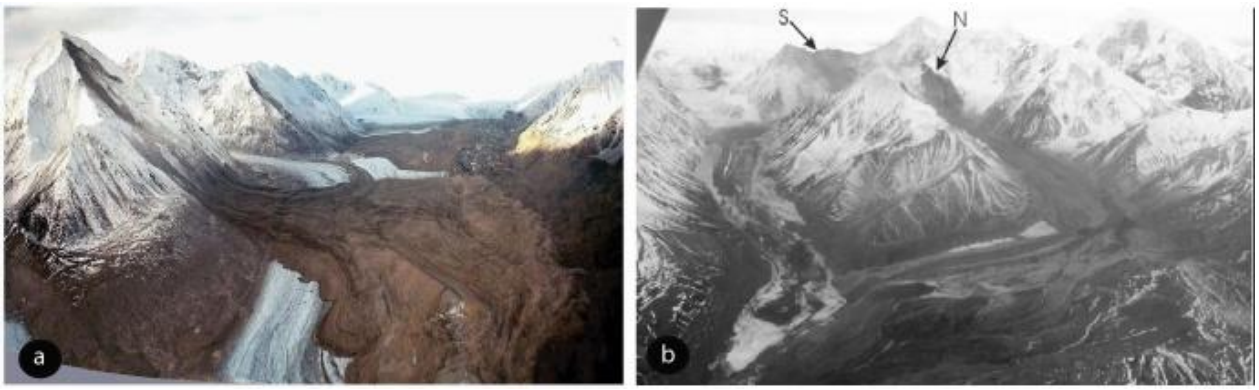

Figure 2.3: Photographs taken by Jibson et al. (2004) showing a) Black Rapids Glacier rock avalanches and b) the McGinnis Peak rock avalanches that originated from the northern (N) and southern (S) ridges of McGinnis Peak

One of the most spectacular recent reports of seismically triggered rock avalanches was made after the M 7.9 Denali Fault, Alaska, earthquake of 3 November 2002 (Fig. 2.3). Jibson and co-authors (Harp et al., 2003; 2004; Jibson et al., 2006) investigated the rupture zone of the fault and discovered several rock avalanches that originated from mountain ridge crests and mountain tops. The Black Rapids rock avalanche source scar exposed multiple joint surfaces both sub-parallel and orthogonal to the slope face with failure surfaces extending beneath the ridge top and causing the whole top of the edifice to fail. It is interesting that failures occurred in similar topographic locations on different edifices (Fig.2.3 a).

Evans and co-authors (1987) inspected a rock avalanche in the Canadian Cordillera, that was triggered by the M 6.6 North Nahanni earthquake. The rock avalanche (volume: 5-7 x 10^6 m^3) originated from the northern end of an isolated anticlinal ridge (about 400 m high). The rock avalanche involved massively bedded limestone with down-slope dipping bedding.

Further observations of seismically triggered rock avalanches were made after the Chi-Chi earthquake 1999 in Taiwan. Huang et al. (2001), Shou & Wang (2003), Chang et al. (2005b), and Wu et al. (2005) investigated the Jiufengershan landslide that originated from the crest of a approximately 500 m high mountain on a down-slope dipping bedding-controlled failure surface.

Sepúlveda et al. (2005b) investigated landslides that were triggered in the Tachia Valley, Central Taiwan, and described topographic amplification site effects as a characteristic behavior of rock slides and rock avalanches in that area. The head scarps of the landslides were mainly located

close to the tops of slopes or mountain edifices. They suggest that slope orientation, slope height and wavelength of the seismic waves control the amplification of ground motions.

Investigations of rock avalanches in the Northern Tien Shan province, Kyrgyzstan, undertaken by Havenith et al. (2003b; 2003c) revealed an earthquake induced triggering mechanism.

Tibaldi et al. (1995) investigated seismogenic landslides and their relation with faults and mountain slope geometry in the Ecuadorian Andes. They reported that sliding usually started from the uppermost part of the mountain slope. Amplification of ground response took place when the slope is perpendicular or sub-perpendicular to the seismogenetic fault plane and lies along its strike. Maximum attenuation occurred on slopes parallel or sub-parallel to the seismic fault plane.

Cases of rock avalanches that were most likely seismically triggered by earthquakes are also documented in New Zealand (Fig. 2.4). These cases show that the rock avalanches all originated from the ridge top of the mountain edifice. Whitehouse (Whitehouse, 1981; Whitehouse, 1983; Whitehouse and Griffiths, 1983) identified and analyzed about 50 rock avalanche deposits within the Torlesse Supergroup greywacke of the central Southern Alps of New Zealand, and concluded that the majority were most likely triggered by earthquakes.

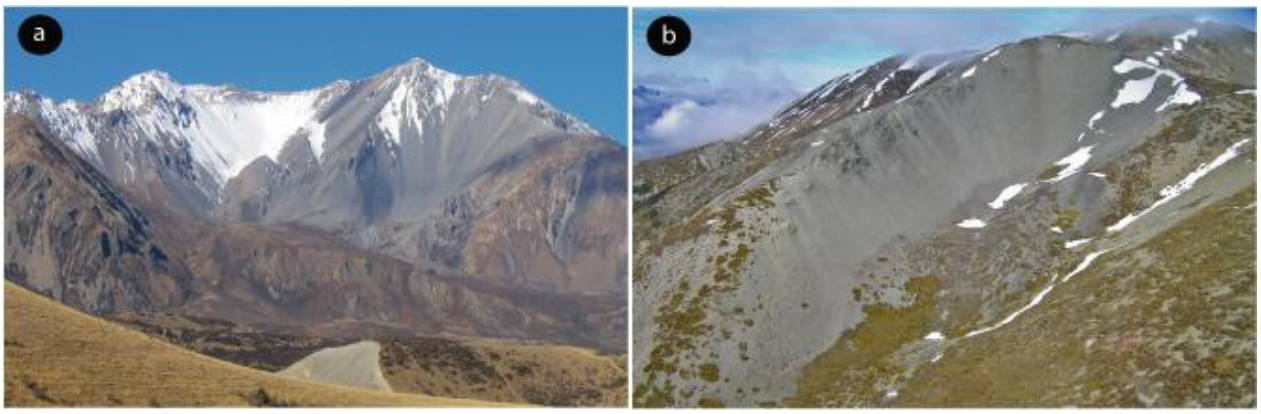

Figure 2.4: Photographs showing the rock avalanche source scars located at the very top of the mountain for a) the Craigieburn rock avalanche and b) the Acheron rock avalanche. Both are located in the central Southern Alps of New Zealand

On that basis detailed investigations were for example conducted on the Craigieburn rock avalanche (Orwin, 1998; Whitehouse, 1981), the Acheron rock avalanche (Smith, 2003; Smith et

al., 2006), and the Coleridge rock avalanche (Lee, 2004). In the case of the Craigieburn rock avalanche (volume: approx. 500 x 10^6 m^3), the source area is dominated by well-indurated, highly fractured siltstone and sandstone of the Torlesse Supergroup (compare with chapter 3). Failure did not occur directly on surfaces dipping down slope as the main bedding dips at 40-70° almost perpendicular to the slope. Discontinuities in the rock mass, steeply dipping, closely spaced, and open joint sets assisted a failure that removed part of the ridge-top.

Wright (1998) investigated the Round Top debris avalanche (volume: approx. 45 x 10^6 m^3, Westland, New Zealand), which originated from the top of a 600 m high elongated mountain edifice. Wright suggested that a seismic event is one of the most likely triggering mechanisms for the initiation of the debris avalanche, next to a heavy rainfall event.

2.2 TOPOGRAPHIC EFFECTS ON GROUND MOTION - EXPERIMENTAL FIELD STUDIES & NUMERICAL MODELING

To study the effects that topographic irregularities can have on seismic ground motion, field experiments have been conducted utilizing arrays of seismometers to collect ground motion data from earthquakes, earthquake aftershocks, and nuclear explosion experiments. A number of different experimental field studies, their techniques and main findings are presented in the following paragraphs. Accompanied by accelerating progress in computer technology, numerical modeling techniques have been developed to simulate topographic effects on different seismic wave forms and to confirm observations made during field experiments. A number of papers on fundamental theoretical and numerical techniques are discussed in this chapter.

Borcherdt (1970) analyzed measurements of ground motion generated by nuclear explosions in Nevada for 37 locations near San Francisco Bay, California and compared them with intensities from the 1906 earthquake and recordings of an earthquake in 1957. He focused on amplification effects due to differences in local geology. Sites underlain by bay mud deposits showed a predominant period of about 1 second and maximum ground velocities were greater by a factor of about 2 than at sites underlain by bedrock. Horizontal analog amplifications seem to be dependent on direction.

To study the effects of topography on seismic motion, Davis and West (1973) performed field experiments at Kagel Mountain and Josephine Peak near Pacoima Dam, California. Seismic instruments deployed at the crest and the base recorded several aftershocks of the February 9, 1971, San Fernando earthquake. Instruments that were at Butler Mountain, Nevada, recorded the seismic signal generated by the cavity collapse following the Nevada test site detonation, ALGODONES. Frequency-dependent amplification of the motion at the crest relative to the base was observed at all three mountains. Amplification of up to 30 in the frequency domain was measured at Kagel Mountain. The smallest mountain (Butler Mountain) amplified the motion in a narrow range of periods (peaking around 0.3 to 0.5 sec), the medium-size mountain (Kagel Mountain) showed amplification over a slightly broader range (peaking at periods of 0.4 to 0.5 sec), whereas the largest mountain (Josephine Peak) showed less amplification, but it occurred over a broader range of periods (0.15, 0.2-0.3 and 1.5-2.0 sec). The peak spectral ratios (pseudo-

relative-velocity spectra PSRV) were considerably greater than the peak amplitude ratios. Because the PSRV amplitudes are dependent on the duration of motion, this is an indication of increased signal duration at the tops of the mountain. The increased duration could be caused by resonance of the mountain or could be the effects of body-wave reflection and refraction within the mountain.

For Kagel Mountain the wavelength obtained coincides with the half width of the mountain and could therefore be the reason for shear waves to cause resonance.

After a nuclear detonation test, named CLARKSMOBILE, which was conducted on May 17, 1968, at the Nevada Test Site (NTS), instruments on mountain tops recorded larger amplitudes than those at sites in the valley. Davis and West (1973) concluded that topography can have a significant effect on seismic signals. They pointed out that the widely accepted belief that structures built on hard rock are less susceptible to damaging ground motions than those on unconsolidated materials could be a misleading generalization. The relationship between the incoming wavelengths and the dimensions of the mountain (half-width) might be important for the amount of amplification.

Bard and Tucker (1985) compared experimental observations and theoretical predictions of the effects of underground and ridge sites on the amplitude of seismic waves. Ratios of smoothed Fourier amplitude spectra of S waves recorded on the ridge and in the tunnel were calculated. Results showed that differences in the ridge and tunnel signals can be as large as a factor of 8 in the band between 5 and 10 Hz. A slightly larger scatter noticed in the spectral ratios for the local events, compared to spectral ratios of more distant events, was interpreted as a possible result of greater variability of the azimuth and incidence angles of the local events. Bard and Tucker developed models to resolve the difference between theoretical predictions and experimental observations of topographic effects by modifying a simple homogeneous half-space model to include two naturally occurring phenomena: neighboring ridges and low-velocity layers. The models showed following results (amplification factors of 2-3):

a) The effect of thin, low-velocity surface layers increases the response of the ridge
b) That increase is larger than would be expected from a similar layer in the absence of topography
c) The presence of two neighboring ridges produces narrow-band peaks with amplification

d) Amplification effects could not be predicted using theoretical techniques

Wilson and Pavlis (2000) showed that a near-surface weathered layer of surface bedrock (weathered granites) can significantly influence recorded ground motions and lead to a high local amplitude variability, and causes patterns of high and low spectral response which differ with direction of the incoming wave field.

Poppeliers and Pavlis (2002) present experimental results from a dense seismic array installed on a 50 m high slope of an abandoned surface coal mine near Sullivan (Indiana/USA). Thirty-five three-component seismometers were deployed on a grid with an inter-station spacing of 10 m. The ground motion records resulted from a series of underwater explosions (20 explosions at a fixed shot point in Glendora Lake). The analysis of the data showed that amplitude of the particle motion was largest at the concave part of the slope. Ground motion amplitudes showed the largest effect for the components perpendicular to the slope face and for stations on the steep slope. The largest amplitude occurred at the slope crest.

Field experiments which evaluated topographic effects on ground motion and observed amplification effects on hard rock sites in the presence of irregular topography and geologic structures were conducted by Anderson (1984), Chávez-García et al. (2002; 1990; 1997), Del Gaudio & Wasowski (2007), Gagnepain-Beyneix et al. (1995), Griffiths & Bollinger (1979), Hartzell et al. (1994), LeBrun et al. (1999), Montalvo-Arrieta et al. (2003), Siddiqi (2000), Stewart & Sholtis (2005), Wang et al. (2006), and Wilson & Pavlis (2000).

Various numerical modeling techniques have been incorporated in field studies on topographic effects on ground motions to try to explain the observations experienced in the field (Alves, 2005; Chávez-García et al., 1996; Havenith et al., 2003a; Havenith et al., 2003c; Havenith et al., 2002; Paolucci et al., 1999).

A hill site (Cedar Hill) in Tarzana, California, was chosen to study the three-dimensional response of the site to incident shear waves polarized in different directions (Bouchon et al., 1996; Lee, 1994; Lee et al., 1994; Spudich et al., 1996). That hill produced one of the highest ground accelerations ever recorded (1.78 g) in an earthquake during the Northridge earthquake, California, in 1994. The ground motion was consistently amplified at stations at or near the top of

the hill compared with stations at the base of the hill. The local amplification factors calculated were in the range from about 1.5 to 4.5 depending on frequency and direction of motion. The largest amplifications occurred for motions transverse to the elongation of the hill, whereas the smallest occurred parallel to the direction of elongation. The authors inferred a rotation of polarization of particle motions from the base to the top of the hill. The amount of rotation depended on the polarization of the incident source wave field.

A numerical simulation (Bouchon, 1996) based on observations showed that at 3.2 Hz ground motion was amplified all over the upper part of the hill. It was largest at the centre of the top (up to 45% amplification) whereas at the base deamplification (5-10%) occurred. This pattern is indicative of a fundamental oscillatory resonance mode of Cedar Hill. At 5 Hz values of amplification reached 60% at the top. At 10 and 15 Hz the zone of largest amplification shifted from the top to the northern and southern edges of the hilltop platform (66% at 10 Hz; 100% at 15 Hz). At the same time the centre part of the hilltop experienced deamplification at 15 Hz. The largest amplification took place near the northern edge of the hill platform, above the steepest flank of the hill. Motion on the hill flanks was amplified, particularly in areas where the slopes were steepest. The calculated amplification values were lower than those observed.

Seismic records of local and regional earthquakes were used to study amplification and wave diffraction on an elongated ridge near Sourpi in central Greece (Pedersen et al., 1994). The data were analyzed in the frequency and time domains. The ridge used for this study is about 5 km long, 2.5 km wide and 300 m high and represents a tectonic fold of 400 m thick Middle Triassic-Jurassic limestone. The soil cover is very thin (0-20 cm) with limestone outcrops at the surface. Seven seismological stations (Mark L4C3D) were installed along a profile perpendicular to the topography. They were buried in holes down to hard rock to avoid site effects from surface soil and to reduce noise due to the wind. 14 local and regional shallow earthquakes recorded were selected for analysis. Three of these 14 events were recorded on all stations. Epicenters were distributed quite evenly around the ridge. Spectral ratios were calculated for the 14 events and showed an average maximum of 2.5 for the N-S component, 2 for the E-W component, and 1.5 for the Z-component.

Additional numerical simulations show an emission of a diffracted wave from the top of the ridge. The actual focusing of energy may not necessarily take place at the surface, but can possibly take place at some depth beneath the top of the ridge. It can be shifted horizontally depending on the frequency, azimuth, and the angle of incidence. In most simulations amplification exists near the top of the ridge or on the uppermost part of the flank, possibly due to focusing of energy and constructive interference between the incident and the diffracted waves.

Another site was chosen to study amplification at a very steep ridge. The ridge, Mont Saint Eynard, is located in the French Alps and is an elongated structure that consists of hard rock (Jurassic limestone) with hardly any overburden. 5 seismometers (Mark L4C3D) were installed across the edifice: two on hard rock and three instruments on sites with a shallow sedimentary cover. Time-domain records observed at the hill showed that amplitudes were up to an order of magnitude higher for the stations located on sediment than for those recorded on hard rock.

Spectral ratios show amplifications up to about 3 between 1 and 4 Hz.

Numerical simulations showed an agreement between observations and numerical simulations regarding the level of amplification due to topography, and that absolute amplification takes place at different locations at different frequencies. Amplification can occur at or close to the top of the ridge. The results show also that problems in data analysis are closely connected to a lack of a reference station. The site effects due to topography extend much further in space than the topography itself. Therefore, deamplification at the reference station can be interpreted as amplification elsewhere. Another important fact might be the lack in knowledge on the polarization and complex nature of the incoming wave field. Numerical simulations showed that theoretical spectral ratios are significantly affected by the azimuth, incidence and the type of the incoming waves, whereas the measured ratios seem to be unaffected.

Purely theoretical approaches and numerical modeling techniques have been developed to find analytical solutions for the interaction of seismic waves with arbitrary geometries. Various methods have been used to describe wave propagation in realistic media and to simulate diffraction of seismic waves by irregular 2D and 3D topographies (Aki, 1993; Ashford et al., 1997; Assimaki and Gazetas, 2004; Assimaki et al., 2005; Benites and Olsen, 2005; Boore, 1972; Bouchon, 1973; Bouchon, 1996; Bouchon et al., 1996; Bouckovalas, 2005; Dhakal, 2004;

Havenith et al., 2003a; Jousset et al., 2004; Kaeser, 1999; Komatitsch and Tromp, 1999; Luo et al., 2004; Luzon et al., 1997; Luzón et al., 1999; Moczo et al., 1997; Narayan and Prasad Rao, 2003; Oprsal, 2000; Paolucci, 1999b; Paolucci, 2002; Robertson and Holliger, 1997; Sánches-Sesma and Campillo, 1993; Savage, 2004; Shinozuka et al., 1999; Sincraian and Oliveira, 2000; Wang et al., 2000; Wong and Jennings, 1975).

Ashford et al. (1997) conducted a frequency-domain study numerically (Generalized consistent transmitting boundary method; Deng (1991)) to evaluate the significance of topographic effects on the seismic response of steep slopes and concluded that there is a relation between the slope height (H) and the wavelength of the motion (λ). The peak topographic effect occurs at $H/\lambda = 0.2$ and is most apparent for slopes steeper than 60°.

Geli et al. (1988) reviewed experimental and theoretical results about topographic effects on ground motion. It has been recognized that the observed amplifications in the field are systematically larger than the results of theoretical approaches. On top of that, they investigated the effect of neighboring ridges and complex subsurface geological conditions on ground motion variation across an edifice. They concluded that as in previous studies, results are consistent only on a qualitative basis. Even up-to-date numerical approaches cannot quantitatively explain the high values of amplification of ground motion due to topographic irregularities that were observed in field experiments.

2.3 MATHEMATICAL MODELS EVALUATING THE RESPONSE OF WEDGE-SHAPED EDIFICES TO ARBITRARY VIBRATION INPUT

Simplified theoretical approaches in two-dimensional systems have been used in engineering seismology to evaluate resonance frequencies, lateral response, and stability of earth dams, rock filled dams, embankments, and soil profiles to seismic vibration input.

Ambraseys (1960) presented a mathematical investigation of the shear response of two-dimensional wedges (Fig. 2.5) subjected to arbitrary horizontal disturbance.

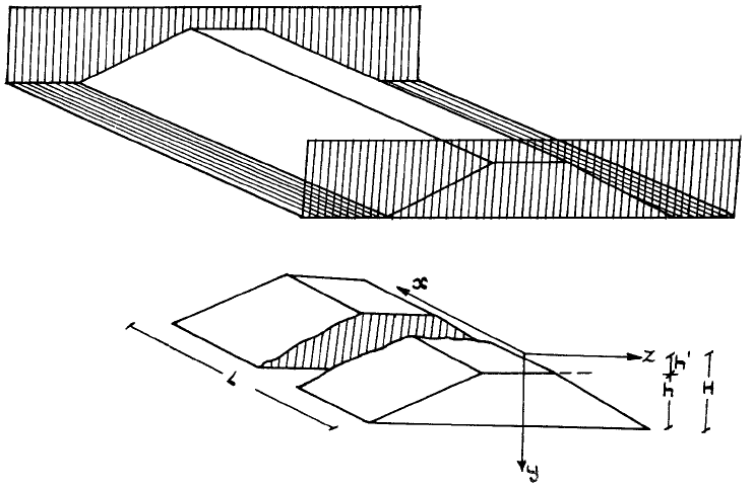

Figure 2.5: Ambraseys model of a two-dimensional and symmetrical wedge of height H and length L. x, y, and z represent the orthogonal coordinate system. The horizontal disturbance acts in z-direction only. h' represents the level of truncation.

The wedge-shaped structure is assumed to be perfectly elastic and made up of material with constant rigidity. The simplified analysis deals with oscillations that arise from horizontal disturbance acting normal to the main axis of the edifice at the base and vertical sides of the wedge. Oscillations are treated as oscillations in simple shear. Bending moments were neglected. An example of a calculation using Ambraseys approach is presented in chapter 3.6.2. Figure 2.6 shows the graphic solution for the three-dimensional deformation of a homogeneous wedge-shaped edifice for the first longitudinal mode and the first two transverse modes of vibration.

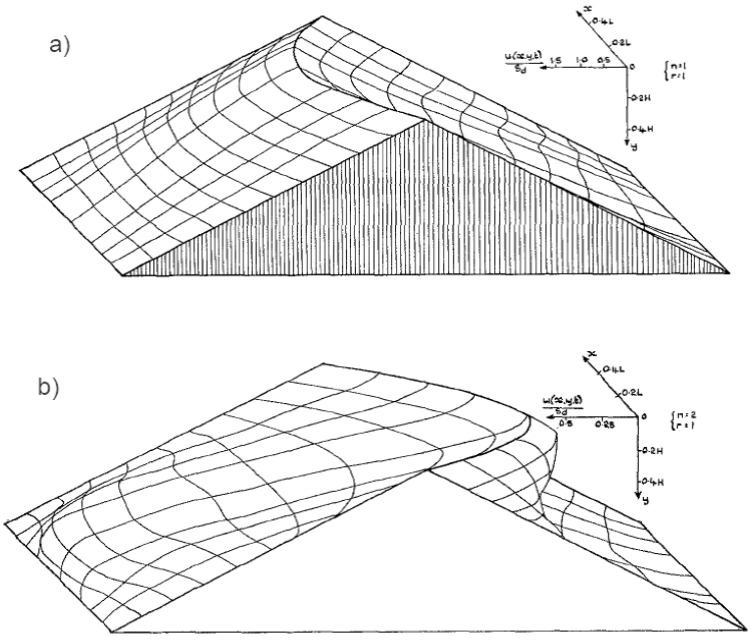

Figure 2.6: Three dimensional distortion of a complete wedge for the first two transverse modes a) n=1 & b) n= 2 and first longitudinal mode (r=1) of oscillation. (modified after Ambraseys, 1960)

A widely used and accepted method is the shear beam analysis. The analysis considers a wedge-shaped structure, for example a dam, as a shear beam. The structure is sliced at both ends perpendicular to its main axis. The resulting plate is then analyzed as a whole shear beam or on individual blocks section by section (Fig. 2.5, Fig. 2.7).

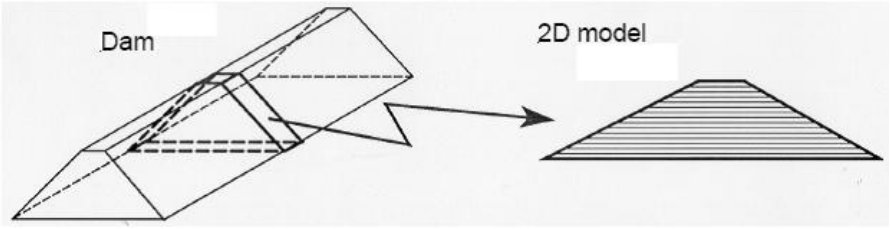

Figure 2.7: Two-dimensional model of a wedge-shaped structure (after Darbre, 2000)

The shear beam theory is based on two assumptions:

1. The structure is considered a beam with variable wedge-shaped cross sections. Shear strains, shear stresses, and displacements are horizontal only and uniformly distributed across the width of the structure
2. The structure deforms in simple shear only

Two-dimensional shear beam models have been used for example by Okamoto (1973), Dobry et al. (1976) and Dakoulas & Gazetas (1985) and gained popularity because of their simplicity and realistic output. A summary presenting the essentials of the shear beam approach can be found in Kramer (1996). Paolucci (1999a) presents a different procedure based on Rayleigh's method for estimating fundamental vibration frequencies of two-dimensional, homogeneous but asymmetric mountain edifices.

These mathematical models are based on idealized, simple homogeneous geometries and only simple shear. However, they can be used as a first approximation to evaluate the shear response of an edifice, for example a mountain ridge of simple symmetric geometry and uniform lithology. In chapter 3.6.2 three different simplified mathematical approaches are used to evaluate theoretically the response of a symmetric and bedrock dominated mountain edifice. The theoretical results are then compared with field observations.

2.4 PHYSICAL LABORATORY MODELING STUDIES

Little has been done to study seismic wave propagation and topographic effects on ground motion utilizing small-scale physical laboratory modeling techniques. Focus has been mainly on the performance of man-made structures during moderate to strong ground motion input. A common physical laboratory technique, utilized in earthquake geotechnical engineering to evaluate the seismic response and performance of structures, is the application of shaking table experiments. Only a few small-scale physical approaches have been conducted to study the effects of elevated topography (e.g. mountain ridges etc.) on seismic ground motions.

Rogers et al. (1974) conducted a scale model experiment to study the effect of topography on ground motion for incident P waves. They found that a simple topographic feature does not trap seismic energy caused by P waves to any great extent. Most of the incident P-wave energy propagates away from the top as down-scattered body waves and two large Rayleigh waves moving away from the ridge crest in opposite directions. Amplifications occur for a predominant input wavelength equal to the width of the base of the edifice. The flanks and the base show the most complex motions. The authors also pointed out that the combination of topography and

near-surface layering may interact in a complex way to produce amplification or deamplification at a particular site.

After exceptionally large horizontal ground accelerations (PGA of ~ 1.25 g) were recorded during the 1971 San Fernando, California earthquake on a ridge crest in the vicinity of Pacoima Dam, studies were focused on topographic effects on recorded seismic waves. Anooshehpoor and Brune (1989) constructed a small-scale (1:816 in scale), three-dimensional foam rubber model of the actual topography around the Pacoima Dam accelerometer site to study the dynamic interaction between the Pacoima Dam and the adjacent ridge (Fig. 2.8).

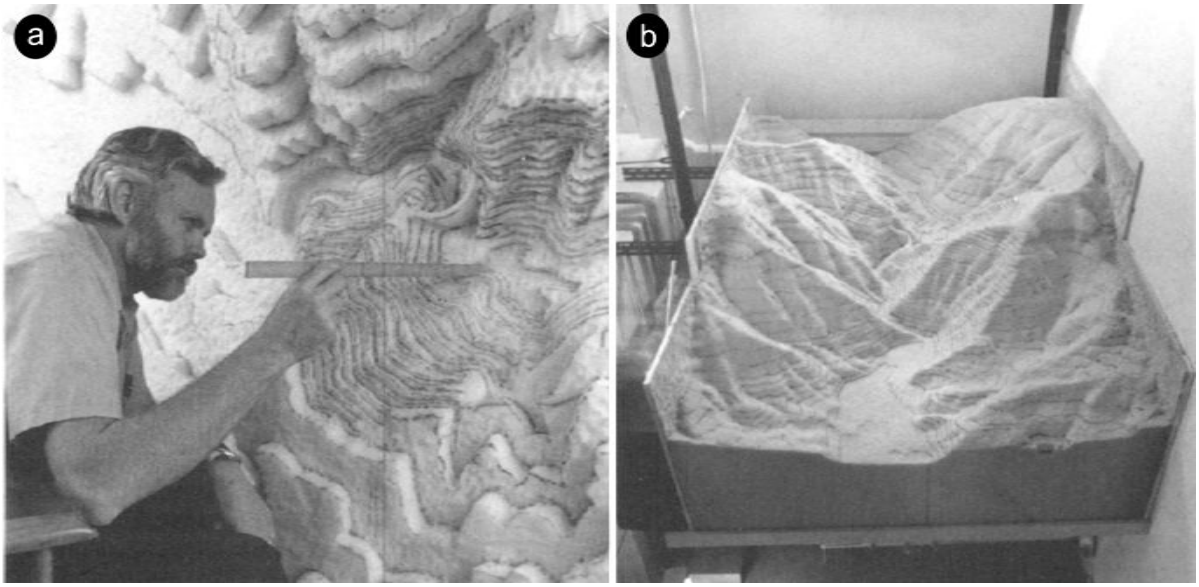

Figure 2.8: Pictures showing a) the method of checking the contour levels at the area around Pacoima dam during the process of constructing the 3D foam rubber model and b) the complete 3-D foam rubber model of the topography around Pacoima Dam (scale 1:816)

To simulate near plane shear waves of vertical incidence, a fiberglass plate was glued to the flat bottom of the model. It was coupled to an electromagnetic driver that excited the plate impulsively parallel to the flat side of the model. The shear wave velocity the field was assumed to be 2000 m/s. The surface displacement was measured using position sensing detectors that were capable of measuring two orthogonal components of the surface motion simultaneously. The results showed amplification of ground motion at the ridge crest for vertically incident SH waves up to 60% compared to the flat ground at a frequency that is comparable to 6 Hz in reality. Because the large peak acceleration was observed at near 10 Hz and the results from the foam

rubber model indicated deamplification at that frequency range, they concluded that the foam rubber model showed little evidence of amplification of the ground motion due to the surface topography and therefore cannot explain the high accelerations observed. They pointed out that the accuracy of the scaled frequency in their study depends on the accuracy of the assumed shear wave velocities.

Lohn (1989) continued experimenting with the detailed Pacoima Dam model setup and also tested the seismic response of different simple geometric shapes (ridges with different slope angles, pyramids, etc.) using low-density foam rubber. The displacement was measured for each site on various geometric shape models. Fourier spectra were calculated and compared with spectra for the free field. The ridge models all showed amplification of the incoming seismic waves at the crest. Two models, representing shallow- and steep-sided hills with a concave-formed crest, amplified the signal at the top. Further tests with the detailed Pacoima Dam model showed in general complex amplification of the seismic signal at ridges and de-amplification in canyons compared to the free field. The data also showed a proportional relationship between the distance of the vertical wavefront and the level of amplification at the topographic prominence.

These experiments are the only physical laboratory models mentioned in the literature that simulated topographic effects on ground motion using an impulsive earthquake input that simulated shear wave propagation at frequencies in audio range which propagated through the model.

Chemenda et al. (2005) and Bachmann et al. (2004) used a technique based on a new elasto-brittle-plastic analogue material combined with a vertical accelerator device to simulate and study the failure of rock mass due to increased gravitational acceleration causing deep seated landslides.

Other physical experiments have been conducted using centrifuge or shaking table tests to study slope conditions or the response of engineering structures under dynamic load (Campbell et al., 1991; Dewoolkar et al., 2000; Gibson, 1996; Katz and Aharonov, 2006; Lin and Wang, 2006; Madabhushi, 1996; Prasad et al., 2004; Rogers, 1930; Williams and Blakeborough, 2001).

2.5 APPLICATIONS – SEISMIC SLOPE STABILITY ANALYSIS & HAZARD ASSESSMENT

A commonly used tool to implement and process the known background information on topographic effects on seismic ground motion is the use of slope stability analysis techniques to model and evaluate the performance of slopes subjected to dynamic input forces. Slope stability analyses are the basis of every landslide hazard assessment. Various authors have presented different techniques to evaluate the factor of safety for slopes under dynamic load, to determine threshold values for earthquake induced landslide initiation, and to discuss related dependencies on earthquake source parameters (Al-Homoud and Tahtamoni, 2000; Carro et al., 2003; Chang et al., 2005a; Dhakal, 2004; Fernandez Merodo et al., 2004; Genevois and Romeo, 2003; GovindaRaju et al., 2004; Harp and Wilson, 1995; Malamud et al., 2004; Nasim, 2005; Refice and Capolongo, 2002; Rocscience, 2001; Romeo, 2000; Wilson and Keefer, 1983)

The literature review showed that there is no simple way of explaining topographic effects on ground motion. It represents one of the main input parameters for slope stability analysis under dynamic load and the assessment of seismically triggered landslide hazards. Therefore slope stability analyses and predictive modeling are highly dependent on the quality, complexity, and accuracy of the input. Uncertainties and missing input parameters will subsequently lead to a more simplistic output which has to be handled with care (Murphy, 2006; Murphy et al., 2002).

2.6 TOPOGRAPHIC EFFECTS ON GROUND MOTION – LITERATURE RÉSUMÉ

The literature on the effects of topography on seismic ground motions can be summarized as follows. The main aspects and key information are summarized, subdivided into Geological & Geotechnical aspects and Seismological & Geometrical aspects, and listed in the following paragraphs:

2.6.1 GEOLOGICAL & GEOTECHNICAL ASPECTS

- Parameters such as slope angle, slope orientation, and lithology influence the amount of topographic amplification of ground motion
- Discontinuity orientation is an important control on slope instability

- Increased landsliding due to the presence of topographic effects
- Threshold displacements of about 2-5 cm leading to significant strength reduction and disrupted/non-cohesive slides (Sepúlveda et al., 2005a)
- Vertical accelerations may have a significant impact on slope stability by affecting the shear and normal stresses on sliding blocks with steep shear surfaces and by a loosening effect on the block interlocking
- Earthquakes tend to both trigger failure of the most susceptible material on the slope and to fracture and dilate the underlying rock mass and thus set the stage for additional deep-seated failures in future earthquakes
- The widely accepted belief that structures built on hard rock are less susceptible to damaging ground motions than those on unconsolidated materials could be a misleading generalization
- Topographic site effects contribute to the initiation of large-scale mass movements during strong earthquakes
- If site response directivity occurs during moderate-strong earthquakes along potential sliding directions, it would considerably increase the susceptibility of slopes to seismically induced failures

2.6.2 SEISMOLOGICAL ASPECTS & GEOMETRICAL ASPECTS

- There is a distinct variation in ground motion amplitudes between ridge crests and valley sites
- Topographic amplification and resonance of the edifice is most pronounced when the seismic wave length is about the same as the dimension of the topographic feature
- Amplification is strongly influenced by the angle, the direction of incidence, and the complexity of the seismic wave field
- High amplification values are mainly controlled by the presence of low-velocity layers at the surface, with a 3D effect at the crest of the edifice. The presence of a deeply weathered layer of bedrock of various thickness all over the mountain turns out to be a significant factor constraining local site effects and increasing the response of the ridge sites

- Multiple reflected and diffracted body waves within a mountain ridge, and a complex interaction between Rayleigh and Love waves, can contribute to high levels of damage and ground disruption
- Transverse oscillations of elongated 3D mountain edifices are dominant over the ridge-parallel modes
- There is no strong topographic effect on vertical ground motion
- Comparisons of observations with theoretical and numerical results indicate that the 3D shape of the mountain edifice and its internal structure are important factors affecting its response
- The complex and unknown polarization, the nature of incident wave field, and a lack of information on the internal geological structure of mountain edifices causes discrepancies between numerical models and field observations

3 THE LITTLE RED HILL FIELD EXPERIMENT

3.1 INTRODUCTION

It has been recognized that topography can significantly affect local ground motions during a seismic event. A large number of studies have been published discussing the response of soft soil sites and soft soil basin structures when subjected to ground motions caused by earthquakes. Observations from seismic arrays that recorded earthquake events, their aftershock sequences and recordings from artificial sources (mine blasts, nuclear detonations) provided first insights in the complex interaction of seismic waves with topography (refer to chapter 2).

There is however a lack of studies which provide high-quality data on the response of bedrock mountain edifices to seismic waves. To study site effects of topography on seismic ground motion in a field situation, a small, elongated, bedrock-dominated mountain ridge was chosen and equipped with a seismic array.

This chapter outlines the results from the seismic field study at Little Red Hill. A site description presenting a geographic overview, geological and geotechnical introduction is followed by presentation of the data acquisition techniques and details of the seismic array. A brief summary of data from the field study leads to the data analysis and its results for a number of selected earthquake recordings. Data are summarized, further interpretation provided and results are discussed at the end of this chapter.

3.2 SITE DESCRIPTION

The Little Red Hill (LRH) test site is located about 100 km west of Christchurch in the South Island of New Zealand. It is situated near the base of Red Hill at the southern end of the Craigieburn Range, east of Lake Coleridge. A topographic map with an overview of the test site location is presented in figure 3.1.

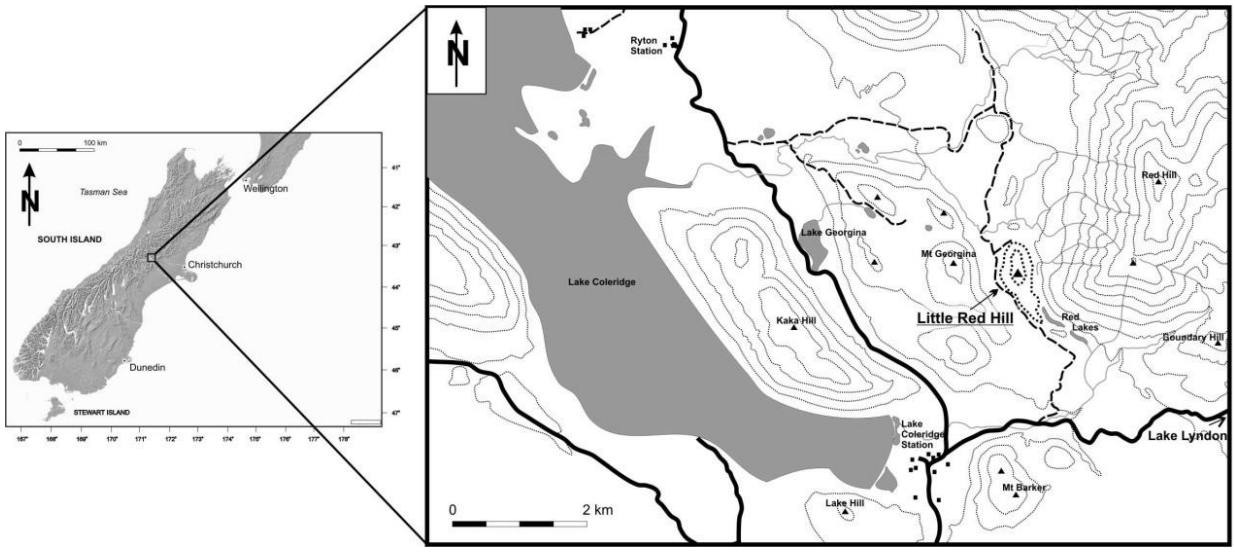

Figure 3.1: Location of the Little Red Hill test site

The main axis of LRH is elongated in a nearly N-S direction. Little Red Hill is surrounded by a flat area which comprises glacial outwash gravels and moraine deposits, whereas the mountain edifice itself is made up of heavily indurated sandstones and argillites of the Mesozoic Torlesse Supergroup (Bradshaw, 1971). Bedding strikes approximately transverse to the main axis of the edifice, in an E-W direction, dipping northward between 36 and 89 degrees. Massive sandstone beds dominate the edifice but alternate with interbedded sequences of both sandstone and argillite that show bedding thicknesses of a few centimeters to decimeters. A simplified geological overview of Little Red Hill and the surrounding area is presented in figure 3.2.

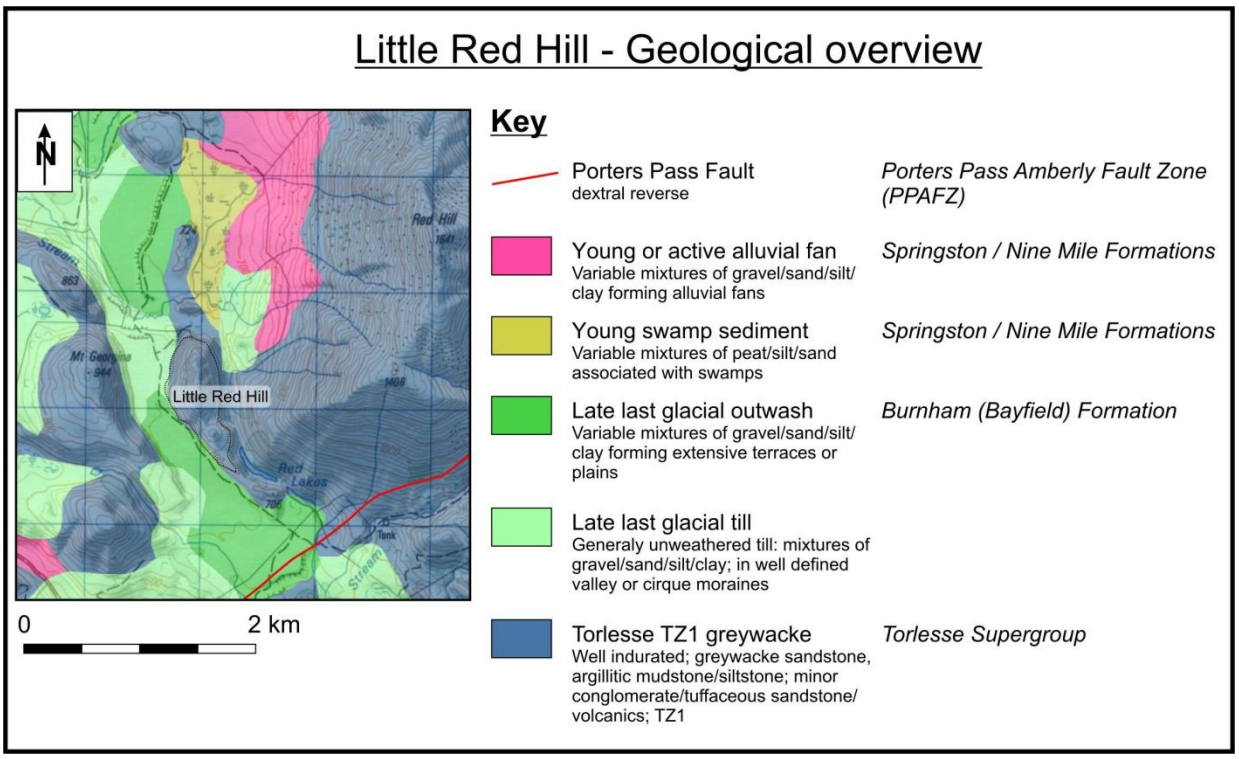

Figure 3.2: Geological overview, based on QMAP 15 Aoraki (GNS 2007)

The edifice was chosen for the test because, in contrast to prior experimental studies of this kind (Lee, 1994; Lee et al., 1994; Paolucci et al., 1999; Spudich et al., 1996), it is dominated by exposed bedrock and has only minor talus deposits on its flanks. Prominent features at the top of the edifice are areas with heavily fractured bedrock and seismogenic block fields with individual blocks reaching 2-3 m in diameter. A map of Little Red Hill that shows an overview of major geotechnical features is presented in figure 3.3.

Little Red Hill - Geotechnical overview

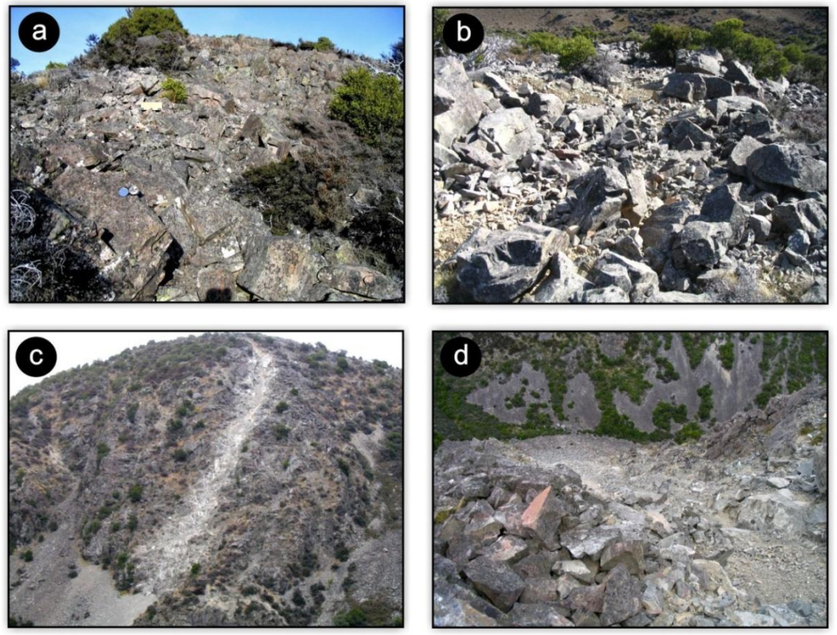

a, b) Extensive seismogenic blockfield at the very top of Little Red Hill, close to station rh6. Individual boulders reach up to 2 m in diameter.

c, d) View towards the rockfall channel at the eastern flank of Little Red Hill and view from its source scar downslope (located at the top of the edifice next to station rh6).

Key

- 76 — Strike & dip
- • rh0 — Seismograph / station ID
- 600 — Topographic contours [mASL]
- Seismogenic block field, (individual blocks > 1.5m), heavily fractured bedrock
- Debris / Blocky debris (>0.5 m)
- Rock fall - wedge failure source scar
- Bedrock (Mesozoic Torlesse Supergroup, indurated, complexly deformed sandstones & argillites)

Figure 3.3: Little Red Hill – map and photographs presenting an overview of major geotechnical features of the edifice

3.3 DATA ACQUISITION

An array of seven seismic stations was temporarily installed on Little Red Hill to record seismic activity (Fig. 3.4). The seismographs were placed solely on bedrock; five stations (rh2-rh6) along the ridge crest and one station (rh1) on the flank of the edifice.

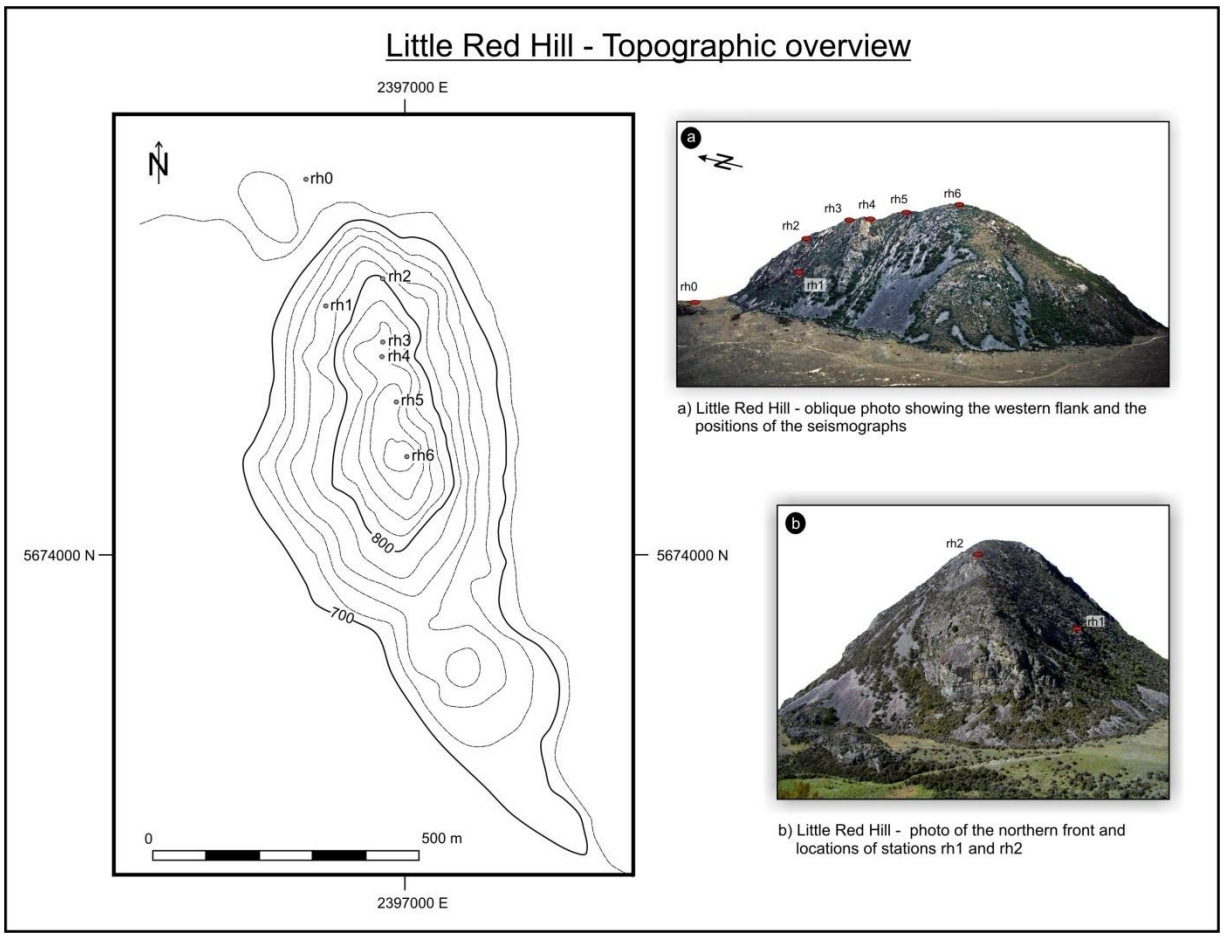

Figure 3.4: Topographic map of the Little Red Hill and photographs, showing the locations of installed seismographs (rh0-rh6)

The sites were chosen in order to give spatial information of ground motion across the elongated edifice. A base station (rh0) was placed on bedrock within the flat area next to the hill, firstly to minimize topographic effects, and secondly to act as a reference station for the other instruments.

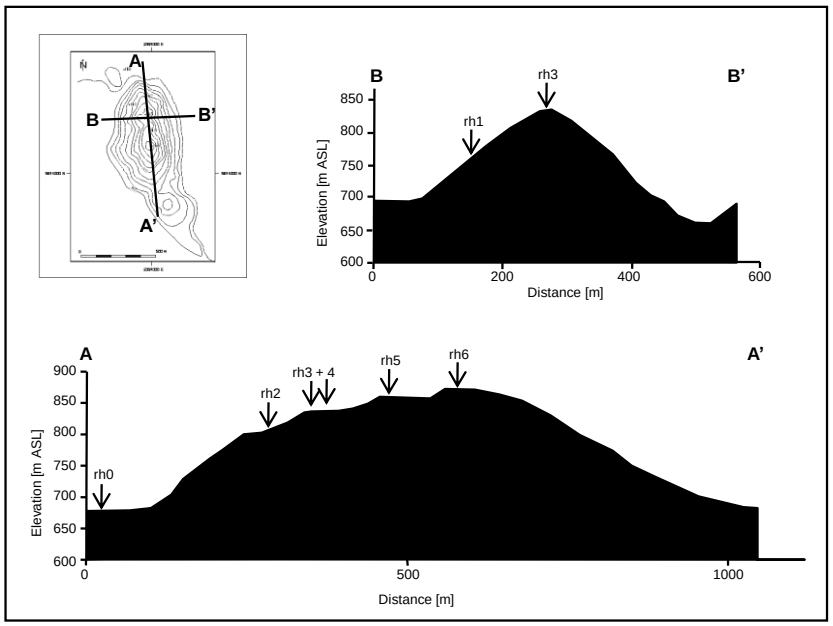

Figure 3.5: Little Red Hill – Topographic profiles showing the distribution of the seismic stations along the profiles marked A-A' and B-B'

The data were recorded by seven Mark Products L-4-3D velocity sensors with a natural frequency of 1 Hz. Each of the sensors was connected to a portable EARSS data acquisition system, version 9.12 (Gledhill et al., 1991). The sampling frequency was set to 50 Hz, gains were set to two. The seismometers were all orientated in a north-south, east-west coordinate system to be able to compare the recordings of every station. Each seismometer was placed on a leveled concrete paving slab that was fast-concreted onto bedrock. The sites were GPS-surveyed to give precise locations, both horizontally and vertically. Table 3.1 shows their exact locations and elevations.

Table 3.1: Station coordinates (New Zealand Map Grid and World Geodetic System 1984)

Station	Altitude [m a.s.l.]	Northing [m N]	Easting [m E]	Latitude [°South]	Longitude [°East]
rh0	684.65	5764706.52	2396811.28	43.316555	171.604428
rh1	759.46	5764471.76	2396848.88	43.318673	171.604843
rh2	812.60	5764522.28	2396955.93	43.318235	171.606173
rh3	858.01	5764403.30	2396955.01	43.319305	171.606137
rh4	862.29	5764375.86	2396952.97	43.319552	171.606107
rh5	874.56	5764292.14	2396981.09	43.320310	171.606436
rh6	892.35	5764190.01	2396999.14	43.321232	171.606637

Details regarding the instrument setup and technical specifications of the equipment are presented in appendix A.1.

The field experiment was divided into two main stages.

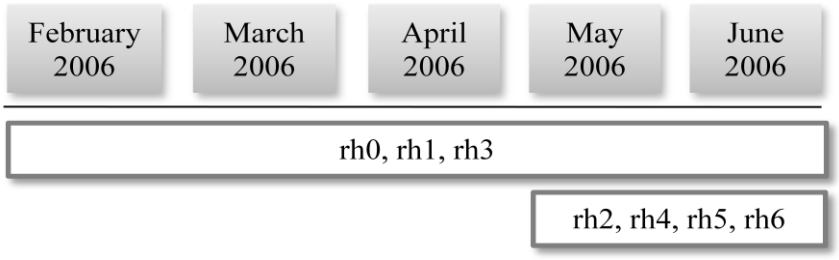

Figure 3.6: Instrument setup periods, showing stations rh0, rh1, rh3 were deployed for a period of 5 months (February 2006 – June 2006). Stations rh2, rh4, rh5 and rh6 were added in May 2006

Measurements during stage one were carried out using the base station rh0, as well as stations rh1 and rh3 from the end of February 2006 onwards. Four additional instruments (rh2, rh4, rh5, rh6) were placed along the ridge crest in May 2006.

At the end of the last phase of the field experiment a detonation of 8 kg of *Powergel™*, about 1.5 km north of the edifice, provided ground motion data from an artificial source. The explosives were placed in 13 boreholes, each 3.2 m deep, which were drilled into Torlesse bedrock to provide maximum energy transmission towards the test site. Because it turned out that the detonation had a less significant effect on the response of the edifice than expected, data analysis and results of this test are presented and briefly discussed in appendix A.5.

3.4 RECORDED EARTHQUAKE EVENTS

In total 313 regional and teleseismic events were recorded between February 2006 and June 2006. The majority of events were recorded during the first instrument setup period which comprised only three instruments (rh0, rh1, rh3). A delay in delivery and technical problems at the time unfortunately made it impossible to set up the extended array of seven instruments that covered the entire ridge of the edifice from the start. The decision was made to place emphasis on processing array recordings that were collected with all seven instruments to deliver a better insight of the response of the entire ridge. The fact that these events triggered all seven stations

implies that the input was more or less uniform across the region and should result in a distinct response of the edifice.

Therefore this study uses data from 8 events for analysis, representing earthquakes of a wide range of magnitudes (M 1.8 – 7.4), focal depths (5.0 – 151.6 km), epicentral distances (10.2 – 1500 km), and different azimuth towards the test site (23 - 356°). A distribution of the epicenters is shown in figure 3.7. Source parameters of the selected earthquakes are presented in table 3.2.

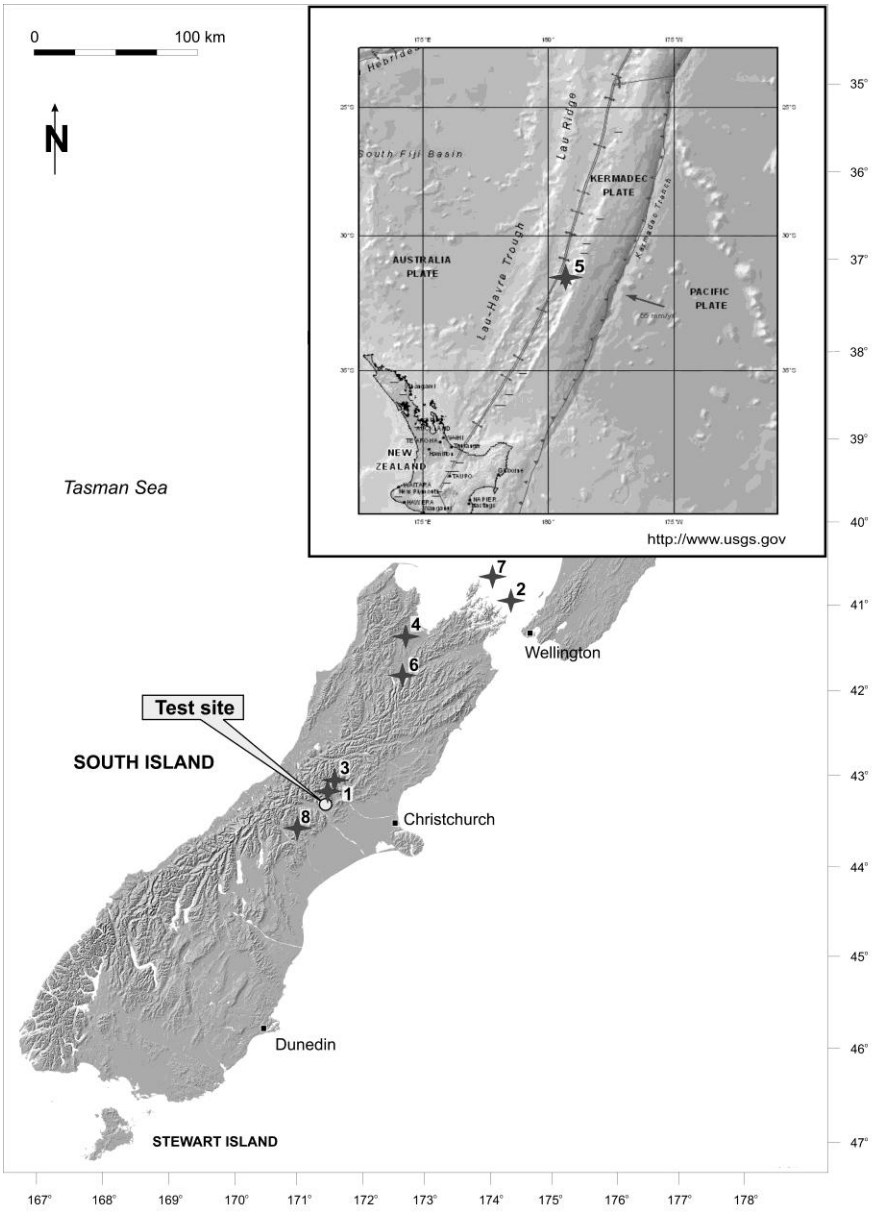

Figure 3.7: Epicentre distribution of the selected earthquake events in respect to the test site location (labeled using event ID as listed in table 3.2)

Table 3.2: Earthquake parameters for selected events (Source: Geonet, USGS). The azimuth represents the angle of the epicentre towards the test site, measured clockwise from north

Event	*EQ Location Date.Time (yyyymmdd.hmin)*	*Latitude [°South]*	*Longitude [°East]*	*Depth [km]*	*Magnitude [M_L]*	*Epicentral Distance [km]*	*Azimuth [°]*
1	NZ, Mt Olympus 20060512.2320	43.23	171.60	5	1.8	10	356
2	NZ, Porirua 20060514.1733	40.94	174.45	59.4	5.0	353.66	42
3	NZ, SE' Arthur's Pass 20060515.2027	42.99	171.90	12.0	3.0	44.22	32
4	NZ, SW' Nelson 20060515.2038	41.27	172.81	146.2	3.8	248.72	23
5	Kermadec Islands 20060516.1042	31.53	179.30	151.6	7.4 (M_w)	1500	29
6	NZ, SW' St Arnaud 20060516.1121	41.87	172.80	89.1	3.5	188.61	31
7	NZ, NW' Cook Strait 20060517.0147	40.60	174.33	64.0	3.7	376.75	37
8	NZ, NW' Mt Somers 20060519.1900	43.54	171.17	12.0	2.6	43.04	234

A full catalogue of acceleration records of the three components of ground motion at the seven stations rh0 to rh6 for the selected earthquakes events can be found in appendix A.2.

3.5 DATA ANALYSIS AND RESULTS

Three different approaches are used to analyze earthquake waveform data for the site response evaluation of Little Red Hill:

- Calculation and comparison of peak ground accelerations (PGA)
- Power spectral density (PSD) analysis
- Standard spectral ratio (SSR) analysis

In order to provide reliable estimates of the site response, a reference station that is free of any site effects had to be installed (seismograph station rh0).

The reference site rh0 fulfills the two following conditions:

a) The reference site is located close enough to the examined stations to ensure that resulting differences at each site are only due to site conditions and not to variations in source radiation or travel path. This will be assured if the hypocentral distance is about 10 times larger than the array aperture;
b) The reference station is located on the same geological formation to be unaffected by any kind of site effect.

For the time-domain analysis the PHA (Peak Horizontal Acceleration) as well as the Peak Acceleration for the vertical ground motion (PVA – Peak Vertical Acceleration) were calculated for every instrument on the mountain edifice and compared with the base reference station rh0. The following section presents the resulting amplification factors for the ground motion components in vertical direction (Z), and the horizontal direction parallel (N-S) and transverse (E-W) to the direction of elongation of the mountain edifice for each of the selected earthquakes. The data are plotted as a percentage increase or decrease of the signal received at each station (rh1-rh6) across the hill compared to the base reference station rh0.

In order to investigate the distribution (over frequency) of the power contained in the recorded signals and to extract dependencies of all ground motion components of the selected earthquake events presented above the multitaper method (MTM; Percival & Walden (1993)) was used to

estimate the power spectral densities (PSD) of the time series data. A time window of constant duration was chosen around the S-wave amplitudes of the seismograms. The PSD multitaper method (MTM) utilizes the sampling frequency of the seismograph (50 Hz) to compute the PSD over frequency. This method provides detailed information about the frequency response of the stations along the edifice for the different earthquake events. A complete presentation of the PSD analyses plots is attached in appendix A.3.

The widely used standard spectral ratio (SSR) technique was first introduced by Borcherdt (1970); it compares recordings at nearby sites through spectral ratios to identify characteristic site effects. Calculating standard spectral ratios allows one to evaluate distinct resonance modes of the edifice at respective stations while eliminating, or at least reducing, the influence of source, path, and instrument response effects. Spectral ratios were computed for each of the three components for the selected event as follows. First, the Fourier amplitude spectra were calculated for a constant time window (of up to 30s) for each event around the largest amplitudes of the seismograms. The Fourier amplitude spectra represent information on how the amplitude of the motion is distributed with respect to frequency. All spectra were smoothed with a three-point moving average filter. Then, the spectral ratios were computed by dividing the smoothed Fourier spectrum of each station at the edifice (rh1-rh6) by the Fourier spectrum of the base reference station rh0.

In this project, the SSR technique was used to confirm results gained by the time domain and PSD analysis. The calculation of the PSD is closely related to SSR method (Aki and Richards, 2002). SSR uses a single Fourier transform to present the ratios of Fourier amplitude spectra, whereas PSD represents a measure of power, which is proportional to the square of displacement of an elastic material. Therefore the PSD technique results in a display of a more distinct peak response.

The results of the three techniques are presented for each of the selected earthquake events in the following paragraphs. The time domain analysis and the Pseudo Spectral Density analysis are calculated and displayed for all three components of ground motion within the main chapter, while the Standard Spectral Ratios are only shown for the horizontal E-W component. A complete presentation of the SSR analyses plots is attached in appendix A.4.

3.5.1 MT OLYMPUS EARTHQUAKE 20060512.2320

3.5.1.1 Time domain analysis

Table 3.3: Mt Olympus earthquake – observed time-domain data at the station with the greatest amplitudes (rh6)

Location /component		Peak ground acceleration [g]	Peak ground velocity [cm/s]	Peak ground displacement [cm]	Effective duration [s]
S' Mt Olympus 20060512.2320	Z	0.0058	0.0750	0.0015	3.22
	N-S	0.0054	0.1054	0.0039	3.74
	E-W	0.0079	0.1728	0.0057	3.12

Ground motions recorded for the magnitude 1.8 Mt Olympus earthquake were greatest at the top of the hill at station rh6. Table 5.3 shows that the PGA at the hilltop station rh6 was greatest in the E-W direction with a value of 7.9 milli-g. A displacement of 0.057 mm was measured in E-W direction, followed by the N-S component with 0.039 mm. The displacement in vertical direction reached a maximum of 0.015mm for this earthquake.

The effective duration of ground motion varied between 3.12 s for the horizontal component parallel to the axis of the edifice (N-S) and 3.74 s in transverse direction (E-W).

Peak Ground Acceleration (PGA)

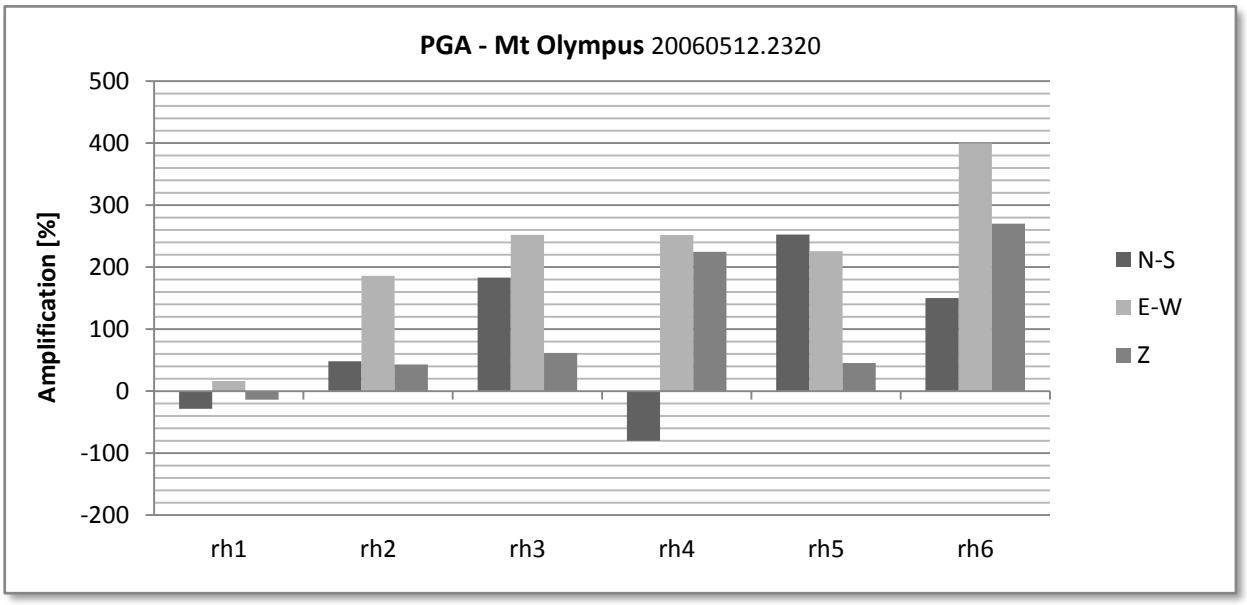

Figure 3.8: Mt Olympus earthquake - Amplification of Peak Ground Accelerations relative to reference station rh0 – Motion component transverse (E-W), parallel (N-S) to the main axis and in the vertical direction (Z)

Figure 3.8 presents the amplification of ground motion of every station on the hill compared to the base reference station. The results are shown for the three components of motion.

The N-S motion component shows de-amplification at the flank of the hill (station rh1; -29 %) and at station rh4 (-80 %), all other stations show amplification of ground motion compared to the base station. Maximum amplification recorded in the north-south direction is 250 % at station rh5.

Amplification was recorded at all stations for the E-W component (motion perpendicular to the main axis of the edifice). The largest amplification, with a value of 400 %, was calculated for station rh6. Station rh1 shows the least amplification at 16 % relative to station rh0.

In the vertical direction of ground motion amplification values of 270 % were reached at the top of the hill at station rh6. The flank of the edifice at station rh1 experienced de-amplification (-14 %).

3.5.1.2 ***Frequency domain analysis***

Power Spectral Density (PSD) – Multitaper Method (MTM)

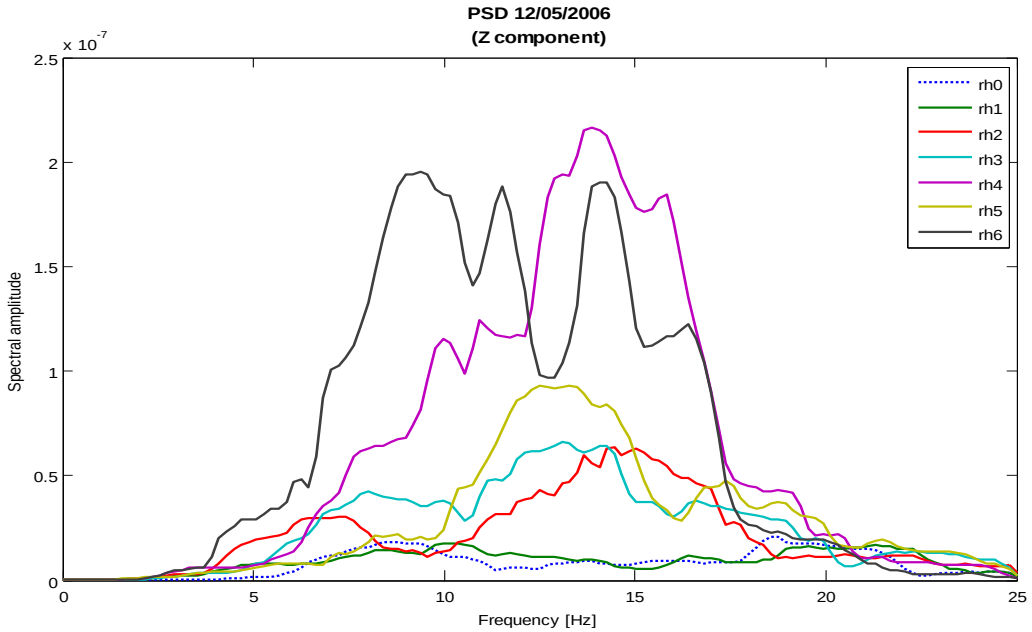

Figure 3.9: Mt Olympus earthquake - Power spectral densities of the vertical component at each station

The power distribution for the vertical component (Fig. 3.9) shows a maximum at about 14 Hz for station rh4. Station rh6 reflects a similar response with additional maxima at about 12 Hz and 9 Hz.

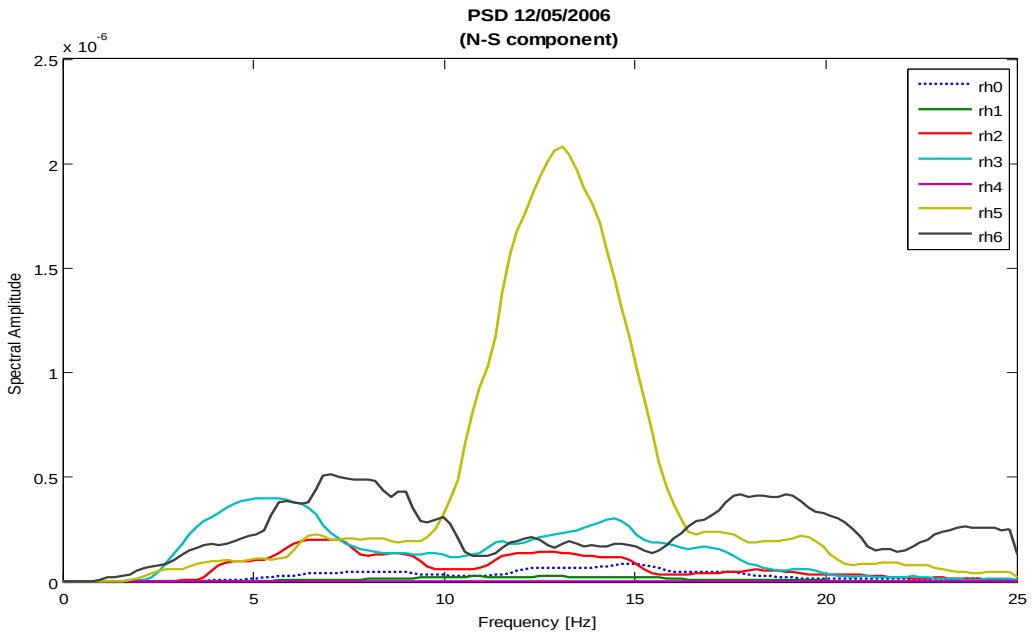

Figure 3.10: Mt Olympus earthquake - Power spectral densities of the N-S component at each station

The response for the motion parallel to the main axis of the edifice (Fig. 3.10) has a distinct maximum peak at 13 Hz for station rh5. Station rh6 has a wide power distribution for frequencies around 7 Hz and 17 Hz. Station rh3 shows a response at a slightly lower frequency of around 5 Hz.

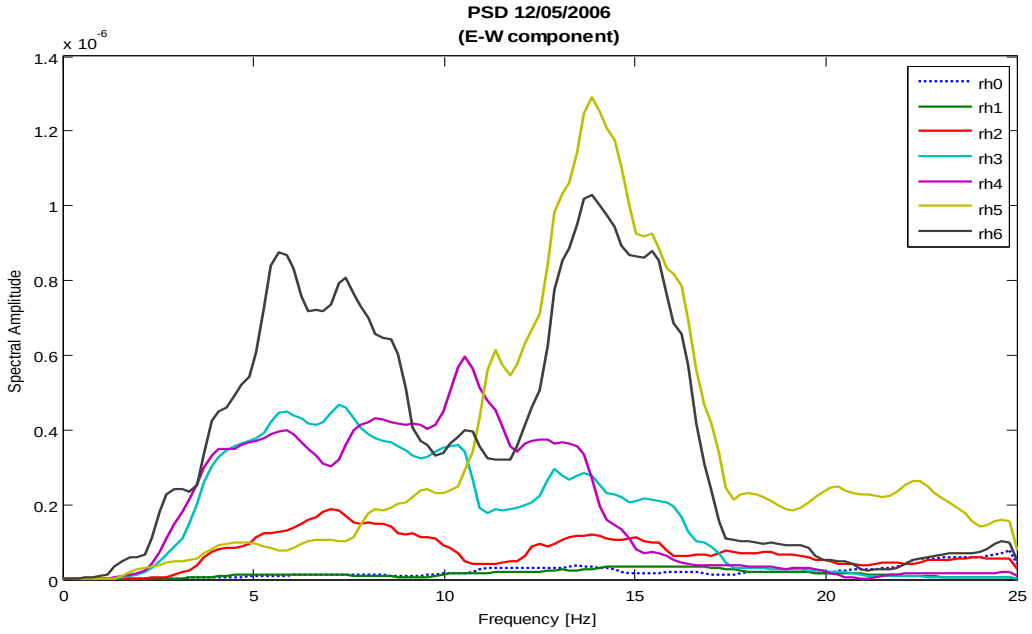

Figure 3.11: Mt Olympus earthquake - Power spectral densities of the E-W component at each station

Power spectral densities calculated for the E-W component of ground motion show maxima for the hilltop at station rh5 and rh6 at about 14 Hz (Fig.3.11). Harmonics are shown for station rh6 at about 6 and 7.5 Hz. Station 4 has a broad power distribution that covers increased amplitudes for frequencies from 5 Hz up to 13.5 Hz. A similar behaviour can be seen for the other stations along the ridge.

Standard Spectral Ratios (SSR)

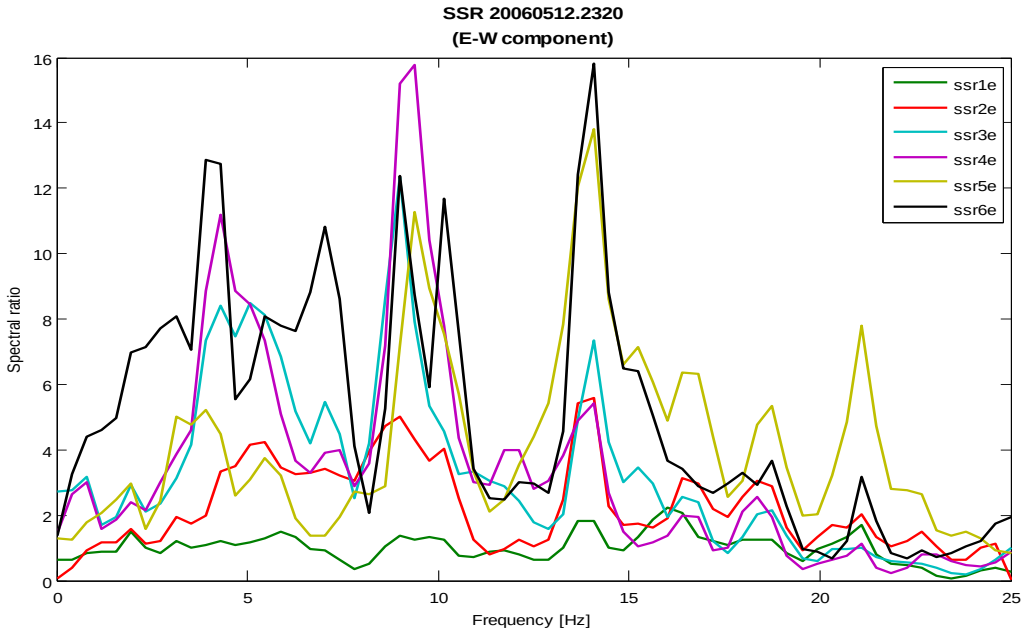

Figure 3.12: Mt Olympus earthquake – Standard Spectral ratios of the E-W component for each station relative to the base reference station rh0

As observed in the PSD analysis, the standard spectral ratio analysis confirms maximal response is shown for the hilltop stations rh5 and rh6 at 14 Hz (Fig.3.12). Spectral ratios reach about 14 for station rh5 and 16 for station rh6. Further significant spectral amplification of about 16 can be seen at station rh4. Amplification effects can be observed for all stations along the ridge at 5 Hz, 9 Hz and 14 Hz, while station rh1 at the flank of the edifice shows an insignificant response.

3.5.2 PORIRUA EARTHQUAKE 20060514.1733

3.5.2.1 Time domain analysis

Table 3.4: Porirua earthquake – observed time-domain data at the station with the greatest amplitudes (rh6)

Location /component		Peak ground acceleration [g]	Peak ground velocity [cm/s]	Peak ground displacement [cm]	Effective duration [s]
Porirua, NZ 20060514.1733	Z	0.0044	0.1455	0.0061	34.64
	N-S	0.0171	0.5443	0.0267	13.36
	E-W	0.0277	0.8936	0.0388	9.10

Station rh6 recorded the highest ground motions (0.028g) during the magnitude 5.0 Porirua earthquake (Table 3.4). These motions occurred in the E-W direction. Displacements of up to 0.388 mm were measured in the east-west direction and 0.267 mm in the N-S direction. The vertical displacement reached a maximum of 0.061 mm for this earthquake.

The effective duration of ground motion ranges from 9.1 s for the horizontal component perpendicular to the axis of the edifice and 34.64 s in the vertical direction.

Peak Ground Acceleration (PGA)

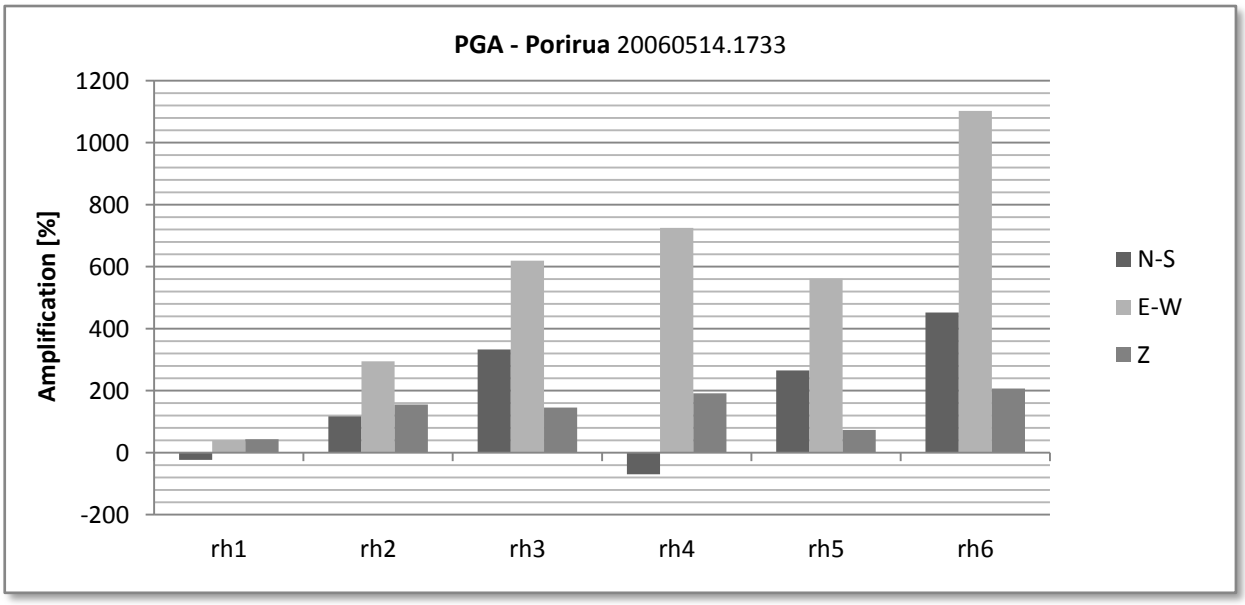

Figure 3.13: Porirua earthquake - Amplification of Peak Ground Accelerations relative to reference station rh0 – motion component transverse (E-W), parallel (N-S) to the main axis and in vertical direction (Z)

Amplifications of ground motions in the N-S direction occurred at all but two stations. The highest amplification was calculated for station rh6 (452 %). Following the trend seen in the Mt Olympus earthquake dataset, stations rh1 and rh4 show de-amplifications of -23 % and -70 % respectively (Fig. 3.13).

Amplification was recorded at all stations for the E-W component. The largest amplification in the E-W direction was 1102 %, observed at station rh6. Station rh1 shows the least amplification at 40 % relative to station rh0.

In the vertical direction of ground motion amplification values of 207 % are reached at the top of the hill at station rh6. The flank of the edifice at station rh1 experienced an amplification of 43 %.

3.5.2.2 ***Frequency domain analysis***

Power Spectral Density (PSD) – Multitaper Method (MTM)

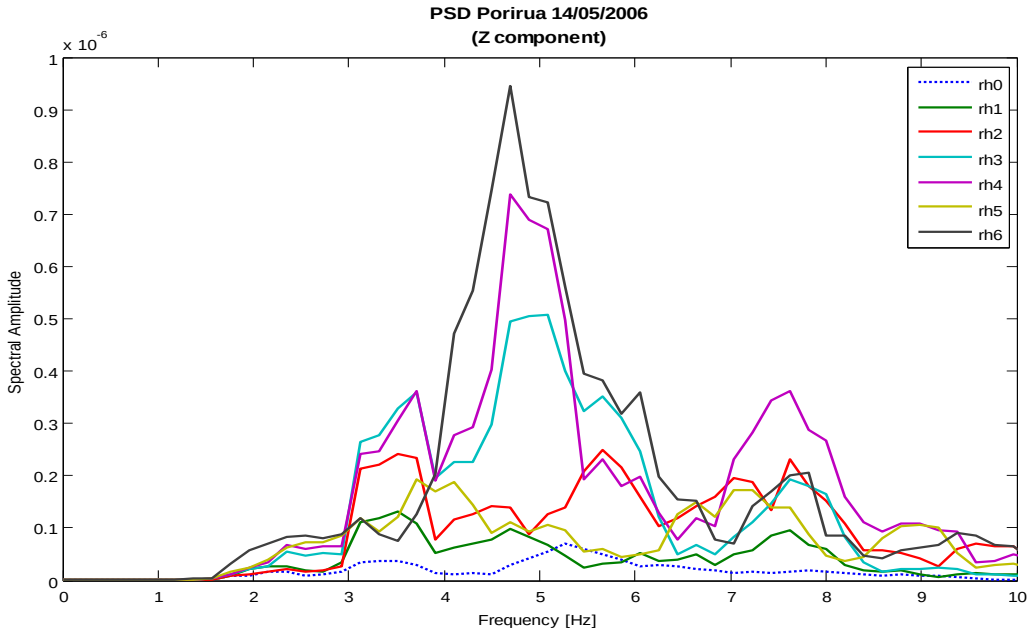

Figure 3.14: Porirua earthquake - Power spectral densities of the vertical component at each station

Distinct maxima at 5 Hz are shown in figure 3.14 for the vertical component at stations rh6, rh4, and rh3. Harmonic frequencies appear at 3.5 Hz and 7.5 Hz.

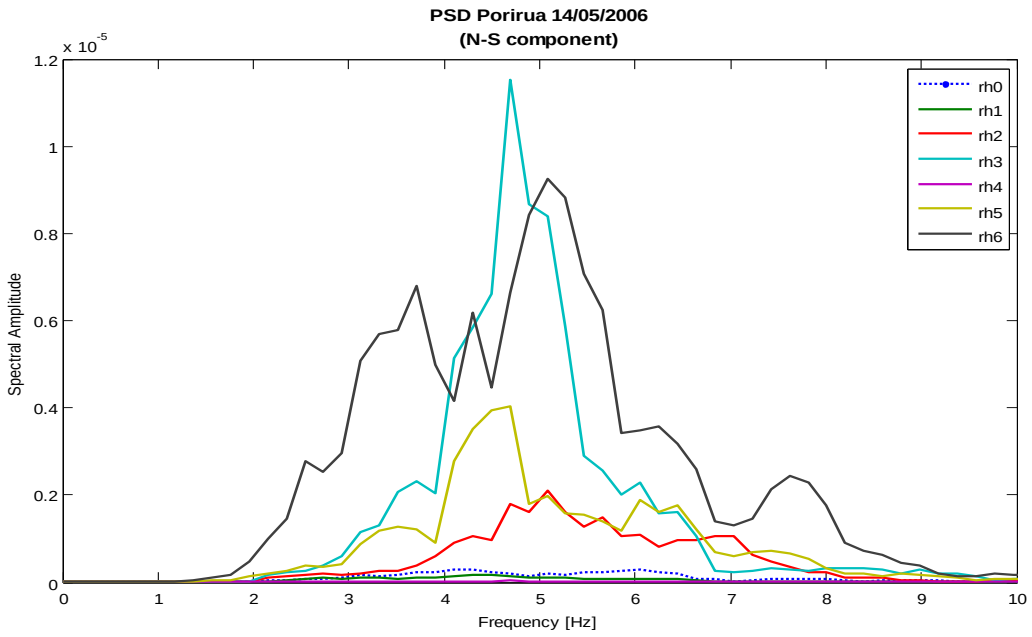

Figure 3.15: Porirua earthquake - Power spectral densities of the N-S component at each station

The power distribution shows similar characteristics in the direction parallel to the axis of the hill (Fig. 3.15) as seen in the vertical direction. Maxima at approximately 5 Hz are shown for the majority of stations along the ridge. The spectral amplitudes for the station at the flank and the base are insignificant.

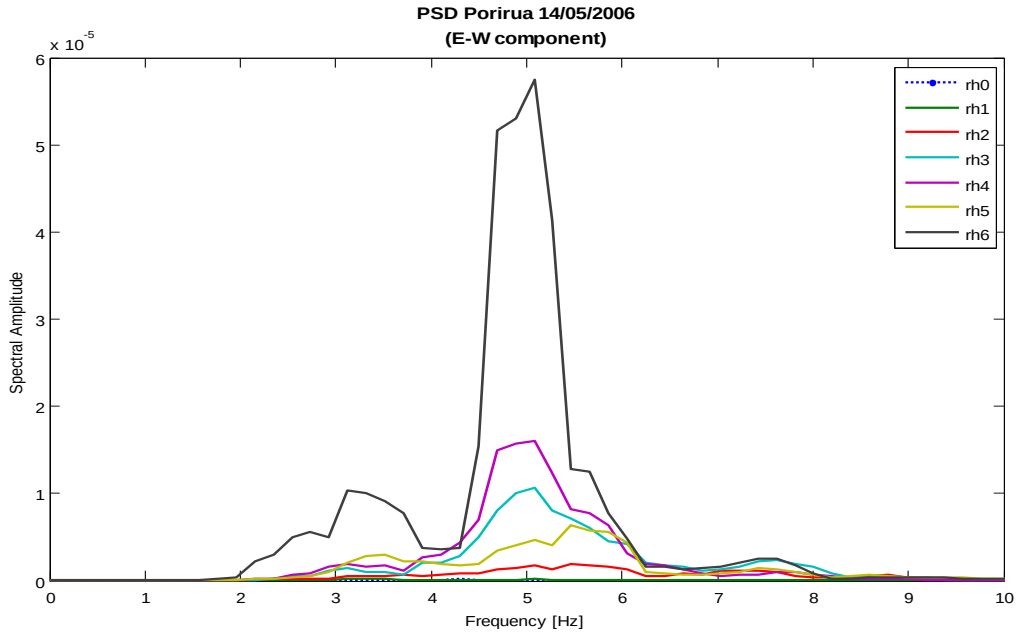

Figure 3.16: Porirua earthquake - Power spectral densities of the E-W component at each station

A narrow power density spectrum can be observed in figure 3.16 for the hilltop station rh6 at 5 Hz in the E-W direction. Stations rh3 and rh4 also show a distinct maximum at that frequency.

Standard Spectral Ratios (SSR)

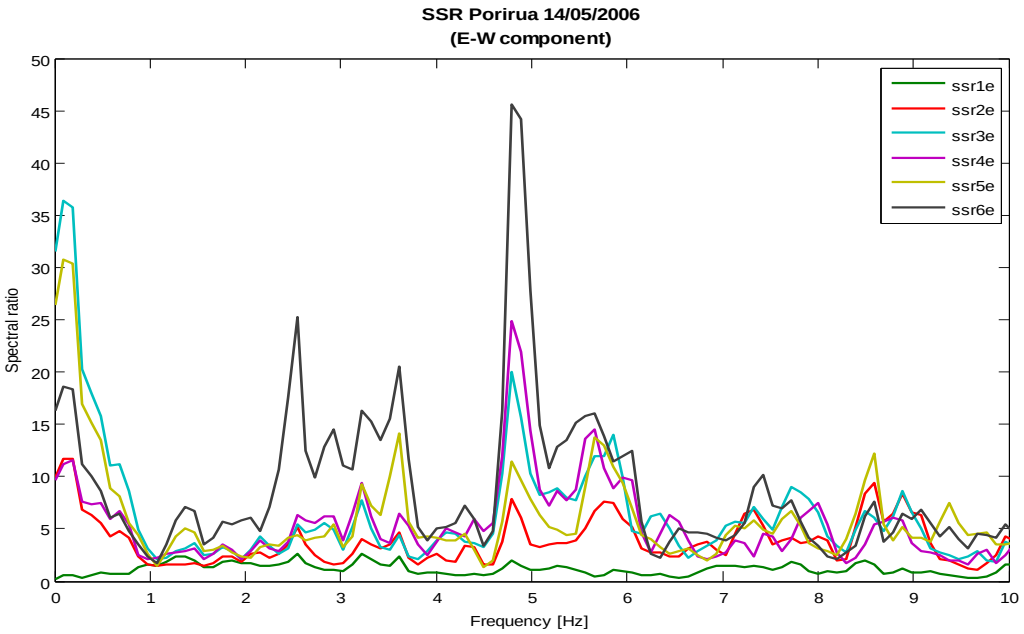

Figure 3.17: Porirua earthquake – Standard Spectral ratios of the E-W component for each station relative to the base reference station rh0

Large amplifications were calculated for all stations along the ridge of the edifice for the Porirua event (Fig. 3.17). All instruments on the mountain ridge crest show a similar response between 5 and 6 Hz. Spectral ratios reach 7 at station rh2 and up to 47 at the very top of the hill (rh6).

3.5.3 ARTHUR'S PASS EARTHQUAKE 20060515.2027

3.5.3.1 Time domain analysis

Table 3.5: Arthur's Pass earthquake – observed time-domain data at the station with the greatest amplitudes (rh3)

Location /component		Peak ground acceleration [g]	Peak ground velocity [cm/s]	Peak ground displacement [cm]	Effective duration [s]
Arthur's Pass 20060515.2027	Z	0.0006	0.0162	0.0006	7.84
	N-S	0.0010	0.0218	0.0007	9.84
	E-W	0.0018	0.0536	0.0020	9.78

The highest recorded ground motions for the Arthur's Pass earthquake (M_L= 3.0) were 1.8 milli-g recorded in the E-W direction at station rh3 (Table 3.5). Displacements of 0.020 mm were measured in the E-W direction and 0.007 mm in the N-S direction. The vertical displacement reached a maximum of 0.006 mm for this earthquake.

The effective duration of ground motion ranges from 7.84 s in the vertical direction to 9.84 in the N-S direction.

Peak Ground Acceleration (PGA)

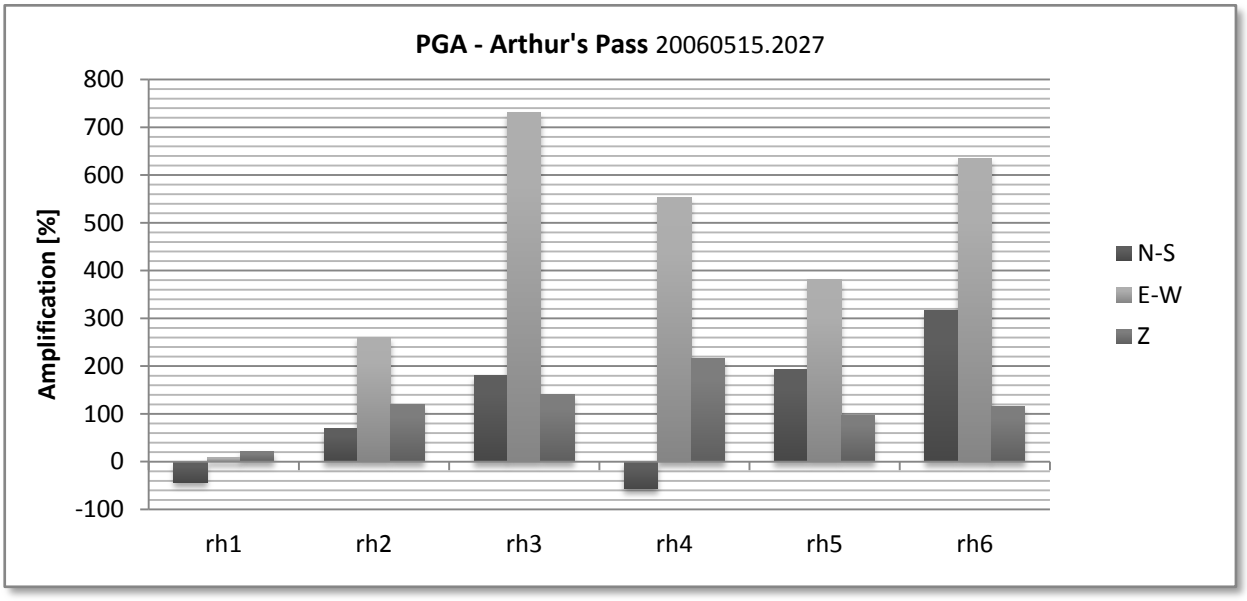

Figure 3.18: Arthur's Pass earthquake - Amplification of Peak Ground Accelerations relative to reference station rh0 – motion component transverse (E-W), parallel (N-S) to the main axis and in vertical direction (Z)

Ground motions in the N-S direction again show de-amplification at stations rh1 and rh4 of -43 % and -57% respectively (Fig. 3.18). All other stations show amplification for ground motions in the N-S direction of up to 317 % (at rh6).

Ground motions recorded in the E-W direction show amplification at all stations. The greatest amplification observed for the E-W direction occurred at station rh3 (730 %). The least amplification was calculated for station rh1 (10 %) relative to the base reference station rh0.

Amplifications were recorded in the vertical direction at all stations. Ground motion amplifications reached 140 % at the top of the hill at station rh6. The flank of the edifice at station rh1 showed the least amplification of 21 %.

3.5.3.2 ***Frequency domain analysis***

Power Spectral Density (PSD) – Multitaper Method (MTM)

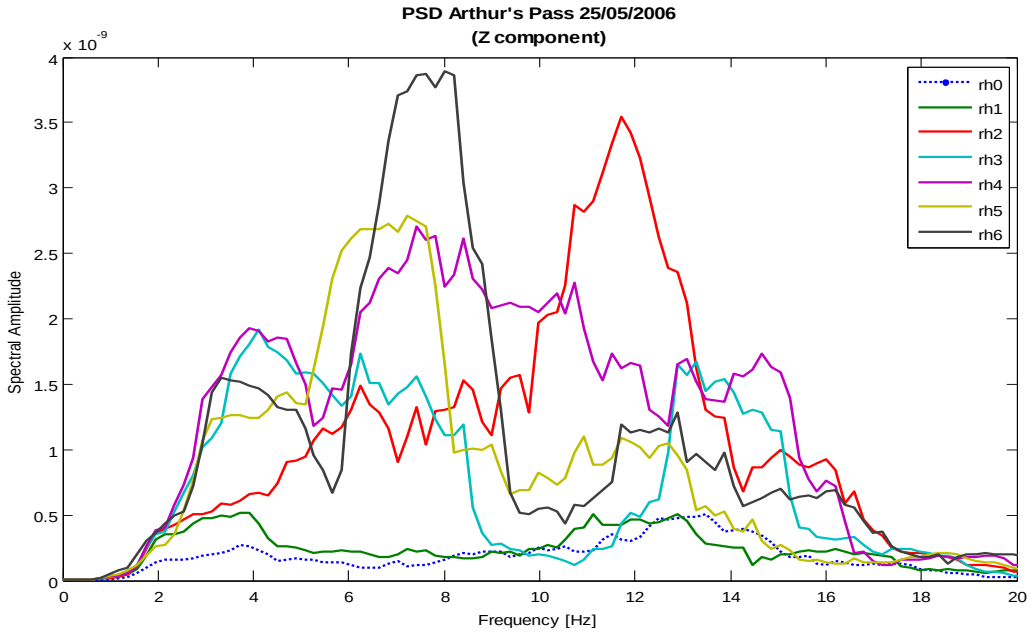

Figure 3.19: Arthur's Pass earthquake - Power spectral densities of the vertical component at each station

Figure 3.19 presents the power spectral distribution for the Z-component for all stations. Two maxima can be pointed out at 8 Hz for station rh6 and at about 12 Hz for station rh2. The other instruments responded at a wider frequency range including 4, 8 and 14 Hz.

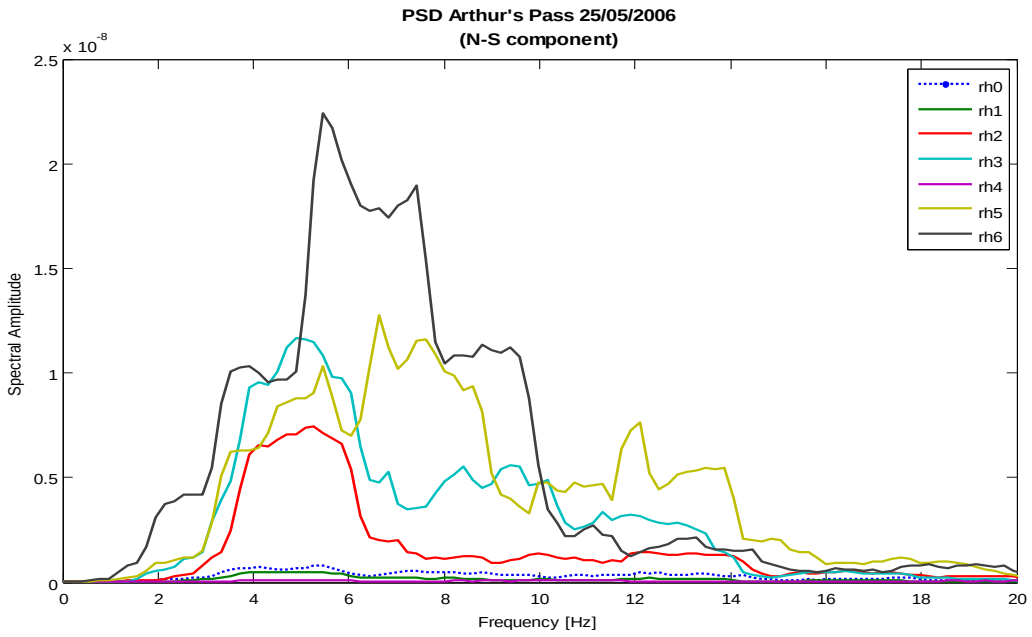

Figure 3.20: Arthur's Pass earthquake - Power spectral densities of the N-S component at each station

The N-S component shows a power distribution over a broad frequency range (3-10 Hz wide) but with pronounced peaks around 5-6 Hz (Fig 3.20).

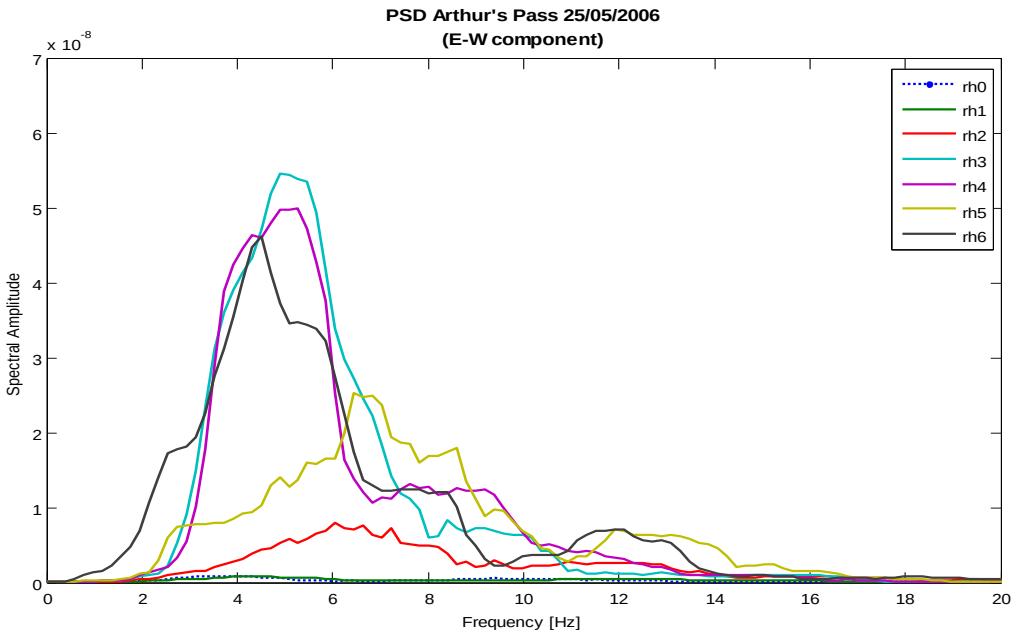

Figure 3.21: Arthur's Pass earthquake - Power spectral densities of the E-W component at each station

The power distribution seen in the N-S direction is similar to that observed in E-W component (Fig. 3.21): relatively wide (2-9 Hz), but well pronounced peaks for stations rh3, rh4 and rh6 at approximately 5 Hz. The power distribution for station rh2 and station rh5 shows a slight shift towards a wider spectrum at 6-7 Hz.

Standard Spectral Ratios (SSR)

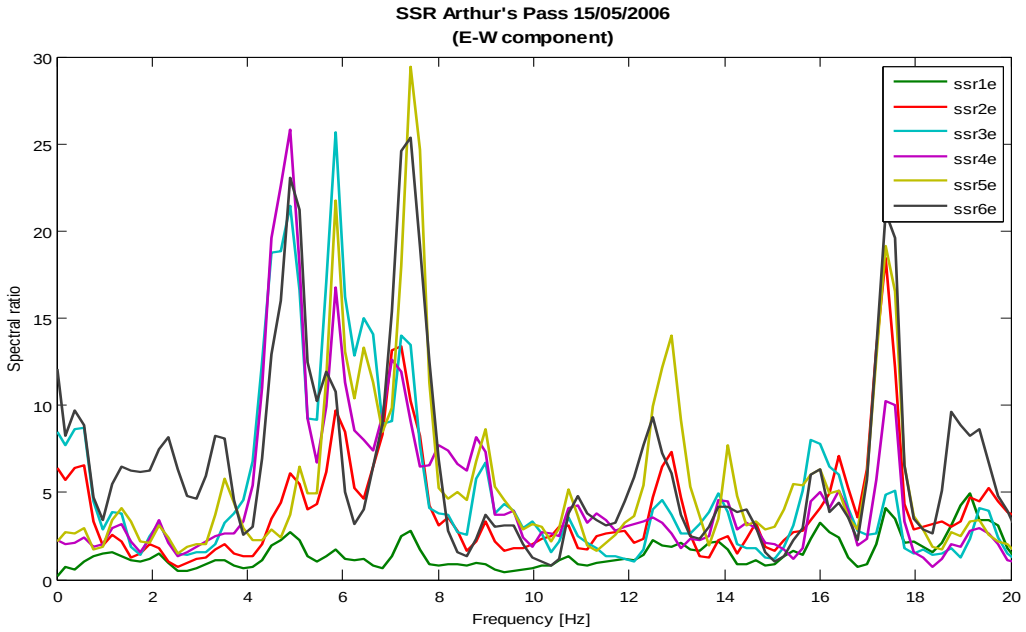

Figure 3.22: Arthur's Pass earthquake – Standard Spectral ratios of the E-W component for each station relative to the base reference station rh0

The spectral ratios calculated for the Arthur's Pass earthquake show amplified response of the hilltop over a wide band of frequencies between 4 and 8 Hz (Fig. 3.22). Maximum ratios are located at about 8 Hz for stations rh5 (29) and rh6 (26). Stations rh3, rh4 and rh6 show high spectral ratios also at 5 Hz, reaching values between 23 and 26.

3.5.4 NELSON EARTHQUAKE 20060515.2038

3.5.4.1 Time domain analysis

Table 3.6: Nelson earthquake – observed time-domain data at the station with the greatest amplitudes (rh6)

Location /component		Peak ground acceleration [g]	Peak ground velocity [cm/s]	Peak ground displacement [cm]	Effective duration [s]
Nelson, NZ 20060515.2038	Z	0.0008	0.0152	0.0004	30.66
	N-S	0.0011	0.0242	0.0011	32.30
	E-W	0.0012	0.0359	0.0016	32.88

The highest ground motions recorded during the magnitude M_L = 3.8 Nelson earthquake occurred in the E-W direction at station rh6 (1.2 milli-g; Table 3.6). Displacements of 0.016 mm were measured in the E-W direction and 0.011 mm in the N-S direction. The vertical displacement reached a maximum of 0.004 mm for this earthquake.

The effective duration of ground motion ranges from 30.66 s in the vertical direction to 32.88 s in the E-W direction.

Peak Ground Acceleration (PGA)

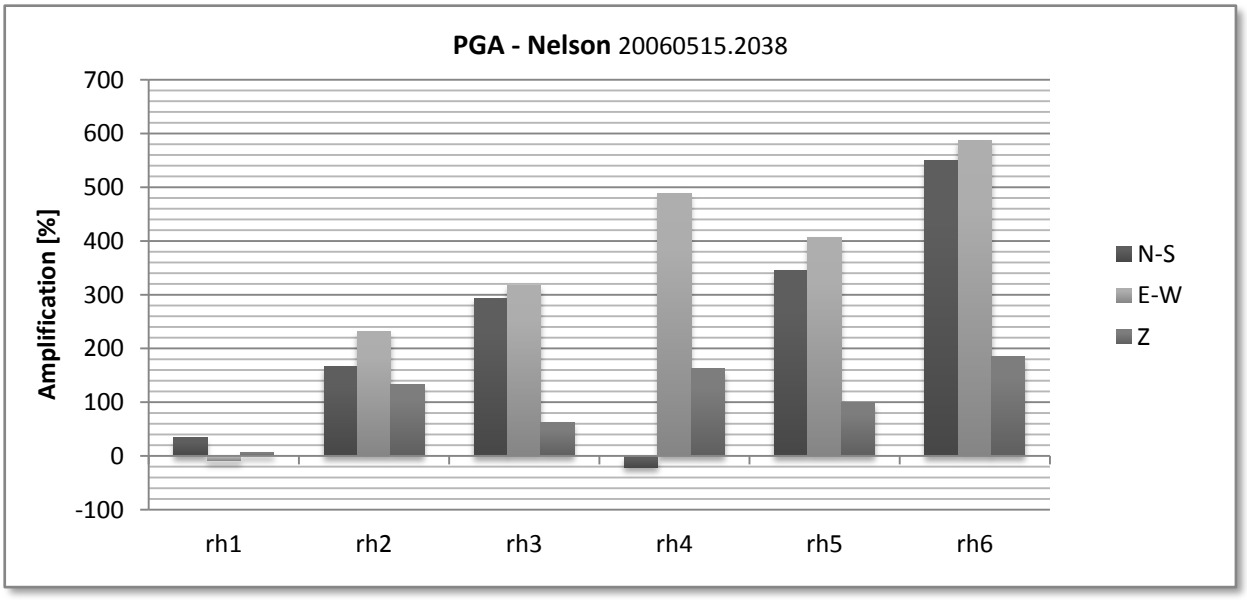

Figure 3.23: Nelson earthquake - Amplification of Peak Ground Accelerations relative to reference station rh0 – motion component transverse (E-W), parallel (N-S) to the main axis and in vertical direction (Z)

Ground motions in the N-S direction show de-amplification at only station rh4 (-21 %; Fig. 3.23). All other stations, including station rh1, show amplification of ground motions in the N-S direction. The highest observed amplification in this direction was 550 % recorded at station rh6.

Ground motions recorded in the E-W direction show amplification at all stations except station rh1 which recorded a de-amplification of -9 %. The greatest recorded amplification in the E-W direction occurred at station rh6 (588 %).

Amplifications were measured in the vertical direction at all stations. Ground motion amplifications reached 184 % at the top of the hill at station rh6. The flank of the edifice at station rh1 experienced the least amplification of 6 %.

3.5.4.2 ***Frequency domain analysis***

Power Spectral Density (PSD) – Multitaper Method (MTM)

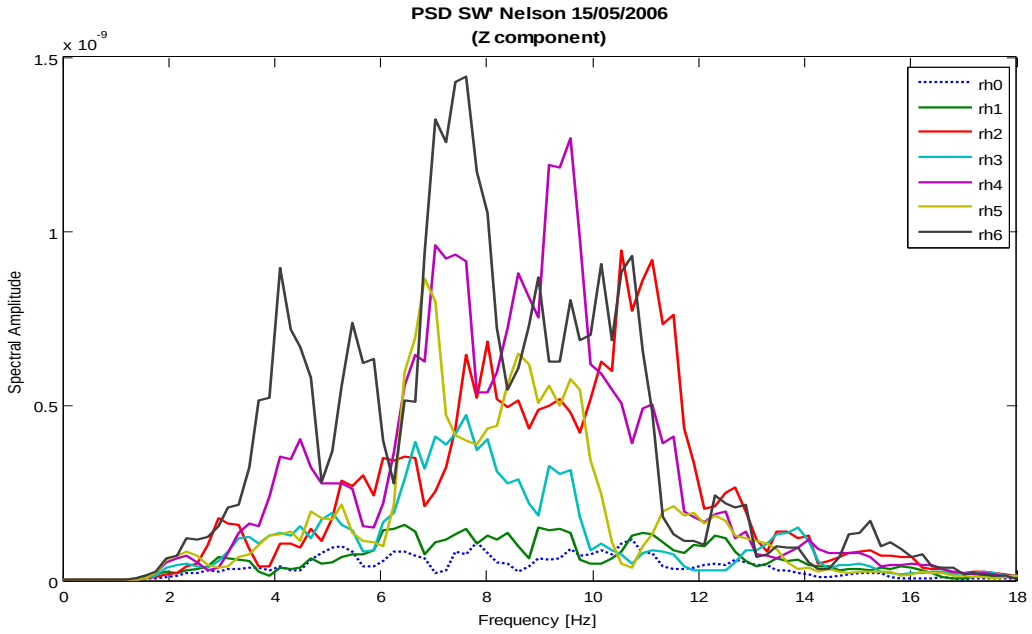

Figure 3.24: Nelson earthquake - Power spectral densities of the vertical component at each station

The power spectral densities calculated for the vertical component of records from the Nelson earthquake at Little Red Hill show a complex distribution over a wide range of frequencies (Fig 3.24). Maxima can be recognized for station rh6 and station rh4 at about 7.5 Hz and 9.5 Hz respectively.

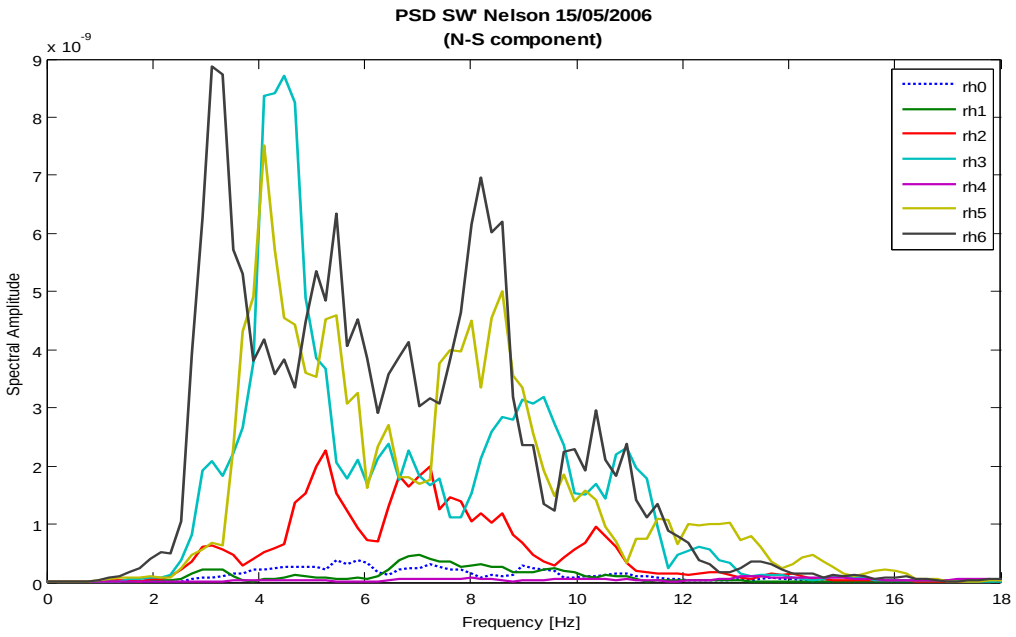

Figure 3.25: Nelson earthquake - Power spectral densities of the N-S component at each station

The power spectrum for the N-S component of the Nelson earthquake shows a variety of maxima over a wide band of frequencies (~ 9 Hz wide; see Fig. 3.25). The hilltop has its highest power spectral densities for station rh6 at 3 Hz, station rh5 at 4 Hz, station 3 at 4.5 Hz, and station rh2 at 5 Hz.

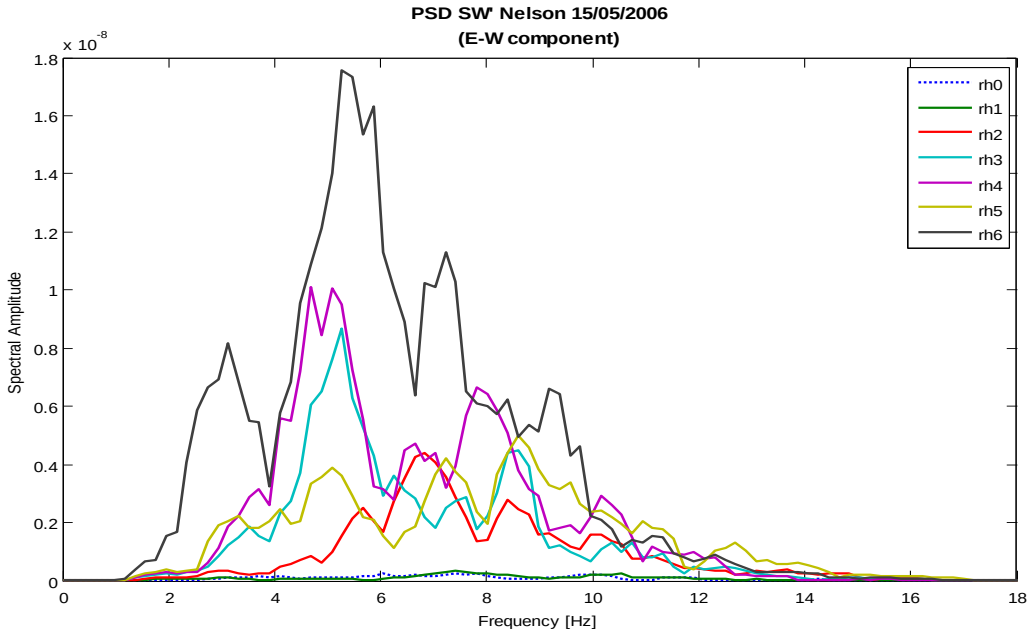

Figure 3.26: Nelson earthquake - Power spectral densities of the E-W component at each station

Looking at the transverse component of motion for the Nelson earthquake (Fig 3.26), distinct peaks are located at about 5 Hz for station rh3 - rh6 along the ridgeline.

Standard Spectral Ratios (SSR)

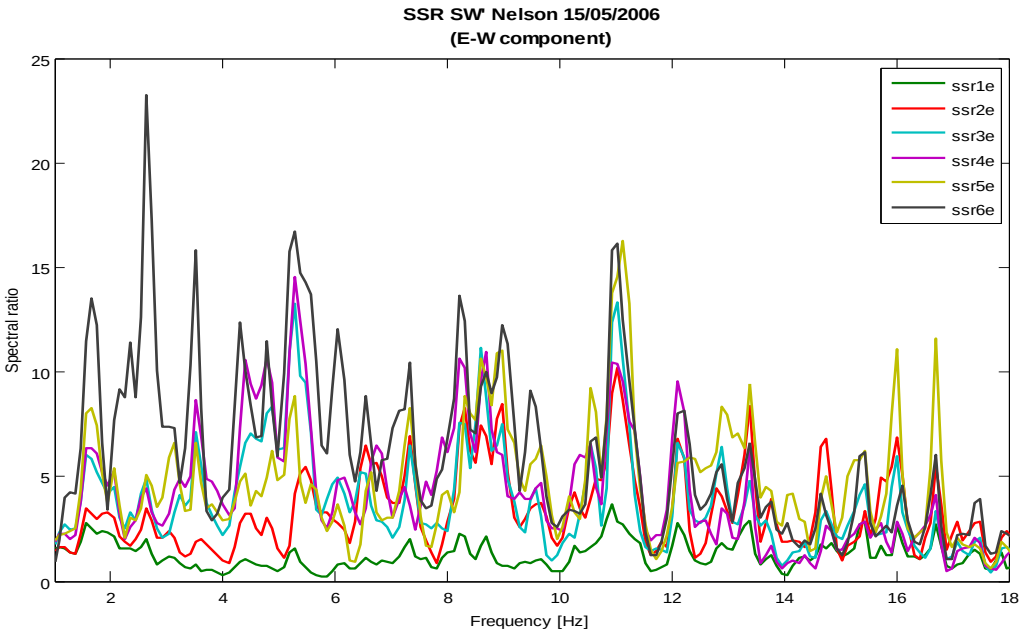

Figure 3.27: Nelson earthquake – Standard Spectral ratios of the E-W component for each station relative to the base reference station rh0

Spectral ratios are distributed over a wide band of frequencies for the Nelson earthquake (Fig. 3.27). Elevated ratios are displayed for station rh6 at 3 Hz (23) and at about 5 Hz for all stations on top of the edifice.

3.5.5 KERMADEC ISLANDS EARTHQUAKE 20060516.1042

3.5.5.1 Time domain analysis

Table 3.7: Kermadec Islands earthquake – observed time-domain data at the station with the greatest amplitudes (rh6)

Location /component		Peak ground acceleration [g]	Peak ground velocity [cm/s]	Peak ground displacement [cm]	Effective duration [s]
Kermadec Islands region 20060516.1042	Z	0.0138	0.5414	0.0461	168.28
	N-S	0.0476	1.8413	0.1292	150.72
	E-W	0.0494	2.1614	0.1711	161.6

The highest ground motions recorded at Little Red Hill from The Kermadec Islands earthquake (M_w= 7.4) occurred in the E-W direction at station rh6 on the ridge crest (0.049 g; Table 3.7). Displacements of 1.711 mm were measured in the E-W direction and 1.292 mm in the N-S direction. The vertical displacement reached a maximum of 0.461 mm for this earthquake.

The effective durations of ground motion from the Kermadec Islands event were the longest recorded during this field study, and ranged between 150.72 s in the N-S direction to 168.28 s in the vertical direction.

Peak Ground Acceleration (PGA)

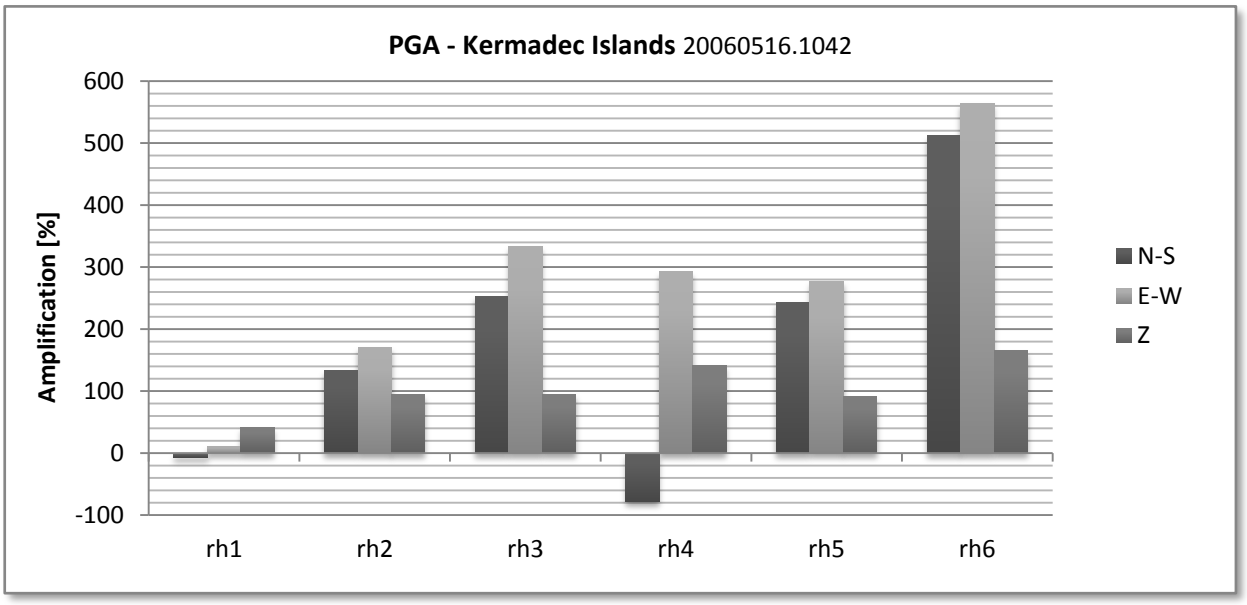

Figure 3.28: Kermadec Islands earthquake - Amplification of Peak Ground Accelerations relative to reference station rh0 – motion component transverse (E-W), parallel (N-S) to the main axis and in vertical direction (Z)

Ground motions in the N-S direction show de-amplification at stations rh1 and rh4 of -6 % and -78 % respectively (Fig. 3 28). All other stations show amplifications of ground motions in the N-S direction. The highest recorded amplification in this direction was 512 %, recorded at station rh6.

In the E-W direction amplification was observed for all stations. The maximum amplification in the E-W direction occurred at station rh6 (565 %). The lowest amplification occurred at station rh1 (11 %).

Amplifications were recorded in the vertical direction at all stations. Ground motion amplifications reached 165 % at station rh6. Station rh1 recorded the least amplification of 42 %.

3.5.5.2 *Frequency domain analysis*

Power Spectral Density (PSD) – Multitaper Method (MTM)

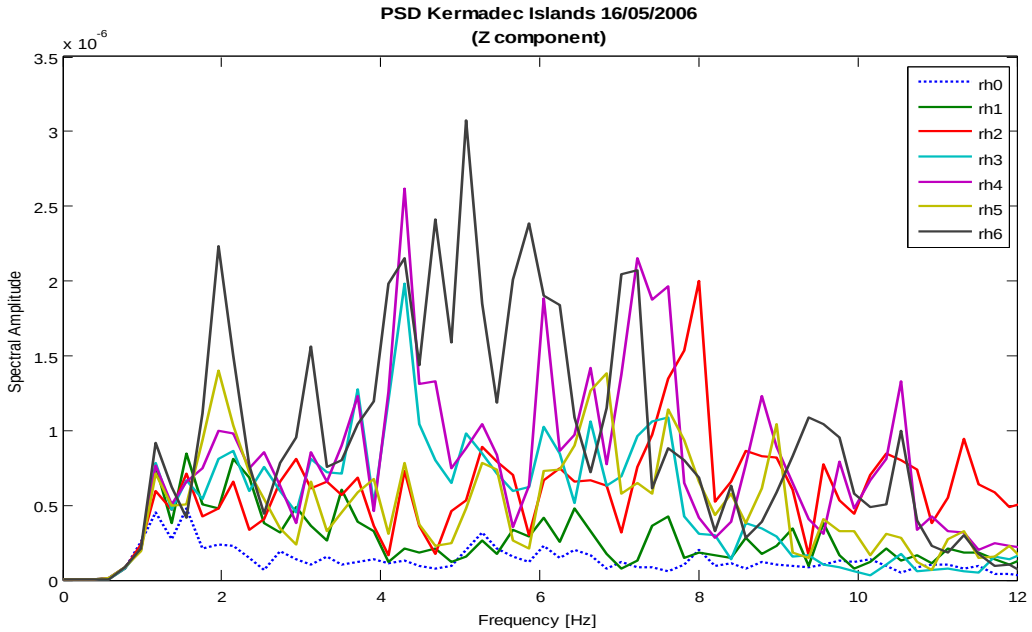

Figure 3.29: Kermadec earthquake - Power spectral densities of the vertical component at each station

A complex power density distribution over a wide band of frequencies (2-12 Hz wide) can be observed for the vertical component of the Kermadec Islands earthquake record (Fig. 3.29). Peaks are located at 5 Hz for station rh6, and at 4.5 Hz for stations rh3 and rh4.

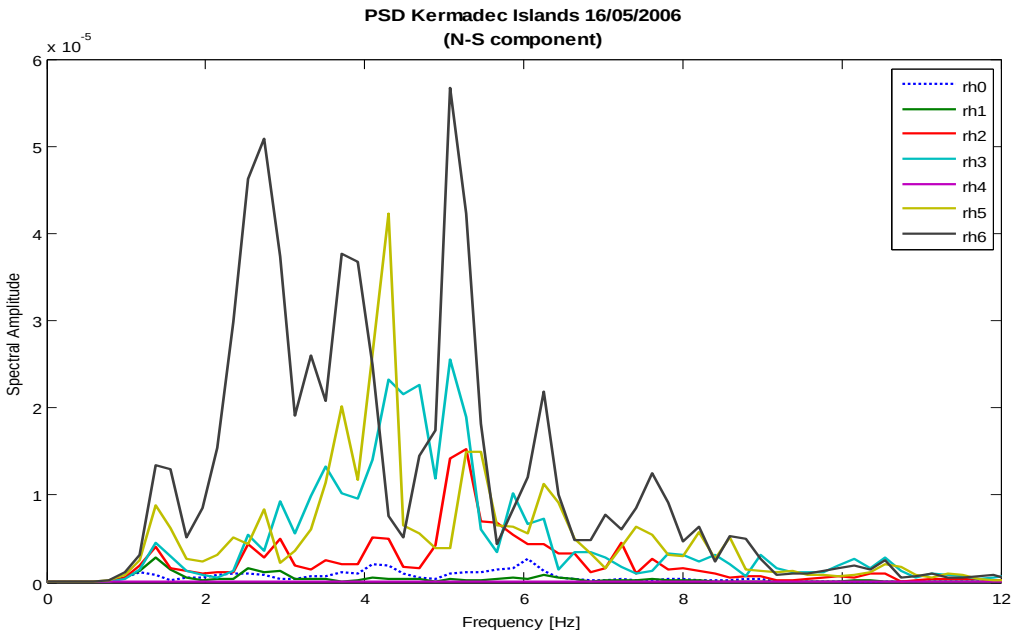

Figure 3.30: Kermadec earthquake - Power spectral densities of the N-S component at each station

The response in the N-S direction is similar to that observed in the vertical direction but within a narrower frequency range (2-8 Hz). As displayed in figure 3.30, the majority of the stations along the ridge of Little Red Hill show an elevated response between 4.5 and 5 Hz for the N-S component.

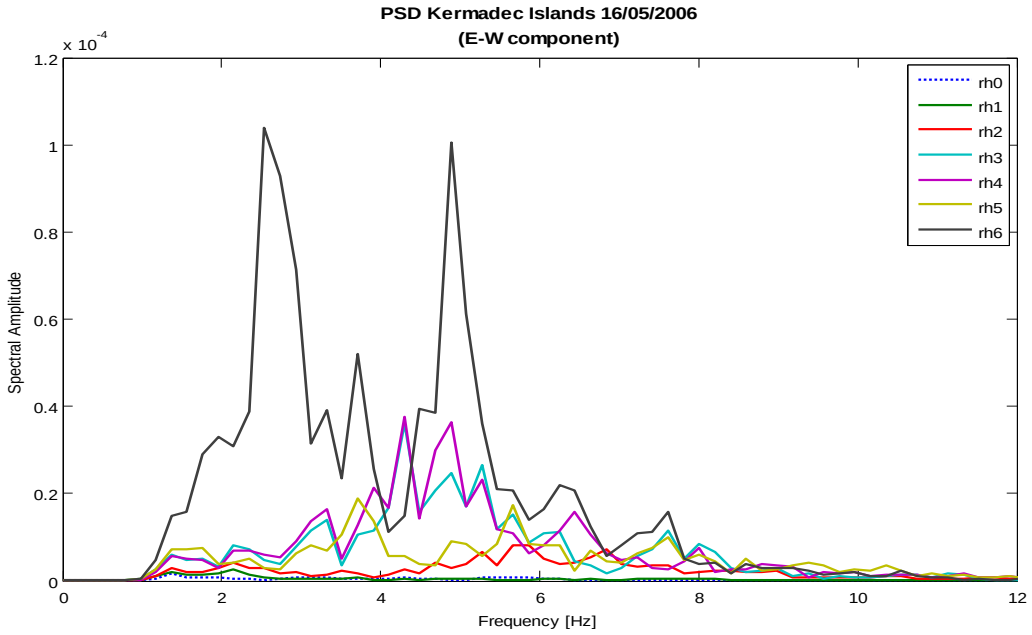

Figure 3.31: Kermadec earthquake - Power spectral densities of the E-W component at each station

Figure 3.31 reveals power spectral densities in the E-W direction are concentrated at 2.5 and 5 Hz for station rh6 at the very top of the edifice. Station rh3 and rh4 also show elevated amplitudes at approximately 5 Hz.

Standard Spectral Ratios (SSR)

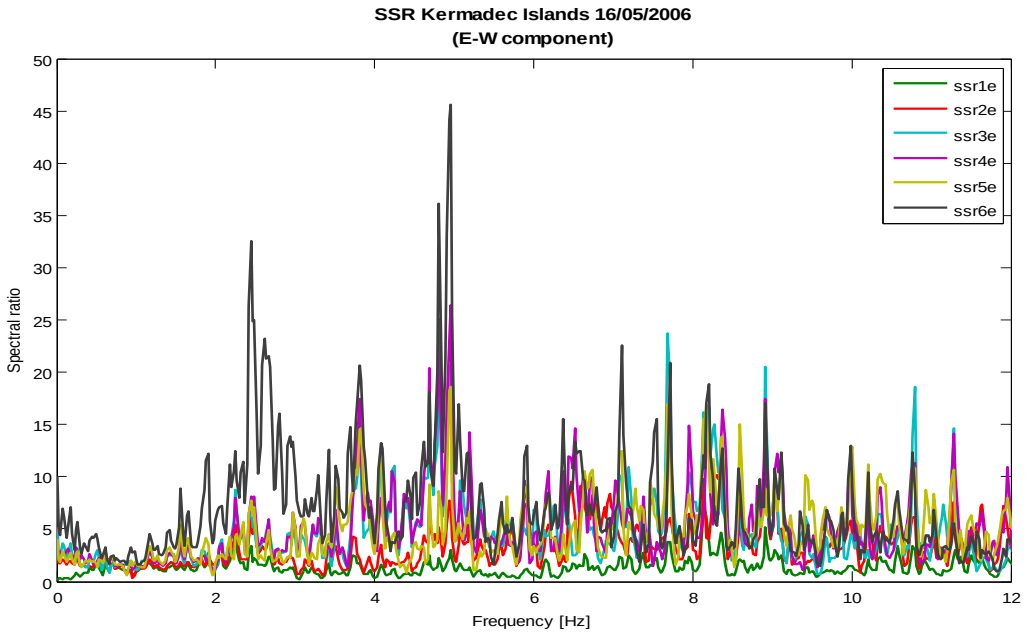

Figure 3.32: Kermadec Islands earthquake – Standard Spectral ratios of the E-W component for each station relative to the base reference station rh0

We observe significant spectral amplification at the hilltop at a frequency of 5 Hz (Fig. 3.32). Spectral ratios reach values of up to 47 for station rh6. Further maxima can be seen at about 2.5 Hz and about 4 Hz.

3.5.6 ST ARNAUD EARTHQUAKE 20060516.1121

3.5.6.1 Time domain analysis

Table 3.8: St Arnaud earthquake – observed time-domain data at the station with the greatest amplitudes (rh6)

Location /component		Peak ground acceleration [g]	Peak ground velocity [cm/s]	Peak ground displacement [cm]	Effective duration [s]
St Arnaud 20060516.1121	Z	0.0002	0.0067	0.0003	22.76
	N-S	0.0008	0.0266	0.0010	23.36
	E-W	0.0012	0.0286	0.0014	19.8

The highest ground motions recorded during the magnitude 3.5 St Arnaud earthquake occurred in the E-W direction at station rh6 (1.2 milli-g; Table 3.8). Displacements of 0.014 mm were measured in the E-W direction and 0.010 mm in the N-S direction. The vertical displacement reached a maximum of 0.003 mm for this earthquake.

The effective duration of ground motion ranged between 19.8 s in the E-W direction to 23.36 s in the N-S direction.

Peak Ground Acceleration (PGA)

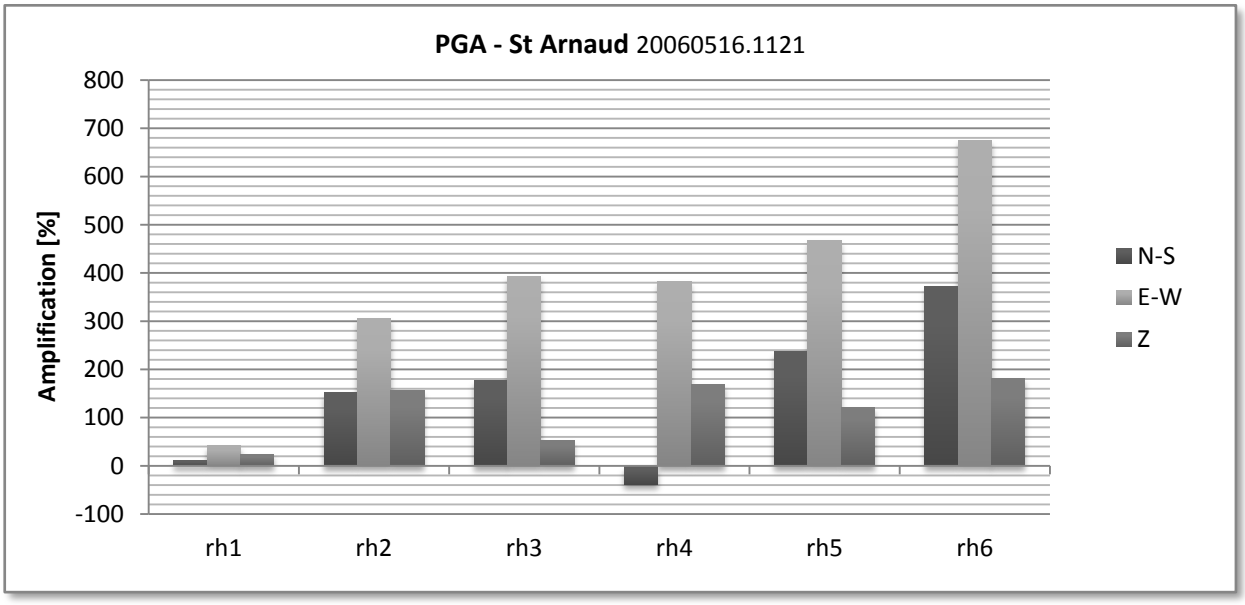

Figure 3.33: St Arnaud earthquake - Amplification of Peak Ground Accelerations relative to reference station rh0 – motion component transverse (E-W), parallel (N-S) to the main axis and in vertical direction (Z)

Ground motions in the N-S direction show de-amplification at station rh4 (-38 %; Fig. 3.33). Amplifications relative to the base reference station rh0 were recorded at all other stations. The highest amplification in the N-S direction (373 %) was calculated for station rh6.

All stations show amplification in ground motions in the E-W direction, with the highest recorded amplification occurring at station rh6 (674 %). The least amplification in ground motion in the E-W direction was observed at station rh1 (41 %).

In the vertical direction all stations show amplified records of ground motion compared to the base station rh0. The highest amplification in this direction was 181 %, recorded at station rh6. Station rh1 showed the least amplification of 24 %.

3.5.6.2 ***Frequency domain analysis***

Power Spectral Density (PSD) – Multitaper Method (MTM)

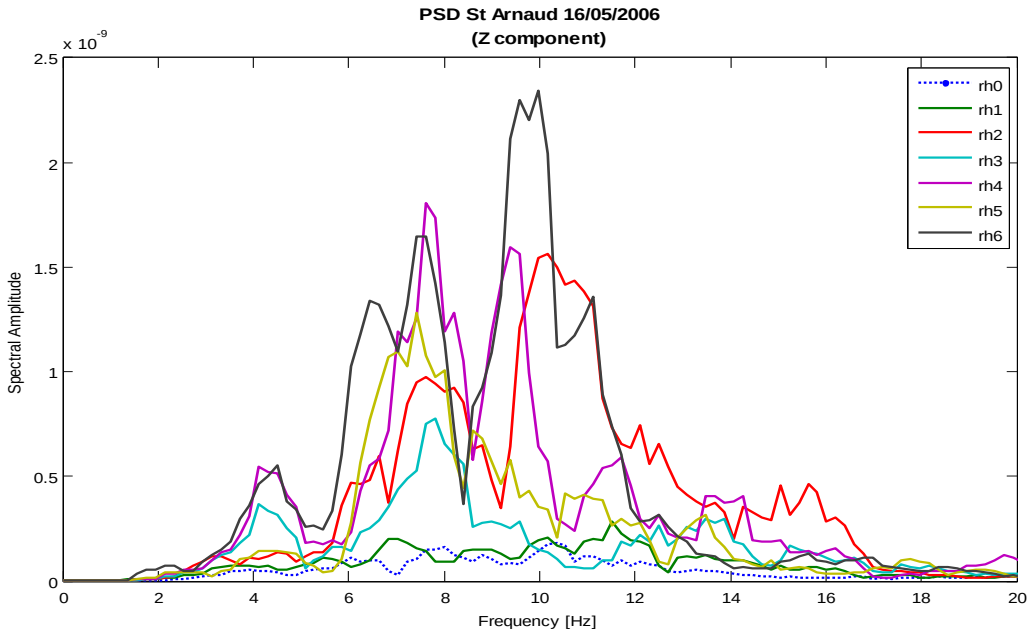

Figure 3.34: St Arnaud earthquake - Power spectral densities of the vertical component at each station

Looking at the calculated power spectral densities of the St Arnaud earthquake in the vertical direction (Fig 3.34), an accumulation of peaks can be seen at 7.5 – 8 Hz and 9 – 11 Hz for the stations along the ridge. Station rh6 shows the highest peak at 10 Hz for this component.

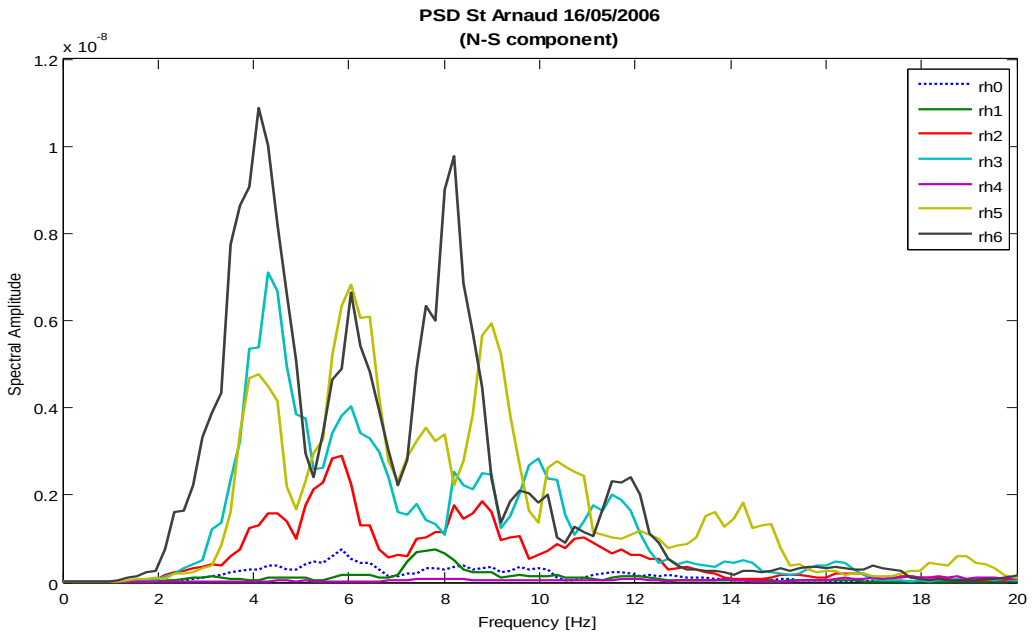

Figure 3.35: St Arnaud earthquake - Power spectral densities of the N-S component at each station

The N-S component represents an almost symmetrical response pattern for stations rh2, rh3, rh5 and rh6, showing peaks and their harmonics approximately at 4, 6, 8, 10, and 12 Hz (Fig. 3.35). The spectral amplitudes for station rh1 at the flank and station rh0 at the base show insignificant values compared to the stations along the crest.

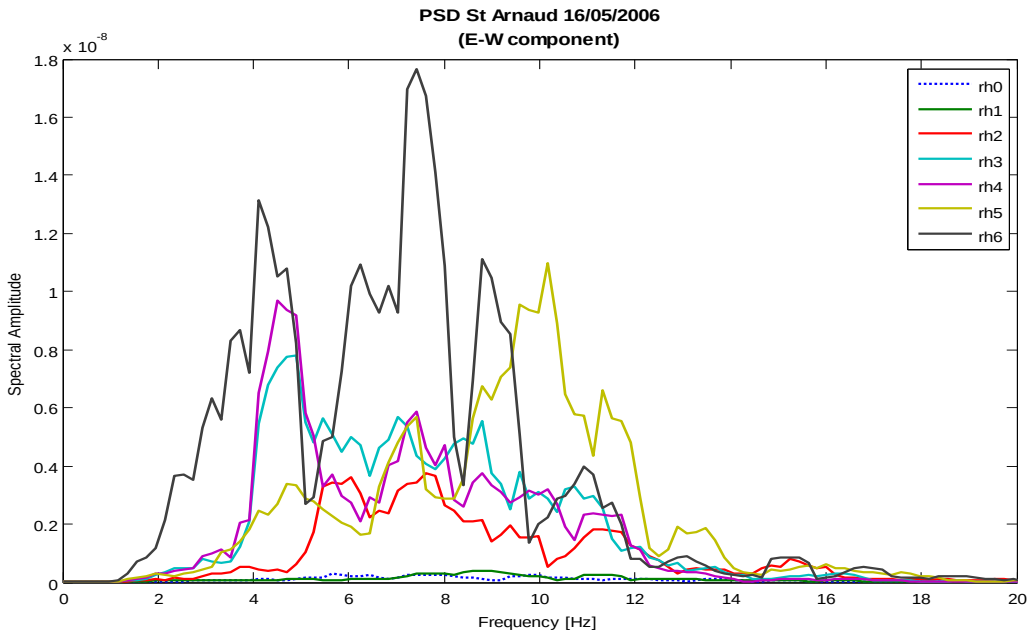

Figure 3.36: St Arnaud earthquake - Power spectral densities of the E-W component at each station

The processed record of the E-W component (Fig. 3.36) shows a focused power spectral density at about 4 Hz for stations rh6, rh3, and station rh4. The largest amplitude occurs at about 7.5 Hz for station rh6.

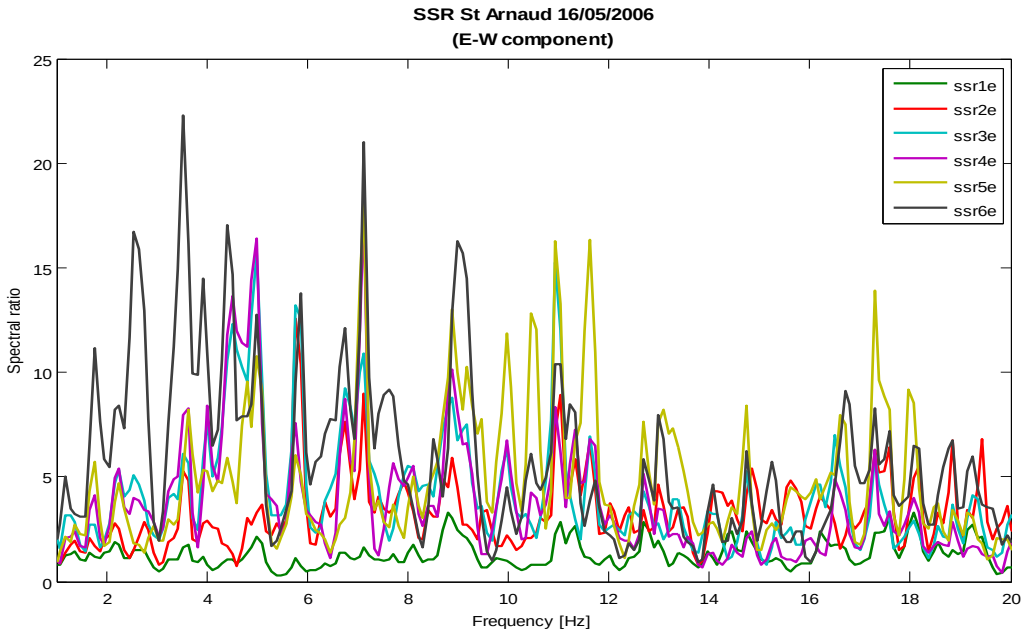

Figure 3.37: St Arnaud earthquake – Standard Spectral ratios of the E-W component for each station relative to the base reference station rh0

A wide distribution over frequencies can be seen in figure 3.37 for the spectral ratios computed for the St Arnaud earthquake. Maxima are located at about 4 Hz and reach up to about 23 at station rh6. Another assembly of elevated spectral ratios is shown at around 7-8 Hz. Amplification factors reach up to 22, again for station rh6.

3.5.7 COOK STRAIT EARTHQUAKE 20060517.0147

3.5.7.1 Time domain analysis

Table 3.9: Cook Strait earthquake – observed time-domain data at the station with the greatest amplitudes (rh6)

Location /component		Peak ground acceleration [g]	Peak ground velocity [cm/s]	Peak ground displacement [cm]	Effective duration [s]
Cook Strait 20060517.0147	Z	0.0002	0.0055	0.0003	46.38
	N-S	0.0006	0.0202	0.0009	45.46
	E-W	0.0007	0.0259	0.0014	44.92

The Cook Strait earthquake had a magnitude of M_L = 3.7. The highest ground motion recorded from this earthquake occurred in the E-W direction at station rh6 (0.7 milli-g; Table 3.9). Displacements of 0.014 mm were measured in the E-W direction and 0.009 mm in the N-S direction. The vertical displacement reached a maximum of 0.003 mm for this event.

The effective duration of ground motion ranged between 44.92 s in the E-W direction to 46.38 s in the vertical direction.

3.5.7.2 ***Peak Ground Acceleration (PGA)***

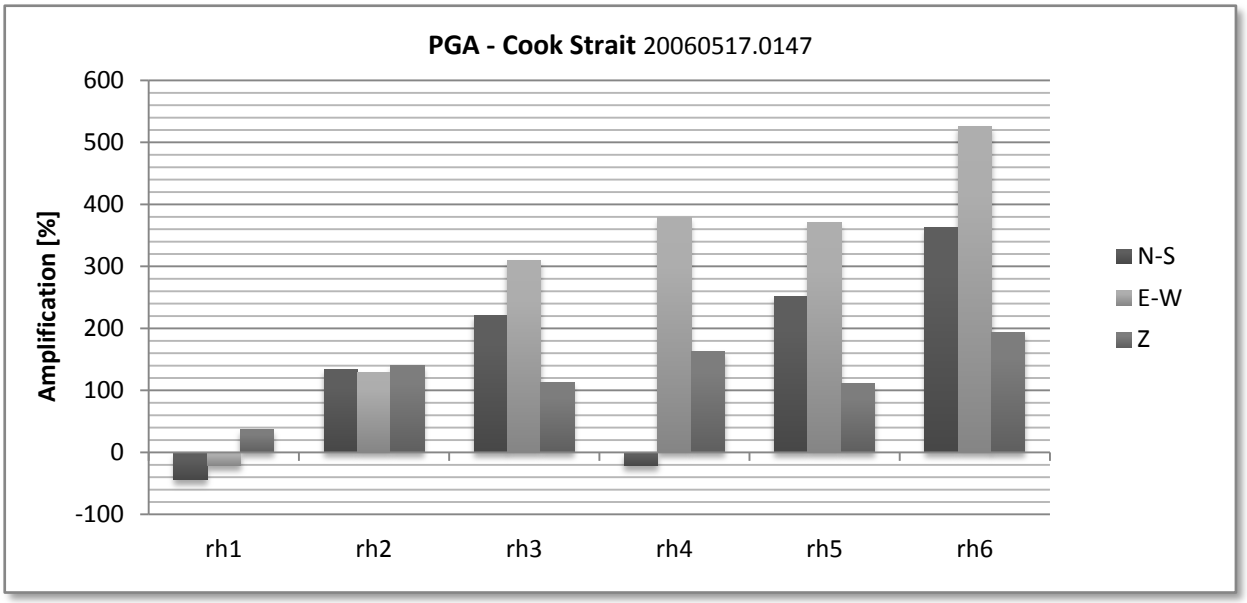

Figure 3.38: Cook Strait earthquake - Amplification of Peak Ground Accelerations relative to reference station rh0 – motion component transverse (E-W), parallel (N-S) to the main axis and in vertical direction (Z)

Ground motions in the N-S direction show de-amplification at stations rh1 and rh4 of -43 % and -22 % (Fig. 3.38). All other stations recorded amplifications in the N-S direction. The maximum amplification recorded in this direction was 363 % at station rh6.

Station rh1 shows a de-amplification of -21 %, all other stations record amplifications relative to station rh0 in this direction. The highest recorded amplification in the E-W direction was 526% at station rh6.

Amplifications were recorded in the vertical direction at all stations. The highest amplification in this direction was 194 %, measured at station rh6. Station rh1 experienced the least amplification of ground motion of 37 %.

3.5.7.3 ***Frequency domain analysis***

Power Spectral Density (PSD) – Multitaper Method (MTM)

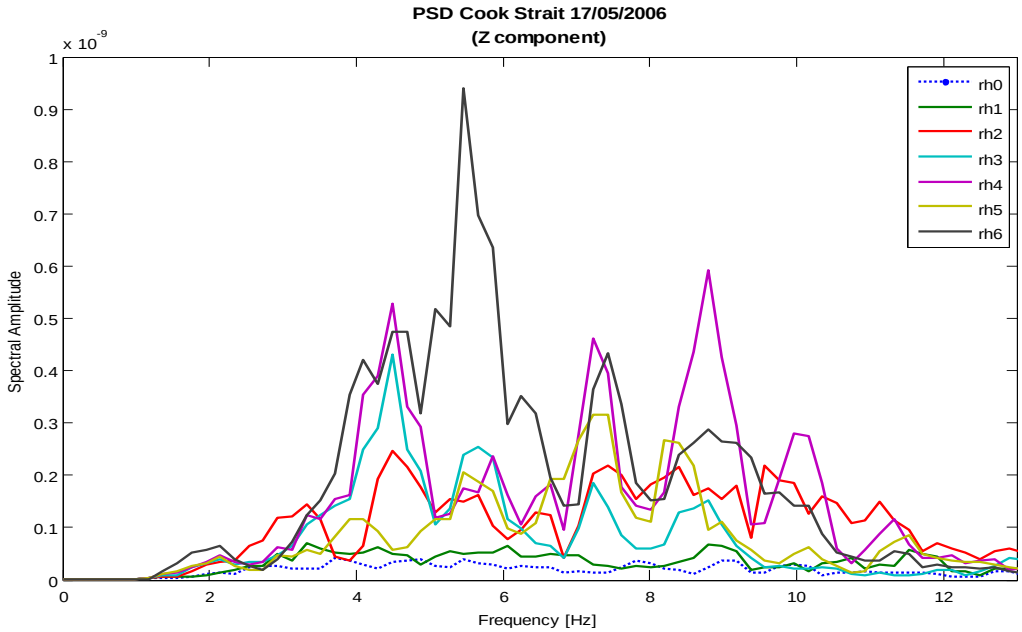

Figure 3.39: Cook Strait earthquake - Power spectral densities of the vertical component at each station

Figure 3.39 shows peaks (~ 1 Hz wide) distributed over a variety of frequencies in the vertical direction. Elevated amplitudes are shown for all stations at the ridgeline between 4.5 and 5.5 Hz. Station rh6 represents the highest amplitude at about 5.5 Hz.

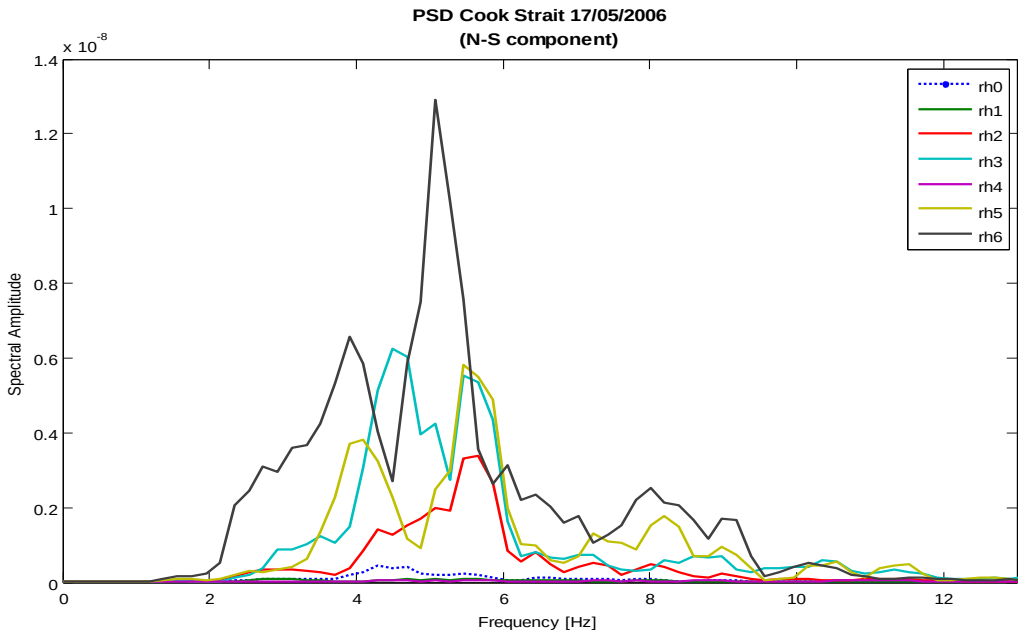

Figure 3.40: Cook Strait earthquake - Power spectral densities of the N-S component at each station

Spectral peaks are concentrated between 4 and 6 Hz for the N-S component. Station rh6 shows the largest response at a frequency of 5 Hz (Fig 3.40).

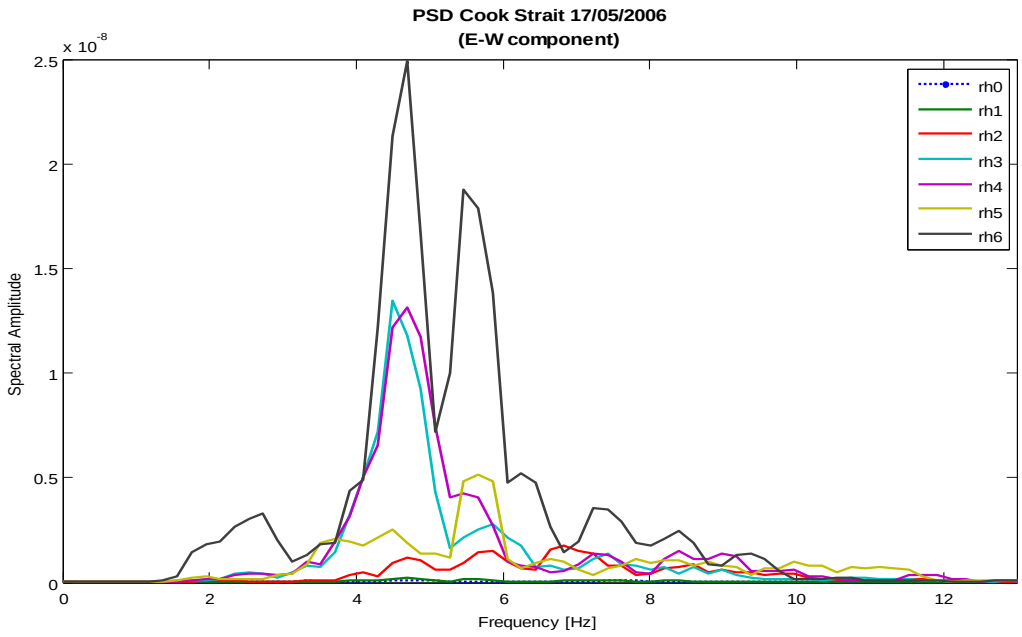

Figure 3.41: Cook Strait earthquake - Power spectral densities of the E-W component at each station

A narrow power distribution (4-6 Hz) is displayed in figure 3.41 for the E-W component of the Cook Strait recordings. Stations rh3, rh4, and rh6 show a distinct response at about 5 Hz.

Standard Spectral Ratios (SSR)

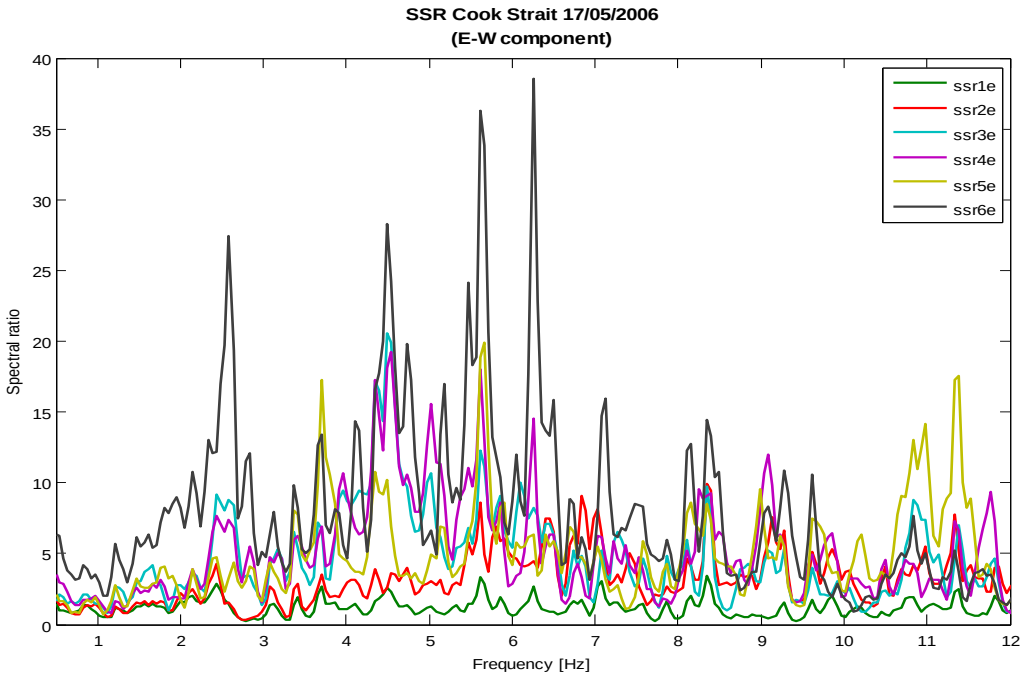

Figure 3.42: Cook Strait earthquake – Standard Spectral ratios of the E-W component for each station relative to the base reference station rh0

Four distinct maxima are presented for the response to the Cook Strait event at station rh6 at 2.5, 4.5, 5.5 and 6.2 Hz (Fig. 3.42). Spectral ratios of 27-39 were calculated at that station at the very top of Little Red Hill. The other stations along the ridge respond for frequencies between 4.5 and 6.5 Hz. Station rh3 and station rh4 reach spectral ratios of up to about 20 at 4.5 Hz.

3.5.8 MT SOMERS EARTHQUAKE 20060519.1900

3.5.8.1 Time domain analysis

Table 3.10: Mt Somers earthquake – observed time-domain data at the station with the greatest amplitudes (rh6)

Location /component		Peak ground acceleration [g]	Peak ground velocity [cm/s]	Peak ground displacement [cm]	Effective duration [s]
Mt Somers 20060519.1900	Z	0.0008	0.0204	0.0008	9.56
	N-S	0.0027	0.0997	0.0049	8.28
	E-W	0.0044	0.1360	0.0051	7.28

The magnitude 2.6 Mt Somers earthquake represents the only earthquake in this study to have its epicenter south of the test site. The highest ground motions recorded from this earthquake occurred in the E-W direction at station rh6 (4.4 milli-g; Table 3.10). Displacements of 0.051 mm were measured in the E-W direction and 0.049 mm in the N-S direction. The vertical displacement reached a maximum of 0.008 mm for this earthquake.

The effective duration of ground motion for the Mt Somers earthquake ranged between 7.28 s in the E-W direction and 9.56 s in the vertical direction.

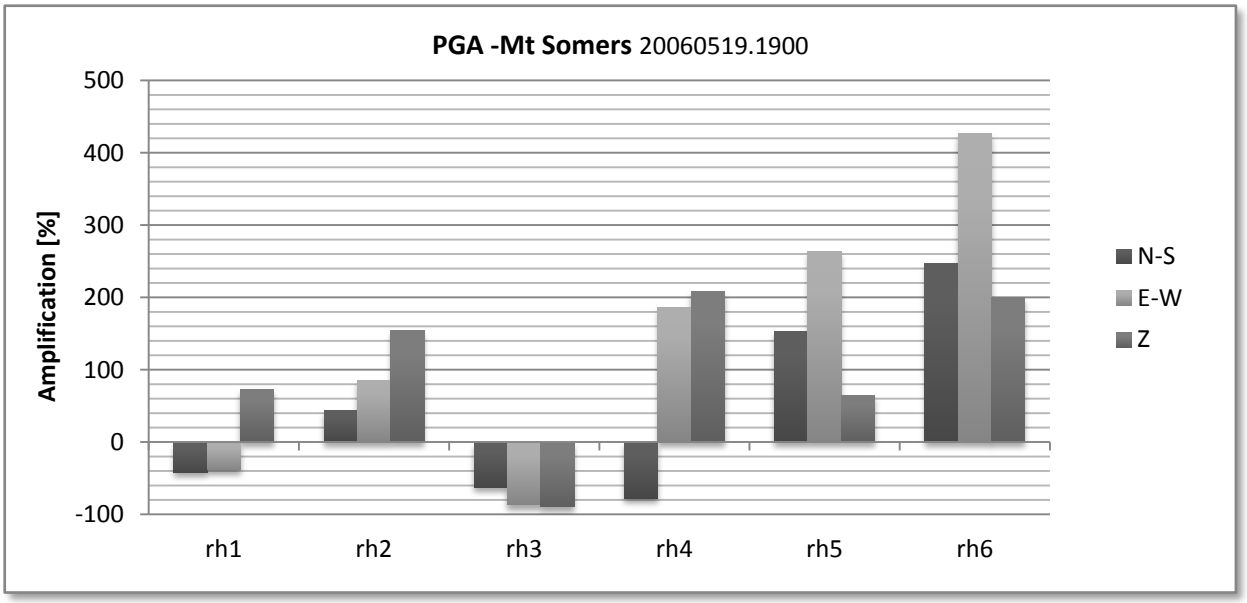

Figure 3.43: Mt Somers earthquake - Amplification of Peak Ground Accelerations relative to reference station rh0 – motion component transverse (E-W), parallel (N-S) to the main axis and in vertical direction (Z)

Ground motions recorded during the Mt Somers event show a different pattern to the other seven earthquakes in this study (Fig. 3.43). De-amplification was observed at half of the stations for ground motions in the N-S direction, rh1 (-42 %), rh3 (-62 %) and rh4 (-78%). The other three stations along the ridge recorded amplifications, with the greatest occurring at station rh6 (247 %).

De-amplification of ground motions were also recorded at stations rh1 (-38 %) and rh3 (-87 %) in the E-W direction. All other stations showed amplified ground motions in this direction, with the maximum amplification occurring at station rh6 (427 %), on the very top of the ridge crest.

Amplifications were recorded in the vertical direction at all stations except station rh3, which recorded a de-amplification of -87 %. The highest amplification in this direction was calculated for station rh4 (208 %).

3.5.8.2 ***Frequency domain analysis***

Power Spectral Density (PSD) – Multitaper Method (MTM)

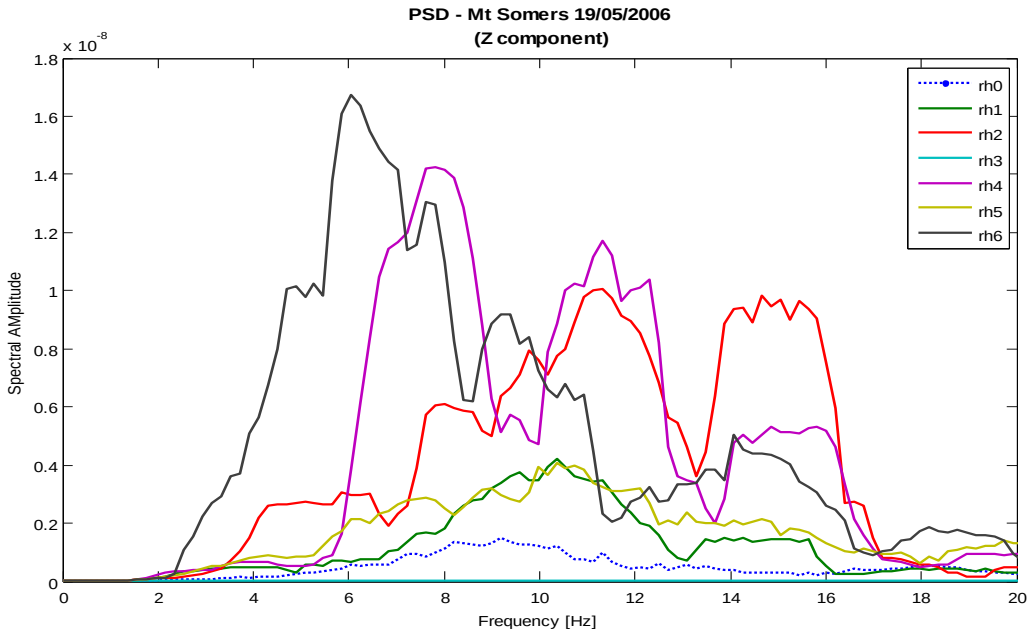

Figure 3.44: Mt Somers earthquake - Power spectral densities of the vertical component at each station

Looking at the power spectral densities calculated from the recordings of the Mt Somers event, we can see the vertical response of the stations is distributed over a wide band of frequencies (14 Hz wide; Fig. 3.44). The largest amplitude was calculated for station rh6 at 6 Hz. The other stations show peaks at higher frequencies between 6 and 16 Hz.

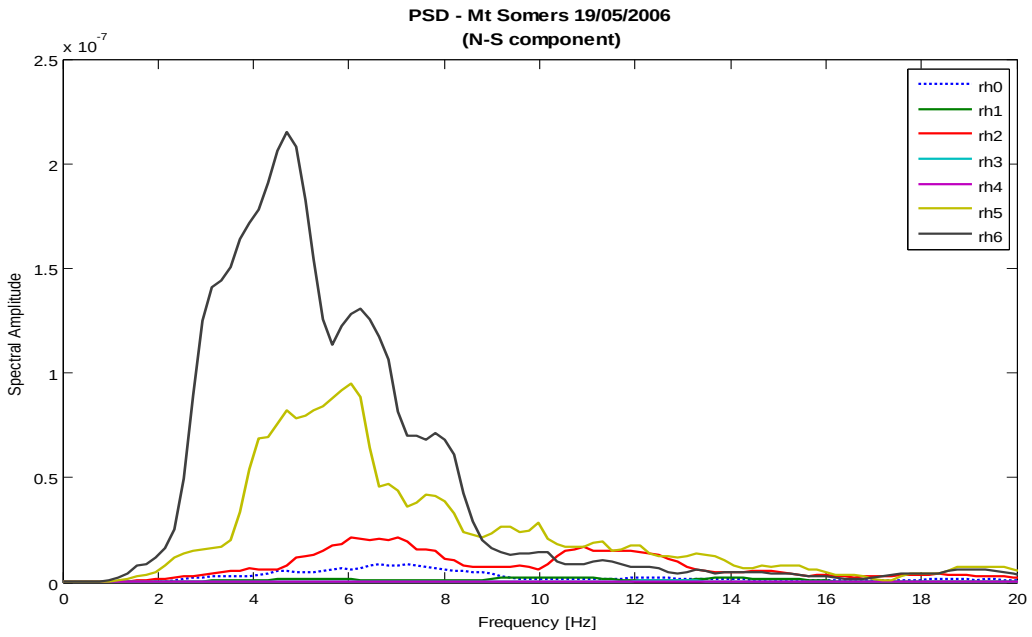

Figure 3.45: Mt Somers earthquake - Power spectral densities of the N-S component at each station

A broad response (3-8 Hz), but with distinct peaks are displayed for the N-S component of ground motion (Fig. 3.45). The power spectral density is concentrated at frequencies between 4 and 6 Hz for the very top of the hill at stations rh5 and rh6. All other stations show very little response at that frequency range.

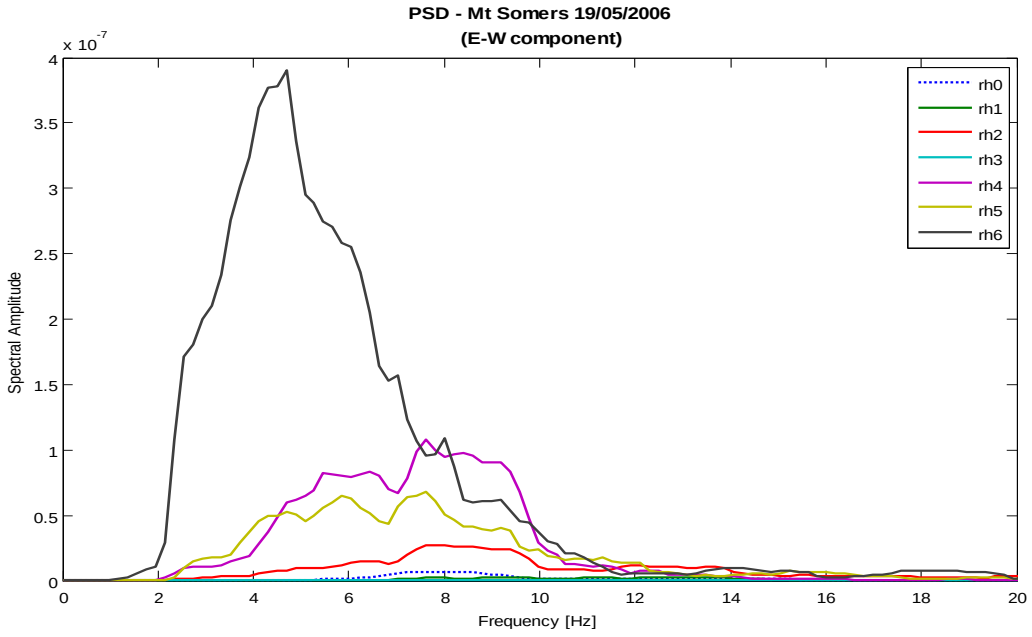

Figure 3.46: Mt Somers earthquake - Power spectral densities of the E-W component at each station

In the E-W direction (Fig. 3.46), power spectral densities are again distributed over a wide range of frequencies (2-10 Hz) for stationsrh2, rh4, and rh5. Their response is highest between 4 and approximately 9 Hz. Station rh6 shows a distinct peak, representing the highest amplitude, at a frequency of 5 Hz.

Standard Spectral Ratios (SSR)

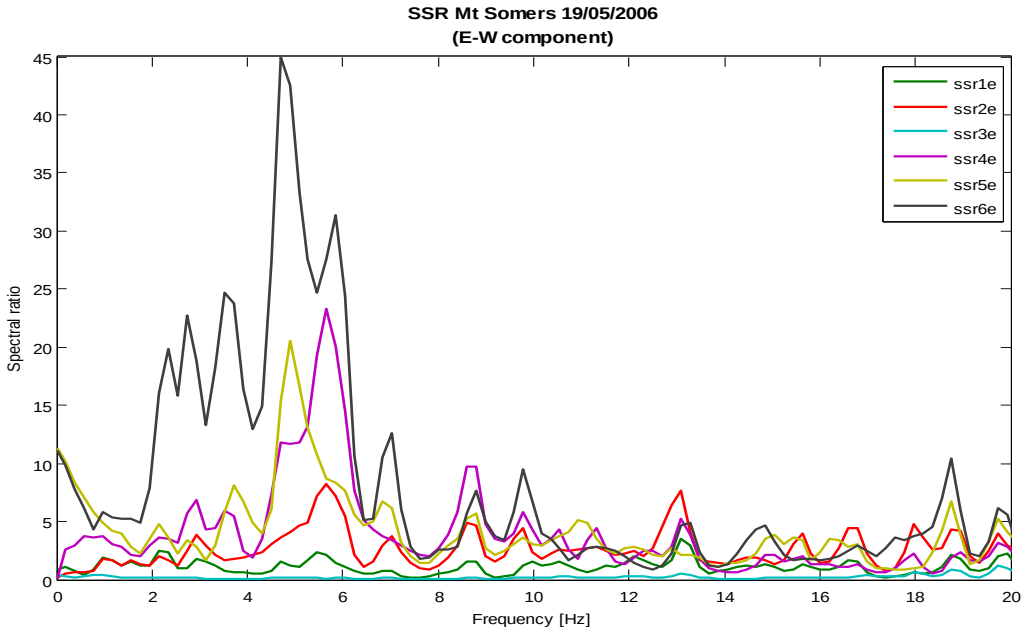

Figure 3.47: Mt Somers earthquake – Standard Spectral ratios of the E-W component for each station relative to the base reference station rh0

Standard spectral ratios calculated for the Mt Somers show a similar response as seen in the PSD analysis (Fig. 3.47). A broad response can be observed for station rh6 at frequencies between 2 and 7 Hz. Maximum spectral amplifications were computed for stations rh4 (20), rh5 (24) and rh6 (45) at 5 to 6 Hz.

3.5.9 RESULTS SO FAR

The following paragraphs present a short summary of the basic time and frequency domain analysis results of the data gained from the Little Red Hill seismic field experiment. The summary consist of a presentation of peak values that were recorded at the seismic array and resumes first trends of the response of Little Red Hill to seismic ground motion in both the time and frequency domain.

*3.5.9.1 **Time domain results***

- Highest peak ground motions, in both horizontal and vertical directions, were recorded for the M_L=7.4 Kermadec Islands earthquake at the very top of the edifice at station rh6. PGA reached maximum values of 0.049 g in the E-W direction, 0.048 g in N-S direction, and 0.014 g for the vertical component. PGVs recorded were 2.16 cm/s (E-W), 1.84 cm/s (N-S), and 0.54 cm/s in vertical direction. This resulted in peak ground displacements of 1.7 mm (E-W), 1.3 mm (N-S), and 0.5 mm (Z).

- Peak ground motions in all cases were the highest for motions perpendicular to the main mountain axis (E-W component) and were followed by motions parallel to the elongation of the edifice. The least peak ground motions were recorded in the vertical direction. Peak ground motions: E-W > N-S > Z.

- Maximum ground motions were recorded at station rh6 at the very top of the edifice for seven earthquake events. Only for the Arthur's Pass event maximum ground motions occurred at a different station along the ridgeline, at station rh3.

- The longest effective duration of 169 seconds was computed for the vertical component of the Kermadec Islands event at station rh3 (see appendix A.2).

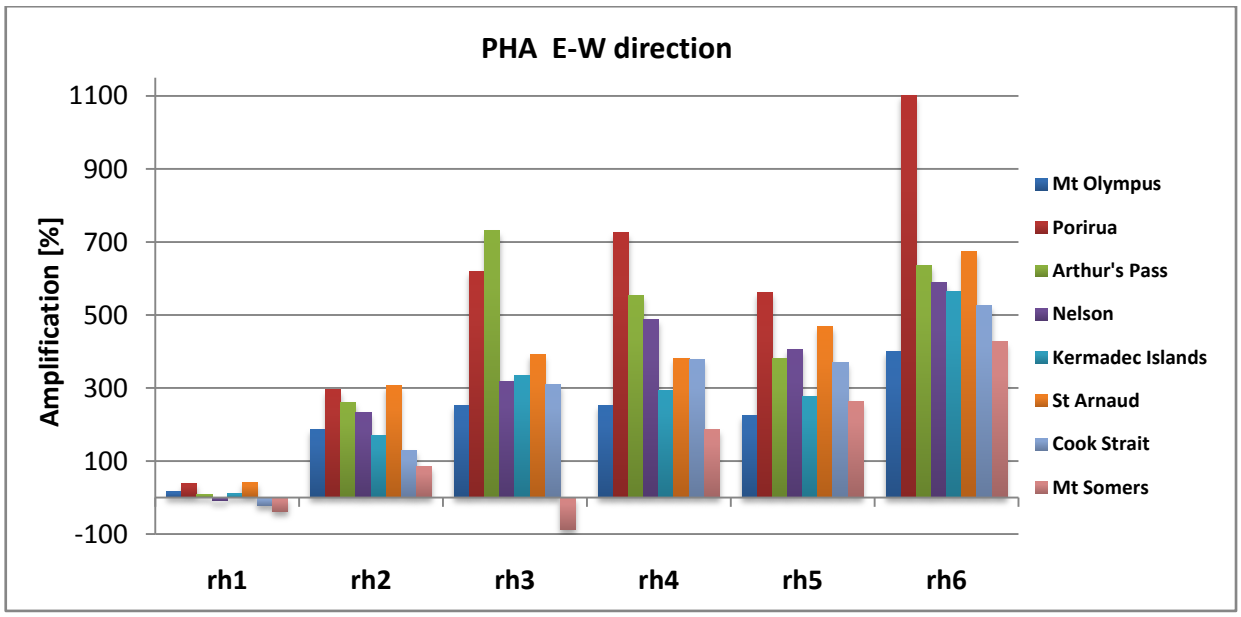

Figure 3.48: Amplification of Peak Ground Accelerations relative to reference station rh0 for selected earthquake events – motion component transverse (E-W) to the main axis

- Highest peak horizontal amplifications were calculated for the E-W component of the Porirua event at station rh6. Ground motions recorded at that station were amplified by 1100 % compared to the base reference station rh0.

- The flank of the edifice at station rh1 experienced only little amplification or small de-amplification of horizontal ground motions orientated perpendicular to the main axis of the mountain. Values of amplification were computed in a range between -39% and +41%.

- Station rh2, located at the front section of the ridge, shows the least amplification of ground motions of all stations along the ridge line.

- The top of Little Red Hill (rh6) experienced the highest amplifications of ground motions in the E-W direction for all earthquake recordings but the Arthurs's Pass event.

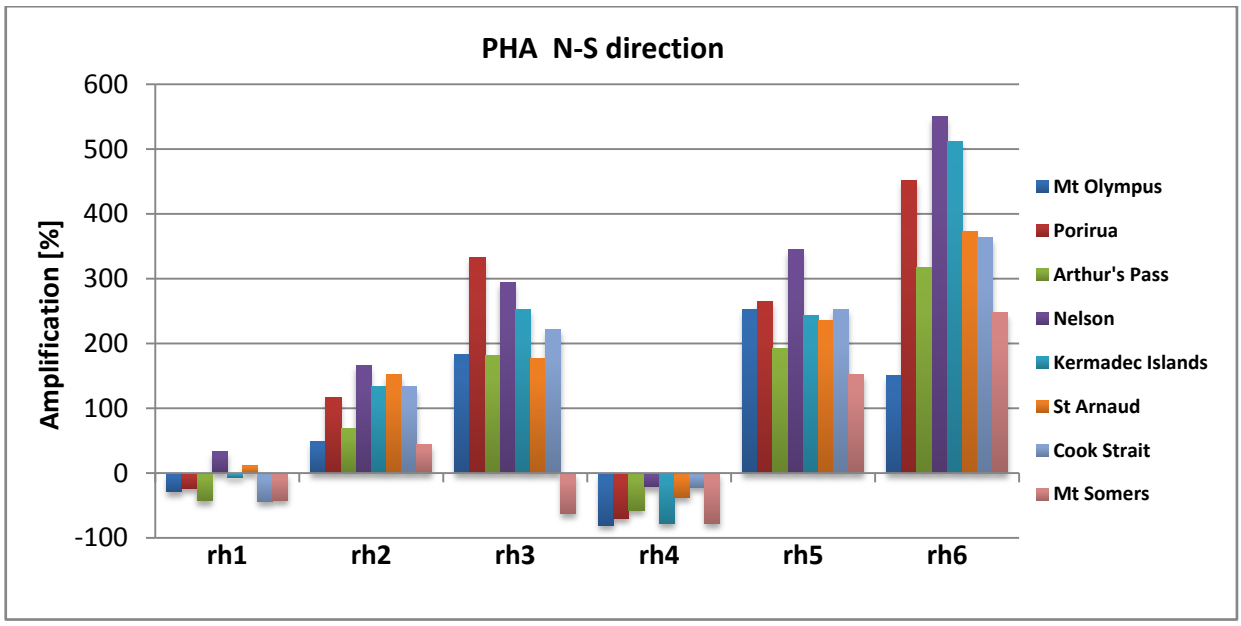

Figure 3.49: Amplification of Peak Ground Accelerations relative to reference station rh0 for selected earthquake events – motion component parallel (N-S) to the main axis

- Maximum amplifications for ground motions along the main axis of the edifice were calculated at station rh6 (550 %, Nelson earthquake).

- The flank of the edifice at station rh1 generally experienced de-amplification of the N-S component.

- Ground motions along the main axis of the edifice are de-amplified at station rh4, located at the centre of the ridge crest for the selected earthquake events.

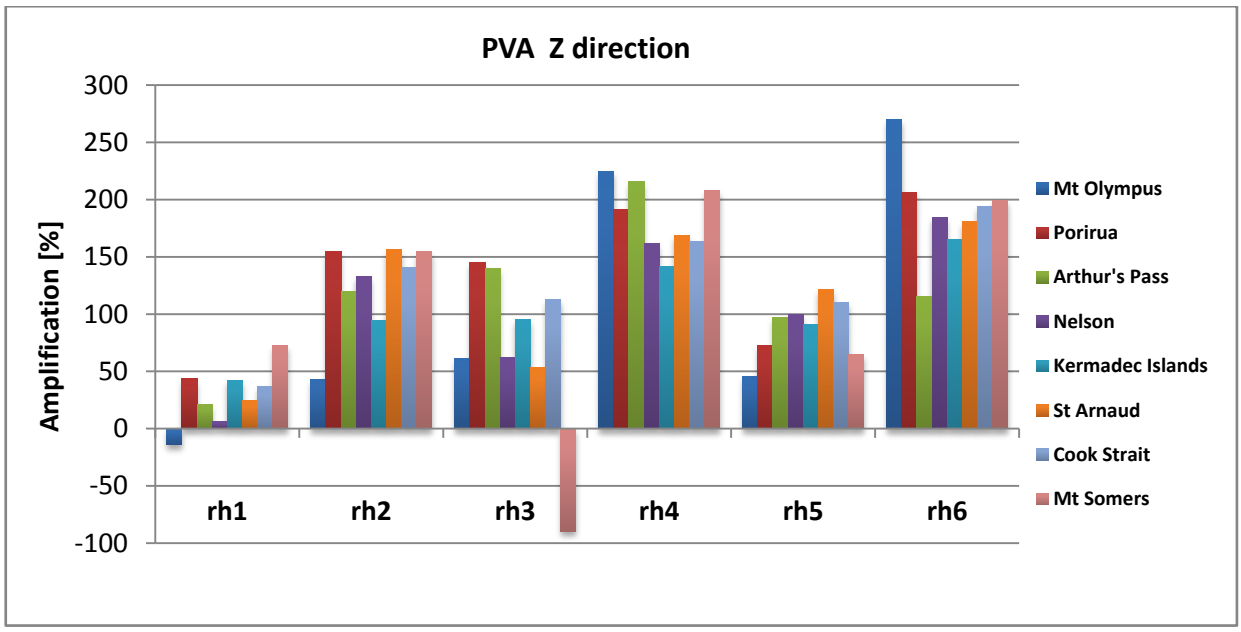

Figure 3.50: Amplification of Peak Ground Accelerations relative to reference station rh0 for the selected earthquake events – motion component in vertical direction (Z)

- Ground motions in the vertical direction were amplified for almost all earthquake events. A maximum amplification of 270 % was computed at station rh6 compared to the base of the hill at station rh0 for the Mt Olympus event.

- De-amplification effects in the vertical direction were only observed at stations rh1 and rh3 for the Mt Olympus event and the Mt Somers event respectively.

*3.5.9.2 **Frequency domain results***

The results from spectral analyses using the power spectral density multitaper method (PSD) and the standard spectral ratio method (SSR) are summarized as follows:

- The largest response along the edifice was observed for ground motions in the E-W direction at the hilltop (station rh6) at a predominant frequency of about 5 Hz. PSD amplitudes of up to 1.05 x 10^{-4} were computed at station rh6 for that motion component. Maximum spectral amplifications of up to 45 were calculated for the Mt Somers, Porirua, and Kermadec event at 5 Hz.

- Stations rh3, rh4 and rh5 also show a distinct response at about 5-6 Hz for the majority of the selected earthquake events in the direction perpendicular to the main axis of the edifice. Only for the Arthur's Pass event, the main resonance at station rh5 occurs at 7.5 Hz. Spectral amplification factors reach values between 20 and 30 times at these stations along the ridge line compared to the reference station rh0 at the base of Little Red Hill.

- The response (E-W component) of station rh2, located at the descending front of the ridge crest, is characterized by lower factors of spectral amplification (SSR up to 16) at higher frequencies (8-9 Hz). Distinct resonance was also observed at 7 Hz (SSR max. of 14) and 5 Hz (SSR max. of 8).

- Spectra calculated for the E-W component of the selected earthquake recordings show resonance at distinct narrow frequency distributions (at 5 Hz) for the distant events (Porirua, Kermadec Islands, Cook Strait). Closer events are characterized by a resonance that is distributed over a broader range of frequencies (3-5 Hz wide).

- The station placed at the flank of the edifice (rh1) has a distinct response for a frequency at about 2.5 Hz. This peak can be seen at smaller amplitudes at the stations along the ridge.

- Spectra calculated for the N-S component, ground motions along the main axis of Little Red Hill, have their highest response mainly located at about 5 Hz at station rh6 at the top of the edifice. The strongest energy input (PSD spectral amplitude of about up to 5.7 x 10^{-5}) was recorded at station rh6 for the Kermadec Islands earthquake. The SSR technique shows amplification of ground motion is amplified at station rh6 at 3 Hz and 5 Hz of up to 15 and 11 times respectively compared to recordings analyzed at the reference station rh0.

- Distinct response can be observed especially for stations rh2, rh3, rh5 and rh6 between 3 and 6 Hz for the majority of the selected events for the N-S component.

- Stations rh1 and rh4 show no significant response for ground motions polarized along the main axis of Little Red Hill compared to the other stations along the edifice.

- The analysis of the vertical component of the selected earthquake recordings shows a maximum response (PSD amplitude of 3.2 x 10^{-6}) at the very top of Little Red Hill (station rh6).

- A maximum spectral amplification (factor of 19) was observed in the Z direction for the Mt Olympus event at station rh4 at about 11 Hz.

- Further distinct modes of resonance for the vertical component of ground motion were observed at 5, 7, and 11 Hz.

3.6 FURTHER ANALYSES

The base data gained from the time and frequency analyses are used in the following section to further evaluate the response of LRH to seismic waves. The main focus is concentrated on evaluating following questions:

- Are there possible correlations between earthquake source parameters such as magnitude, epicentral distance, and azimuth and the response of Little Red Hill?

- Is there a correlation of the response of Little Red Hill, which has been computed by using the field data, with theoretical calculations of the main modes of vibrations for Little Red Hill?

- Is there a relation between the response of Little Red Hill to seismic ground motions and geometric parameters of the mountain edifice?

- Is there a uniform response of Little Red Hill to seismic wave input or are there complex spatial variations across the edifice?

- Is the response of Little Red Hill to weak ground motions, which were recorded during the seismic field experiment, also representative for strong ground motion input?

3.6.1 EDIFICE RESPONSE VS. EARTHQUAKE SOURCE PARAMETERS

3.6.1.1 Frequency response & predominant period of Little Red Hill for regional and teleseismic events

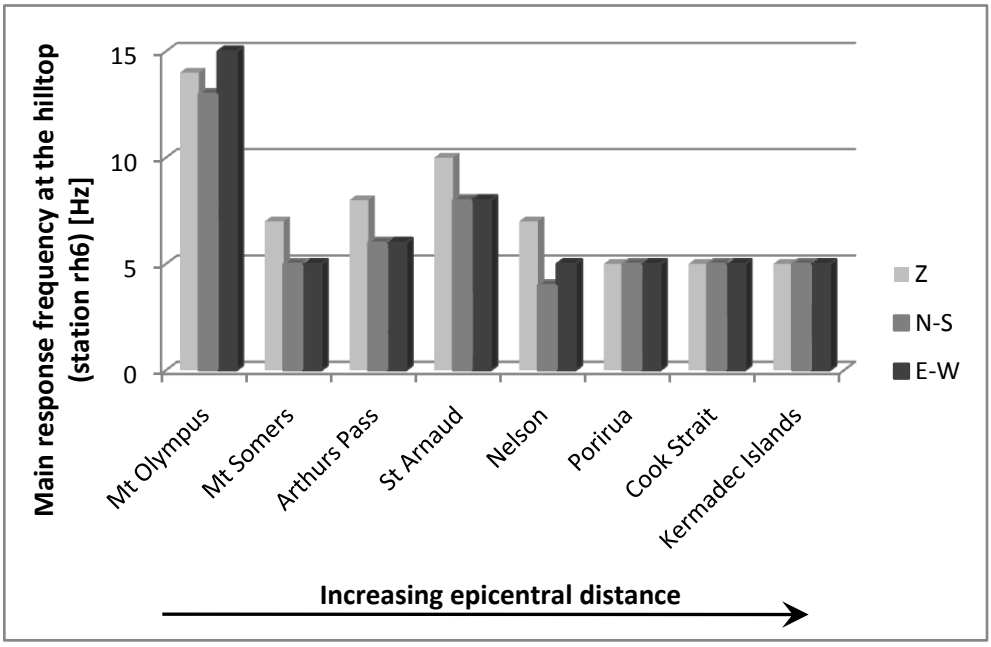

Figure 3.51: Frequency response at the top (station rh6) of Little Red Hill. Chart shows the main response frequencies for the three components of ground motion for the selected events plotted against increasing epicentral distance

Site response evaluation at Little Red Hill shows that the frequency response at the hilltop (station rh6) is related to the epicentral distance of the earthquake (Fig. 3.51). The edifice responds in a uniform fashion at about 5 Hz for all three components of ground motion if the epicentral distance is greater than about 300 km. This can be seen for the Porirua, the Cook Strait, and the Kermadec Islands event. Events that are located closer to the test site show a wideband frequency response with a shift to higher frequencies.

Similar findings were observed by calculating the predominant period Tp at station rh6 for the selected earthquake events (Fig. 3.52). Surface and transverse waves near the surface show a multi reflection phenomenon in the surface layer. This is caused by a velocity decrease in the surface layer compared to higher seismic wave velocities in the deeper crust. The predominant period describes the dominant vibration of the ground at a certain specific period. It corresponds to the maximum value of the Fourier amplitude spectrum and is determined by the structure of the

surface layer (Doyle, 1995; Kramer, 1996). The predominant period is obtained from a smoothed Fourier amplitude spectrum to avoid the influence of individual spikes of the spectrum and widely used in the Earthquake Engineering community to characterize ground motions.

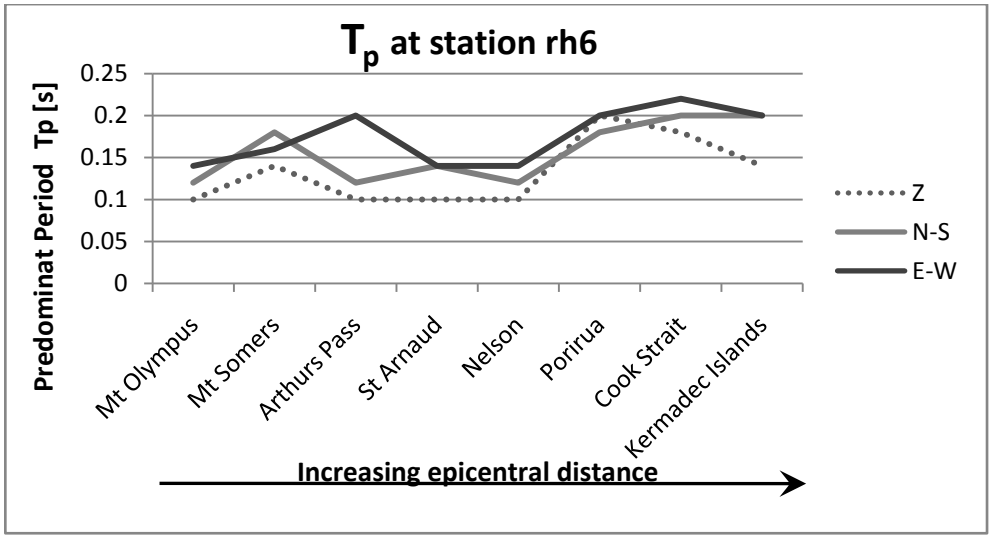

Figure 3.52: Predominant period T_p at the top (station rh6) of Little Red Hill. Chart shows the predominant period of vibration for the three components of ground motion for the selected events plotted against increasing epicentral distance

In the case of Little Red Hill, the predominant period shows a shift from lower periods (< 0.15 s) for the regional events towards longer periods (approx. 0.2 s) with increasing epicentral distance. This trend can be observed for both the N-S as well as the E-W component of ground motion at station rh6 and confirm results gained from the PSD and SSR analysis.

Data analyses reveal Little Red Hill responds along the ridge crest at a main response frequency of about 5 Hz, independent of different earthquake source parameters. A difference in the frequency response can be observed by comparing teleseismic events (for example the Kermadec Island event; epicentral distance: 1500 km) with close by regional events (for example the Mt Somers event; epicentral distance: 43 km). Teleseismic events (distance >10°<103°; 1°=111 km) show a more uniform and narrow band frequency response because of a near vertically incoming wave field. The seismograms are relatively simple and dominated by waves that have travelled through the mantle. This leads to an input at Little Red Hill of more pure horizontally polarized vertically propagating shear waves. A more complex input occurs for the regional events (distance <10°), such as the Mt Somers event. Regional events are dominated by sub vertical

surface wave motions. Incoming waves have travelled dominantly through the crust. A whole variety of wave forms such as strong p-wave and surface wave motions are contributing to the response of the hill during a regional event. During regional events most of the recorded seismic waves have propagated through a much more inhomogeneous crustal path and/or along the Moho (Kulhanek, 1990). This inhomogeneous crustal path of the propagating seismic waves enhances multiple reflections and refractions and produces different types of incoming seismic waves which are approaching Little Red Hill from a variety of angles. The response of Little Red Hill is therefore characterized by a more complex wide band frequency response for regional events compared with the response for teleseismic events (Fig. 3.53).

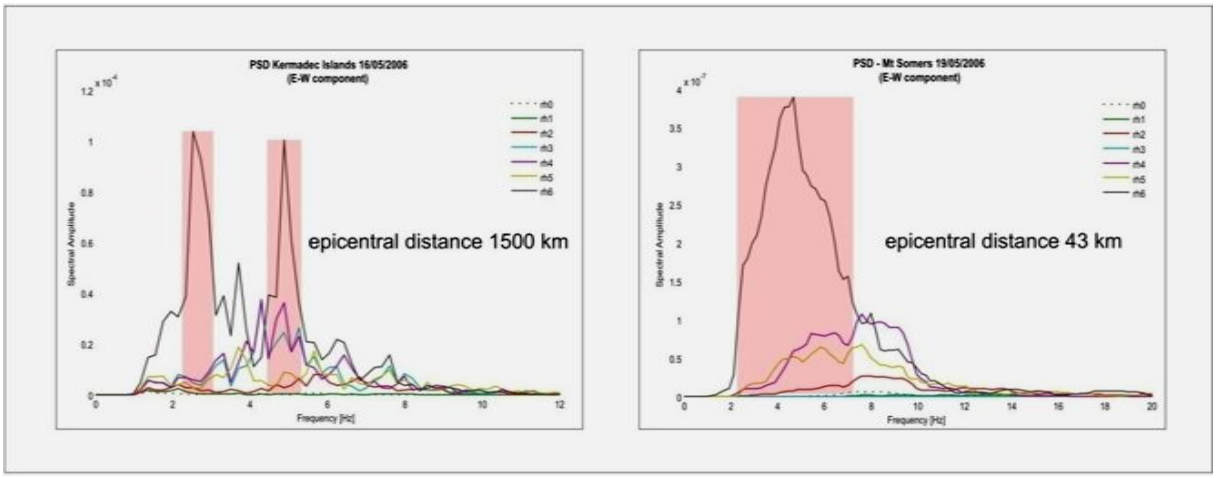

Figure 3.53: Comparison of the frequency response of a teleseismic event (Kermadec Islands, left graph) with a regional event (Mt Somers, right graph). The E-W component of The Kermadec shows a narrow band frequency response, whereas the Mt Somers spectrum is characterized by a broad band frequency response

3.6.1.2 *Site response evaluation compared to the azimuth of the incoming seismic waves*

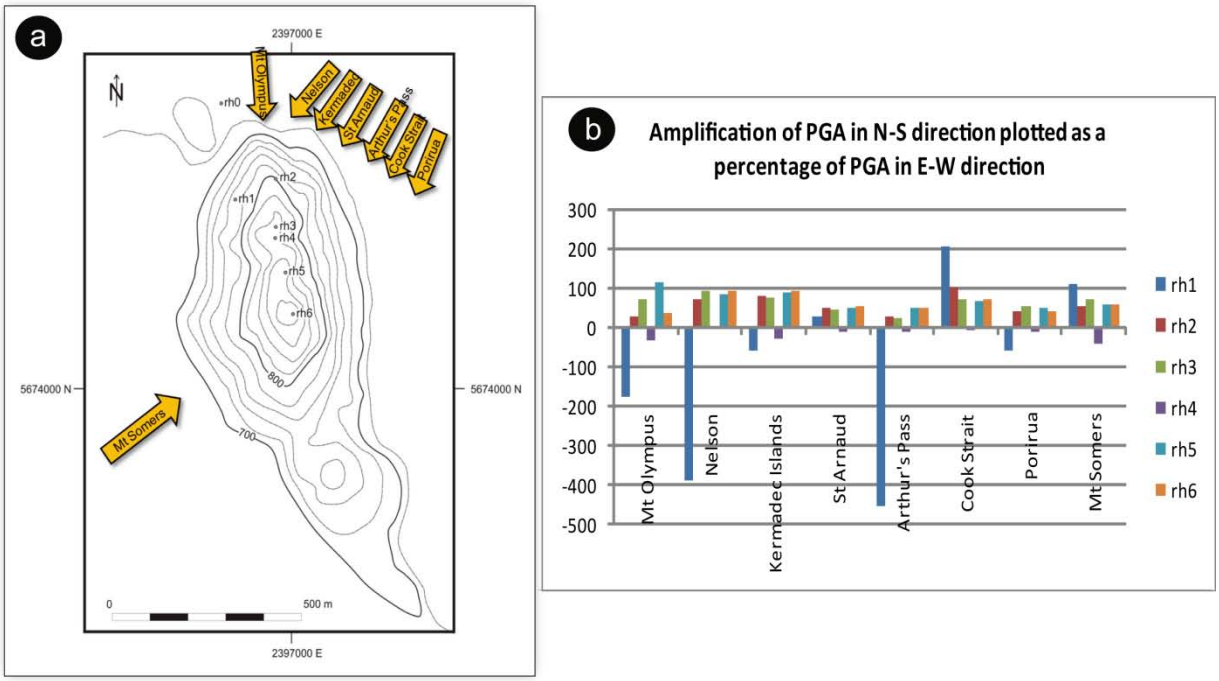

Figure 3.54: a) Topographic map of Little Red Hill showing the distribution of the azimuth of the selected earthquake events towards the test site, presented as yellow arrows; b) Amplification of the peak horizontal acceleration in N-S direction at every station plotted as a percentage of the peak horizontal acceleration in E-W direction

We evaluated if the response of Little Red Hill to dynamic seismic wave input shows any significant relation to the azimuth of the test site towards the earthquake epicenters of the different events. We compared the response of LRH in the different horizontal directions as well as the horizontal amplification with the variation in azimuth towards the test site. Figure 3.54 shows the distribution of the azimuth of the selected earthquake events towards the test site including a chart that presents the amplification of the PGA in N-S direction as a percentage of the PGA in E-W direction. No characteristic pattern that would indicate a change in the response of LRH in relation to different azimuths of the incoming wave field towards the test site could be found.

3.6.2 THEORETICAL EVALUATION OF THE FIRST MODES OF VIBRATION FOR LITTLE RED HILL

The observations of the response of Little Red Hill have shown that the dominant response for the stations along the ridge crest occurs at about 5 Hz. Spectral analyses at station rh1 reveal that the flank of the hill is mainly responding to a frequency of about 2-3 Hz. A slightly amplified response at the same frequency can be observed for other stations along the ridge. This observation could show that the fundamental mode of vibration for Little Red Hill could be located at a frequency of about 2-3 Hz, whereas the main response of the hill top is captured at the second mode of vibration. Theoretically, in the case of a damped system, the peak amplification factor decreases with increasing natural frequency. The greatest amplification factor will occur approximately at the lowest natural frequency, which is known as the fundamental frequency f_0 or the fundamental mode of vibration. As discussed above, Little Red Hill shows a complex response due to complex internal reflection and refraction effects of a variety of involved seismic waves. Therefore the dominant response of stations at the top of the ridge at frequencies of about 5 Hz could represent the second mode of vibration. To clarify this observation, we present in the following section three theoretical methods to calculate the first three modes of vibration for Little Red Hill. First we present a common one-dimensional approach (Kramer, 1996), which uses a simplified technique to analyse dynamic ground response. Then two more complex two-dimensional dynamic response analyses are presented (Ambraseys, 1960; Dakoulas and Gazetas, 1985) to evaluate the natural response frequencies of Little Red Hill.

1) In a simplified one-dimensional case of a uniform, damped layer of soil on rigid rock, the fundamental frequency ω_0 depends only on the thickness H and shear wave velocity v_s of the soil, Eq. (5.1). It provides a useful indication of the frequency of vibration at which the most significant amplification can be expected (Kramer, 1996).

Equation (5.1) provides the value for the n^{th} natural circular frequency, expressed in radians per second:

$$\omega_n = \frac{v_s}{2\,H}\left(\frac{\pi}{2} + n\pi\right) \qquad \text{n= 0, 1, 2,…} \qquad \textbf{(5.1)}$$

with $T = \frac{4\,H}{v_s}$, $f = \frac{v_s}{4\,H}$

The n^{th} natural frequency expressed in Hertz is then given by

$$\omega_n = f_n * 2\pi = \frac{v_s}{2\,H}\,2\pi = f_1$$

$$f_n = \frac{\omega_n}{2\,\pi} \qquad \textbf{(5.2)}$$

We assume Little Red Hill to represent the uniform soil layer (according to the one dimensional approach). In our case we choose H=210 m (height of Little Red Hill) and an average shear wave velocity v_s of 1200 m/s (shallow surface shear wave velocity data of Torlesse argillites and sandstones; Table 3.11).

Table 3.11: Torlesse greywacke data, presenting shallow surface shear wave velocities for Torlesse argillites and sandstones for different degrees of weathering/fracturing, modified after Perrin (2008)

Torlesse argillites and sandstones (shallow surface shear wave velocities, upper 100 m)	
Degree of weathering	**Shear wave velocity v_s**
CW (completely weathered)	500-550 m/s
HW (highly weathered)	550-750 m/s
MW (moderately weathered)	750-1000 m/s
SW-UW (slightly to unweathered)	1000-1200 m/s

Similar values for near-surface shear wave velocities of Torlesse argillites and sandstones have been experienced by Benites and Olsen (2005)[1] and Duffy (2007; 2008)[2]. Borehole-geotechnical data collected by Borcherdt & Eeri (1994) also justify the choice of a mean shear wave velocity of about 1200 m/s (Fig. 3.55).

[1] Benites & Olsen (2005): Lithified, fractured basement rock (Torlesse greywacke): $v_s \approx 1500$ m/s

[2] Duffy (2007, 2008): Multi-channel analysis of surface waves, Torlesse shear wave velocity: $v_s \approx 1400$ m/s

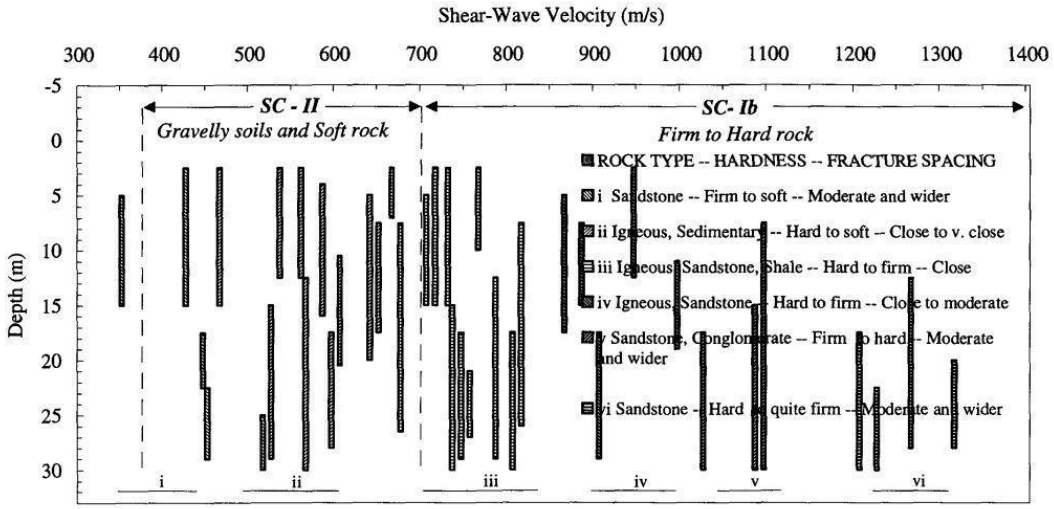

Figure 3.55: Shear-wave velocities for depth intervals determined in bedrock materials in the San Francisco Bay region (from Fumal, 1978). The materials are divided into groups according to fracture spacing, hardness, and lithology. Fracture spacing is defined as: very close 0 to 1cm, close 1 to 5 cm, moderate 5 to 30 cm, and very wide more than 100 cm (after Borcherdt and Eeri, 1994)

Therefore from equations (5.1) and (5.2) the fundamental frequency f_0 is

$$\omega_0 = \frac{\pi\, v_s}{2\, H} = \frac{\pi * 1200\, m/s}{2 * 210\, m}$$

$$\omega_0 = 8.98\, rad/s$$

$$f_0 = \frac{\omega_0}{2\,\pi}$$

$$f_0 = \frac{8.98\, rad/s}{2\,\pi} = 1.43\, Hz$$

The fundamental frequency f_0 of Little Red Hill calculated from this simplified model could be expected at about 1.4 Hz.

The first natural frequency f_1 is given by

$$\omega_1 = \frac{3\pi * 1200\, m/s}{2 * 210\, m}$$

$$\omega_1 = 26.93\, rad/s$$

$$f_1 = \frac{\omega_1}{2\,\pi}$$

$$f_1 = \frac{26.93\ rad/s}{2\,\pi} = 4.36\ Hz$$

The second natural frequency f_2 is given by

$$\omega_2 = \frac{5\pi * 1200\ m/s}{2 * 210\ m}$$

$$\omega_2 = 44.88\ rad/s$$

$$f_2 = \frac{\omega_1}{2\,\pi}$$

$$f_2 = \frac{44.88\ rad/s}{2\,\pi} = 7.14\ Hz$$

The first and second natural frequencies are calculated at 4.3 Hz and 7.1 Hz respectively.

2) A more realistic approach than equation (5.1) to determine the response frequency of the hill is also presented in Kramer (1996) using a shear beam approach for dynamic analysis of earth dams. This approach appears more appropriate for Little Red Hill because Little Red Hill represents an edifice of similar simple shape. However, some of the assumptions in this theory, such as the power function increase of the shear moduli with depth, may not be the most appropriate. The shear beam approach is based on the assumption that a dam deforms in simple shear which results in producing only horizontal displacements. This technique also assumes that either shear stresses or shear strains are uniform across horizontal planes. In this model we assume Little Red Hill is homogeneous and infinitely long. The shear beam approach allows a two-dimensional section of the edifice to be represented as a one-dimensional system (Fig. 3.56).

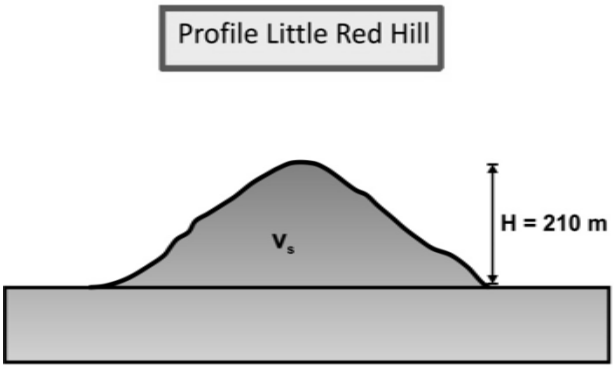

Values of ßn for the first 3 modes of vibration of an earth dam (after Dakoulas & Gazetas, 1985)

	n		
m	1	2	3
0	**2.404**	**5.520**	8.654
1/2	2.903	6.033	9.171
4/7	2.999	6.133	9.273
2/3	3.142	6.283	9.525
1	3.382	7.106	10.174

Figure 3.56: E-W cross-section of Little Red Hill including main parameters + table showing β_n values after Dakoulas & Gazetas (1985). Parameters used for the calculation are printed bold

Therefore the n^{th} natural circular frequency is given by equation (5.3):

$$\omega_n = \frac{v_s}{H}\frac{\beta_n}{8}(4+m)(2-m) \qquad \textbf{(5.3)}$$

The fundamental period is given by equation (5.4):

$$T_1 = \frac{16\,\pi}{(4+m)(2-m)\beta_1}\frac{H}{v_s} \qquad \textbf{(5.4)}$$

where H is the height of Little Red Hill, v_s is the average shear wave velocity of the Torlesse basement rock , and β_n is the n^{th} root of a period relation shown in figure 3.56 for the first three modes of vibration. The parameter *m* represents a factor of inhomogeneity (0 = homogeneous) and affects the mode shapes of vibration. Increased inhomogeneity (higher values of *m*) for the shear beam analysis of an earth dam model, results in large shear strains and high accelerations near the crest of the dam for the second and higher modes of vibration. This effect is known as the "whiplash effect" (Kramer, 1996). In the following calculations a factor of $m = 0$ will be used for our purpose representing Little Red Hill as a homogeneous edifice.

An average near surface shear wave velocity for Torlesse sandstones and argillites of v_s=1200 m/s is used for the calculations (recommended by Perrin (2008)).

Then from equation (5.3), the first three modes of vibration are calculated as follows:

$$\omega_0 = \frac{v_s}{H}\frac{\beta_n}{8}(4+m)(2-m) = \frac{1200\frac{m}{s}}{210\,m}\frac{2.404}{8}(4+0)(2-0) = 13.7\,rad/s$$

$$\Rightarrow f_0 = 2.2\,Hz$$

$$\omega_1 = \frac{v_s}{H}\frac{\beta_n}{8}(4+m)(2-m) = \frac{1200\frac{m}{s}}{210\,m}\frac{5.52}{8}(4+0)(2-0) = 31.5\,rad/s$$

$$\Rightarrow f_1 = 5.0\,Hz$$

$$\omega_2 = \frac{v_s}{H}\frac{\beta_n}{8}(4+m)(2-m) = \frac{1200\frac{m}{s}}{210\,m}\frac{8.654}{8}(4+0)(2-0) = 49.5\,rad/s$$

$$\Rightarrow f_2 = 7.9\,Hz$$

3) Ambraseys' (1960) theoretical approach, based on the shear response of a two-dimensional truncated wedge subjected to an arbitrary disturbance, leads to a fundamental mode of vibration or a natural frequency of about $f_0 = 2.5$ Hz.

The calculation of the fundamental mode of vibration and the results for the two higher modes of vibration using Ambraseys theoretical investigations are given by equation (5.5):

$$\boldsymbol{\omega_{nr} = \left(\frac{v_s}{H}\right)\sqrt{\left[a_n^2 + \left(\frac{r\pi}{\mu}\right)^2\right]}} \qquad \textbf{(5.5)}$$

Where $\mu = \frac{L}{H} = \frac{500\,m}{210\,m}$ and r = 1 represents the first longitudinal mode of vibration. The parameter a_n is the root of a period relation and equivalent to $ß_n$ tabulated in figure 3.56.

Fundamental mode of vibration (f_0):

$$\omega_0 = \left(\frac{1200\,m/s}{210\,m}\right)\sqrt{\left[2.4^2 + \left(\frac{1\pi}{2.4}\right)^2\right]}$$

$$\omega_0 = \left(\frac{1200\,m/s}{210\,m}\right)2.74$$

$$\omega_0 = 15.7\ rad/s$$

$$\Rightarrow f_0 = 2.5\ Hz$$

Second mode of vibration (f_1):

$$\omega_1 = \left(\frac{1200\ m/s}{210\ m}\right)\sqrt{\left[5.52^2 + \left(\frac{1\pi}{2.4}\right)^2\right]}$$

$$\omega_1 = \left(\frac{1200\ m/s}{210\ m}\right)\ 5.67$$

$$\omega_1 = 32.4 rad/s$$

$$\Rightarrow f_1 = 5.2\ Hz$$

Third mode of vibration (f_2):

$$\omega_2 = \left(\frac{1200\ m/s}{210\ m}\right)\sqrt{\left[8.65^2 + \left(\frac{1\pi}{2.4}\right)^2\right]}$$

$$\omega_2 = \left(\frac{1200\ m/s}{210\ m}\right)\ 8.75$$

$$\omega_2 = 50\ rad/s$$

$$\Rightarrow f_2 = 8.0\ Hz$$

Table 3.12: Results of one dimensional and two dimensional dynamic response analyses using three different approaches to evaluate the first three natural response frequencies / modes of vibration of Little Red Hill

Little Red Hill – Theoretical evaluation of the fundamental modes of vibration			
n^{th} natural frequency	**Kramer** 1D wave propagation theory	**Dakoulas & Gazetas** Shear beam approach	**Ambraseys** 2D truncated wedge approach
f_0	1.4 Hz	2.2 Hz	2.5 Hz
f_1	4.3 Hz	5.0 Hz	5.2 Hz
f_2	7.1 Hz	7.9 Hz	8.0 Hz

The theoretical approaches to determine of the fundamental mode of vibration for Little Red Hill reveal the fundamental response to seismic ground motion is located between 1.4 Hz and 2.5 Hz depending on the method used for the calculation (Tab. 3.12). The simplified one-dimensional approach used in Kramer (1996) produces lower values for the natural response frequencies compared to the results that were computed from the field test ($f_0 \approx 2.5$, $f_1 \approx 5$). The two-dimensional approaches (Dakoulas & Gazetas (1985), Ambraseys (1960)) to evaluate the natural response frequencies of Little Red Hill theoretically show results that agree with the field test observations.

3.6.3 GEOMETRIC PARAMETERS VS. RESONANCE OF LITTLE RED HILL

Geli et al. (1988) concluded that there is a significant amplification at hill tops with respect to the base for frequencies corresponding to wavelengths about equal to the mountain width. The following calculation will evaluate the wavelengths of the ground motions that are related to the fundamental mode of vibration and the frequency of maximum response of Little Red Hill.

The wavelength is given by

$$\lambda = \frac{v}{f} \qquad \textbf{(5.6)}$$

Based on equation (5.6) and by using a shear wave velocity v_s of 1200 m/s,

$$\lambda_0 = \frac{v_s}{f_0} = \frac{1200\ m/s}{2.5\ Hz} = 480\ m$$

and

$$\lambda_1 = \frac{v_s}{f_1} = \frac{1200\ m/s}{5\ Hz} = 240\ m$$

This calculation shows that that the fundamental response frequency f_0 of about 2.5 Hz is related to a wavelength λ_0 that is approximately the width of Little Red Hill (w = 500 m).

$$\lambda_0 \approx w$$

The wavelength λ_1, which correlates to the maximum response at the hill top at f_1 of about 5 Hz, is approximately equal to the half-width ($w_{1/2}$ = 250 m) or the height (h = 210 m) of the edifice.

$$\lambda_1 \approx 0.5 * w \approx h$$

This results shows, that there is a definite correlation between the fundamental and maximum response of Little Red Hill and the wavelength of incoming seismic waves. Resonance of Little Red Hill occurs for seismic waves whose wavelength characteristics allows them on their propagating path to get trapped within the geometry of the edifice. In the case of Little Red Hill, resonance can only be expected if the incoming seismic waves have wavelengths approximately equal to or less than the width of the edifice.

3.6.4 LITTLE RED HILL SEISMIC ARRAY – HORIZONTAL DISPLACEMENT VIDEO RESPONSE ANALYSIS

To visualize the response of the whole seismic array at Little Red Hill, the horizontal displacement data was used to produce video sequences of all selected earthquakes, showing the horizontal ground motions at all recording stations. The video sequences were computed to give an insight into overall movements at the different sites and to expose potential relations of ground motions at the sites relative to each other. The raw velocity data of each station for the selected earthquake events were processed and integrated with *SeismoSignal* (SeismoSoft, 2002) and the displacement extracted were imported into MATLAB® (MathWorks, 2005). An identical time window was chosen for each earthquake event. The EARSS instruments were connected to an external GPS clock therefore guaranteed precise timing for every station and a possibility of exact comparisons among all. A MATLAB® script was written that utilized the time data, N-S and E-W displacement data, and the exact GPS coordinates of each station to produce one picture of the array for every time step. The recording interval of the EARSS instruments was set to 50 Hz. Fifty pictures per second were computed for the duration of each of the selected events respectively. The computed assemblies of pictures for each event were then combined to produce a 50 frames-per-second video sequence (avi-format) that displays the horizontal displacement of the whole array. The motions are displayed in slow motion (0.5 times real speed) and displacements were multiplied equally in all directions (1000 – 10,000 times the original displacement, depending on the intensity of the event) to enable the visualization of relative movements of the stations to each other. The video sequences of each of the selected earthquake events are accessible on CD and can be found in appendix A.6.

During the evaluation of the video sequences the following observations were made:

1. There is no simple uniform horizontal vibration of Little Red Hill.
2. The video sequences give definite visual evidence that ground motions are highest at the very top of Little Red Hill (station rh6).
3. Complex response was observed between stations rh3 and rh4. Despite being located close together (only 28 m apart), particle displacements are often almost directly out of

phase (Fig 3.57). The same observation, but less intense, was made when comparing station rh6 to rh5. The out of phase motion could describe a rotation of ground motion within the distance between the sites (Berrill, 2007).

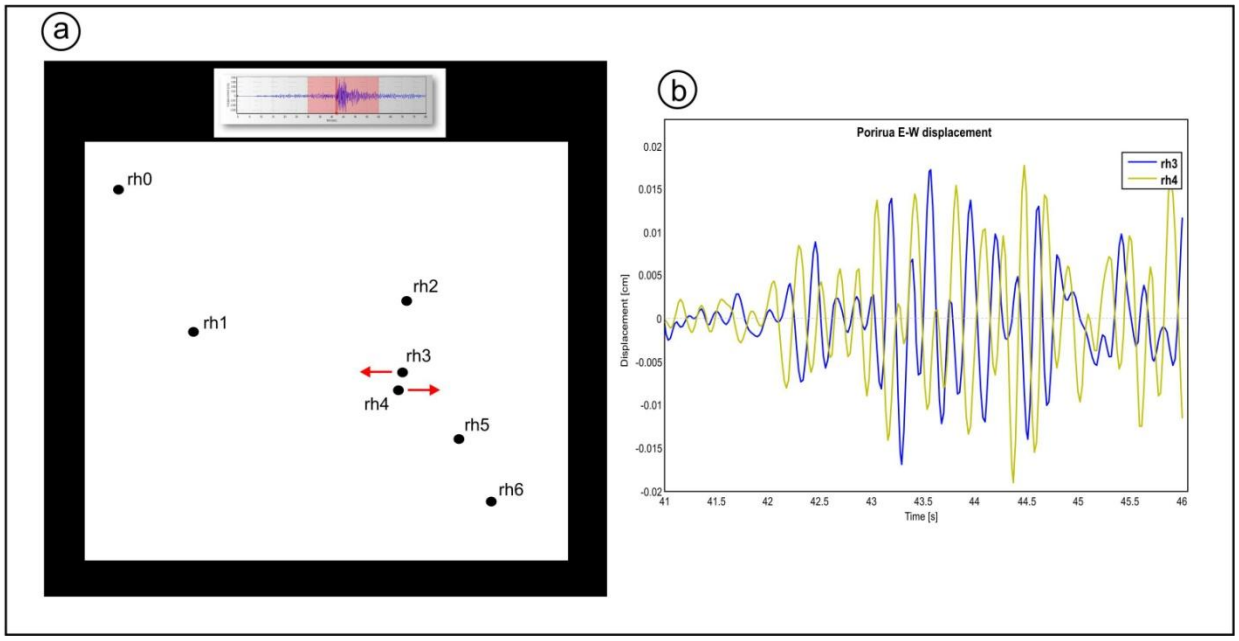

Figure 3.57: a) Snapshot from the Porirua horizontal displacement video sequence. Red arrows are inserted to show the common out of phase movement at station rh3 and rh4; b) Porirua event – time domain displacement data. Out of phase movement shown for the E-W component at adjacent stations rh3 and rh4

4. Stations rh5 and rh2 show in phase particle motion for the majority of the duration for each event.
5. The flank of Little Red Hill (station rh1) shows only insignificant horizontal displacement compared to the strongly responding ridge crest. Particle motions computed for station rh1 and for the base station rh0 are similar in intensity.

3.6.5 LEVEL OF AMPLIFICATION VS. INCREASED GROUND MOTION

During the seismic field test at Little Red Hill only weak ground motions were recorded. Ground motions did not exceed a PGV of about 2.2 cm/s at the hilltop. To evaluate the trend of topographic amplification at the hilltop (station rh6) with increasing ground motions, we plotted the amplification in percentage at station rh6 compared to the base station rh0 against increasing peak ground velocity (Fig. 3.58). We wanted to find out how the topographic amplification effect of ground motion will behave with increasing ground motion.

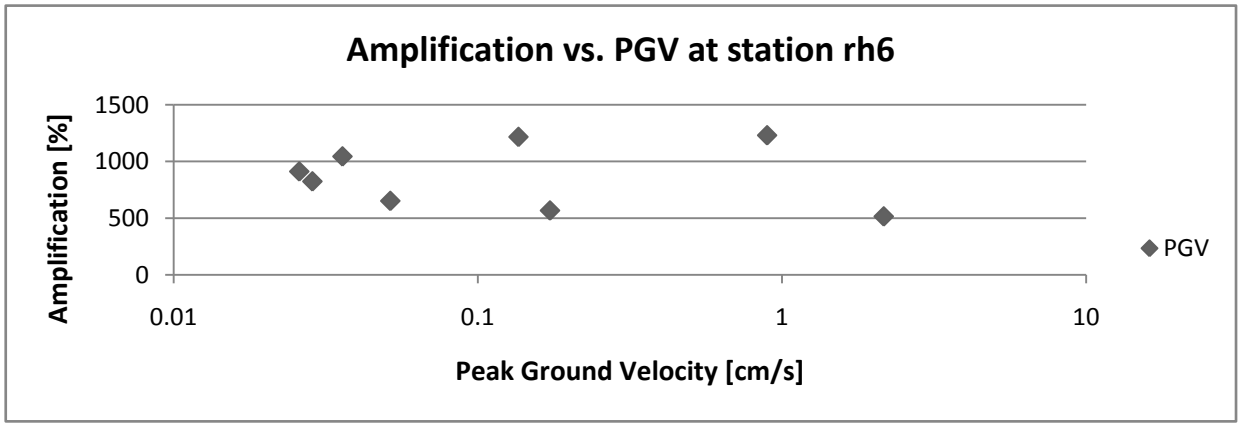

Figure 3.58: Amplification of peak ground velocity PGV recorded in E-W direction at station rh6 relative to base station rh0 plotted against increasing PGV

The amplification of ground motions at the hilltop compared to the base station shows a random distribution for peak ground velocities of up to 2.2 m/s. Amplifications of PGV were recorded in a range between 515 % and 1230 %. No definite relation or trend could be verified. In order to be able to compare our results to possible amplifications for strong ground motion input, we want to show that the rock mass on top of Little Red Hill will follow a quasi-linear behavior, thus amplification effects will always contribute to increase stresses at the top compared to the flat ground next to the hill.

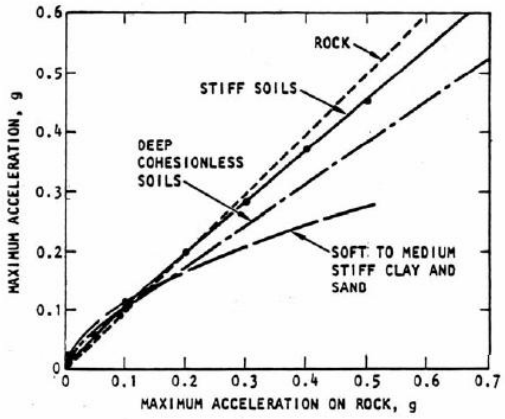

Figure 3.59: Approximate relationships between peak accelerations on rock and different types of soils (after Seed et al. (1976))

Soil deposits behave under increasing dynamic load in a non-linear fashion. With increasing ground motions the soil stiffness will decrease and this softening of the deposit may result in reduction in accelerations in case of strong nonlinearity. Figure 3.59 shows that relation for different types of soils, where the acceleration on rock represents the input motion caused by seismic waves propagating through deeper rock material.

We provide a conservative assumption of the induced shear strain for a maximum ground displacement of 1.7 mm, which represents the PGV that were recorded at station rh6 for the E-W component of the Kermadec event. We assumed that all motion occurs at a single frequency of 5Hz rather than with a wide band of components contributing. Thus, the shear strain estimate is larger than in reality, and therefore conservative (Berrill, 2008). The strains induced by propagating stress waves can be calculated following the wave propagation theory in unbounded media (Berrill, 2008; Kramer, 1996). The calculation is based on a simple harmonic motion represented by a sinusoidal stress wave with displacement amplitude *a* propagating through the rock mass and inducing shear strains that result in a certain displacement *u* (Fig. 3.60). The calculation is presented in trigonometric notation:

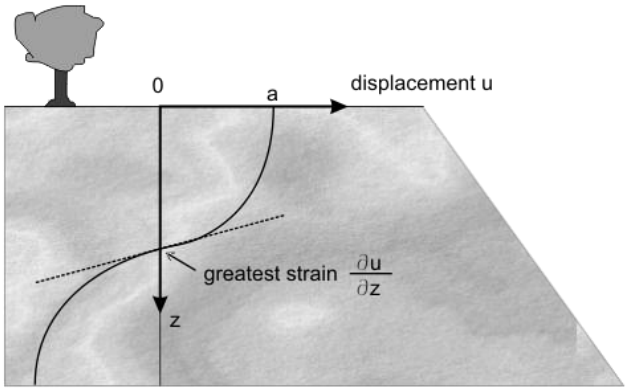

Figure 3.60: Sketch of a simple harmonic sinusoidal vibratory motion causing lateral displacement u and maximum strain $\frac{\partial u}{\partial z}$

Displacement *u* is given by

$$u = a\sin(kz - \omega t) \qquad \textbf{(5.7)}$$

where $k = \frac{\omega}{c}$ is the wave number.

We consider a harmonic S_h-wave, with displacement $u(z,t) = a\sin\frac{\omega}{c}(z - ct)$

then the engineering shear strain γ is given by

$$\gamma = \frac{\partial u}{\partial z} = a\,cos\frac{\omega}{c}(z - ct)\frac{\omega}{c} \qquad \textbf{(5.8)}$$

Harmonic motion occurs when $cos\frac{\omega}{c}(z - ct) = 1$

when argument $(z - ct) = 0$

Then the maximum shear strain can be written as

$$\gamma_{max} = \frac{a\omega}{c} \qquad \textbf{(5.9)}$$

In our case, we suppose that $\omega = 2\pi f$, with f = 5Hz as the predominant response frequency at the hilltop (station rh6), and $c = v_s = 1200$ m/s.

If the amplitude *a* of maximum displacement in our case is 1.7 mm,

then (after equation 5.9)

$$\gamma_{max} = \frac{0.0017m \;\; 2\pi \; 5 \; Hz}{1200 \; m/s} \approx 4.5 * 10^{-5}$$

The inferred shear strain in our case has a value of about $4.5 * 10^{-5}$, calculated from the maximum displacement of 1.7 mm that was recorded during the survey. This represents very small strain which is associated approximately with a linear elastic response in greywacke. Therefore the rock mass behaves linearly for weak motion. Amplification effects are always expected to be present and to decrease with increasing ground motion once effects of nonlinearity are more pronounced.

In case of increasing ground motions, the topographic amplification effect will trigger non-linear behavior. Intensive dynamic loads (strong ground motion) will cause the development of micro fractures within the bedrock (softening), therefore reducing its stiffness and possible exceeding the shear strength of the rock mass, which will consequently lead to failure of the rock mass (Cubrinowski, 2008). Strains of about 0.002 are needed for Torlesse greywacke to cause failure of intact rock mass specimen (Cook, 2001).

3.7 LITTLE RED HILL SEISMIC FIELD EXPERIMENT – DISCUSSION

The Little Red Hill field experiment was conducted to give an insight into the response of a bedrock-dominated, quasi-symmetric mountain edifice to seismic ground motion. The role of topographic amplification of seismic waves causing degradation and possible fatal failure of rock masses was examined.

The data analyses of the eight selected earthquake events that were recorded at the Little Red Hill test site reveal that amplification effects are more significant for horizontal than vertical components and for ground motions perpendicular to the main axis than for motions along the direction of the main axis. Comparing the peak ground velocities of the three components of ground motion at station rh6 with each other shows that the peak velocity in vertical direction is about one third (PGV_z = 0.28 * $PGV_{E\text{-}W}$) of the PGV of the E-W component. The PGVs computed for the N-S component are characterized by values that reach about two thirds of the motions that were measured in E-W direction ($PGV_{N\text{-}S}$ = 0.7 * $PGV_{E\text{-}W}$). This shows that Little Red Hill provides increased resistance to dynamic forces induced by ground motions polarized along the main axis due to a higher stiffness of the edifice in that direction.

⇨ *Ground motions in E-W direction > N-S > Z-direction*

The theoretical calculations are consistent with the results that were computed from the field test data on the evaluation of the frequency response of Little Red Hill to seismic ground motions for the selected earthquake events. Little Red Hill has a fundamental mode of vibration at about 2.5-3 Hz. However, the maximum response of the ridge crest is located at a frequency of about 5 Hz, which represents the second mode of vibration. The theoretical calculations and the field test results exhibit a first maximum for frequencies corresponding to wavelengths comparable to the mountain width and follow observations of previous theoretical and experimental studies (Geli et al., 1988).

We installed a seismic array that covered large parts of the edifice to get information about the spatial response of Little Red Hill to ground motion. The result of the data analysis shows that highest amplifications of ground motions are located at the very top of Little Red Hill (station

rh6) with respect to the base, followed by the stations along the upper ridge crest (station rh3 - rh5). Station rh2, which is located at the declining northern end of the ridge, shows more moderate response to seismic ground motion compared to the response of the higher elevated stations along the ridge crest. The time domain analysis also reveals that the response at station rh1, located at the flank of the edifice, is insignificant compared to the higher amplifications that were observed along the crest. These observations made at Little Red Hill can be explained by a complex interaction of topography and incoming seismic waves. Focusing effects and reinforcement of internally reflected and refracted waves towards the hill top are causing significant amplification at the top of Little Red Hill with respect to the base. The complex response of Little Red Hill to seismic ground motions can also be observed by looking at the amplification pattern computed for station rh4, which is located at the approximate centre of the ridge crest. We observed predominant de-amplification at the middle of the edifice for motions polarized along the main axis of the hill, whereas the other stations along the ridge show amplification relative to the base (Fig. 3.49). Destructive interference of seismic wave dominates at the center of the ridge crest at station rh4 for the N-S component of ground motions while the other stations are experiencing constructive interference.

The direct effect of amplification effects on the stability of rock masses and degradation of rock can be seen in the spatial distribution of seismogenic block fields at Little Red Hill (see site description chapter 3.2, Fig. 3.3). By contrast, the complex reflection and reflection pattern causes only little amplification or de-amplification at the flank of the edifice. The occurrence of seismic block fields correlates with areas of high amplifications of ground motion. Especially at the very top of Little Red Hill (station rh6) the dimensions of dislocated blocks (up to 3 m in diameter) and their extent cannot be explained only by freeze-thaw processes. Topographic amplification of ground motion clearly destabilizes rock masses in these areas.

Although the seismic array at Little Red Hill recorded only weak motion data and a direct impact of strong motion on the response of the edifice could not be experienced, focusing effects and topographic amplification effects will contribute to degradation of the existing bedrock which will lead to a decrease in shear strength and ultimately to possible failure of the rock mass.

4 PHYSICAL LABORATORY MODELING – TOPOGRAPHIC AMPLIFICATION OF SEISMIC WAVES

4.1 INTRODUCTION

During a strong earthquake the potential for a seismically-induced landslide, or in particular large-scale rock slope failure, is mainly determined by the interaction between the incoming seismic waves and local topographic, geologic and geomorphologic conditions.

At a regional scale, seismic waves interfering with given geologic and topographic conditions will determine the stresses developed and produce site-specific ground motions within a mountain edifice.

The position of the mountain with respect to the direction of the incoming seismic wave field, topographic modification of seismic waves and resonance of specific parts of the mountain structure are likely to be important factors for triggering deep-seated failures within the mountain. These failures can lead to catastrophic mountainside collapses with characteristically bowl-shaped source scars (Turnbull & Davies, 2006).

We developed a small-scale 3-D physical laboratory model (~1:1,000) that simulates the response of a homogeneous wedge-shaped mountain, including an underlying part of crustal material, to an incoming seismic wave field.

In contrast to conventional shaking table experiments, the structure being tested is of the same order of dimension as the seismic wavelength, so the travel of the incoming seismic wave through the mountain structure can be investigated. This cannot be represented by conventional shaking table experiments. Available shaking tables also cannot produce vibrations in the required frequency range (up to greater than 150 Hz).

The aim of the physical laboratory modeling is to investigate the effect of topographic amplification of ground motion across a mountain edifice by simulating the situation of the Little Red Hill field experiment in a small-scale laboratory environment. The findings of the physical

laboratory modeling experiments are then compared with results gained from the Little Red Hill field experiment.

To represent realistic conditions at a small-scale, materials of appropriately reduced strength and density, and increased elasticity have to be used to simulate the response of full-scale mountain structures to seismic waves. Dimensional analysis (Appendix B.1) confirms that laboratory models with the required density and elasticity can be accessed. An initial idea of simulating actual seismically induced mountainside collapses at small-scale had to be abandoned because no material could be acquired that would represent rock material with adequate properties (both elasticity and strength).

The decision was made to use material that would represent the elastic properties of rock material (greywacke of the Torlesse Supergroup) in a small-scale laboratory environment. The modeling process was conducted using uniform RTV 585 silicone rubber with high elasticity, representing homogeneous geological conditions at a small-scale (~1:1,000).

This chapter outlines the results from the physical modeling approach to evaluate the role of topographic effects on ground motion and rock slope failure.

A dimensional analysis to establish the scaling laws between the model and the prototype is followed by a description of the main factors contributing to the technical setup and development of the physical model. The evaluation of modeling material, measuring devices, seismic vibration input devices, and the presentation of data acquisition techniques are presented. Edifice response tests are described, evaluating the fundamental mode of vibration of the model edifice in comparison to the Little Red Hill prototype situation. The physical laboratory test data are summarized, further interpretation provided and results are discussed at the end of this chapter.

4.2 DIMENSIONAL ANALYSIS AND THEORY OF SIMILARITY

Modeling of physical phenomena at small scale is based on dimensional analysis and the theory of similarity.

"*A phenomenon that occurs under geometrically similar conditions is said to be similar if the ratio of analogous quantities remains constant at all compatible points*" (Szirtes, 2007).

Dimensional analysis is used to establish the scaling laws between the model and the prototype. Small-scale laboratory models are performed when full-scale tests are either impossible to perform or too expensive. Dimensional modeling is used to experiment on a scaled replica (model) of the physical system that has to be modeled (prototype), and then to project the results obtained from the model to the prototype (Szirtes, 2007). In our case dimensional analysis is applied to establish a theoretical relationship between the parameters used in the laboratory model and the prototype situation. It is also a method for reducing the number and complexity of experimental variables which affect a given phenomenon (White, 1994).

The prototype situation with its specific parameters and properties is in our case represented by the Little Red Hill field experiment (Chapter 3).

The first step in planning an experiment is to decide on governing parameters, or variables, that will have an effect on the phenomenon under investigation.

We specified variables (governing parameters) which affect the phenomenon of earthquake-triggered landslide initiation under small-scale physical laboratory modeling conditions (Fig. 4.1). Pre-event rock fabric controlled instabilities and hydrological aspects have not been incorporated in the physical laboratory modeling. The small-scale laboratory mountain model represents a homogenous bedrock-dominated edifice of symmetric shape.

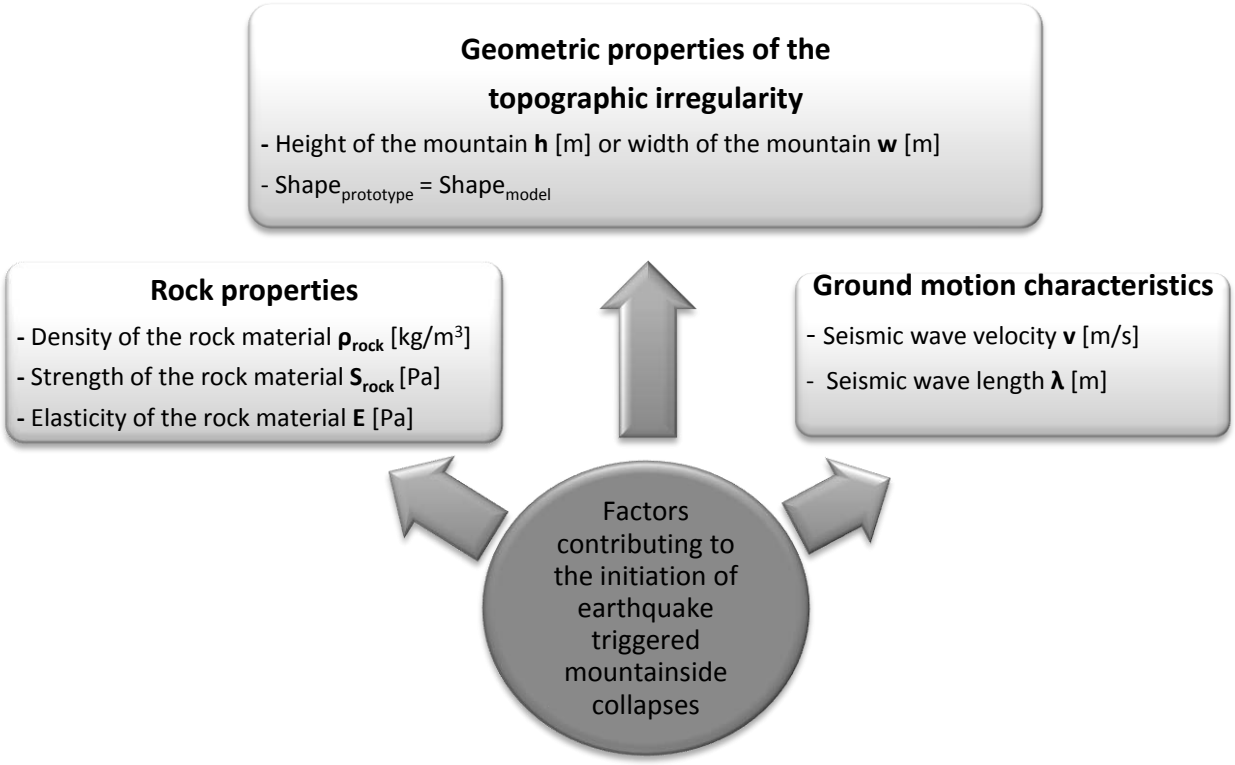

Figure 4.1: Selected variables (governing parameters) affecting the phenomenon of seismically induced mass movements in nature (prototype) and a small-scale physical laboratory experiment environment (model)

Each of the governing parameters with their fundamental units (e.g. m, kg, m/s, etc.) can then be expressed in terms of basic dimensions (Barenblatt, 1987). In our case each of the parameters can be described by using the three basic dimensions M, L, and T (Mass, Length, Time). Dimensional analysis techniques (e.g. Pi-Theorem; Buckingham, 1914) are then applied to establish empirical relationships (formulas) of those governing parameters.

The experiment has to verify the validity of the original assumption and has to show that a condition of similarity exists between the model and the prototype situation (Logan, 1987; Munson et al., 2002; White, 1994). The detailed dimensional analysis for the small-scale physical laboratory modeling of earthquake triggered landslide initiation is set out in appendix B.1.

The following empirical correlations affecting the small-scale laboratory model have been determined using dimensional analysis techniques:

Table 4.1: Empirical correlations affecting the small-scale physical laboratory model. Derived from Dimensional Analysis

I. **Geometry**	$\frac{\lambda}{h}$ or $\frac{h}{\lambda}$ or $\frac{\lambda}{w}$ or $\frac{w}{h}$
II. **Strength**	$\frac{S_r}{\rho_r \; g \; h}$ or $\frac{E}{\rho_r \; g \; h}$ or $\frac{E}{S_r}$
III. **Input**	$\frac{v^2}{gh}$ or $\frac{v^2}{g\lambda}$ $\frac{v^2}{gw}$ (or $\frac{v}{hf}$ where f is the frequency of the seismic wave)

The empirical correlations (Table 4.1) are now used in combination with the prototype properties (Fig. 4.2) to establish scale factors for the governing parameters in the small-scale laboratory environment. The ratios of the empirical correlations have to be kept the same in the prototype and the model situation.

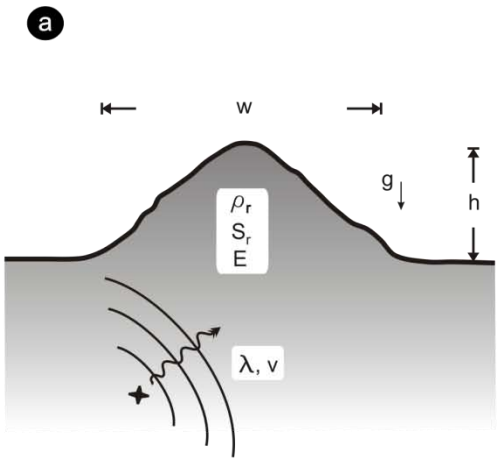

b

Parameter	Value	Unit
Density of rock material ρ_r	2500	[kg/m^3]
Strength of rock material **S_r**	200 x 10^6	[Pa] = [kg/ms^2]
Elasticity of rock material **E**	50 x 10^9	[Pa] = [kg/ms^2]
Height of the mountain **h**	210	[m]
Width of the mountain **w**	500	[m]
Characteristic seismic wave length **λ** (S-wave)	500	[m]
Seismic wave velocity **v** (S-wave)	1200	[m/s]
Gravitational acceleration **g**	9.81	[m/s^2]

Figure 4.2: a) Prototype parameters and b) chosen prototype properties affecting the small-scale physical laboratory modeling of topographic effects on ground motion based on Little Red Hill field experiment data

Scale factors are used to facilitate and enhance the modeling procedure. They always refer to a particular physical variable and represent the quotient of the magnitudes of that variable for the prototype and its model. The capital letter S with the variable as subscript is used as the symbol for the individual scale factors (Szirtes, 2007).

Looking at the geometrical similarity, if the height of the prototype mountain edifice is h_p = 210 m, and the height of the model is h_m = 0.21 m, then the Height Scale Factor $\mathbf{S_h}$ for the mountain edifice is

$$\mathbf{S_h} = \frac{h_{prototype}}{h_{model}} = \frac{h_p}{h_m} = \frac{210\ m}{0.21\ m} = \mathbf{1000}$$

By using the correlations calculated by dimensional analysis, the following scale factors can be derived:

From **I.**:

Modeling at a linear geometric scale of 1000, both the width of the edifice ($\mathbf{S_w = w_p/w_m = 1000}$) and the length of the seismic waves in the model have to be 1/1000 of the prototype situation ($\mathbf{S_\lambda = \lambda_p/\lambda_m = 1000}$).

From **II.**: $S_{S/\rho} = S_g S_h = 1000$

$(S_r)_p = 2.0 \times 10^8$ and $\rho_p = 2.5 \times 10^3$

$\Rightarrow (S_r/\rho)_p = 80000$

$\Rightarrow (S_r/\rho)_m = (S_r/\rho)_p/1000 = 80$

Therefore, if our model material is based on material with a dry density $(\rho_r)_m$ = 1200 kg/m^3, its strength has to be

$\mathbf{(S_r)_m}$ = 1200 x 80 = **96 kPa**

Thus from $(\frac{E}{S_r})_p = \frac{50*10^9}{200*10^6}$ = 250, the elastic modulus of the model material has to be

$\mathbf{E_m}$ = 250 x 96 kPa = **24 MPa**

From **III.**:

The required velocity of seismic waves in the model material is given by

$$S_v = (S_g S_h)^{0.5} \approx 32,$$

$$>> \mathbf{v_m \approx 1/32\ v_p}$$

$$\text{i.e. } \mathbf{\lambda_m = 1/1000\ \lambda_p;}$$

$\Rightarrow S_f = S_v / S_\lambda \approx 1/32$

$\Rightarrow$ the model frequency $\mathbf{f_m \approx 32\ f_p.}$

4.3 TECHNICAL SETUP

The following paragraphs will present the design and development of a small-scale physical laboratory model starting from the initial idea leading towards the final model configuration and its technical setup.

We proposed to develop a seismic wave tank model, in which a bedrock-dominated mountain edifice would be represented by material of appropriately reduced strength and increased elasticity. The mountain topography, placed on a substantial volume of crustal material, would have small-scale seismic wave input from one end so that the waves travel directionally through the topography. The input would have to be similar in 3-D frequency and power spectra to field-scale earthquake spectra, and would have similar time-dependent characteristics.

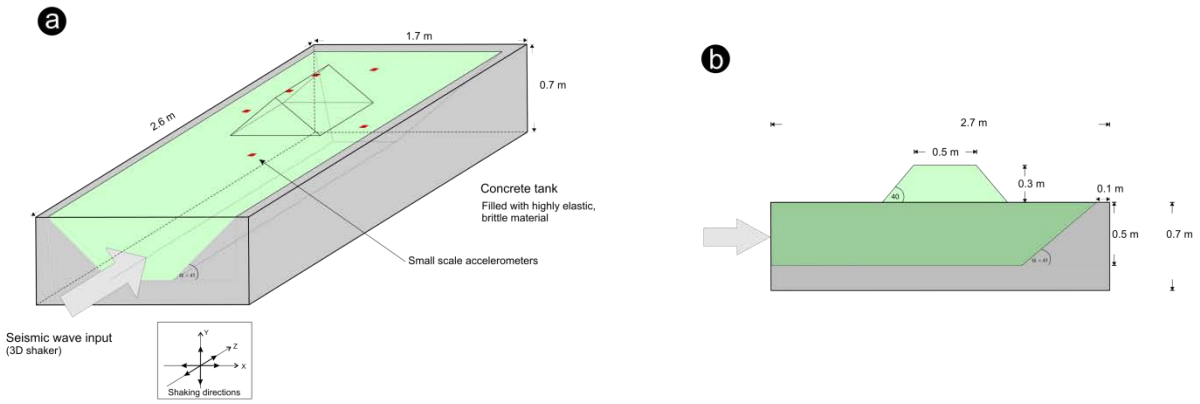

Figure 4.3: Sketch map of the initial idea of a seismic test tank model; a) Oblique front view; b) side view

The initial setup (Fig. 4.3) changed significantly because the amount of material needed for the model would have exceeded the financial limits of the project. A different design based on the material selection process (Chapter 4.3.1) and the availability of seismic wave input devices (Chapter 4.3.3) was developed and used for the final small-scale physical laboratory test of topographic effects on ground motion. The final design idea including main physical parameters and a picture showing the final mountain model are displayed in figure 4.4.

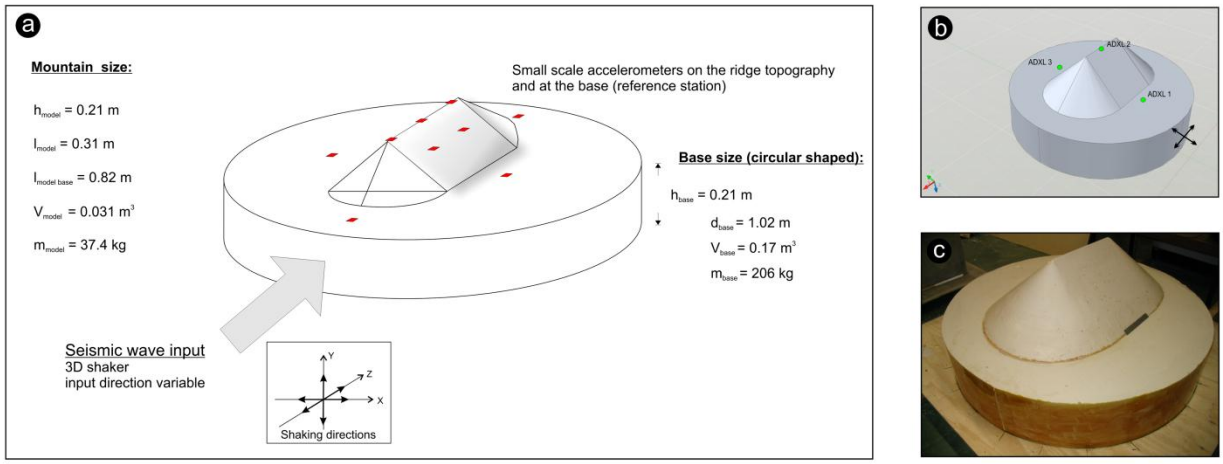

Figure 4.4: Development from a) + b) the advanced physical laboratory model concept, scaling factor 1:1,000 to c) the final design of the small-scale mountain edifice including a base representing crustal material

Further information on curing and constructing techniques of the small-scale physical laboratory model are presented in appendix B.2.

4.3.1 MODELING MATERIAL

The evaluation of material started under the initial background of modeling earthquake triggered mountainside collapses at small-scale in a physical laboratory environment. The theoretical background and appropriately scaled material properties were specified by dimensional analysis. Three main material properties controlled the selection process for possible modeling material; the density ρ, the strength S_r and the Young's Modulus E. After evaluating various possibilities combining these properties with respect to the empirical correlations given by the dimensional analysis (Fig. 4.5), the decision was made to focus only on simulating the elastic behavior of an appropriately down-scaled laboratory model trying to produce amplification and deamplification effects on ground motion across a model mountain edifice. An overview of advantages and limitations of several materials that were considered for the modeling are listed in Table 4.2.

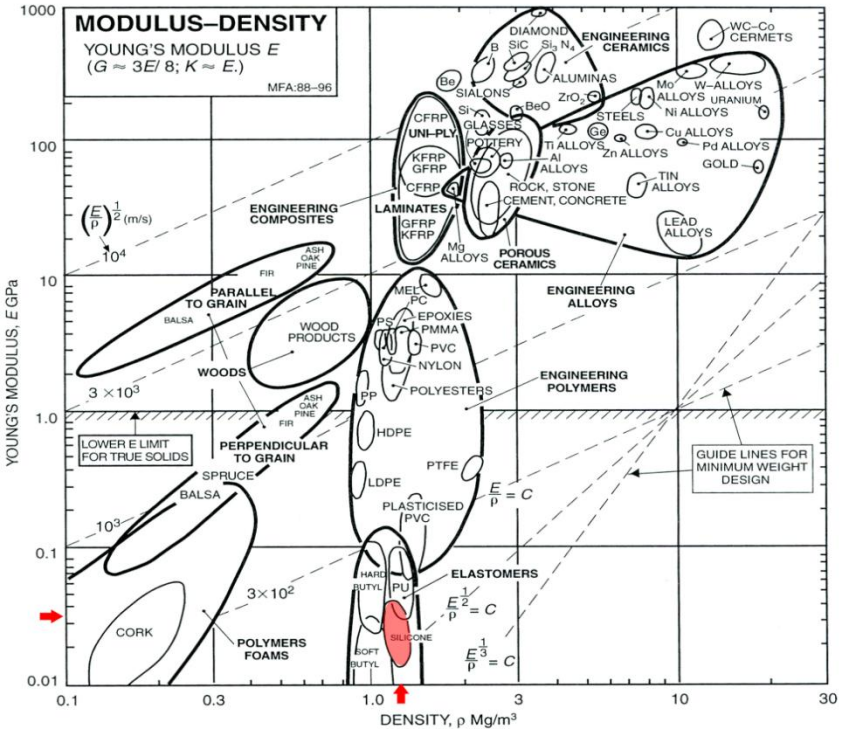

Figure 4.5: Materials selection chart, showing the Young's Modulus, E, plotted against density, ρ for a wide range of engineering materials. The properties that have to be matched by the physical model material are indicated by the red markers. The property range of silicone elastomers is highlighted in red (modified after Waterman & Ashby (1997))

Table 4.2: Material evaluation – Advantages & limitations of various materials which were considered to be used for the small-scale laboratory modeling of topographic effects on ground motions

Material	Advantages	Limitations
Silicone	- suitable range in elasticity - suitable range in density - no special environment needed - stable properties under normal conditions (room temp.) - low shrinkage - wide working temperature range (-60 to +230°C)	- expensive - not a brittle material
Polyurethane	- wide range of elastic properties - cheaper than silicon	- low density - not a brittle material
Foam rubber	- low cost - easy to sculpture - very small Q, prevents boundary reflections	- low density - very small Q, frequencies above 15 Hz attenuate too quickly and signal-to-noise ratio becomes small for any meaningful interpretation of the data (Anooshehpoor, 2005) - not a brittle material
Gelatin	- easy to sculpture	- handling only under climate controlled conditions - material properties are controlled by temperature and humidity - expensive - not a brittle material
Agar Agar	- easy to sculpture - more stable than gelatin	- handling only under climate controlled conditions - material properties are controlled by temperature and humidity - not a brittle material

Rhodorsil® RTV 585 silicone (for technical specifications see Appendix B.5) was chosen to simulate the elastic characteristics of rock material under small-scale physical laboratory conditions. The following tests were conducted to identify exact material properties and to evaluate the overall suitability of the material for the specific physical modeling purpose:

- Voice-coil tests on RTV 585 sample block, to evaluate signal transmission to receiver
- Ultrasonic tests, to evaluate seismic wave velocities and modulus of elasticity
- Uni-axial compression tests on cylindric RTV 585 sample, to evaluate modulus of elasticity
- Tri-axial compression test and shearing test on micro samples using a Dynamic Material Analyser (DMA), to evaluate advanced visco-elastic material properties

Additional descriptions and test results can be found in appendix (B.3).

4.3.2 MEASURING DEVICES

Small accelerometers were selected to measure spatial ground motion variation across the small-scale mountain model. The accelerometers had to fulfill the following technical demands:

1. Adequate sensitivity range
2. Minimum size to a) minimize side effects and to
   b) provide maximum coupling without affecting the model

The accelerometers used for the laboratory experiment are ANALOG DEVICES ADXL320 dual-axis accelerometers with a size of 4 mm x 4 mm x 1.45 mm (AnalogDevices, 2004). The ADXL320 has a measurement range of +/- 5g. The output signals are analog voltages that are proportional to acceleration. Detailed technical specifications can be found in appendix B.5. The accelerometers are mounted on square micro boards (17 x 17 mm) and were either glued with silicone to the surface of the model or stuck into a vertical cut in the material (Fig. 4.6). The accelerometers were horizontally leveled to achieve comparability of the output signal for each individual instrument and data set. The channels were connected to the hardware board by cable connection.

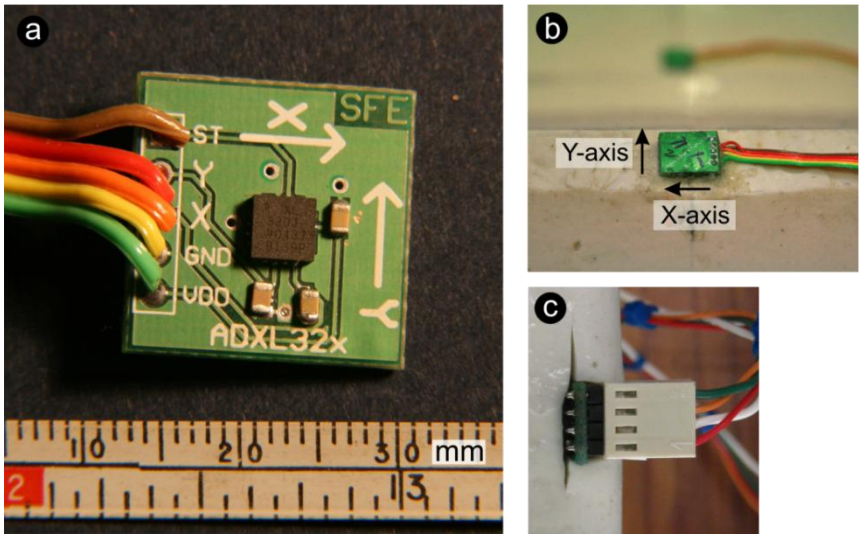

Figure 4.6: Analog Devices ADXL 320 dual-axis accelerometer a) setup including small-scale board; Setup possibilities, showing the accelerometer b) horizontally mounted onto the ridge of the silicone mountain edifice, and c) positioned in a vertical cut in the silicone material

4.3.3 INPUT DEVICES

The input device for the small-scale physical laboratory model had to generate seismic waves (shear and compressional waves) with appropriately reduced wave lengths for the laboratory model scale of 1:1,000. It also had to supply enough energy to produce waves capable of propagating through the model producing accelerations in the measurement range of the accelerometers.

The Little Red Hill experiment revealed that the mountain edifice has a fundamental mode of vibration at about 2.5-3 Hz. However, the maximum response of the ridge crest is located at a frequency of about 5 Hz, which represents the second mode of vibration. The theoretical calculations and the field test results exhibit maxima for frequencies corresponding to wavelengths comparable to the mountain width (400 - 480 m) and about the half-width of the edifice respectively (240 m).

Using this information on governing seismic wave properties gained from the Little Red Hill field experiment and applying dimensional analysis leads to following input characteristics:

- The response maxima at Little Red Hill are located at a frequency band

  f_{p1}= 2.5 – 3 Hz , and

  f_{p2} = 5 Hz.

- Referring to the results of the dimensional analysis the model frequency f_m is given by:

  $$\mathbf{f_m \approx 32\ f_p}$$

- Therefore response maxima should be located at model frequencies of:

  $\mathbf{f_{m1}}$= 32 x f_{p1} = 32 x 2.5 – 3 Hz = **80 – 96 Hz** , and

  $\mathbf{f_{m2}}$ = 32 x f_{p2} = 32 x 5 Hz = **160 Hz**.

The idea of designing and manufacturing a dynamic 3-D seismic shaking input device which would be able to simulate realistic three-dimensional wave input at small-scale had to be abandoned due to the lack of technical resources and financial limitations.

Alternatively, various low-budget input devices and techniques to produce seismic wave input were tested and results evaluated during the process of establishing the physical laboratory model. The following input devices were tested for the suitability of simulating a seismic wave source under small-scale laboratory conditions:

- Electromagnetic actuator (compressional wave input)
- Hammer (shear wave input)
- Sledgehammer (shear wave, compressional wave input)

Detailed test descriptions and test results that were gained during these tests are presented in appendix B.3.

During a technical meeting, Dr Elijah Van Houten (Department of Mechanical Engineering) suggested to find a way to generate steady-state actuation at a fixed frequency. The fact of trying to produce shear wave input at the RTV 585 silicone model turns out to be very complicated

because of the internal structure of the silicone rubber itself. The cross-linked molecules of the silicone rubber structure with its different compounds tend to dissipate a high amount of energy due to molecule interaction. The result is significant attenuation of the signal. Actuation in form of P-waves will reduce this effect due to small incompressibility. Therefore the decision was made to produce a steady-state actuation at fixed frequencies with the available voice coil actuator. The powerful voice coil actuator ("Big Mama") that was used for an initial signal test on a RTV 585 sample block at the mechanical engineering laboratory (Appendix B.3) could unfortunately not be used for our laboratory model due to technical limitations. By using the voice coil device, the actuation with P-waves also result in producing shear waves within the model. P-waves hitting a boundary produce reflected P-waves and also shear waves, due a mode conversion process. Therefore, operating the seismic actuator in steady-state, most of the response of the model edifice itself will be caused by shear waves (Van Houten, 2007). The steady-state mode will also allow an input of a higher amount of energy into the system and will accentuate the wavelength that controls the main response of the edifice.

The boundary effects will influence the amplitude of the received signals but

a) boundary effects for example wave reflections, mode conversion etc also affect the signal being received in a real seismological experiment (prototype situation), and
b) the overall governing wavelength will be constant for a certain frequency using a steady-state actuation.

After discussing the results of the input device tests and narrowing down financial and technical possibilities, an electromagnetic actuator (Aura Instruments Incorporated) was chosen as the input device for the evaluation of topographic effects on ground motions under small-scale physical laboratory conditions (Fig. 4.7). The electromagnetic actuator was the only device that allowed us to have controlled frequency input for frequencies of up to more than 200 Hz.

Figure 4.7: Aura Instruments Interceptor ™ electromagnetic actuator for controlled compressional wave input

4.3.4 DATA ACQUISITION

To generate and measure physical signals, the LabVIEW™ data acquisition system (NI-DAQ™) was applied to the physical laboratory model (Bishop, 2004). LabVIEW™ 7.1 Professional Edition, a graphical programming software for measurement and instrumentation, was used to program a user interface to manage the model data output and input. Combined with the LabVIEW™ software package, NATIONAL INSTRUMENTS hardware devices controlled the electronic devices. The input and output was controlled by two internal computer boards, a NI PCI-6711 12-bit high-speed analog output board, a NI PCI-6220 data acquisition device, and two external NI SCB-68 connector blocks (Fig. 4.8, Fig. 4.9).

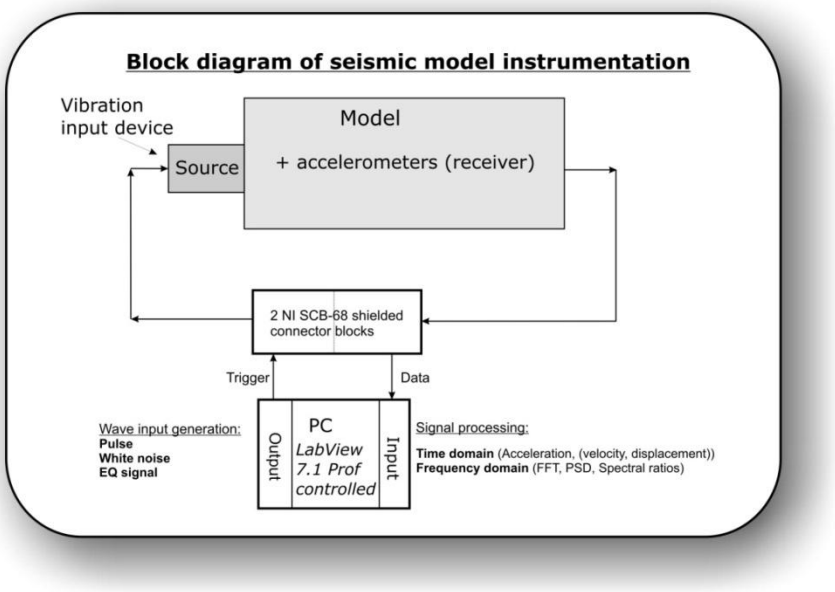

Figure 4.8: Block diagram showing the schematic technical setup of the physical modeling of topographic effects on seismic ground motions

The voice coil actuator and the accelerometers were connected to the two external NI SCB-68 connector blocks by cable connection. Additional details on the software setup and advanced NI-DAQ^{TM} hardware configuration are presented in appendix B.4.

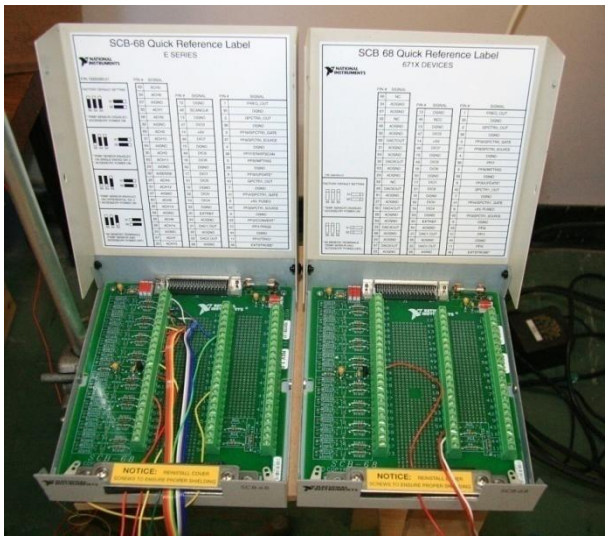

Figure 4.9: Two external National Instruments NI SCB-68 connector blocks establishing an interface between the actuator input device (right block) / the accelerometers (left block) and the computer controlled user interface

4.4 EDIFICE RESPONSE TESTS

A test was conducted to evaluate the response of the silicone mountain model and compare the maxima measured at the ridge crest with expected values that were calculated from the Little Red Hill experiment using dimensional analysis (Chapter 4.3.3). This was done to answer the following question:

- Is the frequency response of Little Red Hill similar to the response of the small-scale physical laboratory situation?

This evaluation will give us an answer to the applicability of dimensional analysis techniques for conducting small-scale physical laboratory tests to simulate the prototype situation and will provide us with information about major factors contributing to topographic effects on ground motions.

4.4.1 MODEL SETUP

The edifice response test followed a similar setup that was used during the Little Red Hill field experiment (Chapter 3).

The model mountain was equipped with an ADXL 320 accelerometer which was positioned at the centre of the ridge crest. A base station was mounted symmetrically onto the surface at the flat side of the mountain, forming a straight line with the instrument on the ridge and the electromagnetic actuator for the initial test. The actuator was positioned at the outside of the base laboratory mountain model (Fig. 4.10).

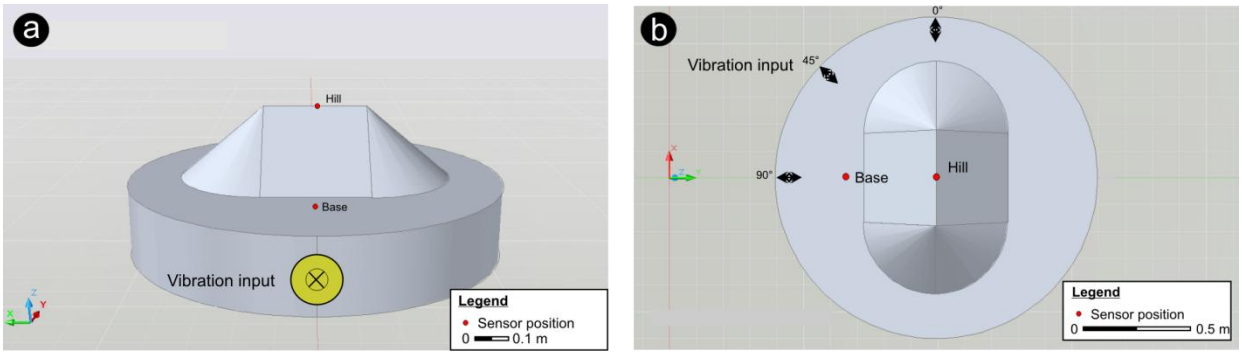

Figure 4.10: Seismic response tests – a) side view and b) top view of the instrument setup showing the locations of the two accelerometers (Base, Hill), the position of the electromagnetic actuator and the direction of the vibration input

The seismic wave input comprised a compressional sinusoidal wave input which was inducted at steady-state mode starting at a frequency of 0 Hz to evaluate the initial noise level. The input frequency was gradually increased in 10 Hz as well as 5 Hz increments up to a frequency of 150 Hz. The chosen frequency band is based on results gained from the Little Red Hill field experiment and dimensional analysis and represents the frequency band where fundamental response of the edifice is expected in the model situation. The electromagnetic actuator was installed at the side of the circular base facing the flank of the edifice to allow maximum excitation and response for the direction perpendicular to the main axis of the edifice. Two additional tests were conducted generating compressional wave input at an angle of incidence of 45 degrees towards the main axis and at zero degrees (parallel to the main mountain axis) to evaluate a possible variance in response depending on the direction of the incoming wave field.

A LabVIEW^{TM} data acquisition environment was designed, consisting of a user interface and a virtual instrument environment, to process the received data from the accelerometers (Appendix B.4).

4.4.2 DATA ANALYSIS AND RESULTS

Due to technical limitations caused by complex visco-elastic behavior of the silicone material and therefore unpredictable damping effects at different frequencies and distances from the source input device, the edifice response test was conducted interpreting only the response of the station at the center of the ridge crest of the silicone mountain edifice. A meaningful comparison between the signals measured at the base station and the station at the ridge could not be

accomplished. The extensive attenuation effect of high frequency components resulted in high amplitude losses for the more distant instrument at the ridge. Therefore the expected amplification effect at the ridge top was at no stage observed. A distinct decreasing difference of the signal amplitude at the top compared to the base was visually observed for different input frequency bands following the real-time virtual instrument user interface (Fig. 4.11).

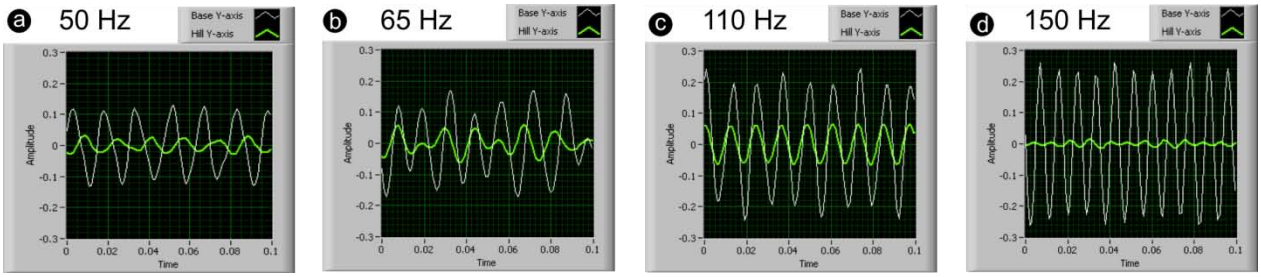

Figure 4.11: Signal amplitude at the base and the top of the hill for the motion perpendicular to the model mountain axis for a set of input frequencies; a) 50 Hz, b) 65 Hz, c) 110 Hz, d) 150Hz. A distinct decreasing difference in signal amplitude between the base and the top of the hill is noticeable at 65 Hz and 110 Hz compared to other input frequencies

To evaluate the response of the ridge top to various input frequencies, the waveform data was analyzed using two different approaches:

- Calculation and comparison of peak ground motion amplitudes at the ridge top for different actuator input frequencies
- Power spectral density (PSD) analysis

The results of the signal response at the ridge of the small-scale mountain model for input frequencies between 0 and 150 Hz and a vibration input perpendicular to the main axis of the edifice can be seen in figure 4.12. The amplitudes were computed analyzing a three second time window for each frequency increment.

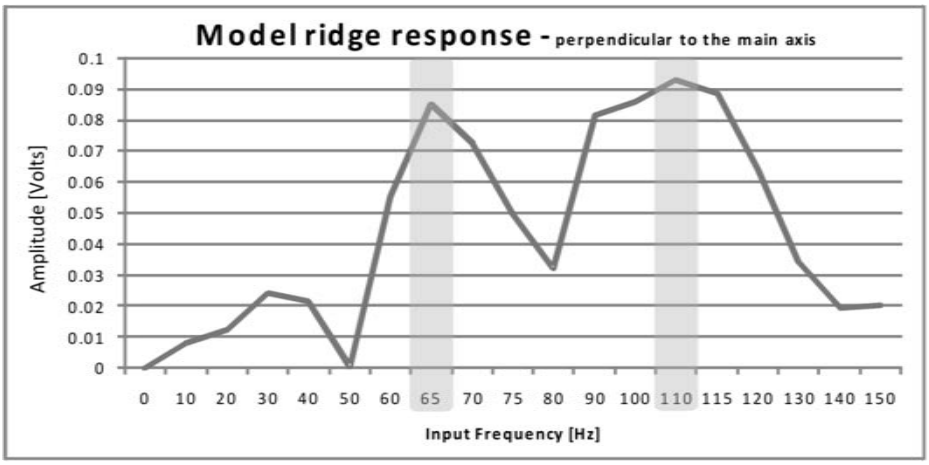

Figure 4.12: Signal response at the ridge of the silicone mountain edifice for various actuator input frequencies (frequency band between 0 Hz and 150 Hz). Compressional sinusoid wave input acting perpendicular to the main model mountain axis

The response for the motion perpendicular to the main mountain axis at the station at the centre of the ridge crest shows two distinct maxima. The first peak is located at about 65 Hz, the second at approximately 110 Hz. The signal amplitude decreases rapidly for both lower and higher frequencies.

An evaluation of the response of the station at the ridge crest for motions parallel to the main mountain model axis revealed insignificant signal amplitudes in that direction (Fig. 4.13).

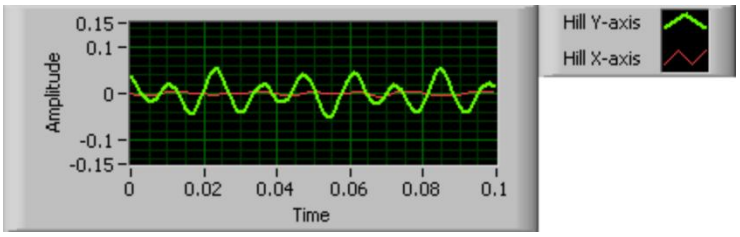

Figure 4.13: Signal response at the ridge, showing both motion components parallel (X-axis) and perpendicular (Y-Axis) to the mountain axis for steady-state wave input at 65 Hz perpendicular to the main axis of the edifice

In order to investigate the distribution (over frequency) of the power contained in the recorded signal at the ridge crest of the silicone model, the power spectral densities (PSD) were analyzed using the real-time virtual instrument environment.

A distinct maximum was observed at the ridge at a frequency of 70 Hz (Fig. 4.14) for an actuator input frequency of 95 Hz.

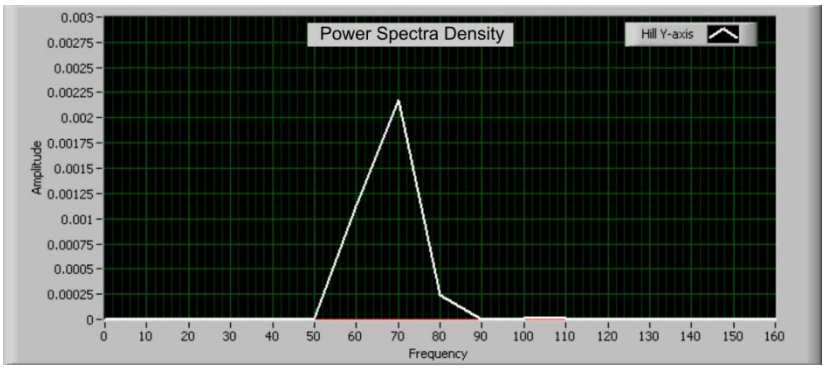

Figure 4.14: Ridge crest station – Power spectral density for the component perpendicular to the main mountain model axis

To evaluate the influence of the direction of the incoming wave field on the response of the edifice at the ridge crest two tests were conducted producing a compressional wave input at 45 and zero degrees towards the main axis of the silicone mountain model (Fig. 4.10)

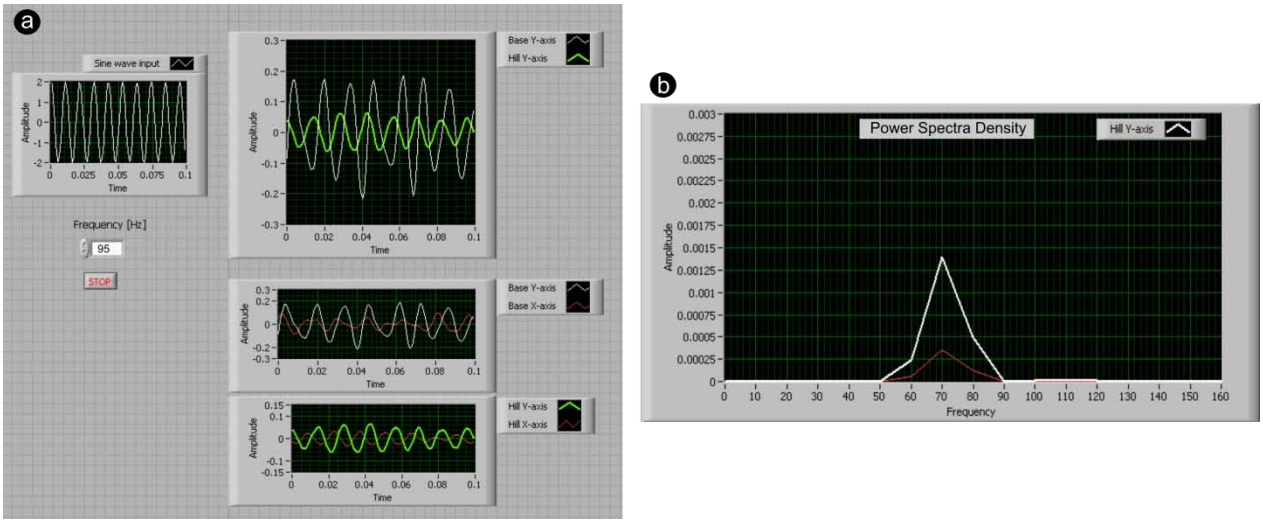

Figure 4.15: Virtual instrument interface showing a) the output of the response test with a sinusoidal wave input at 95 Hz at 45 degrees for the x and y-axis of the base station as well as the hill station at the center of the ridge, and b) the PSD plot for the station at the ridge

In the case of an angle of incidence of 45 degrees towards the long axis of the mountain, maximum response was observed for an input frequency of 95 Hz. The signal response showed signal amplitudes are dominant for motions perpendicular to the mountain axis (Fig. 4.15). The analysis of the power spectral density revealed a maximum response at a frequency of 70 Hz at the ridge crest.

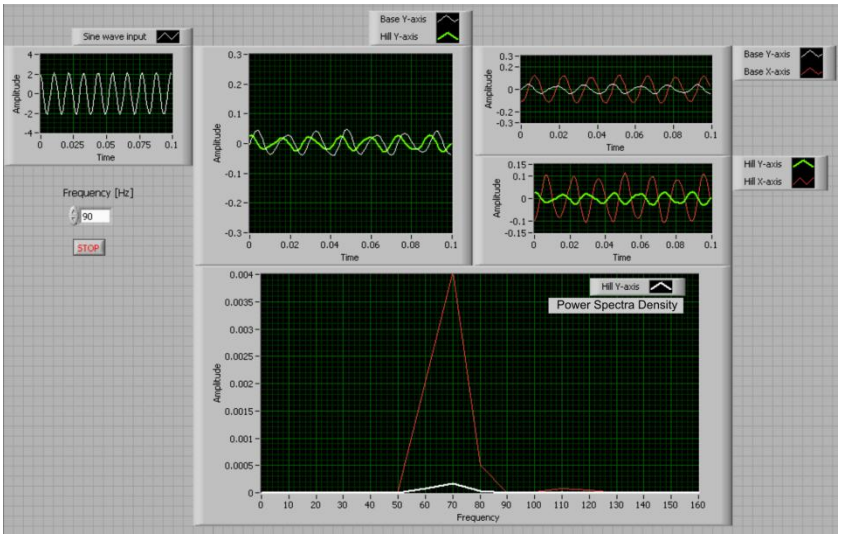

Figure 4.16: Virtual instrument interface showing the output of the response test with a sinusoidal wave input at 90 Hz along the main axis for the x and y-axis of the base station as well as the hill station at the center of the ridge, and the PSD plot for the station at the ridge

The actuation with compressional wave input along the direction of the main axis of the edifice showed that the main response at the ridge crest occurred for motions along the main axis of the mountain at an input frequency of 90 Hz. The power spectral density analysis indicated maximum response was observed for motion frequencies at approximately 70 Hz (Fig. 4.16).

4.5 DISCUSSION

The physical laboratory-scale (1:1,000) model was conducted to provide information on topographic modification of ground motion and to evaluate the kinematic response of mountain edifices to realistically-complex incident seismic waves.

Dimensional analysis techniques were used to ensure that the factors and their empirical correlations which are contributing to the prototype situation and the down-scaled physical laboratory model are identical and geometrical similarity is guaranteed. The empirical correlations were then used to establish scaling factors for the governing parameters at laboratory scale.

The initially proposed idea of simulating seismically triggered mountainside collapses (rock avalanches) under small-scale physical laboratory conditions using material that combines properties of adequately reduced strength and increased elasticity had to be abandoned due to the

unavailability of material with the required property composition. The construction of an input device that would simulate realistic three dimensional seismic wave input failed due to technical and financial limitations.

Material of appropriately increased elasticity was acquired (Rhodorsil® RTV 585 silicone rubber) for physical laboratory modeling to simulate the response of a mountain edifice to seismic wave input and to evaluate topographic amplification effects on ground motion. The physical laboratory setup was used to reproduce topographic effects of ground motion at small-scale and to compare the response of the silicone mountain edifice with results gained from the Little Red Hill field experiment.

Input device tests and advanced material tests on the Rhodorsil RTV 585 silicone rubber revealed a highly complex visco-elastic behavior of the silicone elastomer. Complex damping and attenuation effects of the silicone rubber material prevent amplification of the signal to occur in the physical laboratory model. A meaningful interpretation by comparing the response at the base station with the station at the ridge crest was impossible. Therefore, response tests were conducted focusing on the evaluation of the response of the model mountain ridge to seismic wave input of frequencies between 0 and 150 Hz. An electromagnetic actuator was utilized to produce a controlled compressional sinusoidal seismic wave input.

The test results show the response of the mountain edifice for ground motions perpendicular to the main axis of the edifice follows the same trend as seen in the Little Red Hill field experiment. The fundamental response frequency for the silicone mountain edifice was observed at 70 Hz in the physical laboratory model. Another mode of vibration at higher frequencies was not observed due to a drastic decrease of the signal amplitude above 150 Hz. Applying the scaling factors which we established using dimensional analysis allows us to compare the results of the laboratory modeling experiment with the prototype situation. The scale factor for the frequency is given by:

$$\mathbf{f_m \approx 32\, f_p}$$

Therefore, a frequency in the model situation of f_m = 70 Hz corresponds approximately to a prototype frequency f_p of 2.2 Hz.

Referring to theoretical evaluations of the fundamental modes of vibration for Little Red Hill and results gained from the field experiment (Chapter 3.5.9.2 and Chapter 3.6.2), the fundamental mode of vibration observed at the small-scale laboratory mountain edifice shows good comparison to the prototype situation. The maximum response of the laboratory mountain edifice corresponds to the fundamental mode of vibration at Little Red Hill. This shows that by responding to the fundamental mode of vibration of LRH, the resonance is related to the bedrock edifice and its geometry. This also shows that the existence of low-velocity surface layers (highly-weathered surface bedrock) is not the fundamental cause for high amplification effects because these were not present in the laboratory model.

The comparable results therefore support the applicability of dimensional analysis to establish scaling laws between the model and the prototype.

Additional tests utilizing different angles of incidence for the seismic wave input show that the fundamental mode of response of the model mountain edifice is located at 70 Hz, independent of the angle of incidence. The fundamental response frequency of the hill at 70 Hz (displayed in the PSD plots) was observed using a steady-state vibration input at a frequency of approximately 90-100 Hz. This reflects the complex visco-elastic properties of the silicone rubber. A large amount of the high frequency components of the input signal disappear and only lower frequencies are detected by the receiver.

The results of this small-scale physical laboratory model test on topographic effects on ground motion show that despite critical material property issues and simplified seismic vibration input, that dimensional analysis is a successful technique to simulate prototype phenomena in small-scale laboratory environment.

5 CONCLUSIONS & RECOMMENDATIONS

5.1 CONCLUSIONS

A seismic field experiment and a laboratory-scale physical model were used to study topographic effects of bedrock-dominated mountain edifices on seismic ground motion. The field study at Little Red Hill provided a data set which was used to evaluate the response of the edifice to dynamic seismic wave input and to determine areas of the mountain edifice that are prone to rock mass degradation. The physical laboratory model investigated topographic effects on seismic ground motion in a small-scale environment, designed to be geometrically similar to the Little Red Hill field experiment. The results of these two individual approaches are discussed in Chapter 3.7 and Chapter 4.5., respectively.

The findings of this research can be summarized as follows:

- A geological and geotechnical investigation of Little Red Hill revealed areas of pronounced rock mass degradation on convex formed areas along the ridge crest.

- The response of Little Red Hill to seismic wave input shows ground motions are highest for seismic waves polarized along the short axis of the edifice. No strong topographic effect was observed for the vertical component of ground motion.

- Amplifications of ground motions occur along the ridge of the edifice, with the largest amplifications occurring at the very top of the edifice (up to +1100 %). The flank shows minor amplification as well as deamplification (-39 % to +45%).

- The effect of topographic amplification will make the occurrence of rock mass failures more likely in a given seismic event. Building sites might experience high ground motions on top of elevated ridges due to amplification effects.

- The maximum response of Little Red Hill occurs for incoming seismic waves with wavelengths similar to the half-width (250 m) or height (210 m) of the edifice. This correlates to the second mode of vibration (approx. 5 Hz), based on theoretical analysis techniques.

- It was found that the bandwidth of the frequency response of LRH is related to the epicentral distance. No correlation was found to other earthquake source parameters e.g. magnitude or azimuth.

- Results of the response analysis of Little Red Hill and geological and geotechnical investigations show a distinct correlation exists between areas of high amplification of seismic ground motion and increased rock mass degradation (represented by seismogenic block fields) in these areas.

- A small-scale physical laboratory model was constructed. The triangular wedge-like geometry of the edifice creates a confined zone where the incoming waves are trapped. The results from this model shows that both the model edifice and LRH responded to seismic wave input at the fundamental mode of vibration (70 Hz and 2.2 Hz respectively). This correlates to seismic wavelengths similar to the width at the base of the edifice (0.5 m and 500 m respectively).

- The excellent correspondence between the LRH data and the physical model data show that both edifices respond similarly to seismic excitation. Since the physical model comprised unfractured material, this shows in turn that the bedrock of LRH dominated its response. The effects of any weathered surface layer on edifice response were minor.

5.2 RECOMMENDATIONS FOR FUTURE WORK

By looking at the findings from this study, the following fundamental recommendations are made for the further research:

- Detailed geotechnical field investigations at sites of known seismically-induced rock avalanches in an attempt to evaluate the role of pre-existing bedding and fracture sets will help to increase the understanding of failure mechanisms of rock slopes during strong seismic motion input.
- The results obtained from the field experiment could be made more robust by increasing the time of the seismic data collection. This would increase the chance to collect strong motion data, and provide a larger data set to work with.

- Further field tests would increase the understanding of the response of bedrock-dominated mountain edifices to seismic wave input. Field test sites should be varied to investigate different geometric and geologic conditions.
- Conducting the field test with a denser seismic array would add information to the existing dataset and therefore contribute to a better understanding of the spatial response of the edifice.
- In order to validate and advance the physical laboratory model results, data could be gained by conducting tests with a high-tech input device that generates a three-dimensional wave input of adequate dimensions.
- The findings of this research can be used to test, refine and calibrate numerical computer models that simulate the same process with various edifice geometries and different geological setups. The numerical modeling can then be used to provide information on the dynamic internal stress fields and therefore further increase the understanding of the initiation of seismically-triggered, deep-seated rock slope failures.
- Progress in computer technology and advanced capabilities of numerical software, e.g. Itascas' UDEC^{TM} or PFC 3D^{TM}, represents an advanced tool to study edifice response while avoiding physical laboratory problems of simulating natural properties.

6 BIBLIOGRAPHY

Aki, K., 1993. Local site effects on weak and strong ground motion. Tectonophysics, 218: 93-111.

Aki, K. and Richards, P.G., 2002. Quantitative Seismology. University Science Books, Sausalito, CA, 700 pp.

Al-Homoud, A.S. and Tahtamoni, W.W., 2000. Reliability analysis of three-dimensional dynamic slope stability and earthquake-induced permanent displacement. Soil Dynamics and Earthquake Engineering, 19: 91-114.

Alves, S.W., 2005. nonlinear analysis of Pacoima dam with spatially nonuniform ground motions, Pasadena, California, 252 pp.

Ambraseys, N.N., 1960. On the shear response of a two-dimensional truncated wedge subjected to an arbitrary disturbance. Bulletin of the Seismological Society of America, 50(1): 45-56.

AnalogDevices, 2004. ADXL 320 Accelerometer - Data sheet, pp. 16.

Anderson, J.G., 1984. The 4 September 1981 Santa Barbara Island, California, earthquake: Interpretation of strong motion data. Bulletin of the Seismological Society of America, 74(3): 995-1010.

Anooshehpoor, R., 2005. Personal communication: email contact - Technical advice on small-scale physical modeling.

Anooshehpoor, R. and Brune, J.N., 1989. Foam rubber modeling of topographic and dam interaction effects at Pacoima dam. Bulletin of the Seismological Society of America, 79(5): 1347-1360.

Ashford, S.A., Sitar, N., Lysmer, J. and Deng, N., 1997. Topographic effects on the seismic response of steep slopes. Bulletin of the Seismological Society of America, 87(3): 701-709.

Assimaki, D. and Gazetas, G., 2004. Soil and topographic amplification on canyon banks and the 1999 Athens earthquake. Journal of Earthquake Engineering, 8(1): 1-43.

Assimaki, D., Kausel, E. and Gazetas, G., 2005. Wave propagation and soil-structure interaction on a cliff crest during the 1999 Athens earthquake. Soil Dynamics and Earthquake Engineering, 25: 513-527.

Bachmann, D., Bouisson, S., Chemenda, A., 2004. Influence of weathering and pre-existing large scale fractures on gravitational slope failure: insights from 3-D physical modelling. Natural Hazards and Earth System Sciences, 4: 711-717.

Badger, T.C. and Watters, R.W., 2004. Gigantic seismogenic landslides of Summer Lake basin, south-central Oregon. Geological Society of America Bulletin, 116(5/6): 687-697.

Bard, P.-Y. and Tucker, B.E., 1985. Underground and ridge site effects: A comparison of observation and theory. Bulletin of the Seismological Society of America, 75(4): 905-922.

Barenblatt, G.I., 1987. Dimensional Analysis. Gordon and Breach Science Publishers, 135 pp.

Benites, R. and Olsen, K.B., 2005. Modeling Strong Ground Motion in the Wellington Metropolitan Area, New Zealand. Bulletin of the Seismological Society of America, 95(6): 2180-2196.

Berrill, J., 2007. On the seismic response of Little Red Hill - personal meeting & discussion, University of Canterbury, Christchurch, john.berrill@canterbury.ac.nz.

Berrill, J., 2008. Non-linear behavior of soils - personal meeting & discussion

University of Canterbury, Christchurch, john.berrill@canterbury.ac.nz.
Bishop, R.H., 2004. Learning with LabVIEW 7 Express. Pearson Prentice Hall, 571 pp.
Bommer, J. and Rodriguez, C.E., 2002. Earthquake-induced landslides in Central America. Engineering Geology, 63: 189-220.
Boore, D.M., 1972. A note on the effect of simple topography on seismic SH waves. Bulletin of the Seismological Society of America, 62: 275-284.
Borcherdt, R.D., 1970. Effects of local geology on ground motion near San Francisco Bay. Bulletin of the Seismological Society of America, 60: 29-61.
Borcherdt, R.D. and Eeri, M., 1994. Estimates of Site-Dependend Response Spectra for Design (Methology and Justification). Earthquake Spectra, 10(4): 617-653.
Bouchon, M., 1973. Effect of topography on surface motion. Bulletin of the Seismological Society of America, 63(3): 615-632.
Bouchon, M., Barker, J.S., 1996. Seismic response of a hill: The example of Tarzana, California. Bulletin of the Seismological Society of America, 86(1A): 66-72.
Bouchon, M., Schultz, C.A. and Toksöz, M.N., 1996. Effect of three-dimensional topography on seismic motion. Journal of Geophysical Research, 101(B3): 5835-5846.
Bouckovalas, G.D. and Kouretzis, G., 2001. Review of Soil and Topography Effects in the September 7, 1999 Athens (Greece) Earthquake, Proceedings: Fourth International Conference on Recent Advances in Geotechnical Earthquake Engineering and Soil Dynamics and Symposium in Honor of Professor W.D. Liam Finn, San Diego, California.
Bouckovalas, G.D., Papadimitriou, A.G., 2005. Numerical evaluation of slope topography effects on seismic ground motion. Soil Dynamics and Earthquake Engineering, 25: 547-558.
Bradshaw, J.D., 1971. Stratigraphy and structure of the Torlesse Supergroup (Triassic-Jurassic) in the foot-hills of the Southern Alps near Hawarden, Canterbury: New Zealand. Journal of Geology and Geophysics, 15: 71-87.
Buckingham, E., 1914. On physical similar systems. Physical Reviews, 4(4): 345.
Campbell, D.J., Cheney, J.A. and Kutter, B.L., 1991. Boundary effects in dynamic centrifuge model tests. Centrifuge, 91: 441-448.
Carro, M., De Amicis, M., Luzi, L. and Marzorati, S., 2003. The application of predictive modeling techniques to landslides induced by earthquakes: the case study of the 26 September 1997 Umbria–Marche earthquake (Italy). Engineering Geology, 69: 139-159.
Carver, D. and Hartzell, S.H., 1996. Earthquake site response in Santa Cruz, California. Bulletin of the Seismological Society of America, 86(1A): 55-65.
Chamberlain, C.G., 1996. Seismic harzard from cross-faulting in North Canterbury: Broader implications from the Arthurs' Pass earthquake sequence of 18 June 1994, University of Canterbury, Christchurch, 230 pp.
Chang, K.-J., Taboada, A., Lin, M.-L. and Chen, R.-F., 2005a. Analysis of landsliding by earthquake shaking using a block-on-slope thermo-mechanical model: Example of Jiufengershan landslide, central Taiwan. Engineering Geology.
Chang, K.-J., Taboada, A. and Y-C., C., 2005b. Geological and morphological study of the Jiufengershan landslide triggered by the Chi-Chi Taiwan earthquake. Geomorphology, 71: 293-309.
Chávez-García, F.J., Castillo, J. and Stephenson, W.R., 2002. 3D site effects: A thorough analysis of a high-quality dataset. Bulletin of the Seismological Society of America, 92(5): 1941-1951.

Chávez-García, F.J., Pedotti, G., Hatzfeld, D. and Bard, P.Y., 1990. An experimental study of site effects near Thessaloniki (Northern Greece). Bulletin of the Seismological Society of America, 80(4): 784-806.

Chavez-Garcia, F.J., Rodriguez, M., Field, E.H. and Hatzfeld, D., 1997. Topographic site effects. A comparison of two nonreference methods. Bulletin of the Seismological Society of America, 87(6): 1667-1673.

Chávez-García, F.J., Sánchez, L.R. and Hatzfeld, D., 1996. Topographic site effects and HVSR. A comparion between observations and theory. Bulletin of the Seismological Society of America, 86(5): 1559-1573.

Chemenda, A., Bouissou, S. and Bachmann, D., 2005. Three-dimensional physical modeling of deep-seated landslides: New technique and first results. Journal of Geophysical Research, 10: 8.

Chigira, M., Wang, W.-N., Furuya, T. and Kamai, T., 2003. Geological causes and geomorphological precursors of the Tsaoling landslide triggered by the 1999 Chi-Chi earthquake, Taiwan. Engineering Geology, 68: 259-273.

Cluff, L.S., 1971. Peru earthquake of May 31, 1970; Engineering geology observations. Bulletin of the Seismological Society of America, 61(3): 511-533.

Cook, K.C., 2001. Rock mass structure and intact rock strength of New Zealand greywackes, Canterbury University, Christchurch, 471 pp.

Cubrinowski, M., 2008. Non-linear behavior of soils, University of Canterbury, Christchurch, misko.cubrinovski@canterbury.ac.nz.

Dai, F.C., Lee, C.F., Deng, J.H. and Tham, L.G., 2005. The 1786 earthquake-triggered landslide dam and subsequent dam-break flood on the Dadu River, southwestern China. Geomorphology, 65: 205-221.

Dakoulas, P. and Gazetas, G., 1985. A class of inhomogeneous shear models for seismic response of dams and embankments. Soil Dynamics and Earthquake Engineering, 4(4): 166-182.

Darbre, G.R., 2000. State of practice in earthquake analysis of dams, Nachdiplomskurs in angewandten Erdwissenschaften: Naturgefahren-Erdbebenrisiko, ETH Zuerich und Volkshochschule im Schwarzwald, 15.-19.Mai 2000, Zuerich, pp. 23.

Davis, L.L. and West, L.R., 1973. Observed effects of topography on ground motion. Bulletin of the Seismological Society of America, 63: 283-298.

Del Gaudio, V. and Wasowski, J., 2007. Directivity of slope dynamic resonse to seismic shaking. Geophysical Research Letters, 34(L12301): 1-8.

Deng, N., 1991. Two-dimensional site response analyses, University of California at Berkeley, Berkeley, California.

Dewoolkar, M.M., Ko, H.-Y. and Pak, R.Y.S., 2000. Experimental developments for studying static seismic behavior of retaining walls with liquefiable backfills. Soil Dynamics and Earthquake Engineering, 19: 583-593.

Dhakal, S., 2004. Empirical relations for earthquake response of slopes, Enschede, 122 pp.

Dobry, R., Oweis, I. and Urzua, A., 1976. Simplified procedures for estimating the fundamental period of a soil profile. Bulletin of the Seismological Society of America, 66(4): 1293-1321.

Dowrick, D.J., 1985. Preliminary field observations on the Chilean earthquake of 3 March, 1985. Bulletin of the New Zealand Society for Earthquake Engineering, 18(2): 119-127.

Doyle, H.A., 1995. Seismology. John Wiley, New York, 218 pp.

Duffy, B.G., 2007. Shear wave velocity - Torlesse - personal meeting & discussion, University of Canterbury, Christchurch, New Zealand.

Duffy, B.G., 2008. Development of Multi-channel Analysis of Surface Waves (MASW) for characterising the internal structure of active fault zones as a predictive method of identifying the distribution of ground deformation, University of Canterbury, Christchurch.

Evans, S.G., Aitken, J.D., Wetmiller, R.J. and Horner, R.B., 1987. A rock avalanche triggered by the October 1985 North Nahanni earthquake, District of Mackenzie, N.W.T. Canadian Journal of Earth Sciences, 24(1): 176-184.

Fernandez Merodo, J.A. et al., 2004. Modelling of diffuse failure mechanisms of catastrophic landslides. Computer Methods in Applied Mechanics and Engineering, 193: 2911-2939.

Fumal, T.E., 1978. Correlations between seismic wave velocities and physical properties of near-surface geologic materials in the southern San Francisco Bay region, California. 78-1067, U.S. Geological Survey.

Gagnepain-Beyneix, J., Lepine, J.C., Nercessian, A. and Hirn, A., 1995. Experimental study of site effects in the Fort-de-France area (Martinique Island). Bulletin of the Seismological Society of America, 85(2): 478-495.

Gao, S., Liu, H., Davis, P.M. and Knopoff, L., 1996. Localized amplification of seismic waves and correlation with damage due to the Northridge earthquake: Evidence for focusing in Santa Monica. Bulletin of the Seismological Society of America, 86(1B): 209-230.

Geli, L., Bard, P.-Y. and Jullien, B., 1988. The effect of topography on earthquake ground motion; A review and new results. Bulletin of the Seismological Society of America, 78(1): 42-63.

Genevois, R. and Romeo, R.W., 2003. Probability of Failure Occurrence and Recurrence in Rock Slopes Stability Analysis.

Gibson, A.D., 1996. Physical scale modeling of gewotechnical structures at one-G, California Institute of Technology, Pasadena, California, 413 pp.

Gledhill, K., Randall, M.J. and Chadwick, M.P., 1991. The EARSS digital seismograph: System description and field trials. Bulletin of the Seismological Society of America, 81(4): 1380-1390.

GovindaRaju, L., Ramana, G.V., HanumanthaRao, C. and Sitharam, T.G., 2004. Site-specific ground response analysis. Current Science, 87(10): 1354-1362.

Griffiths, D.W. and Bollinger, G.A., 1979. The effect of Appalachian mountain topography on seismic waves. Bulletin of the Seismological Society of America, 69: 1081-1105.

Hancox, G.T., Cox, S.C., Turnbull, I.M. and Crozier, M.J., 2003. Reconnaissance studies of landslides and other ground damage caused by the Mw 7.2 Fiordland earthquake of 22 August 2003. 2003/30, Lower Hutt.

Harp, E.L. and Jibson, R.W., 2002. Anomalous concentrations of seismically triggered rock falls in Pacoima Canyon; are they caused by highly susceptible slopes or local amplification of seismic shaking? Bulletin of the Seismological Society of America, 92(8): 3180-3189.

Harp, E.L. et al., 2003. Landslides and liquefaction triggered by the M 7.9 Denali Fault earthquake of 3 November 2002. GSA TODAY, 13(8): 4-10.

Harp, E.L. and Wilson, R.C., 1995. Shaking intensity thresholds for rock falls and slides: Evidence from 1987 Whittier Narrows and Superstition Hills earthquake strong-motion records. Bulletin of the Seismological Society of America, 85(6): 1739-1757.

Hartzell, H.S., Carver, D.L. and King, K.W., 1994. Initial investigation of site and topographic effects at Robinwood Ridge, California. Bulletin of the Seismological Society of America, 84(5): 1336-1349.

Havenith, H.-B., Strom, A., Calvetti, F. and Jongmans, D., 2003a. Seismic triggering of landslides. Part B: Simulation of dynamic failure processes. Natural Hazards and Earth System Sciences, 3: 663-682.

Havenith, H.-B. et al., 2003b. Seismic triggering of landslides. Part A: Field evidence from the Northern Tien Shan. Natural Hazards and Earth System Sciences(3): 135-149.

Havenith, H.-B., Vanini, M., Jongmans, D. and Faccioli, E., 2003c. Initiation of earthquake-induced slope failure: influence of topographical and other site specific amplification effects. Journal of Seismology, 7: 397-412.

Havenith, H.B., Jongmans, D., Faccioli, E., Abdrakhmatov, K. and Bard, P.Y., 2002. Site effect analysis around the seismically induced Ananevo rockslide, Kyrgyzstan. Bulletin of the Seismological Society of America, 92(8): 3190-3209.

Huang, C.-C., Lee, Y.-H., Liu, H.-P., Keefer, D.K. and Jibson, R.W., 2001. Influence of surface-normal ground acceleration on the initiation of the Jih-Feng-Erh-Shan landslide during the 1999 CHi-Chi, Taiwan, earthquake. Bulletin of the Seismological Society of America, 91(5): 953-958.

Jibson, R.W. and Crone, A.J., 2001. Observations and Recommendations Regarding Landslide Hazards Related to the January 13, 2001 M-7.6 El Salvador Earthquake. 01-141, U.S. Department of Interior, U.S. Geological Survey.

Jibson, R.W., Harp, E.L., Schulz, W. and Keefer, D.K., 2004. Landslides triggered by the 2002 Denali Fault, Alaska, earthquake and the inferred nature of the strong shaking. Earthquake Spectra, 20(3): 669-691.

Jibson, R.W., Harp, E.L., Schulz, W. and Keefer, D.K., 2006. Large rock avalanches triggered by the M 7.9 Denali Fault, Alaska, earthquake of 3 November 2002. Engineering Geology, 83: 144-160.

Jousset, P., Neuberg, J. and Jolly, A., 2004. Modelling low-frequency volcanic earthquakes in a viscoelastic medium with topography. Geophys. J. Int., 159: 776-802.

Kaeser, M.A., 1999. Simulation of seismic wave propagation on irregular grids, Ludwig-Maximilians- Universitaet, Munich, Germany, 103 pp.

Katz, O. and Aharonov, E., 2006. Landslides in vibrating sand box: What controls types of slope failure and frequency magnitude relations? Earth and Planetary Science Letters, 247: 280-294.

Keefer, D.K., 1984a. Landslides caused by earthquakes. Geological Society of America Bulletin, 95: 406-421.

Keefer, D.K., 1984b. Rock avalanches caused by earthquakes: source characteristics. Science, 223: 1288-1293.

Keefer, D.K., 1994. The importance of earthquake-induced landslides to long-term slope erosion and slope-failure hazards in seismically active regions. Geomorphology, 10(1-4): 265-284.

Keefer, D.K., 2002. Investigating Landslides Caused by Earthquakes - A Historical Review. Surveys in Geophysics, 23(6): 473-510.

Khazai, B. and Sitar, N., 2003. Evaluation of factors controlling earthquake-induced landslides caused by Chi-Chi earthquake and comparison with the Northridge and Loma Prieta events. Engineering Geology, 71: 79-95.

Komatitsch, D. and Tromp, J., 1999. Introduction to the spectral element method for three-dimensional seismic wave propagation. Geophys. J. Int., 139: 806-822.
Konagai, K. et al., 2002. Las Colinas landslide caused by the January 13, 2001 off the coast of El Salvador earthquake. Journal of Japan Association for Earthquake Engineering, 2(1).
Kramer, S.L., 1996. Geotechnical Earthquake Engineering. Prentice-Hall International Series in Civil Engineering and Engineering Mechanics. Prentice-Hall, New Jersey, 653 pp.
Kulhanek, O., 1990. Anatomy of seismograms. Developments in solid earth geophysics. Elsevier, New York, 178 pp.
LeBrun, B., Hatzfeld, D., Bard, P.Y. and Bouchon, M., 1999. Experimental study of the ground motion on a large scale topographic hill in Ktiherion (Greece). Journal of Seismology, 3: 1-15.
Lee, J.A., 2004. Engineering Geological investigations of the Lake Coleridge Rock Avalanche deposits, Inland Canterbury, University of Canterbury, Christchurch, 220 pp.
Lee, W.H.K., 1994. Observations of Northridge aftershocks and artificial sources in Tarzana, California, using a dense seismic array. EOS Transactions, American Geophysical Union, 75(44 Suppl.): 167-X.
Lee, W.H.K. et al., 1994. Digital seismograms of selected aftershocks of the Northridge Earthquake recorded by a dense seismic array on February 11, 1994 at Cedar Hill Nursery in Tarzana, California. Open-File Report 94-234, U.S. Geological Survey.
Lin, M.-L. and Wang, K.-L., 2006. Seismic slope behavior in a large-scale shaking table model test. Engineering Geology, 86(2): 118-133.
Logan, J.D., 1987. Applied Mathematics: A Contemporary Approach. John Wiley & Sons, Inc., New York, 572 pp.
Lohn, H.L., 1989. The Effects of Topography on the Amplification and Deamplification of Seismic Waves, University of Nevada, Reno, 257 pp.
Luo, H.Y., Zhou, W., Huang, S.L. and Chen, G., 2004. Earthquake-induced landslide stability analysis of the Las Colinas landslide in EL Salvador. International Journal of Rock Mechanics & Mining Sciences, 41(3).
Luzon, F. et al., 1997. Diffraction of P, S and Rayleigh waves by three-dimensional topographies. Geophys. J. Int., 129: 571-578.
Luzón, F., Sánchez Sesma, F.J., Gil, A., Posada, A. and Navarro, M., 1999. Seismic response of 3D topographical irregularities under incoming elastic waves from point sources. Phys. Chem. Earth, 24(3): 231-234.
Madabhushi, G.S.P., 1996. Modelling of deformations in Dynamic Soil-Structure Interaction problems, VELACS Extension Conference 28 (Verification of Liquefaction Analysis by Centrifuge Studies), University of California.
Malamud, B.D., Turcotte, D.L., Guzzetti, F. and Reichenbach, P., 2004. Landslide, earthquakes, and erosion. Earth and Planetary Science Letters, 229: 45-59.
MathWorks, T., 2005. MATLAB®. The MathWorks.
Moczo, P., Bystricky, E., Kristek, J., Carcione, J.M. and Bouchon, M., 1997. Hybrid modeling of P-SV seismic motion at inhomogeneous viscoelastic topographic structures. Bulletin of the Seismological Society of America, 87(5): 1305-1323.
Montalvo-Arrieta, J.C., Reinoso-Angulo, E. and Sánchez-Sesma, F.J., 2003. Observations of strong ground motion at hill sites in Mexico City from recent earthquakes. Geofísica International, 42(2): 205-217.

Morton, D.M., Campbell, R.H., Jibson, R.W., Wesson, R.L. and Nicholson, C., 1989. Landslides and ground fractures produced by the July 8, 1986 North Palm Springs, California earthquake (abstract). Geol. Soc. Am. Abs. with Prog., 21: 119.

Munson, B.R., Young, D.F. and Okiishi, T.H., 2002. Fundamentals of Fluid Mechanics. John Wiley & Sons, Inc., 840 pp.

Murphy, W., 2006. The role of topographic amplification in the initiation of rock slope failures during earthquakes. In: S.G.e.a. Evans (Editor), Landslides from Massive Rock Slope Failure. Springer, pp. 139-154.

Murphy, W., Petley, D.N., Bommer, J. and Mankelow, J.M., 2002. Uncertainty in ground motion estimates for the evaluation of slope stability during earthquakes. Quarterly Journal of Engineering Geology and Hydrogeology, 35: 71-78.

Narayan, J.P. and Prasad Rao, P.V., 2003. Two and half dimensional simulation of ridge effects on the ground motion characteristics. Pure and Applied Geophysics, 160: 1557-1571.

Nasim, A.S.M., 2005. Mechanisms of earthquake-induced deformation in slopes and embankments, Drexel University, Philadelphia, 519 pp.

Okamoto, S., 1973. Introduction To Earthquake Engineering. University of Tokyo press.

Oprsal, I., 2000. Hybrid modeling of seismic waves, Charles University, Prague.

Orwin, J.F., 1998. The application and implications of rock weathering-rind dating to a large rock avalanche, Craigieburn Range, Canterbury, New Zealand. New Zealand Journal of Geology and Geophysics, 41: 219-223.

Paolucci, R., 1999a. Fundamental vibration frequencies of 2D geological structures. In: Balkema (Editor), Earthquake Geotechnical Engineering. Balkema Rotterdam, Lisbon, pp. 255-260.

Paolucci, R., 1999b. Numerical evaluation of the effect of cross-coupling of different components of ground motion in site response analysis. Bulletin of the Seismological Society of America, 89(4): 877-887.

Paolucci, R., 2002. Amplification of earthquake ground motion by steep topographic irregularities. Earthquake Engineering and Structural Dynamics, 31: 1831-1853.

Paolucci, R., Faccioli, E. and Maggio, F., 1999. 3D Response analysis of an instrumented hill at Matsuzaki, Japan, by a spectral method. Journal of Seismology, 3: 191-209.

Pearce, A.J. and O'Loughlin, C.L., 1985. Landsliding during a M 7.7 earthquake: Influence of geology and topography. Geology, 13: 855-858.

Pedersen, H.A., LeBrun, B., Hatzfeld, D., Campillo, M. and Bard, P.Y., 1994. Ground motion amplitude across ridges. Bulletin of the Seismological Society of America, 84: 1786-1800.

Percival, D.B. and Walden, A.T., 1993. Spectral Analysis for Physical Applications: Multitaper and Conventional Univariate Techniques. Cambridge University Press.

Perrin, N., 2008. Shear wave velocities in Torlesse. In: F. Buech (Editor). GNS Science, Lower Hutt, n.perrin@gns.cri.nz.

Plafker, G., 1967. Surface faults on Montague Island associated with the 1964 Alaska earthquake, U.S. Geological Survey.

Plafker, G., Ericksen, G.E. and Fernandez Concha, J., 1971. Geological aspects of the May 31, 1970, Peru earthquake. Bulletin of the Seismological Society of America, 61(3): 543-578.

Ponti, D.J. and Wells, R.E., 1991. Off-fault ground ruptures in the Santa Cruz Mountains, California: ridge-top spreading versus tectonic extension during the 1989 Loma Prieta earthquake. Bulletin of the Seismological Society of America, 81(5): 1480-1510.

Poppeliers, C. and Pavlis, G.L., 2002. The Seismic Response of a Steep Slope: High-Resolution Observations with a Dense, Three-Component Seismic Array. Bulletin of the Seismological Society of America, 92(8): 3102-3115.
Prasad, S.K., Towhata, I., Chandradhara, G.P. and Nanjundaswamy, P., 2004. Shaking table tests in earthquake geotechnical engineering. Current Science, 87(10): 1398-1404.
Prestinzini, A. and Romeo, R., 2000. Earthquake-induced ground failures in Italy. Engineering Geology, 58: 387-397.
Refice, A. and Capolongo, D., 2002. Probabilistic modeling of uncertainties in earthquake-induced landslide hazard assessment. Computers & Geosciences, 20: 735-749.
Robertson, J.O.A. and Holliger, K., 1997. Modeling of seismic wave propagation near the earth's surface. Physics of the Earth and Planetary Interiors, 104: 193-211.
Rocscience, I., 2001. Application of the Finite Element Method to Slope Stability, Toronto.
Rodriguez, C.E., Bommer, J.J. and Chandler, R.J., 1999. Earthquake-induced landslides: 1980-1997. Soil Dynamics and Earthquake Engineering, 18: 325-346.
Rogers, A.M., Katz, L.J. and Bennett, T.J., 1974. Topographic effects on ground motion for incident P waves: A model study. Bulletin of the Seismological Society of America, 64: 437-456.
Rogers, F.J., 1930. Experiments with a shaking machine. Bulletin of the Seismological Society of America, 20: 147-159.
Romeo, R., 2000. Seismically induced landslide displacements: a predictive model. Engineering Geology, 58: 337-351.
Sánches-Sesma, F.J. and Campillo, M., 1993. Topographic effects for incident P, SV and Rayleigh waves. Tectonophysics, 218: 113-125.
Savage, W.Z., 2004. An exact solution for effects of topography on Free Rayleigh waves. Bulletin of the Seismological Society of America, 94(5): 1706-1727.
Schneider, J.F., 2006. Earthquake triggered mass movements in Northern Pakistan with special reference to the Hattian slide. In: A.B. Kausar, Khan, T. (Editor), International Conference on 8 October 2005 earthquake in Pakistan: Its implications & hazard mitigation, Islamabad, Pakistan.
Seed, H.B., 1976. Some aspects of sand liquefaction under cyclic loading, Conference on behavior of offshore structures. Norwegian Institute of Technology, Oslo.
SeismoSoft, 2002. SeismoSignal. http://www.seismosoft.com/SeismoSignal/index.htm.
Sepúlveda, S.A., Murphy, W., Jibson, R.W. and Petley, D.N., 2005a. Seismically induced rock slope failures resulting from topographic amplification of strong ground motions: The case of Pacoima Canyon, California. Engineering Geology, 80: 336-348.
Sepúlveda, S.A., Murphy, W. and Petley, D.N., 2005b. Topographic controls on coseismic rock slides during the 1999 Chi-Chi earthquake, Taiwan. Quarterly Journal of Engineering Geology and Hydrogeology, 38: 189-196.
Shinozuka, M., Deodatis, B., Zhang, R. and Papageorgiou, A.S., 1999. Modeling, synthetics and engineering applications of strong earthquake wave motion. Soil Dynamics and Earthquake Engineering, 18: 209-228.
Shou, K.-J. and Wang, C.-F., 2003. Analysis of the Chiufengershan landslide triggered by the 1999 Chi-Chi earthquake in Taiwan. Engineering Geology, 68: 237-250.
Siddiqi, J.A., 2000. Horizontal-to-vertical component ratios for earthquake ground motions recorded on hard rock sites in Canada, Chleton University, Ottawa, Ontario, Canada, 150 pp.

Sincraian, M.V. and Oliveira, C.S., 2000. Nonlinear seismic response of a volcanic hill using the finite element method. Soil Dynamics and Earthquake Engineering, 20: 145-154.
Smith, G.M., 2003. The coseismicity and morphology of the Acheron rock avalanche deposit in the Red Hill Valley, New Zealand, University of Canterbury, Christchurch, 277 pp.
Smith, G.M., Davies, T.R., McSaveney, M.J. and Bell, D.H., 2006. The Acheron rock avalanche, Canterbury, New Zealand - morphology and dynamics. Landslides, 3(1): 62-72.
Speight, R., 1933. The Arthur's Pass Earthquake of 9 th March, 1929. The New Zealand Journal of Science and Technology, 15(3): 173-182.
Spudich, P.A., Hellweg, M. and Lee, W.H.K., 1996. Directional topographic site response at Tarzana observed in aftershocks of the 1994 Northridge, California, earthquake; implications for mainshock motions. Bulletin of the Seismological Society of America, 86(1 Part B suppl.): 193-208.
Stewart, J.P. and Sholtis, S.E., 2005. Case study of strong ground motion variations across cut slope. Soil Dynamics and Earthquake Engineering, 25: 539-545.
Szirtes, T., 2007. Applied Dimensional Analysis and Modeling. Elsevier Inc., 820 pp.
Tibaldi, A., Ferrari, L. and Pasquarè, G., 1995. Landslides triggered by earthquakes and their relations with faults and mountain slope geometry: an example from Equador. Geomorphology, 11: 215-226.
Turnbull, J.M. and Davies, T.R.H., 2006. A mass movement origin for cirques. Earth Surface Processes and Landforms, 31: 1129-1148.
Van Houten, E., 2007. Technical meeting: Silicone - seismic wave actuator, University of Canterbury, Christchurch, elijah.vanhouten@canterbury.ac.nz.
Varnes, D.J., 1978. Slope movement types and processes, in Schuster, R.L. and Krizek, R.J., Landslides - Analysis and control: National Academy of Sciences Transportation Research Board Special Report 176, p.12-33.
Wang, G.-Q., Tang, G.Q., Jackson, C.R., Zhou, X.-Y. and Lin, Q.-L., 2006. Strong ground motions observed at the UPSAR during the 2004 M 6.5 San Simeon and 2004 M 6.0 Parkfield, California, earthquakes. Bulletin of the Seismological Society of America, 96(4B): 159-182.
Wang, Y.-C., Yin, X.-C., Ke, F.-J., Xia, M.-F. and Peng, K.Y., 2000. Numerical Simulation of Rock Failure and Earthquake Process on Mesoscopic Scale. Pure and Applied Geophysics, 157: 1905-1928.
Waterman, N.A. and Ashby, M.F., 1997. The Materials Selector, 1. Chapman & Hall, London.
White, F.M., 1994. Fluid Mechanics. McGraw-Hill International, 736 pp.
Whitehouse, I.E., 1981. A large rock avalanche in the Craigieburn Range, Canterbury. New Zealand Journal of Geology and Geophysics, 24: 415-421.
Whitehouse, I.E., 1983. Distribution of large rock avalanche deposits in the central Southern Alps, New Zealand. New Zealand Journal of Geology and Geophysics, 26: 271-279.
Whitehouse, I.E. and Griffiths, G.A., 1983. Frequency and hazard of large rock avalanches in the central Southern Alps, New Zealand. Geology, 11: 331-334.
Williams, M.S. and Blakeborough, A., 2001. Laboratory testing of structures under dynamic loads: a introduction review. Philosophical Transactions: Mathematical, Physical and Engineering Sciences, 359(1786): 1651-1669.
Wilson, D.C. and Pavlis, G.L., 2000. Near-surface site effects in crystalline bedrock: A comprehensive analysis of spectral amplitudes determined from a dense, three-component seismic array. Earth Interactions, 4(2): 1-31.

Wilson, R.C. and Keefer, D.K., 1983. Dynamic analysis of a slope failure from the 6 August 1979 Coyote Lake, California, earthquake. Bulletin of the Seismological Society of America, 73(3): 863-877.

Wong, H.L. and Jennings, P.C., 1975. Effects of topography on strong ground motion. Bulletin of the Seismological Society of America, 65(5): 1239-1257.

Wright, G.A., 1998. The AD 930 long-runout Round Top debris avalanche, Westland, New Zealand. New Zealand Journal of Geology and Geophysics, 41: 493-497.

Wu, J.-H., Wang, W.-N., Chang, C.-S. and Wang, C.-L., 2005. Effects of strength properties of discontinuities on the unstable lower slope in the Chiu-fen-erh-shan landslide, Taiwan. Engineering Geology, 78: 173-186.

APPENDICES

Appendix A.1

Little Red Hill Field Experiment – Site Setup

SEISMIC FIELD TEST SITE SETUP

The feasibility of conducting a seismic field experiment as being a part of the research project was assessed during a reconnaissance field trip in October 2005. Little Red Hill was chosen for the experiment considering following aspects:

- Almost symmetrical triangular, elongated shape (height: 210 m; length: 800 m, width: 500 m)
- Bedrock dominated edifice represented by near vertically bedded sandstones and argillites of the Mesozoic Torlesse Supergroup
- Availability of suitable sites for the installation of the seismic equipment on the edifice and for the base reference station
- Seismograph sites can be installed on bedrock and show a minimal level of noise
- Remote backcountry provided a quiet environment
- Close driving distance and easy site access for experiment setup and instrument maintenance

A first signal test was carried out in December 2005 detonating a total of 2 kg of *Powergel Magnum 365*™ explosives at a site north of the edifice to test the response of two installed instruments and the signal to noise ratio. The explosives were placed in 3 holes, drilled 3.2m deep into Torlesse bedrock, and detonated simultaneously to provide maximum energy transmission towards the test site. Two instruments were installed for the signal test at site rh0 (base station) and rh3 (ridge crest) on concrete paving slabs (350 x 350x 50 mm) which were fast-concreted onto bedrock and horizontally leveled.

GNS Science provided the main seismic equipment for the field experiment; Mark Products L-4-3D tri-axial velocity sensors (natural frequency 1 Hz) connected to portable EARSS (Equipment for the Automatic Recording of Seismic Signals) data acquisition systems, version 9.12 (Gledhill, 1991); Unfortunately the supply of new Kinemetrics units failed after a few months of delay in shipping from the US which was followed by additional technical calibration problems.
The data storage capacity of the EARSS instruments varied depending on the individual seismograph between 512 Mb and 2 Gb. A GPS unit controlled the internal system clock. The EARSS system has a pre-event memory that record earthquake events with a pre-event time slot retroactively. The pre-event memory was set to 10 seconds. To keep the instruments operational

over a longer period, each seismograph was connected to one or two 12 V car /truck batteries which stored the energy supplied by a solar panel (40 W – 62 W). The seismometers were covered by a plastic bucket to reduce the noise caused by wind (same technique recommended by GNS and successfully used in previous field tests). A sketch of the setup is shown in figure A.1.1. After successfully installing the instruments and initial test runs the sampling frequency was set to 50 Hz. All instrument sites showed minimal background noise. Gains were set to two.

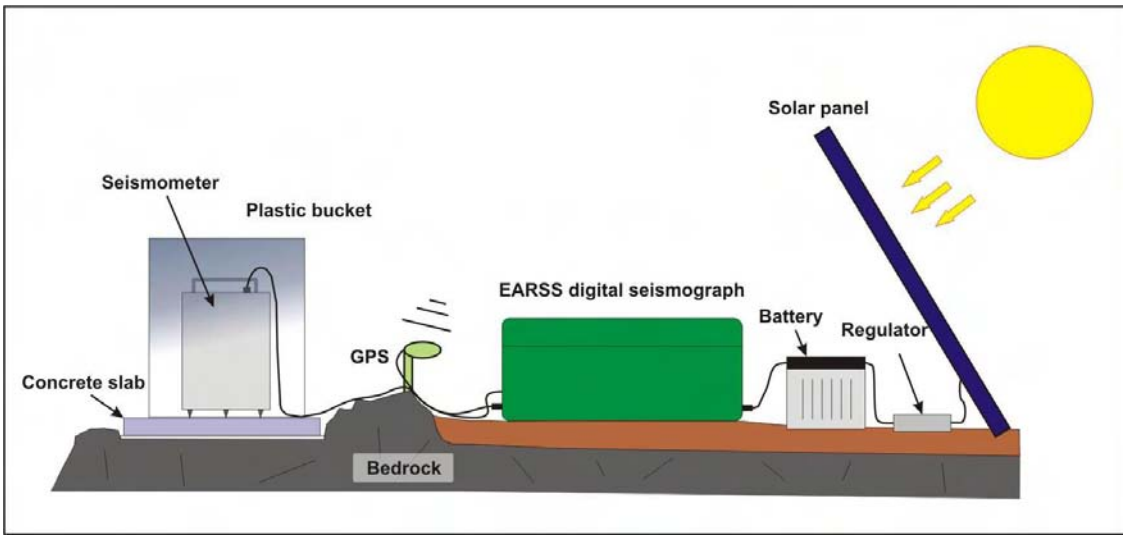

Figure A.1.1: Sketch of EARSS seismograph setup

From 10th February till 11th of May station rh0, rh1, and rh3 were equipped with EARSS instruments. On May 12th additional 4 instruments were installed (rh2, rh4, rh5, rh6) across the ridge. Instrument de-installation took place on the 16th of July.

The instruments were serviced at a 10 day interval. The regular maintenance included:

- A general instrument operational check (the EARSS system is equipped with an audio-visual alarm system that would be triggered by any system failure or malfunction, e.g. power drop below minimal threshold value)
- Inspection of cable connections
- Battery voltage level check
- Inspection and readjustment of the solar panels
- Data download, hardware storage formatting, and system setup and reset using a small portable notebook (Toshiba Libretto). The communication with the EARSS seismograph was established through a MS-DOS operated and command controlled user interface, called “EARSS Talk” (Fig. A.1.2), and a PCI Bus-cable connection.

Using a small Libretto notebook turned out to be a big benefit considering the steep terrain and often bad weather conditions.

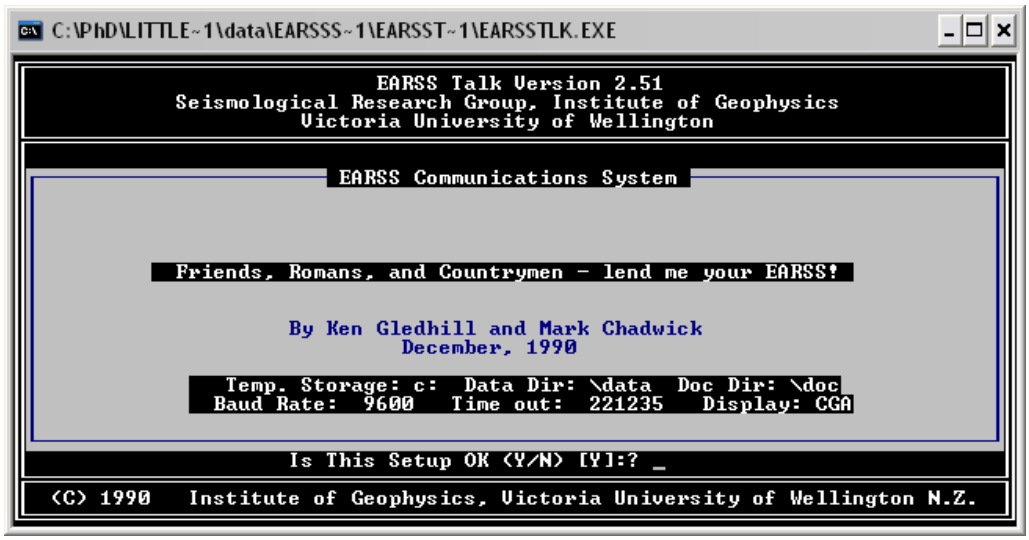

Figure A.1. 1: Screenshot showing the "EARSS Talk" user interface developed by Gledhill & Chadwick (1990)

Problems noted:

- The decrease in sunshine hours and temperature drop in the winter months caused increasing problems with the power supply for the seismic stations.
- The availability of solar panels with high capacity was limited (1 x 62 W, 6 x 40 W) and , due to temperatures dropping below the 5°C mark, decreased the storage capacity of the batteries in May and June.

Weak batteries were replaced and critical instrument were provided with additional solar power supply. Even with weekly servicing intervals, a constant operational mode of all seismic station could not be achieved in June 2006. By mid of June the decision was made to abort the seismic field experiment and to recover all instruments.

Data processing:

On-site inspection of the recorded data was done using a MS-DOS software package, called *BUFDAT*, version 2.2. The software was written by Ken Gledhill and was used in the field to get an overview of the buffer storage and to check the setup parameters for the recorded events.

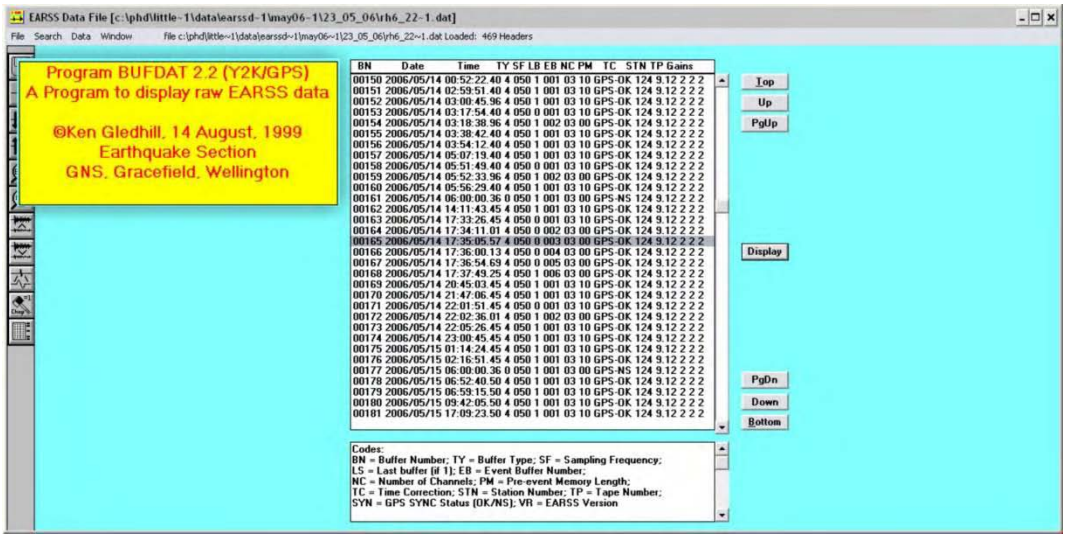

Figure A.1.3: Screenshot of the MS-DOS based program BUFDAT, written by Gledhill, 1999

The EARSS raw data are stored as DAT-files. Opening a file with BUFDAT allows the user to have an instant check on stored data and main setup parameters by looking at the directory file that shows all buffers that were recorded (Fig. A.1.3).

The initial steps of data processing took place at the Institute of Geophysics at Victoria University of Wellington. The raw DAT-files were processed using a compilation of different UNIX-based programmes called *VUWEarth* (Victoria University of Wellington Seismological Processing System) which was especially developed for the initial analysis of EARSS data by Mark Chadwick (1994). Further data processing was accomplished utilizing the programs *SAC* (Seismic Analysis Code; (Peng, 2006), SeismoSignal (SeismoSoft, 2002) and MATLAB® (MathWorks, 2005).

Table A.1.1: Exact instrument positions inclusive station- & instrument ID

Station	ID	Altitude [mASL]	Northing [N]	Easting [E]
rh0	103	684.65	5764706.52	2396811.28
rh1	119	759.46	5764471.76	2396848.88
rh2	116	812.60	5764522.28	2396955.93
rh3	125	858.01	5764403.30	2396955.01
rh4	114	862.29	5764375.86	2396952.97
rh5	122	874.56	5764292.14	2396981.09
rh6	124	892.35	5764190.01	2396999.14

The exact positions as well as station- and instrument ID are presented in table A.1.1.

Pictures of the individual station setup are shown in figure A.1.4 and figure A.1.5.

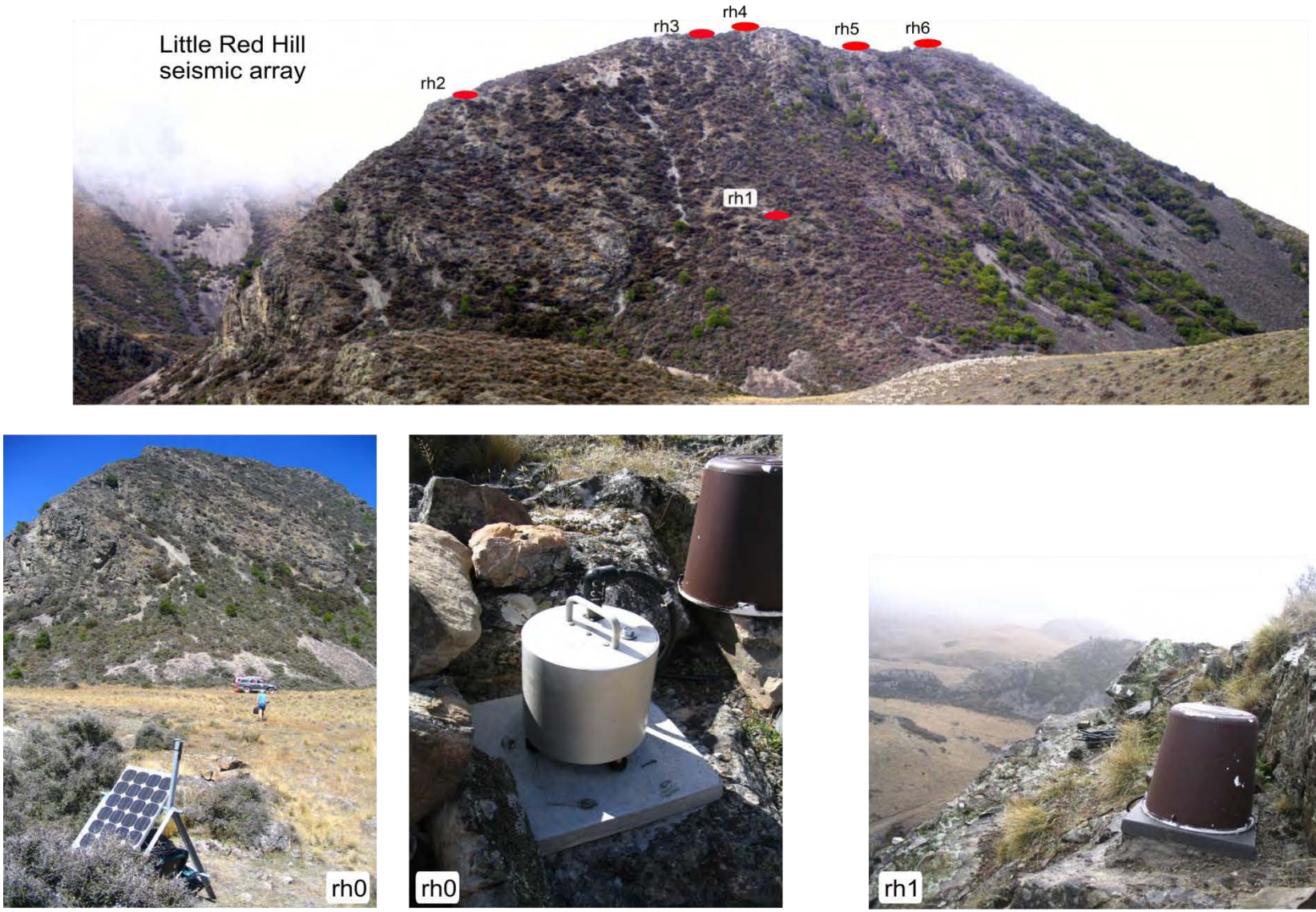

Figure A.1.4: Little Red Hill seismic array - seismograph stations A; Pictures showing a station overview and the setup of station rh0 and rh1

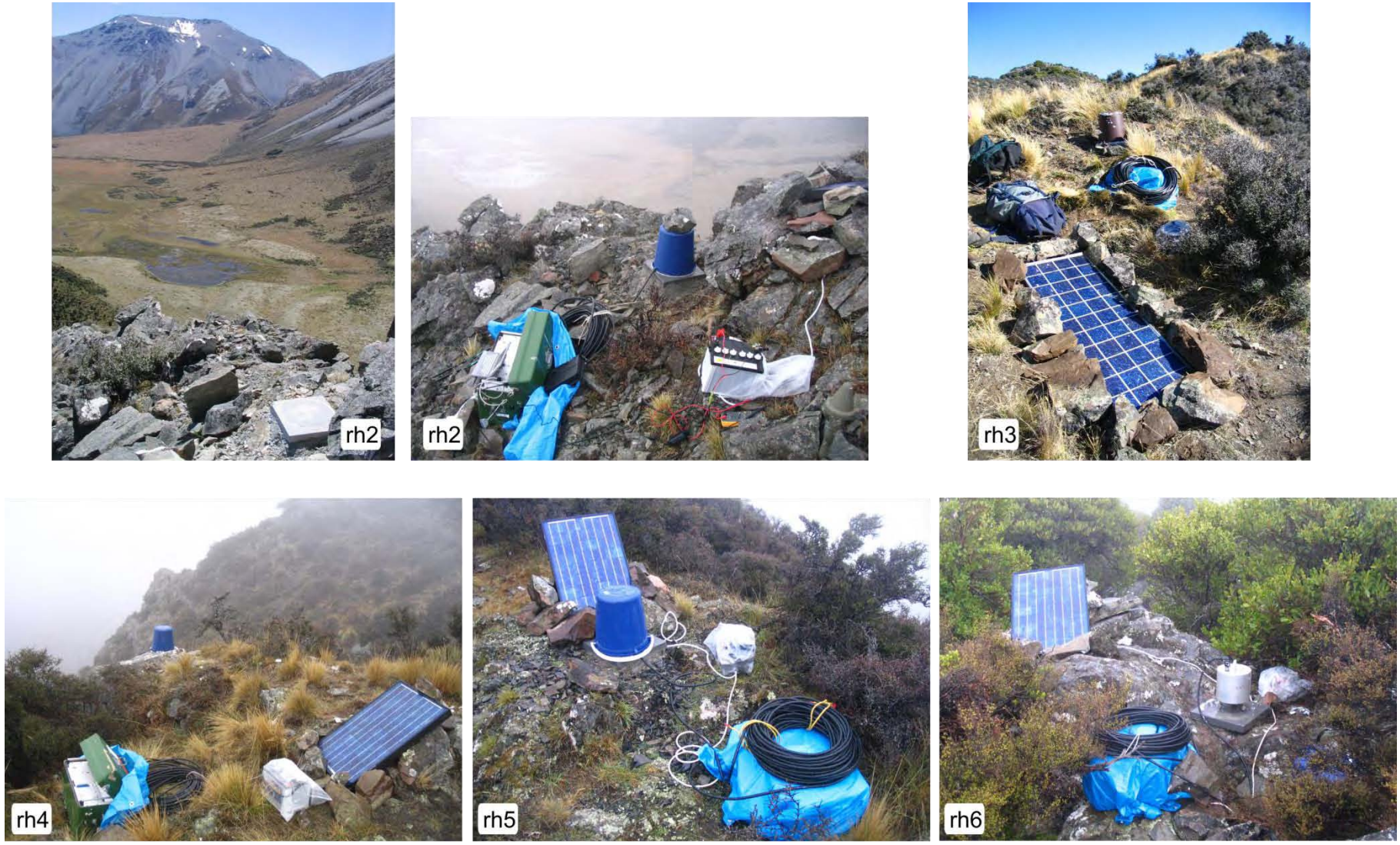

Figure A.1.5: Little Red Hill seismic array - seismograph stations B; Pictures showing setup of station rh2, rh3, rh4, and rh6

REFERENCES

Gledhill, K., Randall, M.J., Chadwick, M.P., 1991. The EARSS digital seismograph: System description and field trials. Bulletin of the Seismological Society of America, 81(4): 1380-1390.

Chadwick, M.P., 1994. The VUWEarth Seismological Processing System, Wellington, pp. 5.

Laboratory, L.L.N., SAC (Seismic Analysis Code). Lawrence Livermore National Laboratory - University of California, Livermore.

MathWorks, T., 2005. MATLAB®. The MathWorks.

Peng, Z., Huang, X., McGuire, J., 2006. MatSAC. zhigang.peng@eas.gatech.edu

SeismoSoft, 2002. SeismoSignal. http://www.seismosoft.com/SeismoSignal/index.htm.

Appendix A.2

Little Red Hill Field Experiment – Time domain data

Selected earthquakes - accelerograms

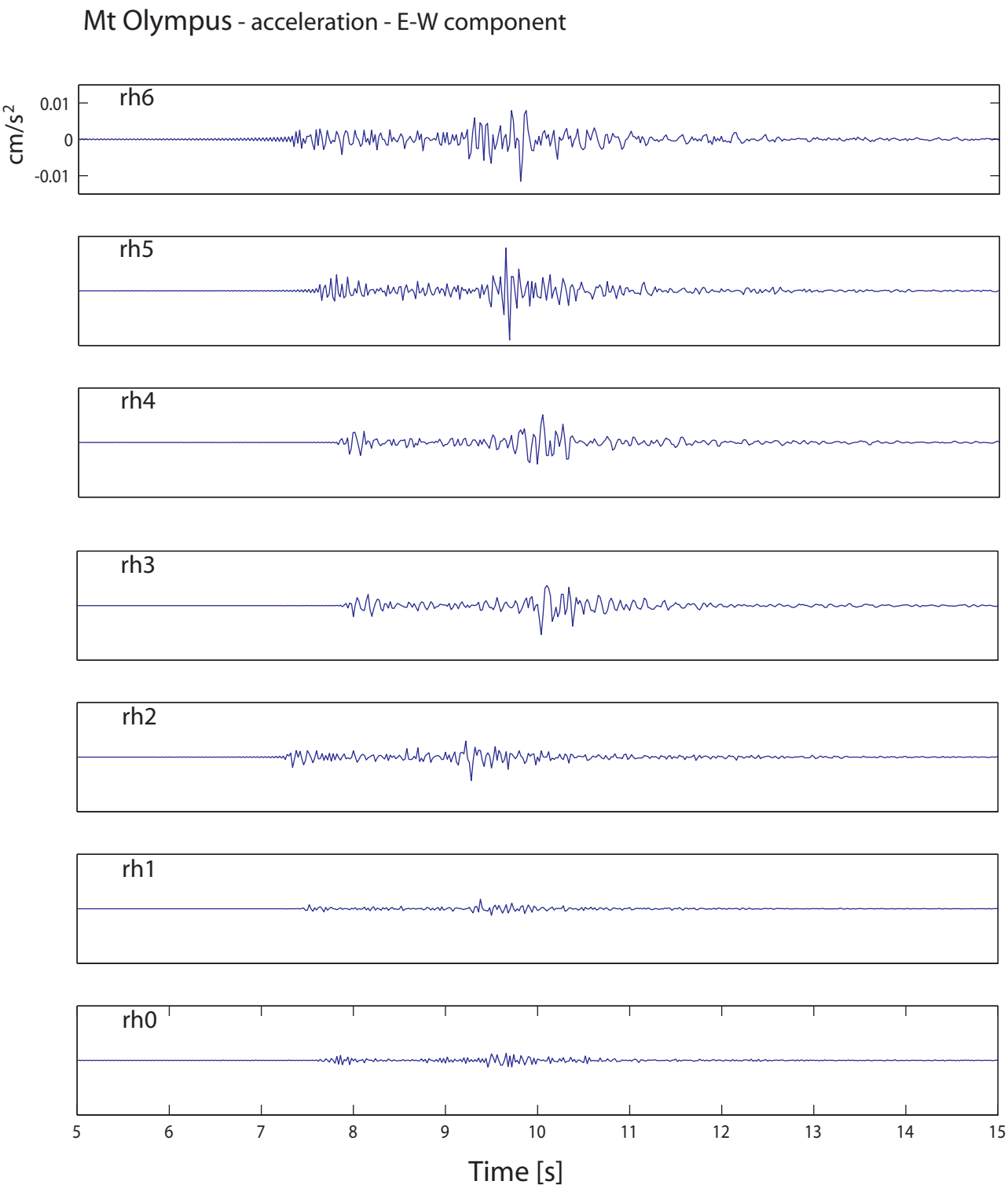
Mt Olympus - acceleration - E-W component
cm/s2
0.01
0
-0.01
rh6
rh5
rh4
rh3
rh2
rh1
rh0
5
6
7
8
9
10
11
12
13
14
15
Time [s]

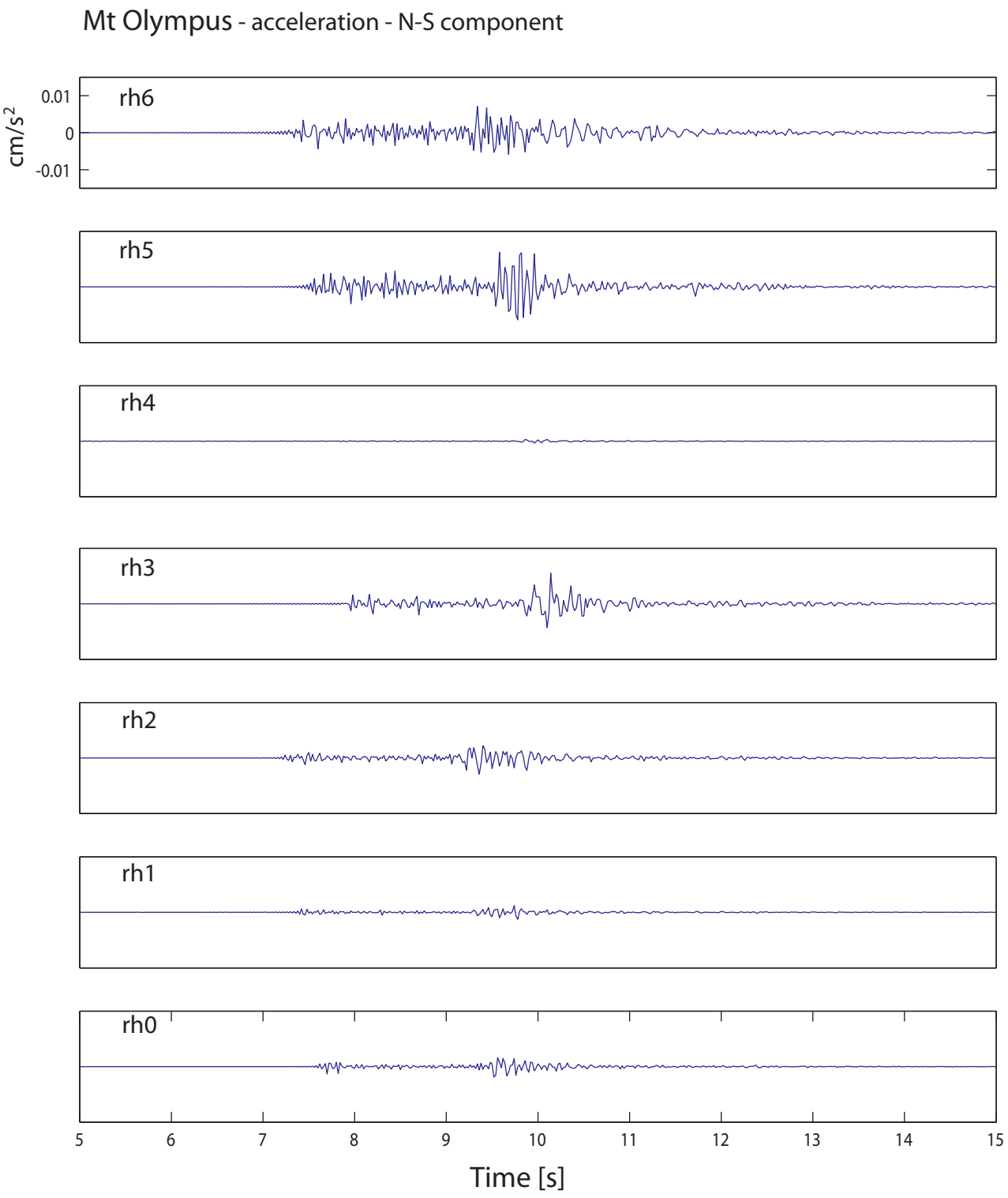
Mt Olympus - acceleration - N-S component
cm/s2
0.01
0
-0.01
rh6
rh5
rh4
rh3
rh2
rh1
rh0
5
6
7
8
9
10
11
12
13
14
15
Time [s]

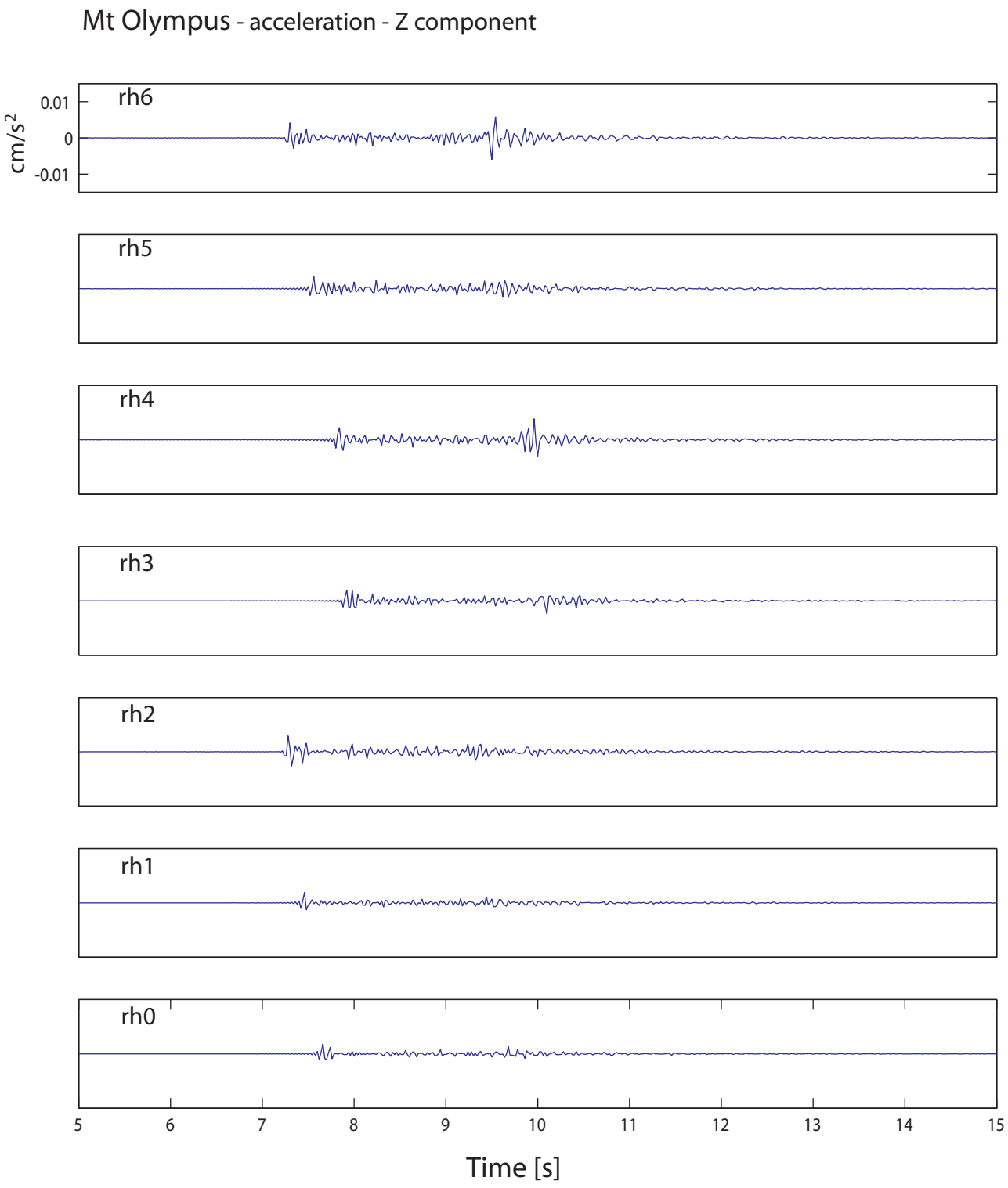
Mt Olympus - acceleration - Z component
cm/s2
0.01
0
-0.01
rh6
rh5
rh4
rh3
rh2
rh1
rh0
5
6
7
8
9
10
11
12
13
14
15
Time [s]

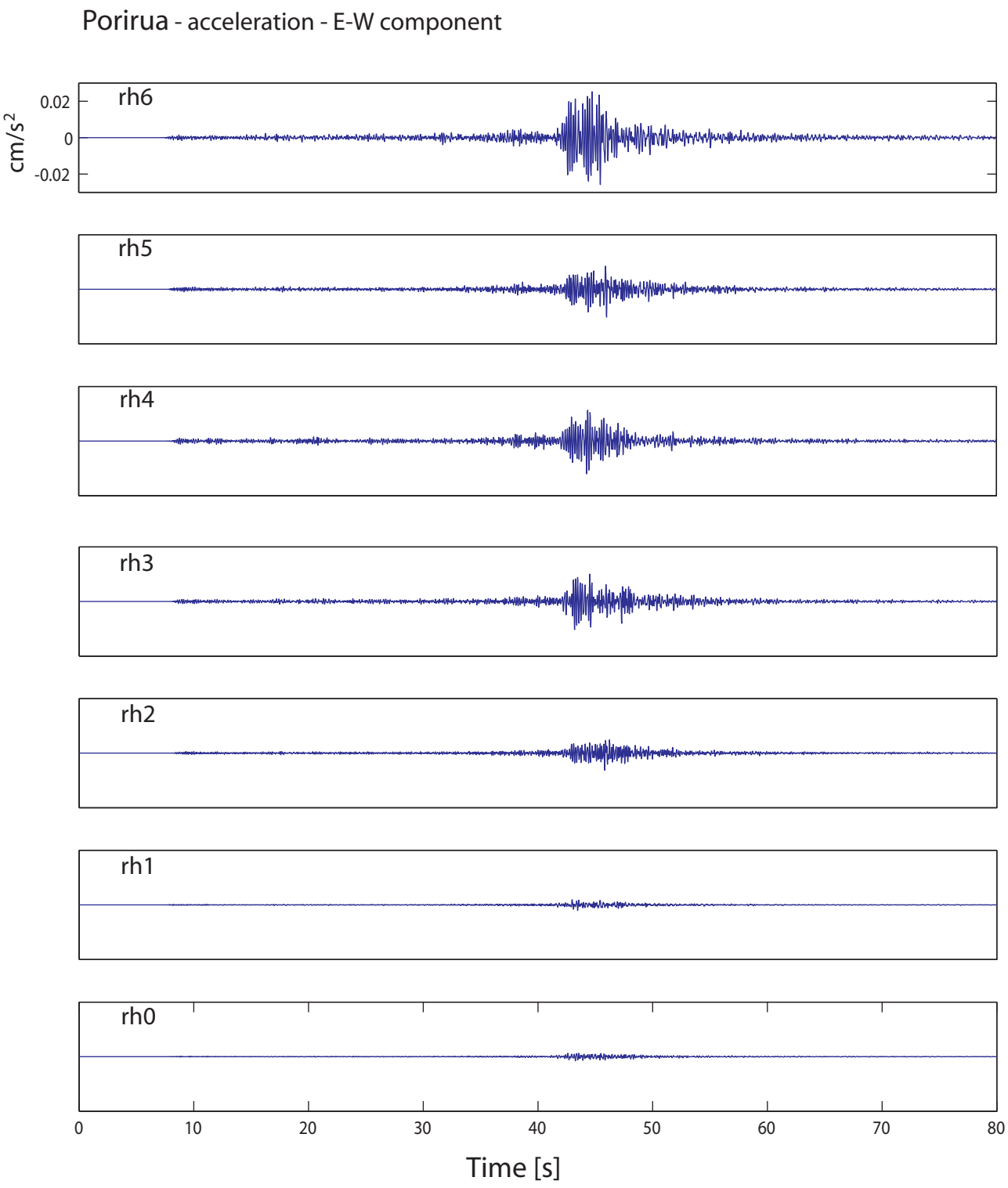
Porirua - acceleration - E-W component
cm/s2
0.02
0
-0.02
rh6
rh5
rh4
rh3
rh2
rh1
rh0
0
10
20
30
40
50
60
70
80
Time [s]

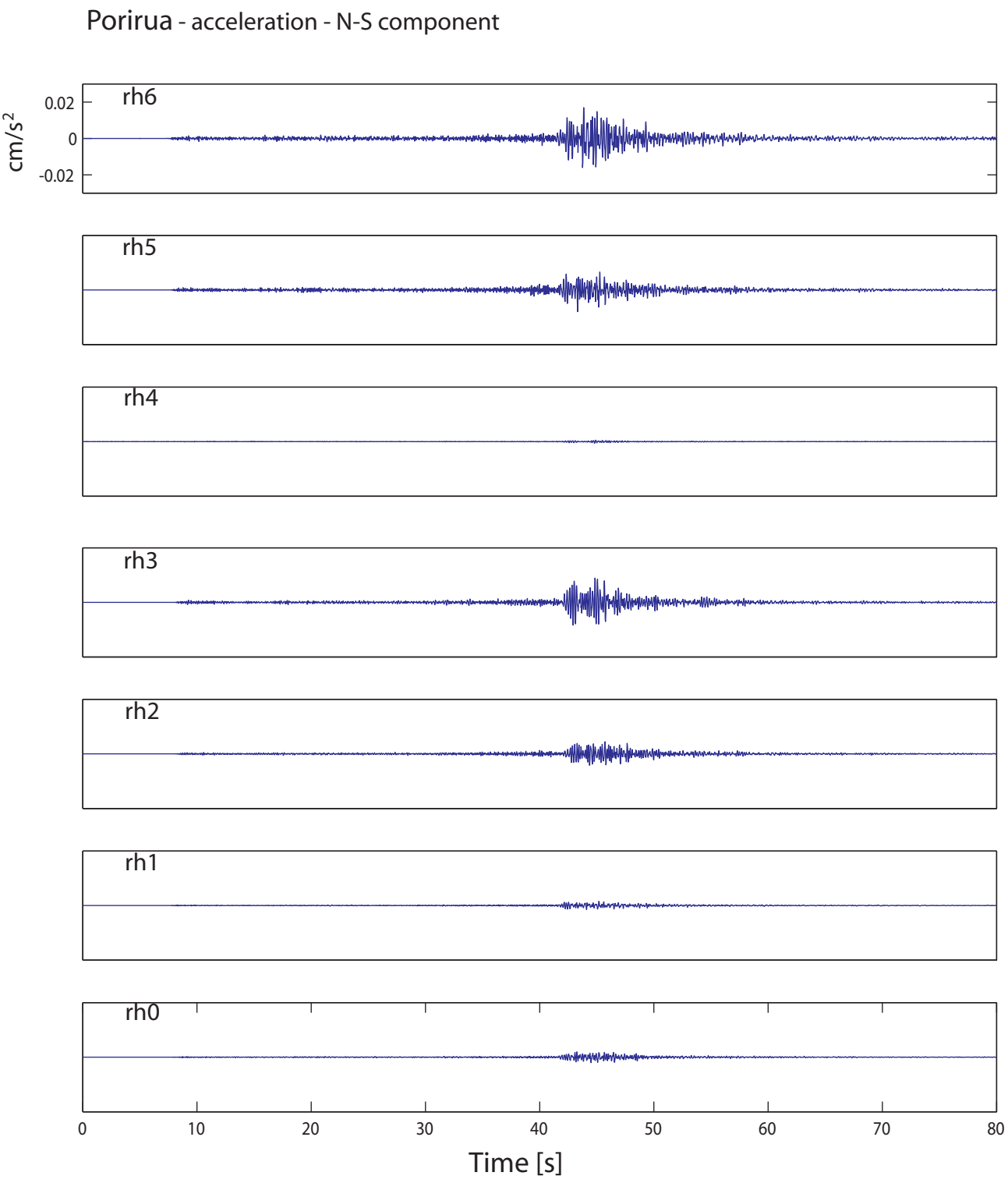
Porirua - acceleration - N-S component
cm/s2
0.02
0
-0.02
rh6
rh5
rh4
rh3
rh2
rh1
rh0
0
10
20
30
40
50
60
70
80
Time [s]

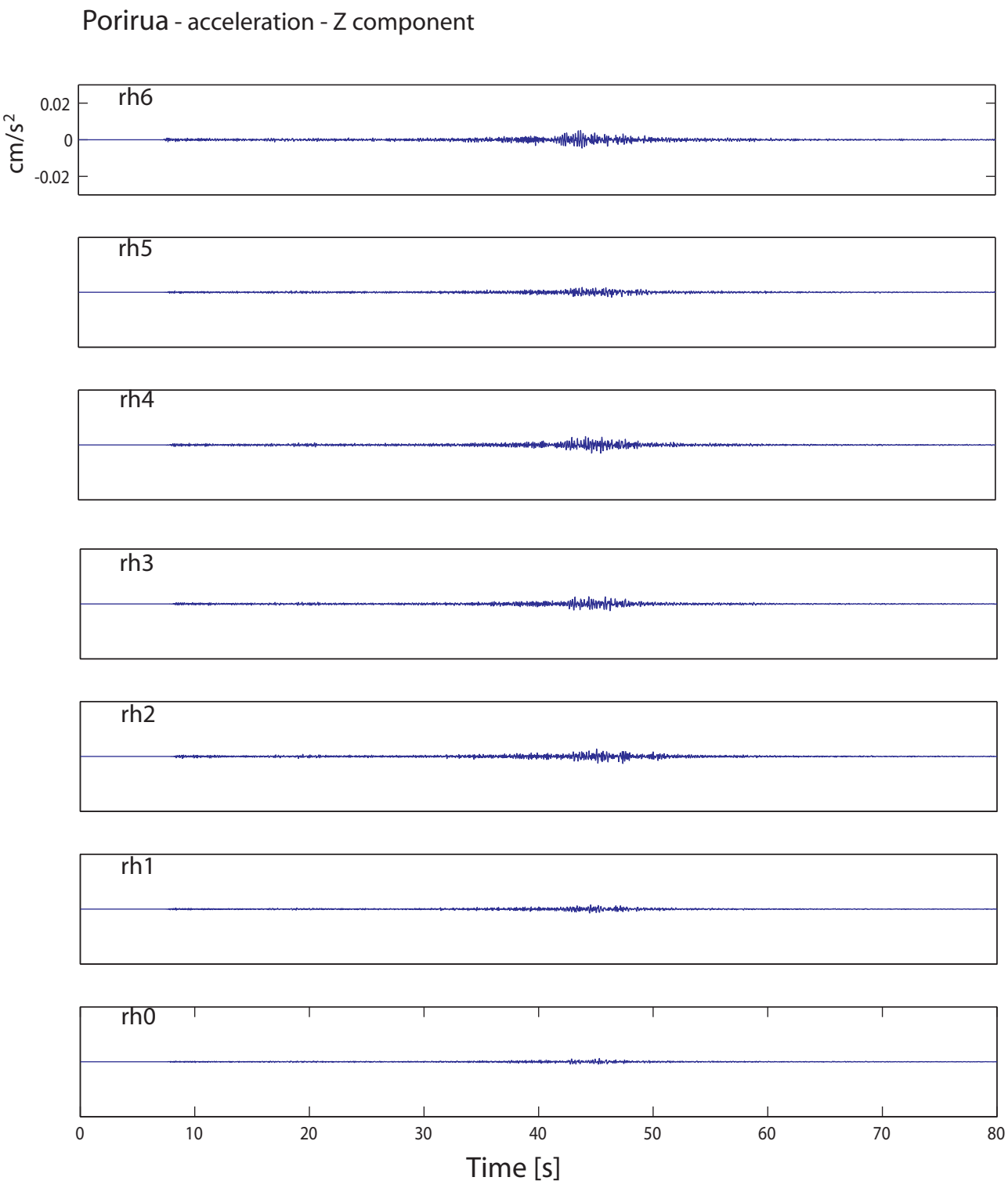
Porirua - acceleration - Z component
cm/s2
0.02
0
-0.02
rh6
rh5
rh4
rh3
rh2
rh1
rh0
0
10
20
30
40
50
60
70
80
Time [s]

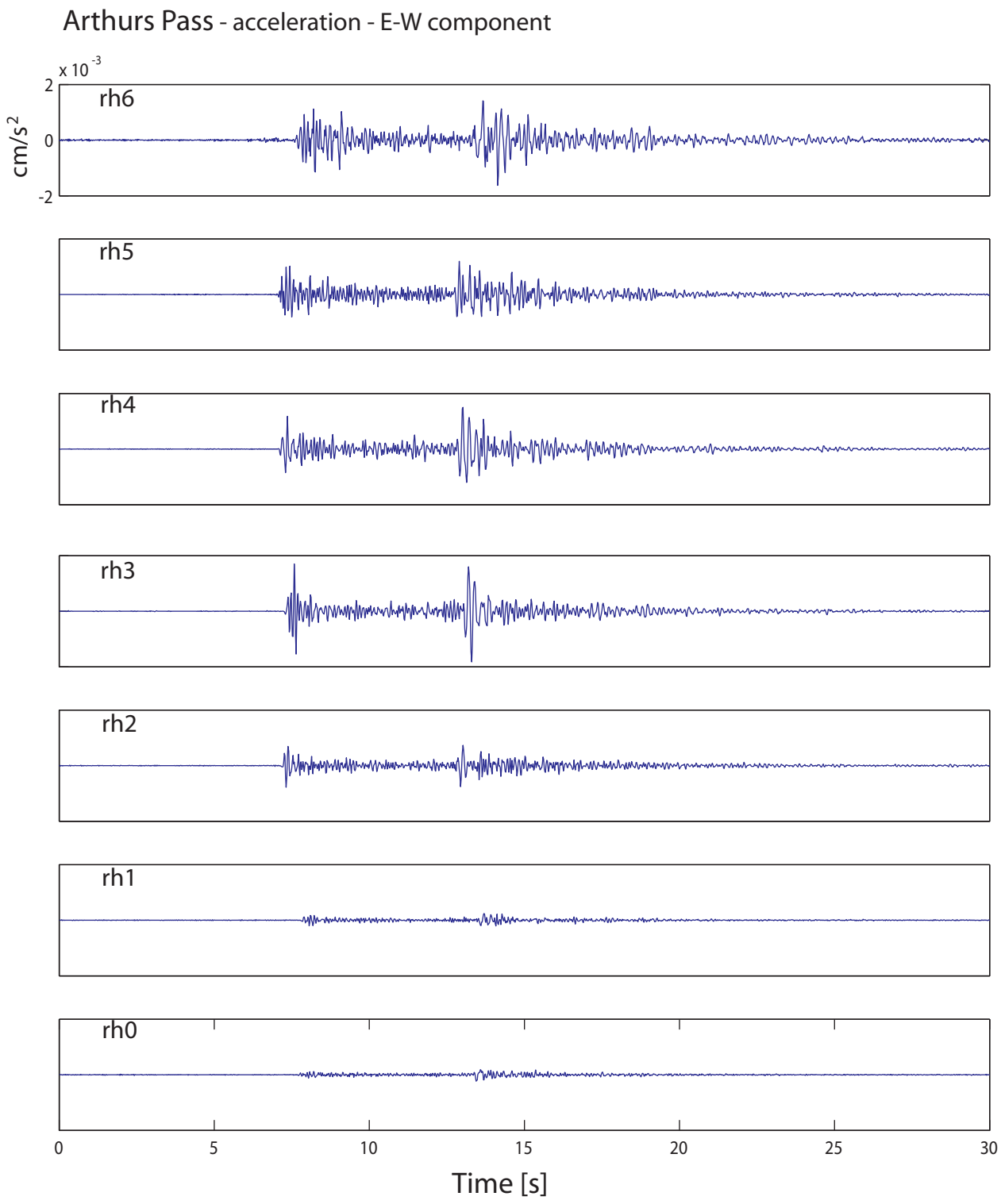
Arthurs Pass - acceleration - E-W component
x 10 -3
cm/s2
2
0
-2
rh6
rh5
rh4
rh3
rh2
rh1
rh0
0
5
10
15
20
25
30
Time [s]

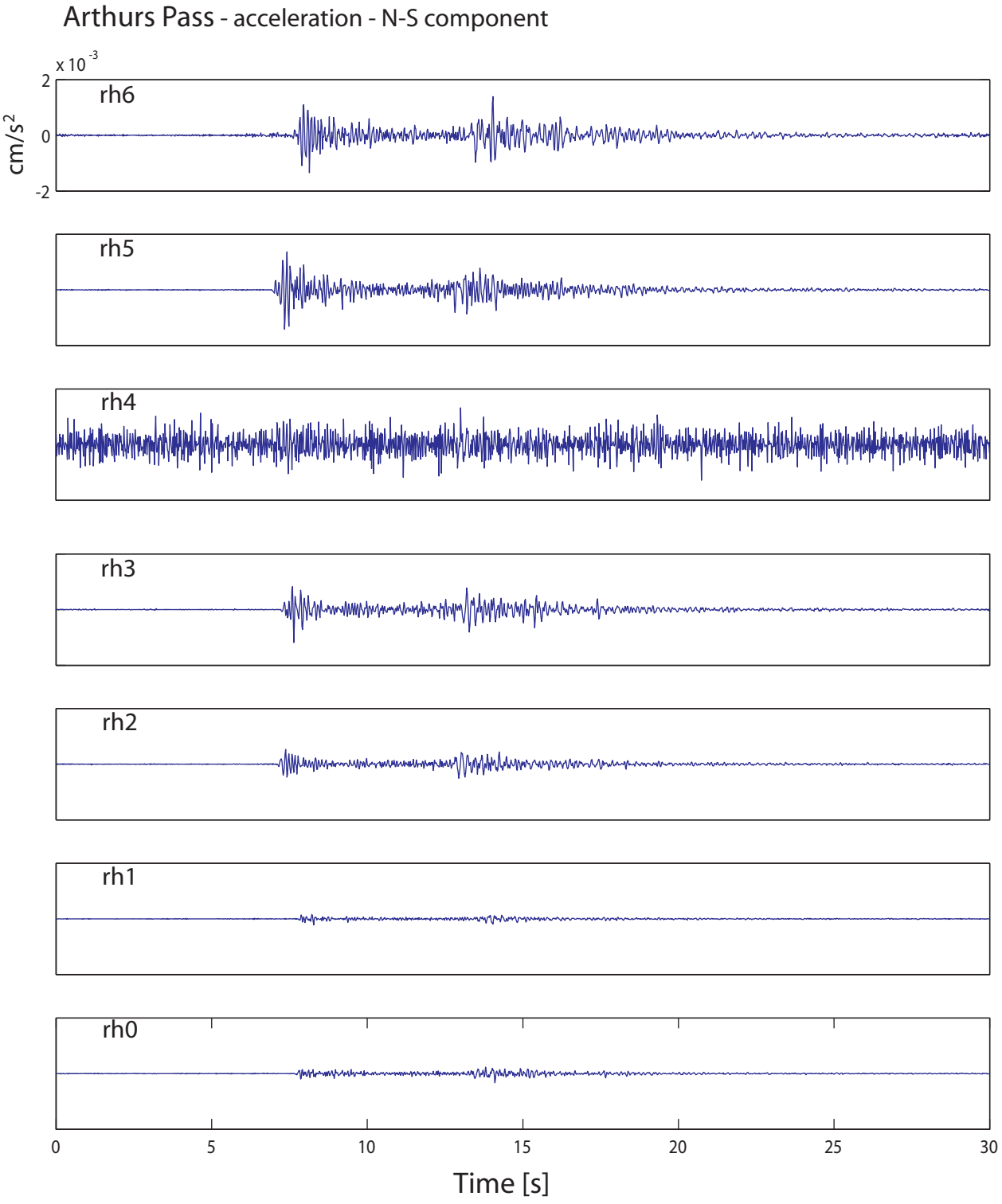
Arthurs Pass - acceleration - N-S component
x 10 -3
cm/s2
2
0
-2
rh6
rh5
rh4
rh3
rh2
rh1
rh0
0
5
10
15
20
25
30
Time [s]

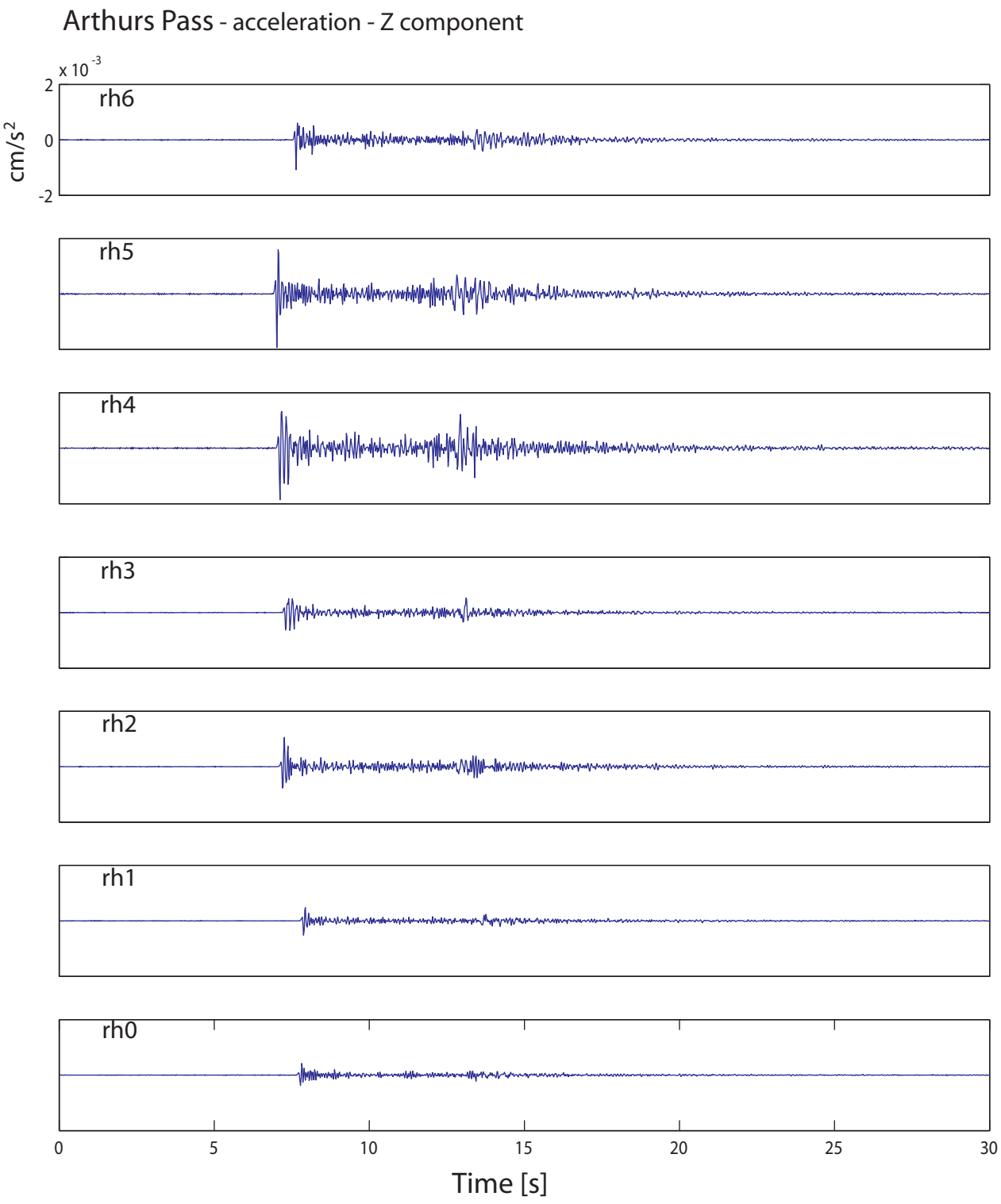
Arthurs Pass - acceleration - Z component
x 10 -3
cm/s2
2
0
-2
rh6
rh5
rh4
rh3
rh2
rh1
rh0
0
5
10
15
20
25
30
Time [s]

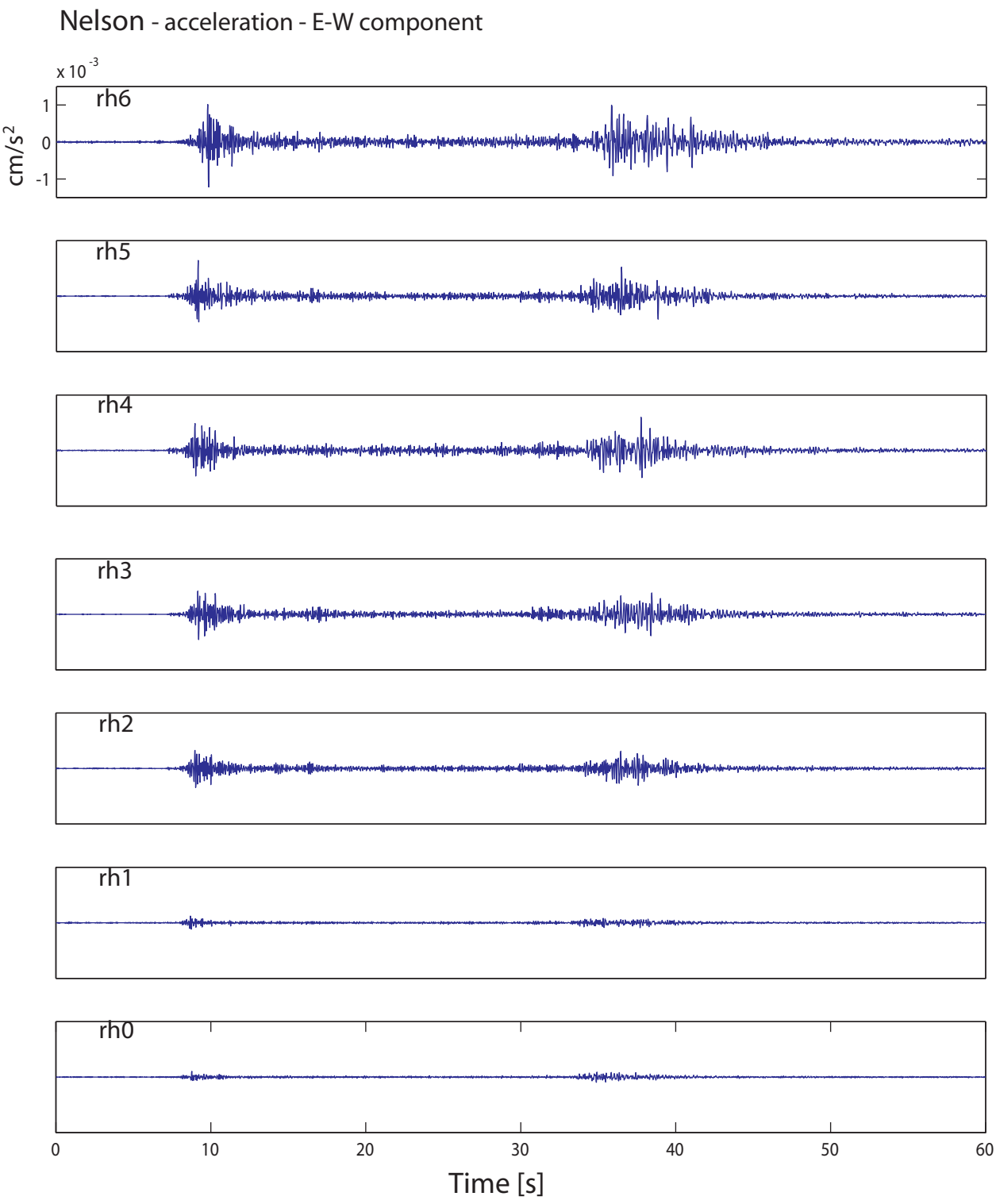
Nelson - acceleration - E-W component
x 10 -3
cm/s2
1
0
-1
rh6
rh5
rh4
rh3
rh2
rh1
rh0
0
10
20
30
40
50
60
Time [s]

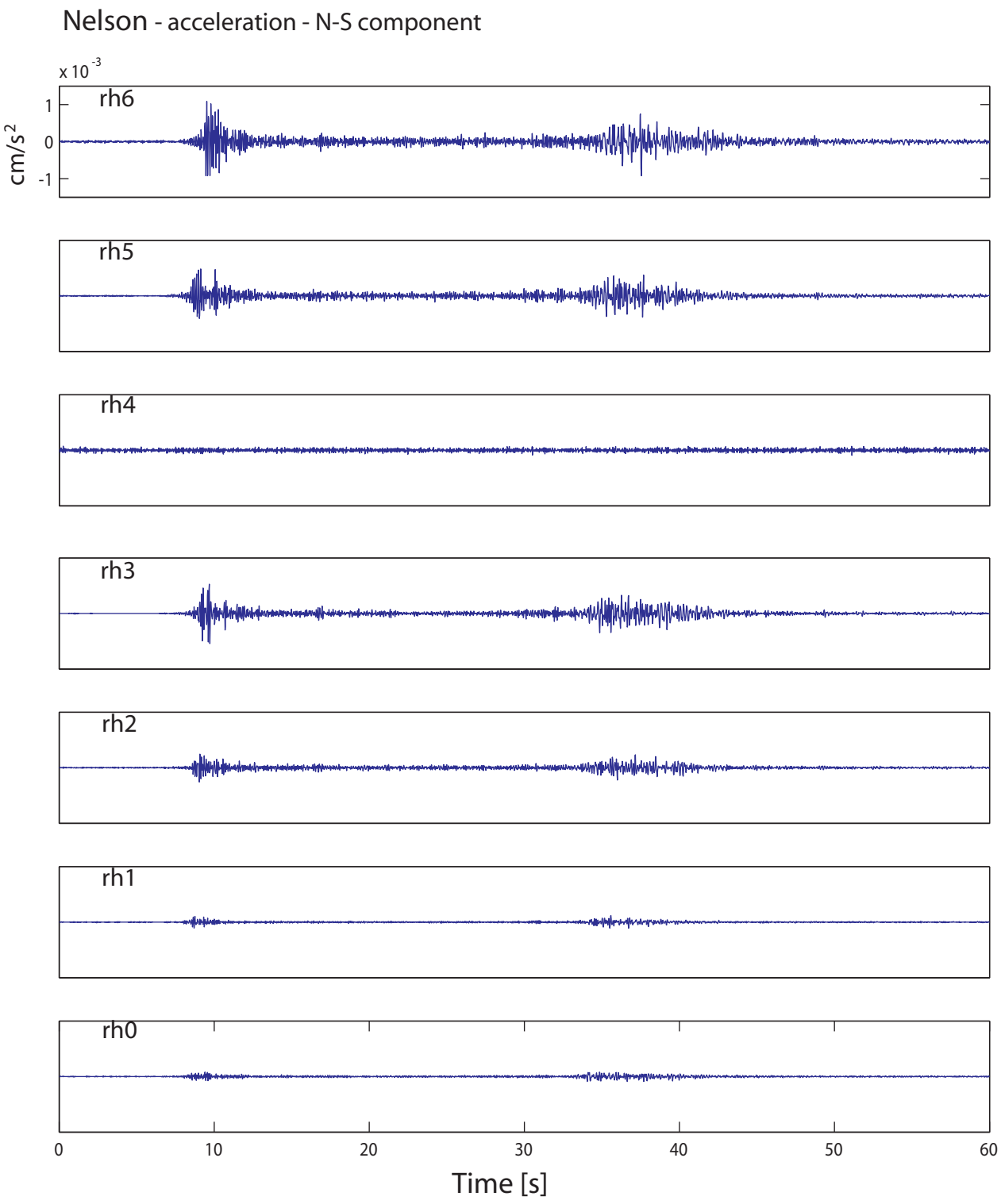
Nelson - acceleration - N-S component
x 10 -3
cm/s2
1
0
-1
rh6
rh5
rh4
rh3
rh2
rh1
rh0
0
10
20
30
40
50
60
Time [s]

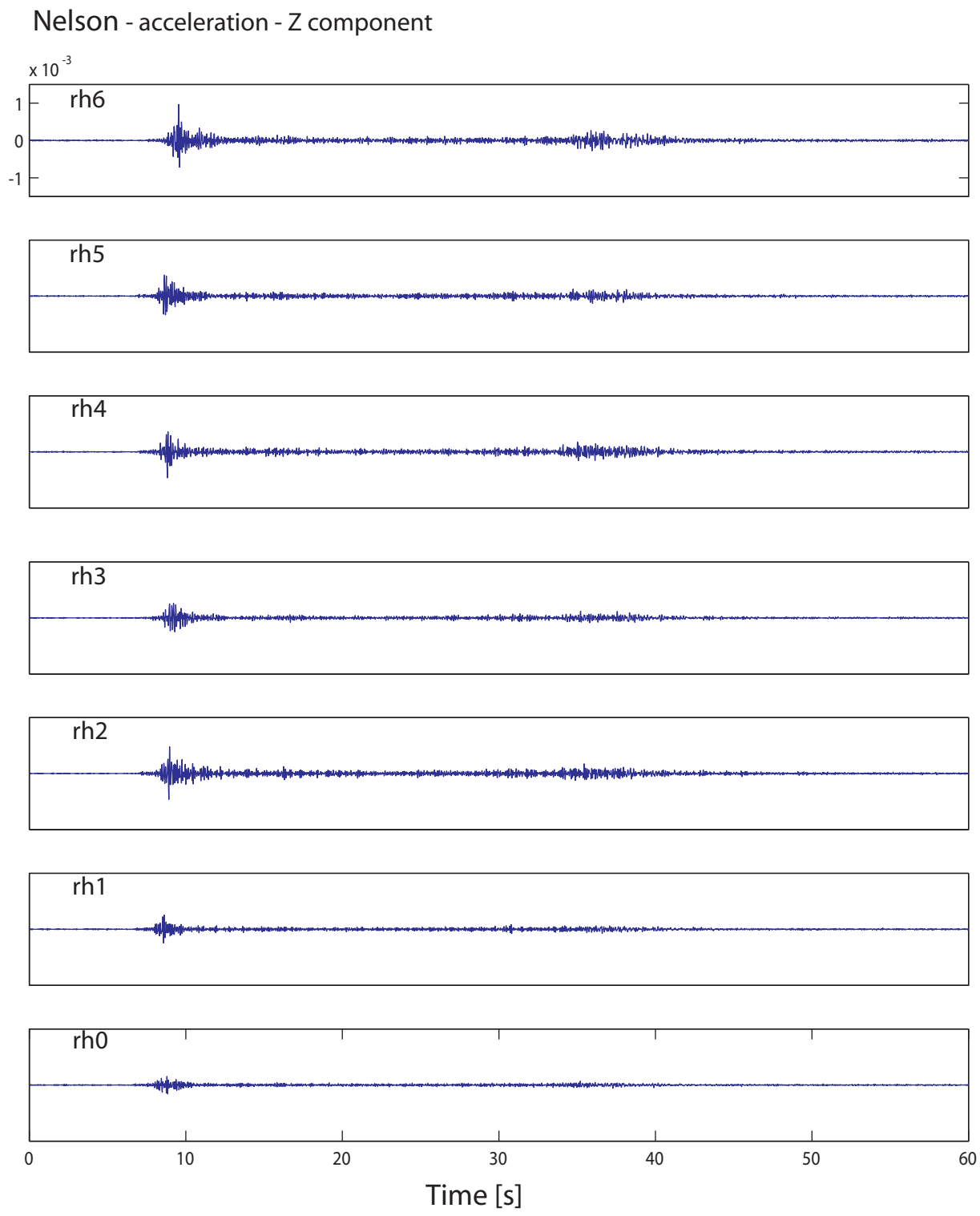
Nelson - acceleration - Z component
x 10 -3
1
0
-1
rh6
rh5
rh4
rh3
rh2
rh1
rh0
0
10
20
30
40
50
60
Time [s]

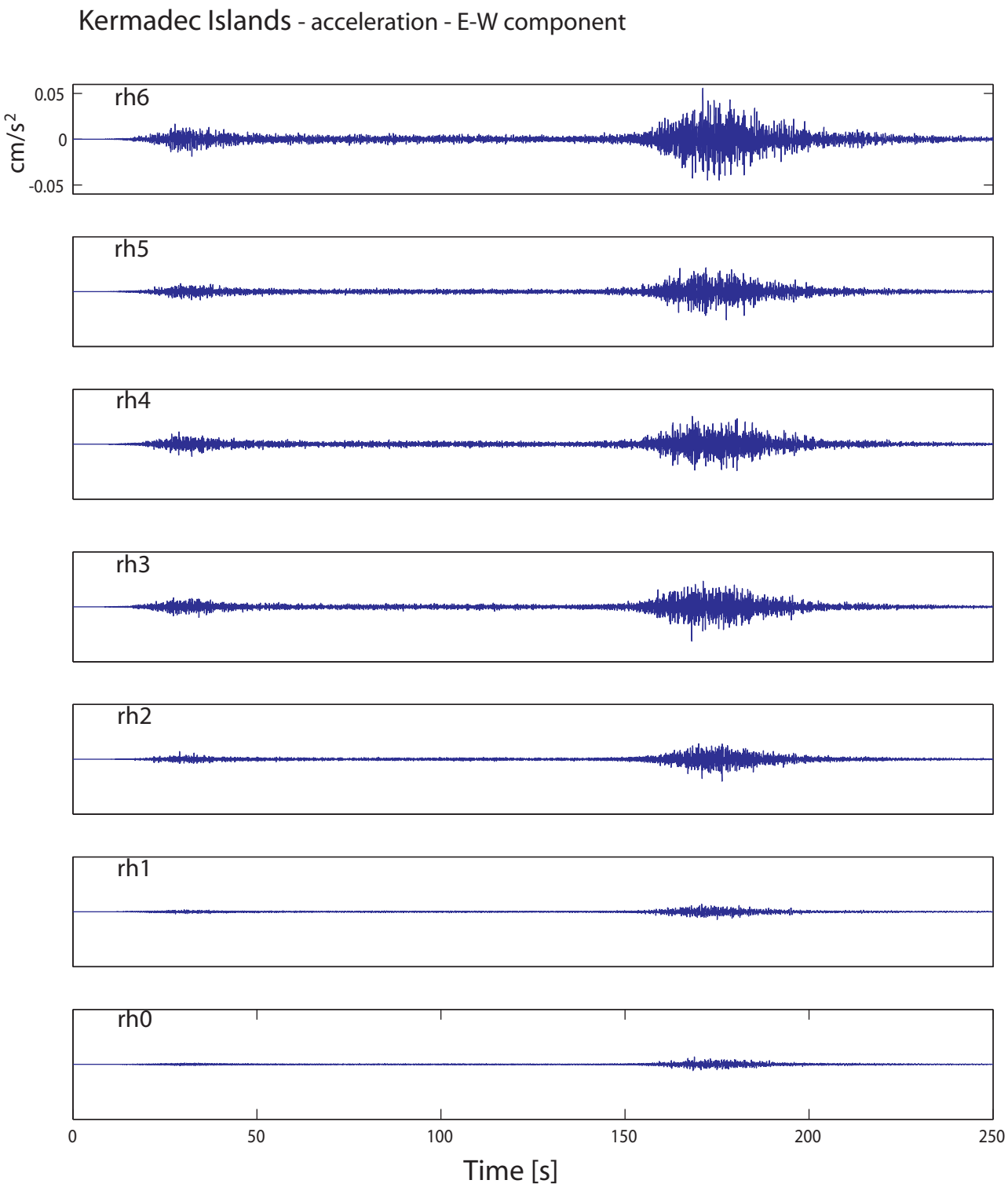
Kermadec Islands - acceleration - E-W component
cm/s2
0.05
0
-0.05
rh6
rh5
rh4
rh3
rh2
rh1
rh0
0
50
100
150
200
250
Time [s]

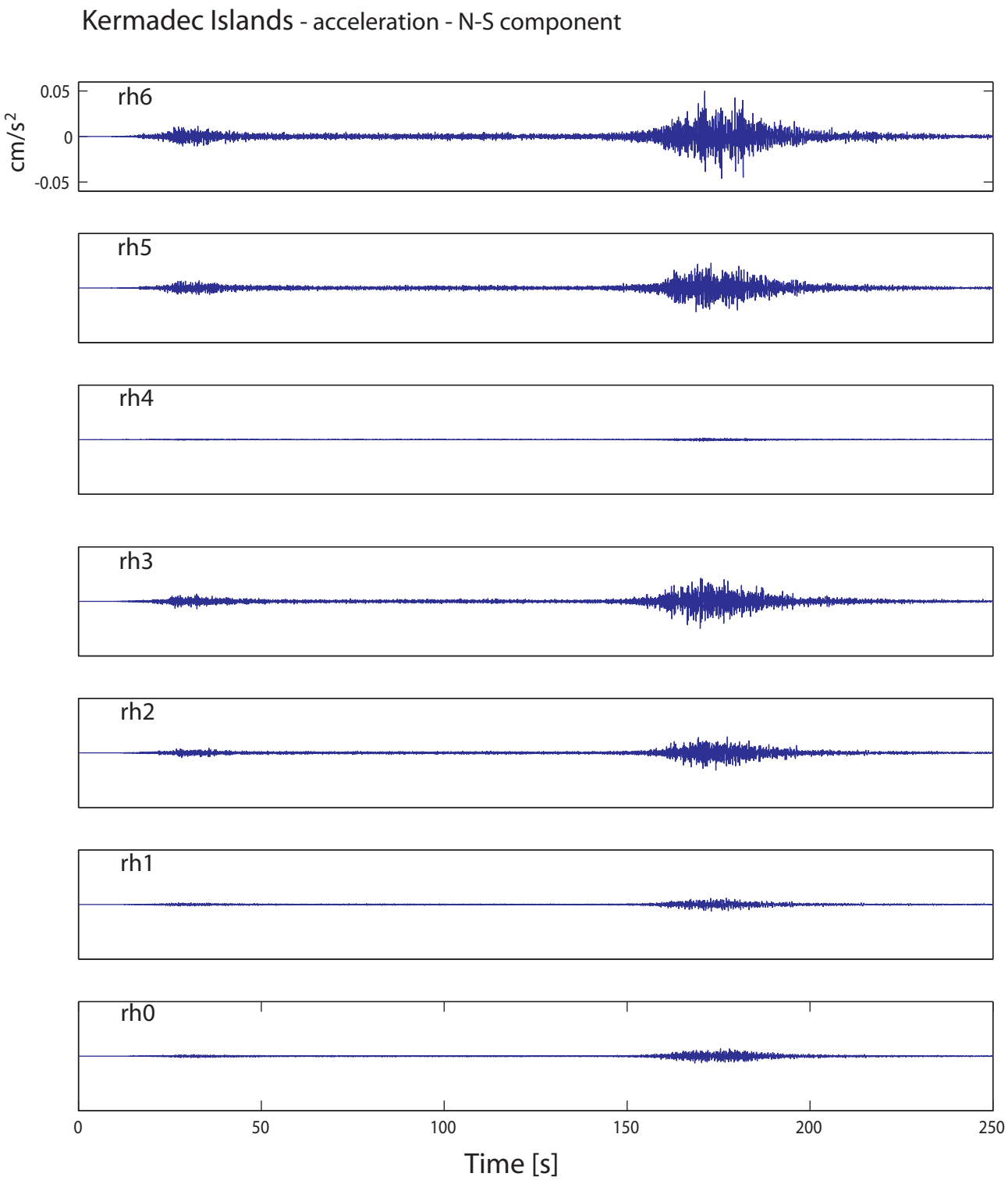
Kermadec Islands - acceleration - N-S component
cm/s2
0.05
0
-0.05
rh6
rh5
rh4
rh3
rh2
rh1
rh0
0
50
100
150
200
250
Time [s]

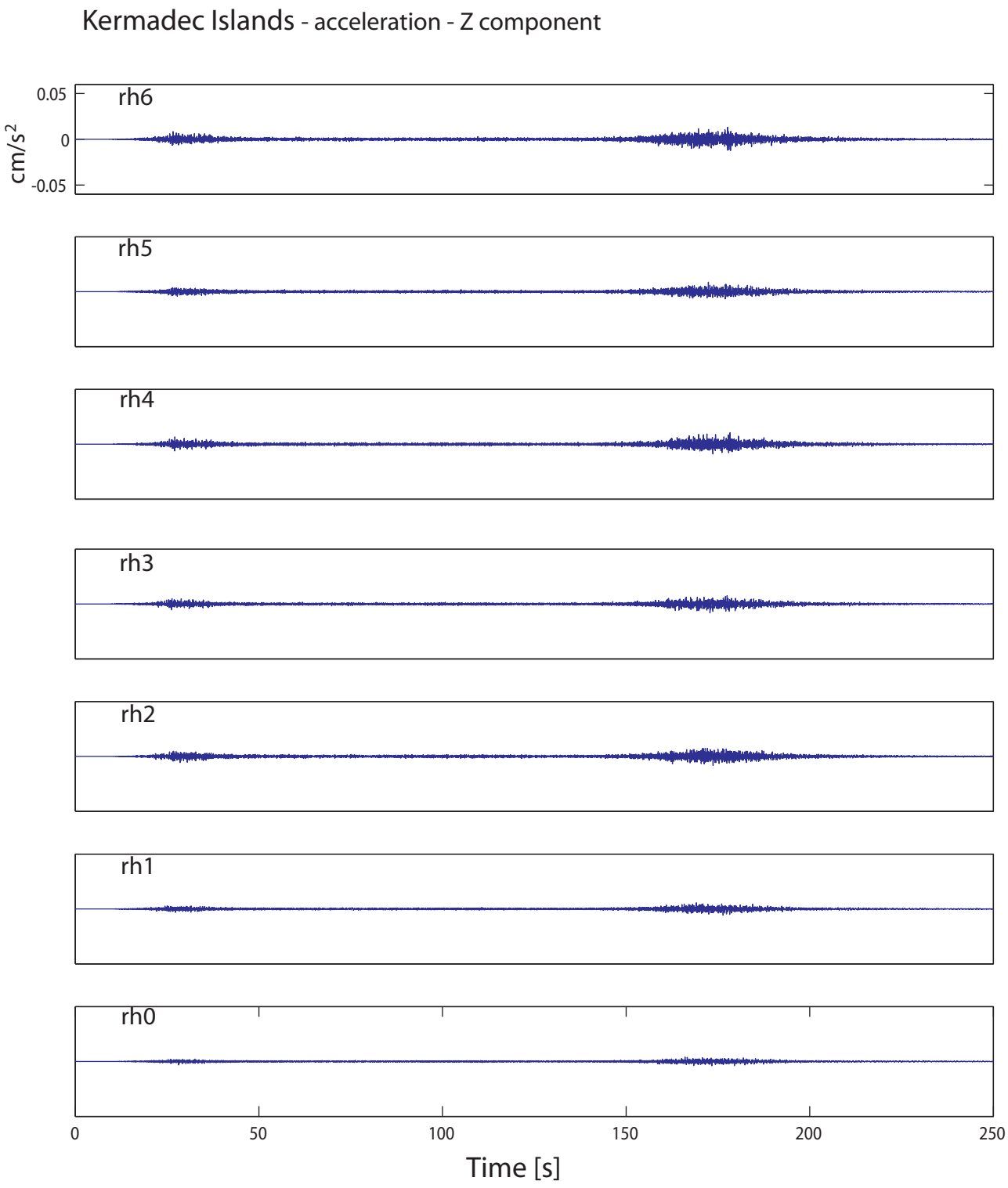
Kermadec Islands - acceleration - Z component
cm/s2
0.05
0
-0.05
rh6
rh5
rh4
rh3
rh2
rh1
rh0
0
50
100
150
200
250
Time [s]

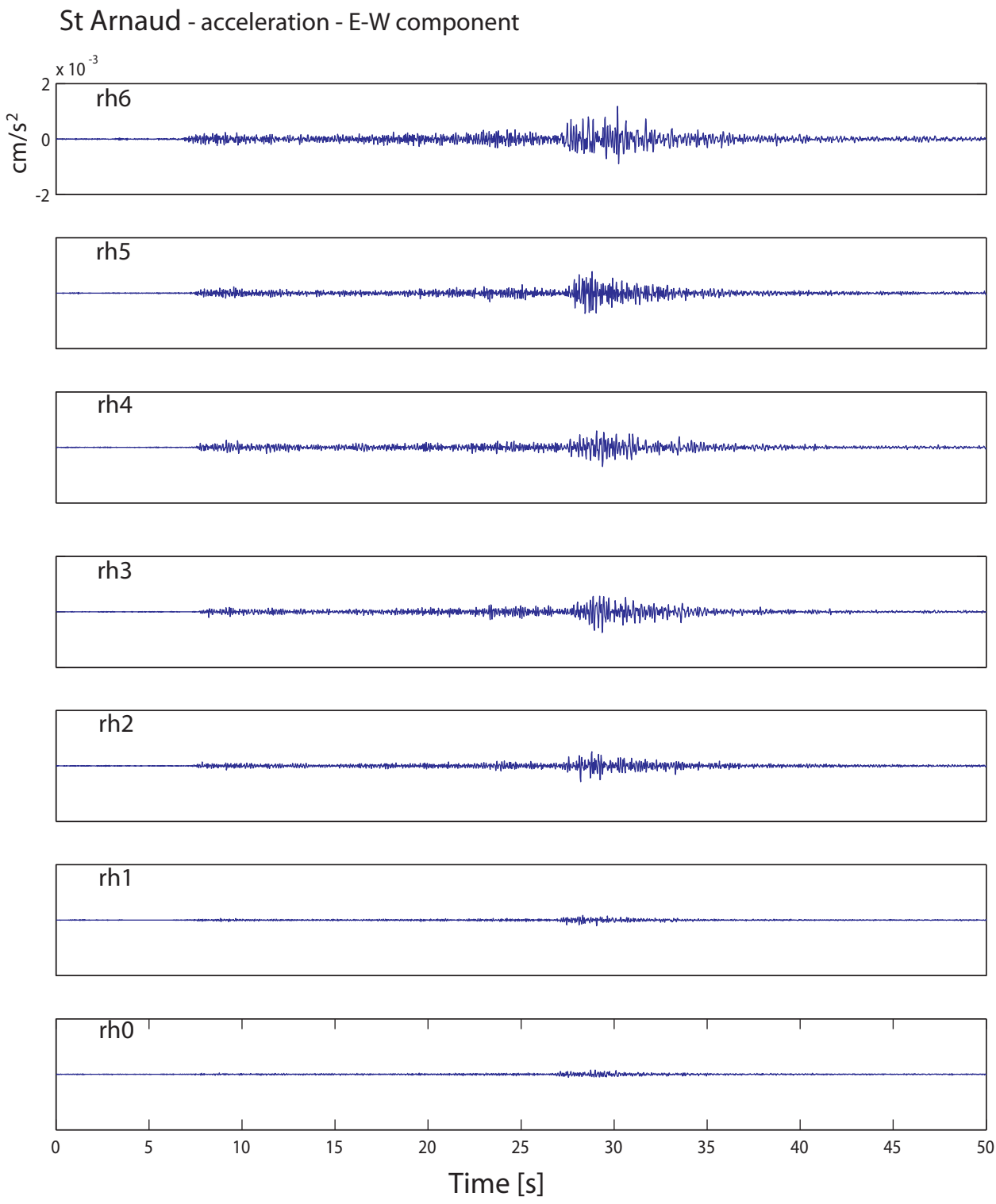
St Arnaud - acceleration - E-W component
x 10 -3
2
0
-2
cm/s2
rh6
rh5
rh4
rh3
rh2
rh1
rh0
0
5
10
15
20
25
30
35
40
45
50
Time [s]

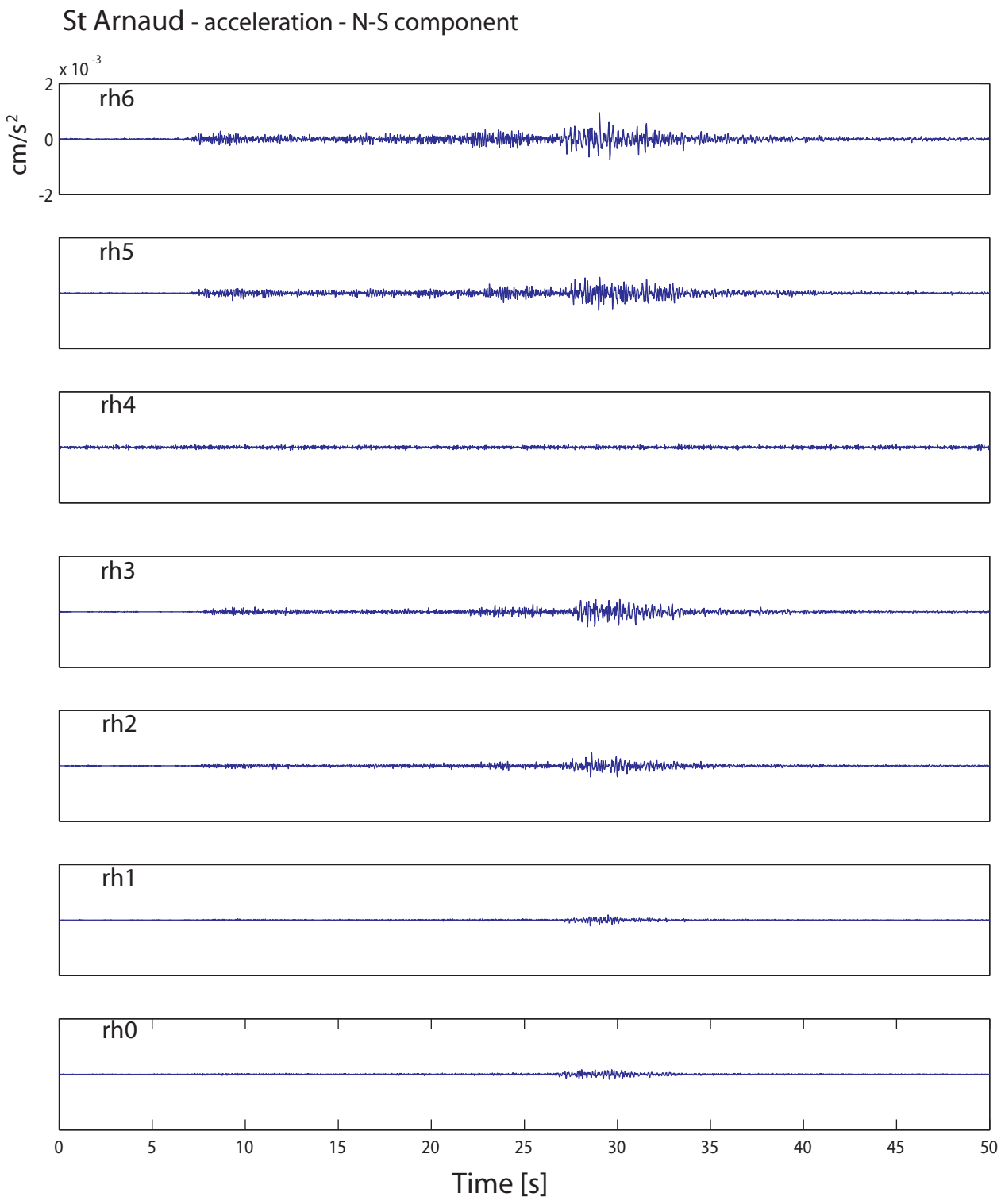
St Arnaud - acceleration - N-S component
x 10 -3
2
0
-2
cm/s2
rh6
rh5
rh4
rh3
rh2
rh1
rh0
0
5
10
15
20
25
30
35
40
45
50
Time [s]

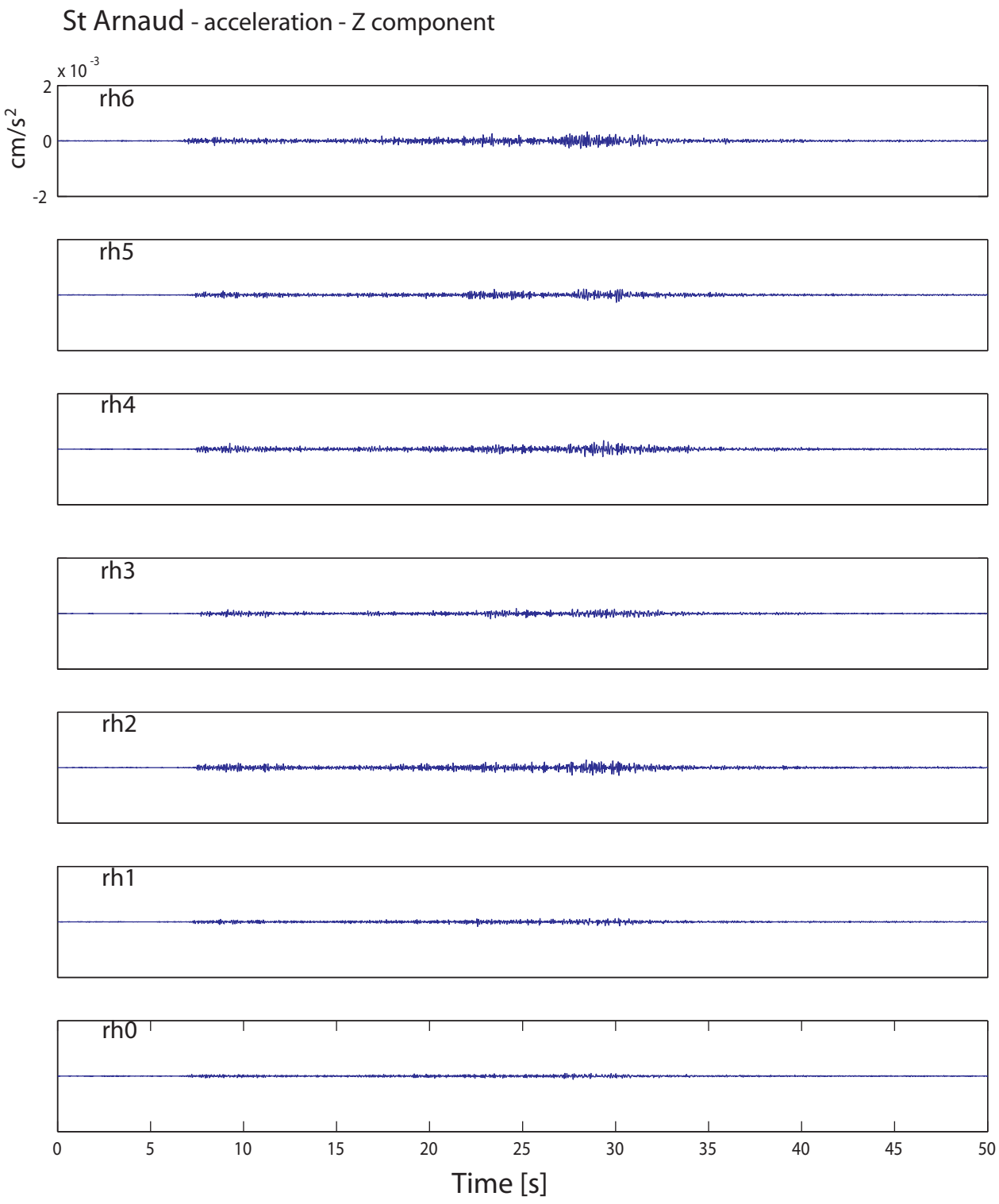
St Arnaud - acceleration - Z component
x 10 -3
2
0
-2
cm/s2
rh6
rh5
rh4
rh3
rh2
rh1
rh0
0
5
10
15
20
25
30
35
40
45
50
Time [s]

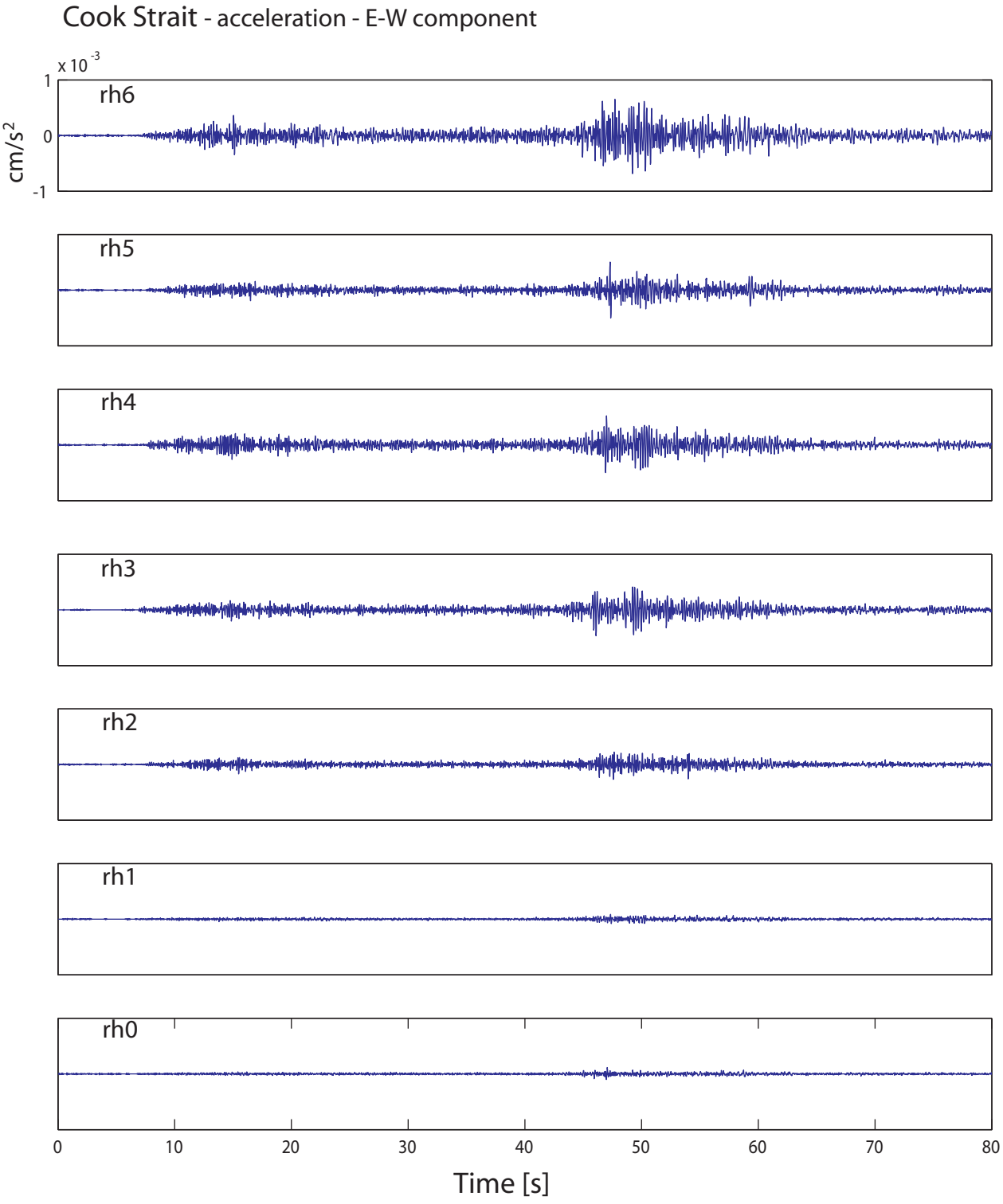
Cook Strait - acceleration - E-W component
x 10 -3
cm/s2
1
0
-1
rh6
rh5
rh4
rh3
rh2
rh1
rh0
0
10
20
30
40
50
60
70
80
Time [s]

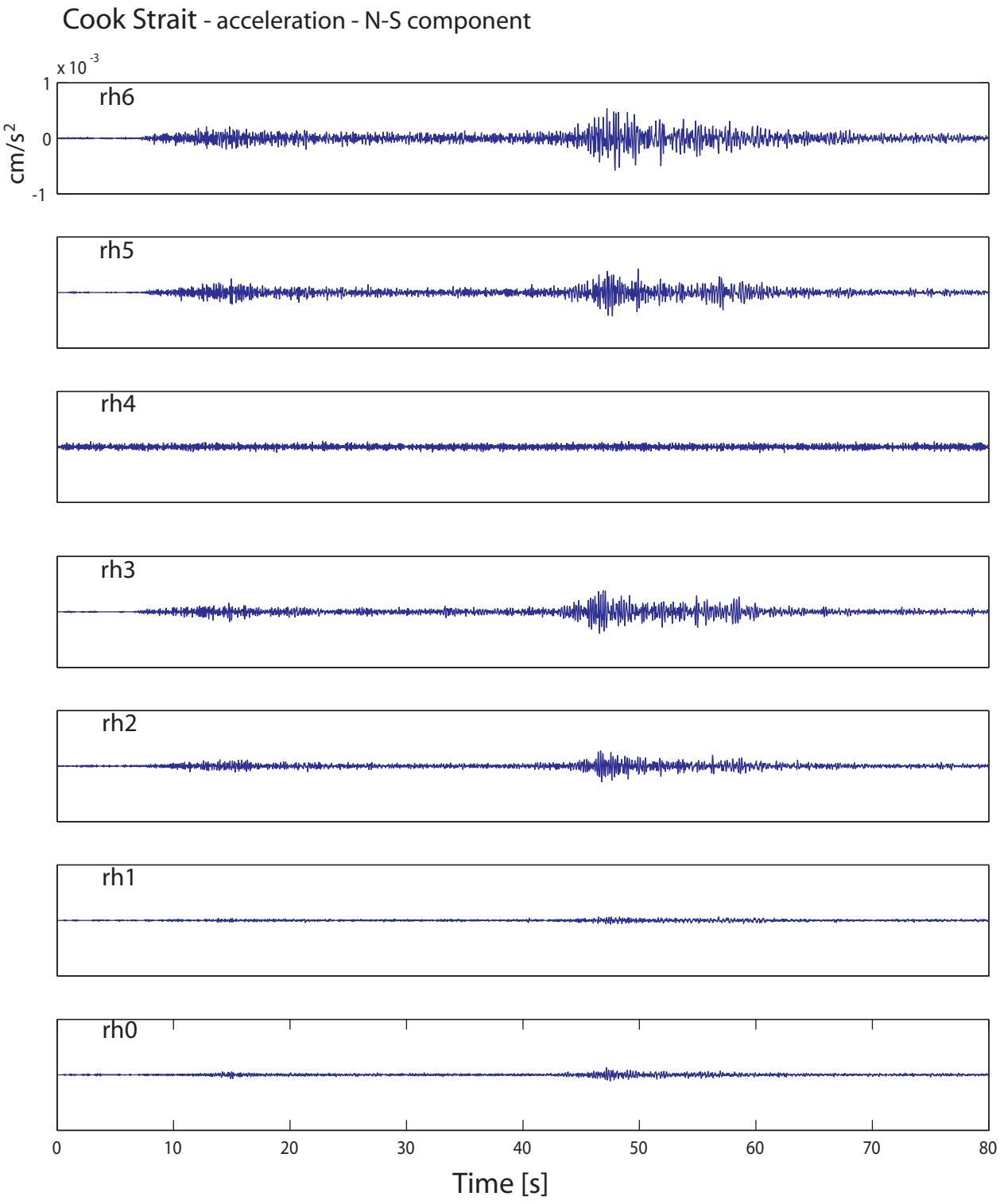
Cook Strait - acceleration - N-S component
x 10 -3
cm/s2
1
0
-1
rh6
rh5
rh4
rh3
rh2
rh1
rh0
0
10
20
30
40
50
60
70
80
Time [s]

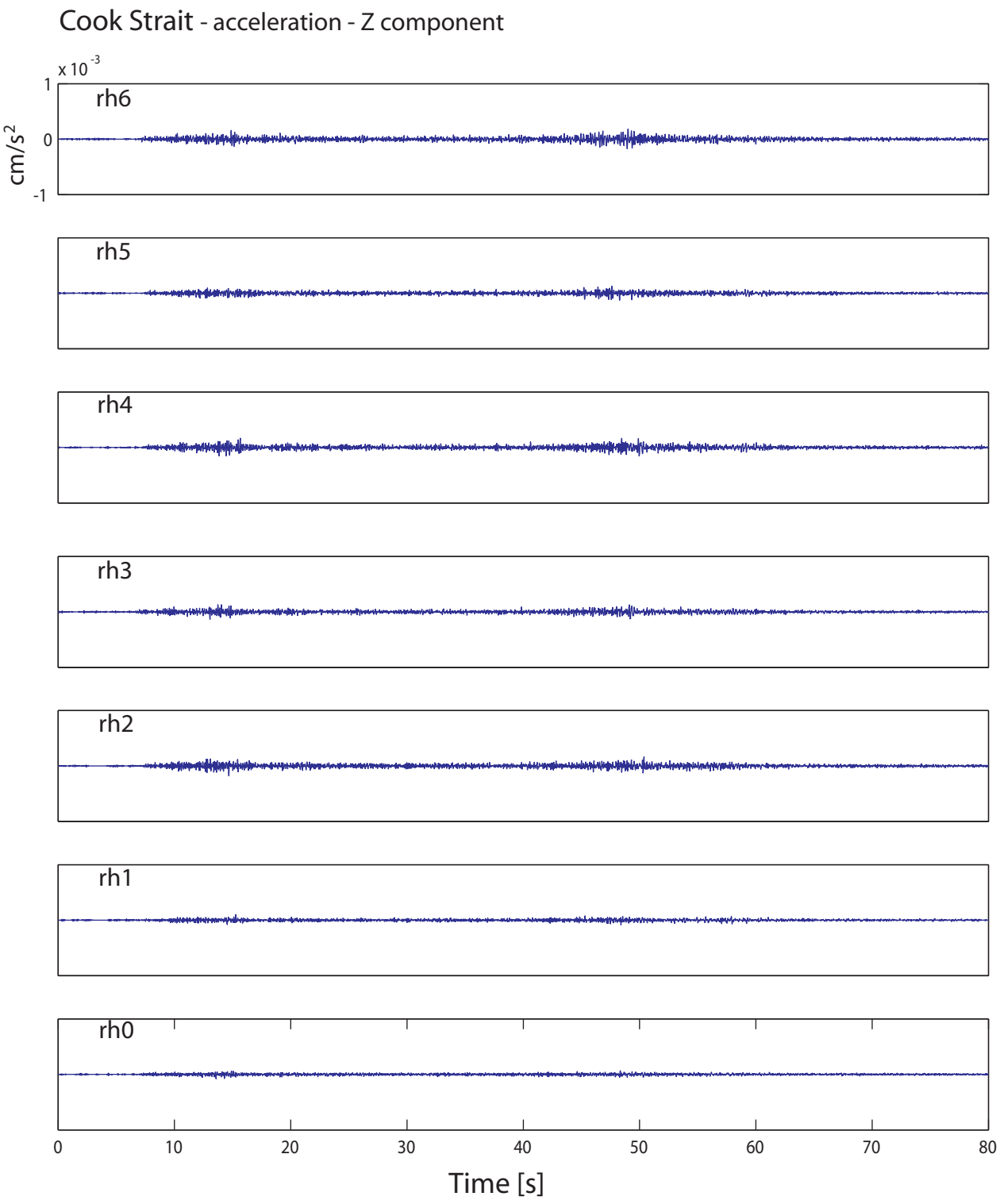
Cook Strait - acceleration - Z component
x 10 -3
cm/s2
1
0
-1
rh6
rh5
rh4
rh3
rh2
rh1
rh0
0
10
20
30
40
50
60
70
80
Time [s]

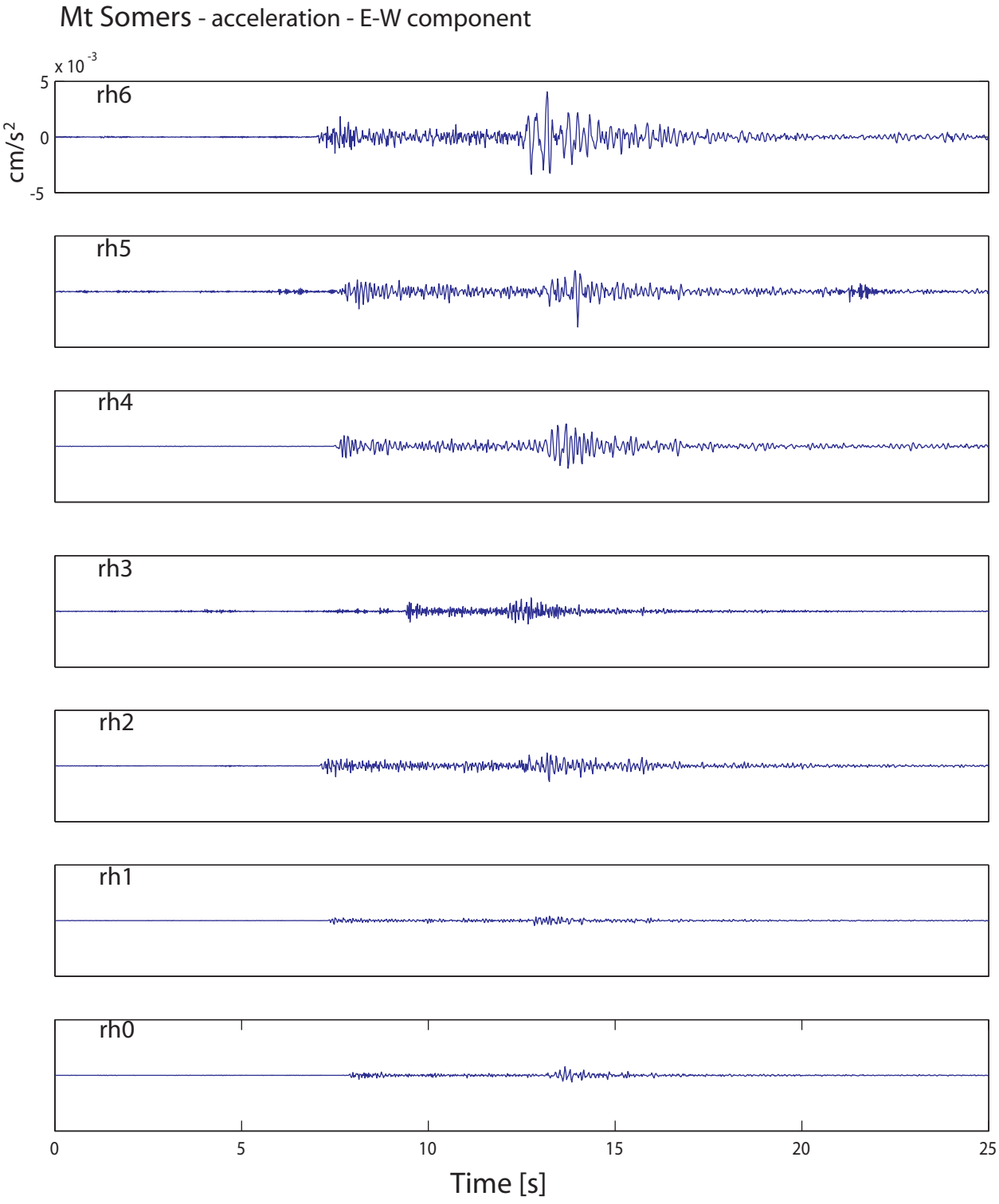
Mt Somers - acceleration - E-W component
x 10 -3
5
0
-5
cm/s2
rh6
rh5
rh4
rh3
rh2
rh1
rh0
0
5
10
15
20
25
Time [s]

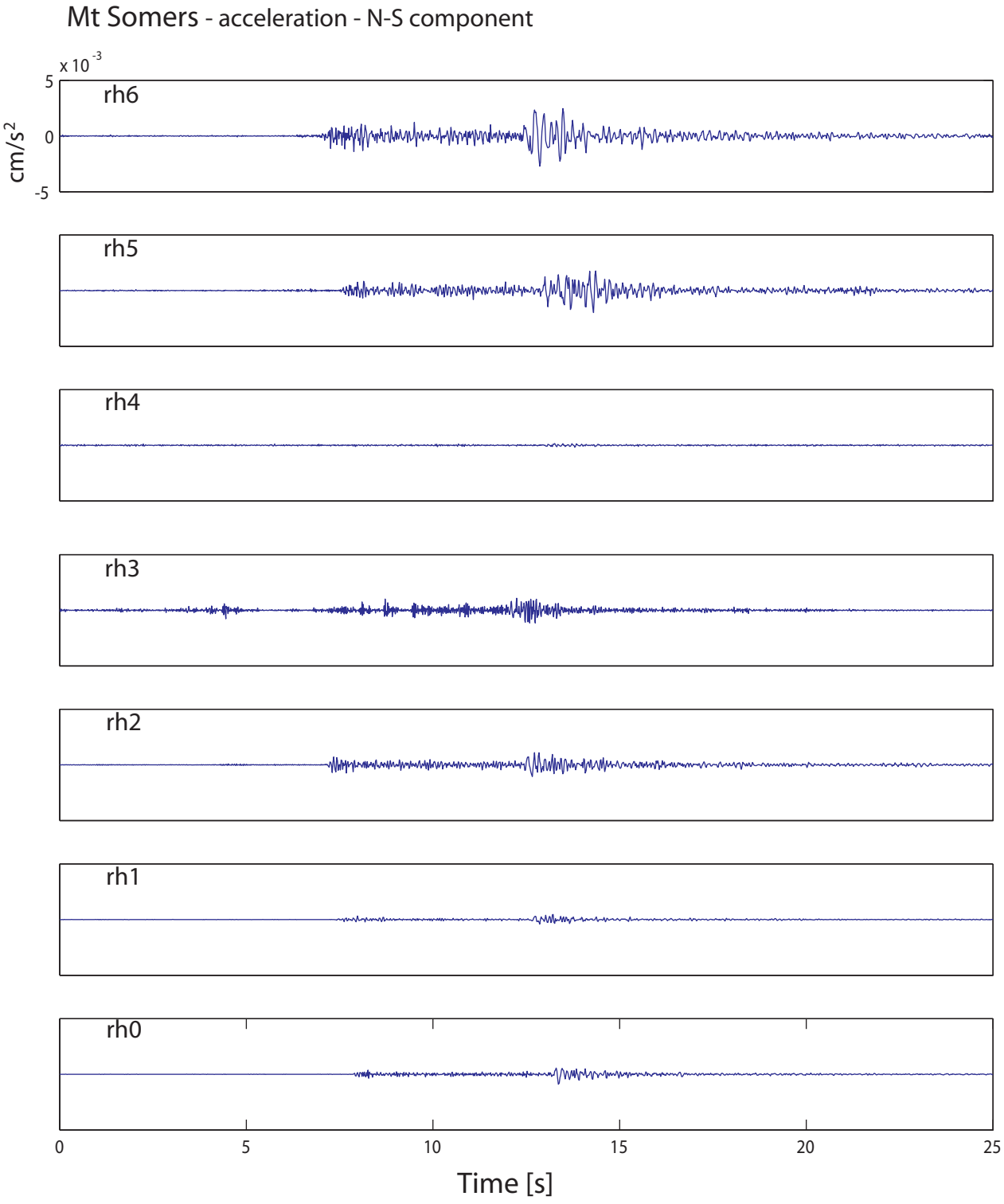
Mt Somers - acceleration - N-S component
x 10 -3
cm/s2
5
0
-5
rh6
rh5
rh4
rh3
rh2
rh1
rh0
0
5
10
15
20
25
Time [s]

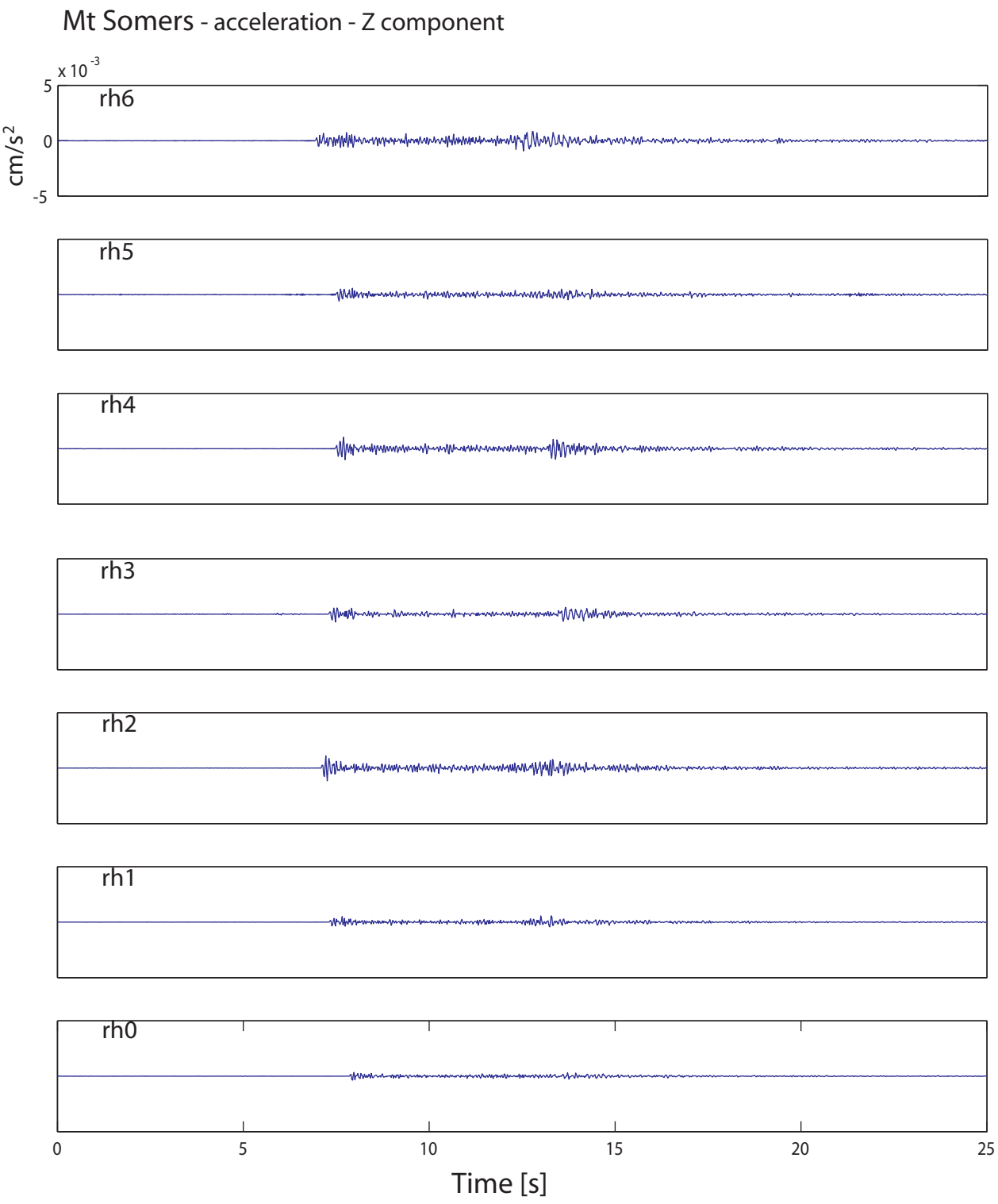
Mt Somers - acceleration - Z component
x 10 -3
5
0
-5
cm/s2
rh6
rh5
rh4
rh3
rh2
rh1
rh0
0
5
10
15
20
25
Time [s]

Appendix A.3

Little Red Hill Field Experiment – Pseudo Spectral Density Plots

Appendix A.3 Little Red Hill - Pseudo Spectral Density plots

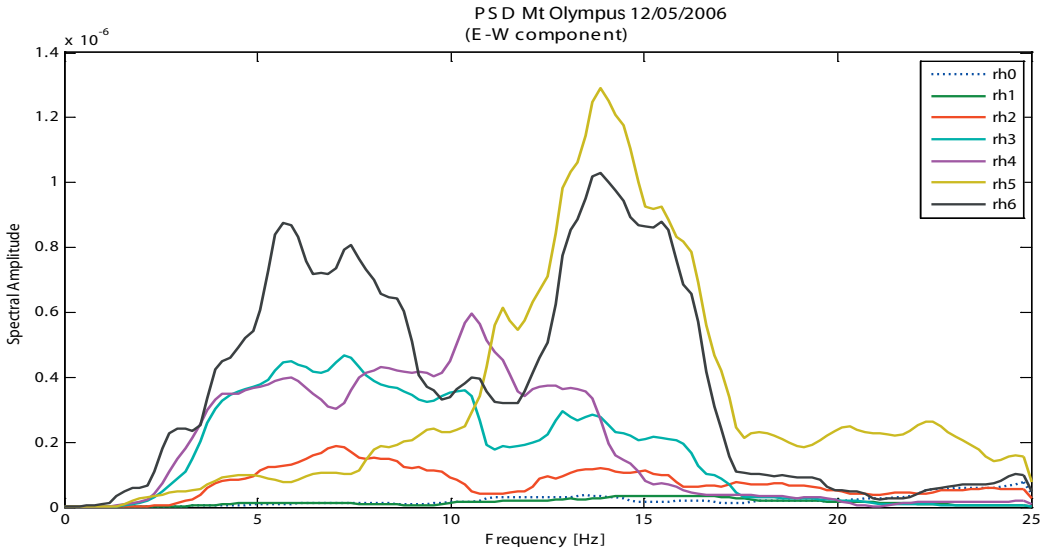

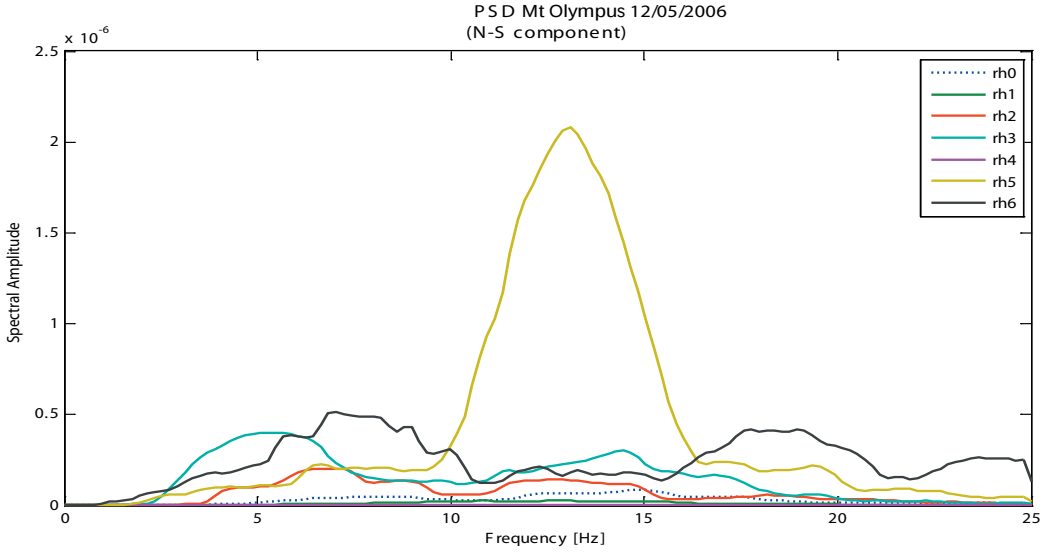

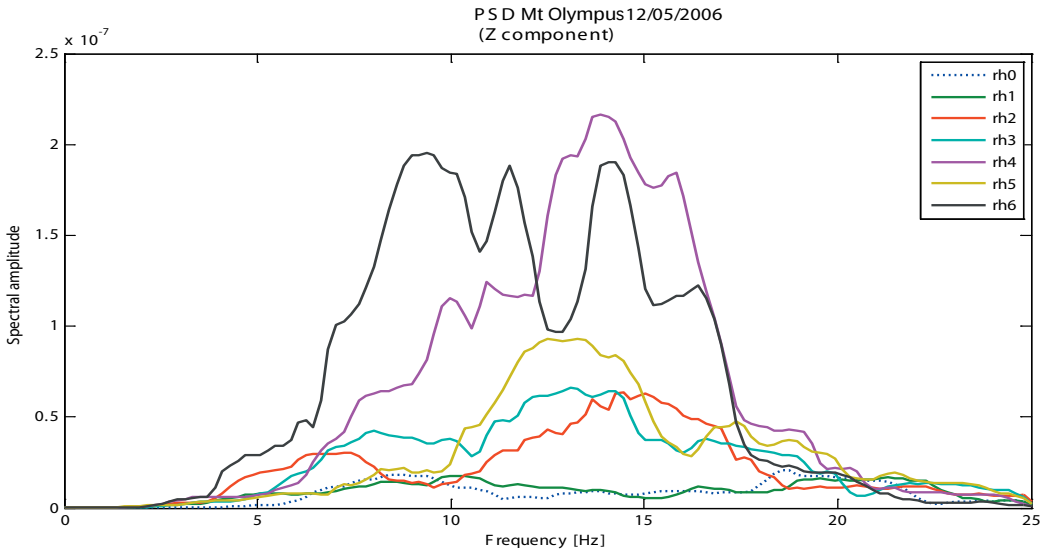

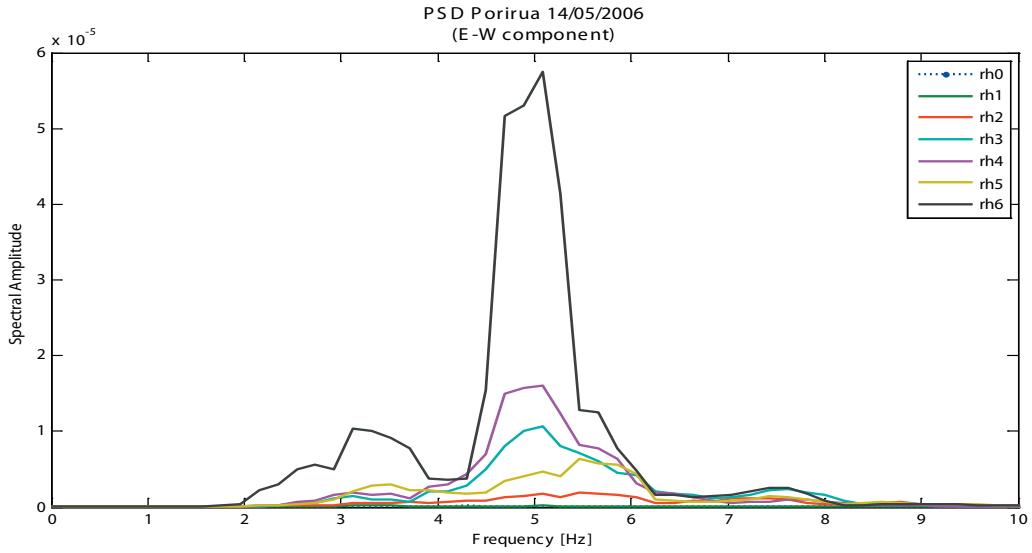
PSD Porirua 14/05/2006
(E-W component)
x 10^-5
Spectral Amplitude
Frequency [Hz]
rh0
rh1
rh2
rh3
rh4
rh5
rh6

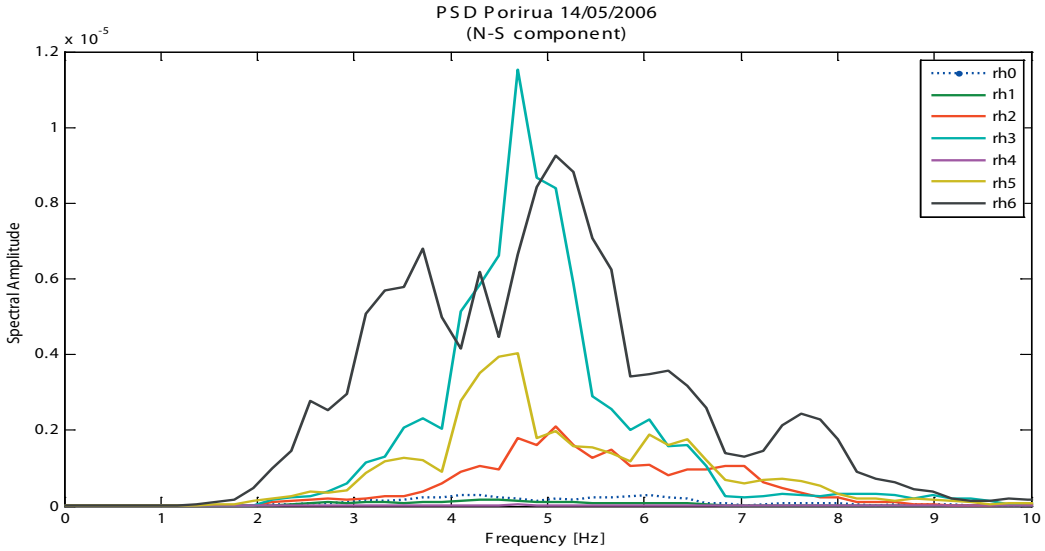
PSD Porirua 14/05/2006
(N-S component)
x 10^-5
Spectral Amplitude
Frequency [Hz]
rh0
rh1
rh2
rh3
rh4
rh5
rh6

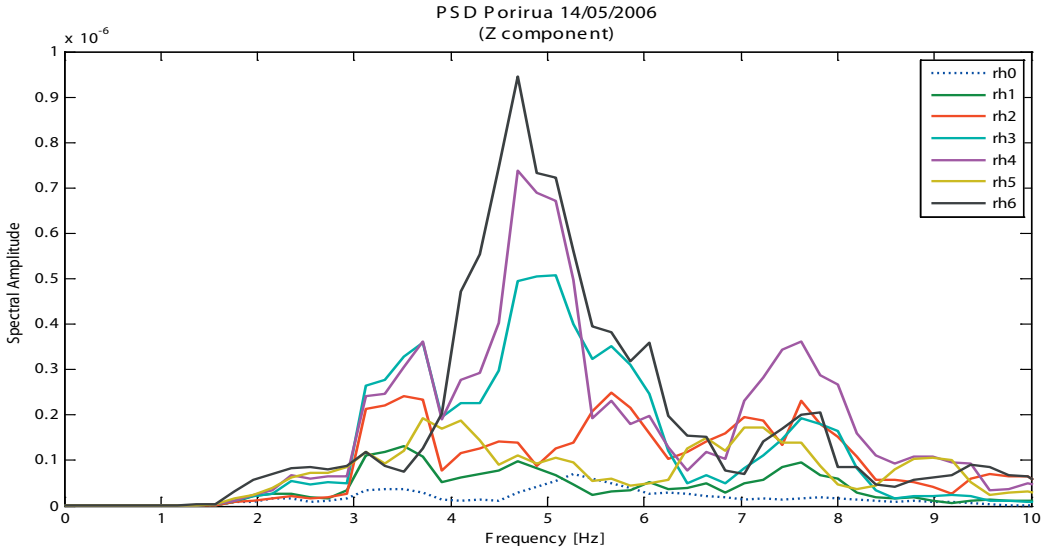
PSD Porirua 14/05/2006
(Z component)
x 10^-6
Spectral Amplitude
Frequency [Hz]
rh0
rh1
rh2
rh3
rh4
rh5
rh6

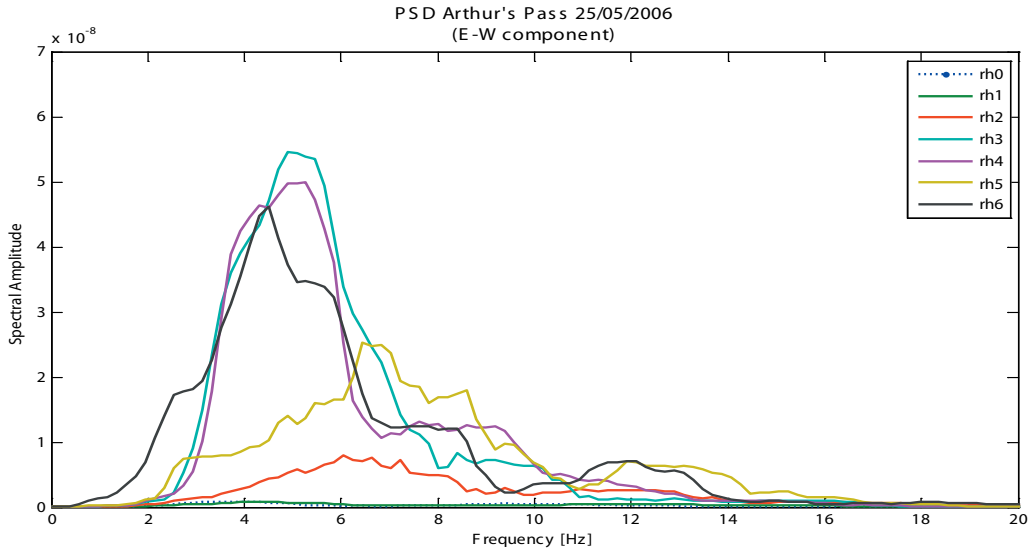
PSD Arthur's Pass 25/05/2006
(E-W component)
x 10^-8
Spectral Amplitude
Frequency [Hz]
rh0
rh1
rh2
rh3
rh4
rh5
rh6

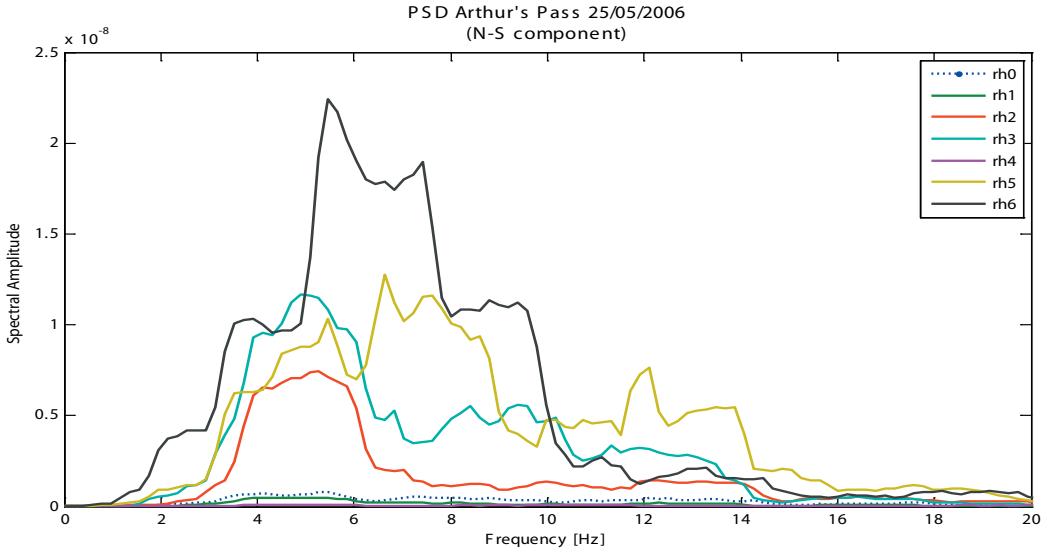
PSD Arthur's Pass 25/05/2006
(N-S component)
x 10^-8
Spectral Amplitude
Frequency [Hz]
rh0
rh1
rh2
rh3
rh4
rh5
rh6

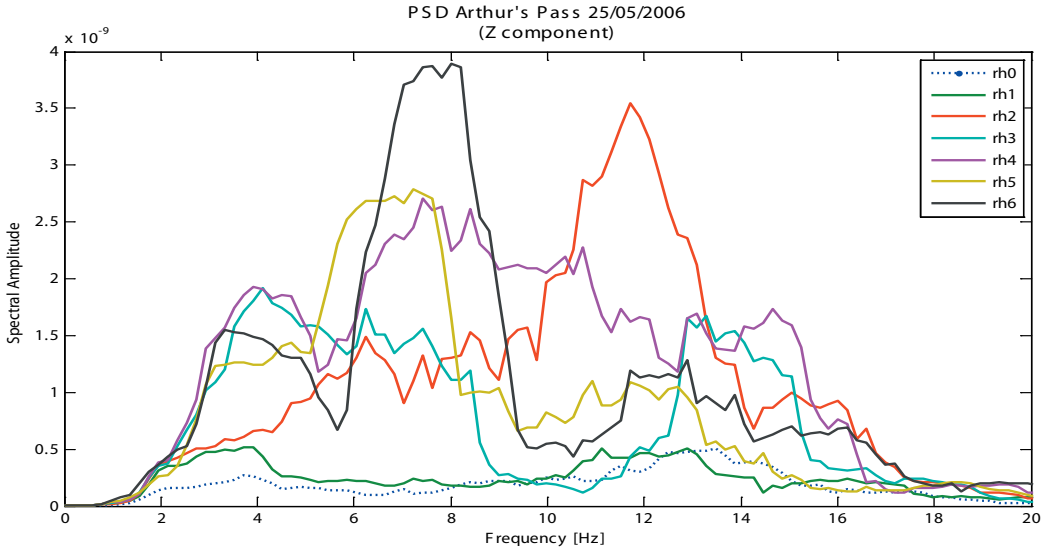
PSD Arthur's Pass 25/05/2006
(Z component)
x 10^-9
Spectral Amplitude
Frequency [Hz]
rh0
rh1
rh2
rh3
rh4
rh5
rh6

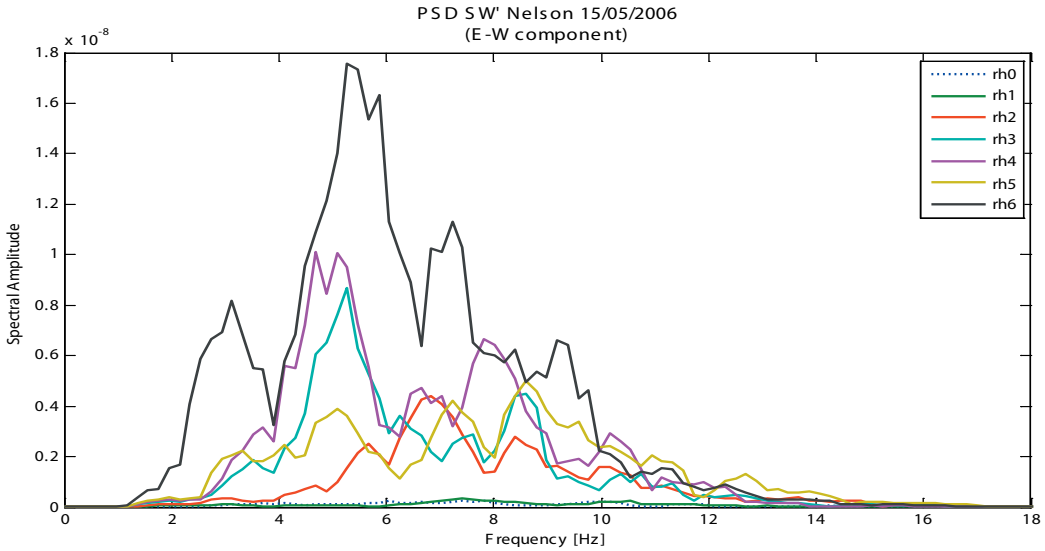
PSD SW' Nelson 15/05/2006
(E-W component)
x 10^-8
Spectral Amplitude
Frequency [Hz]
rh0
rh1
rh2
rh3
rh4
rh5
rh6

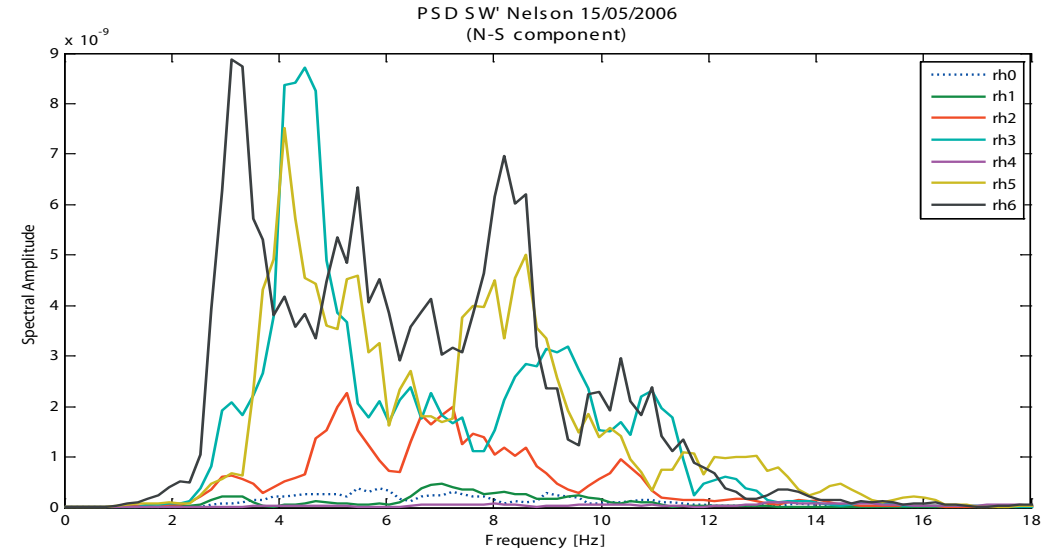
PSD SW' Nelson 15/05/2006
(N-S component)
x 10^-9
Spectral Amplitude
Frequency [Hz]
rh0
rh1
rh2
rh3
rh4
rh5
rh6

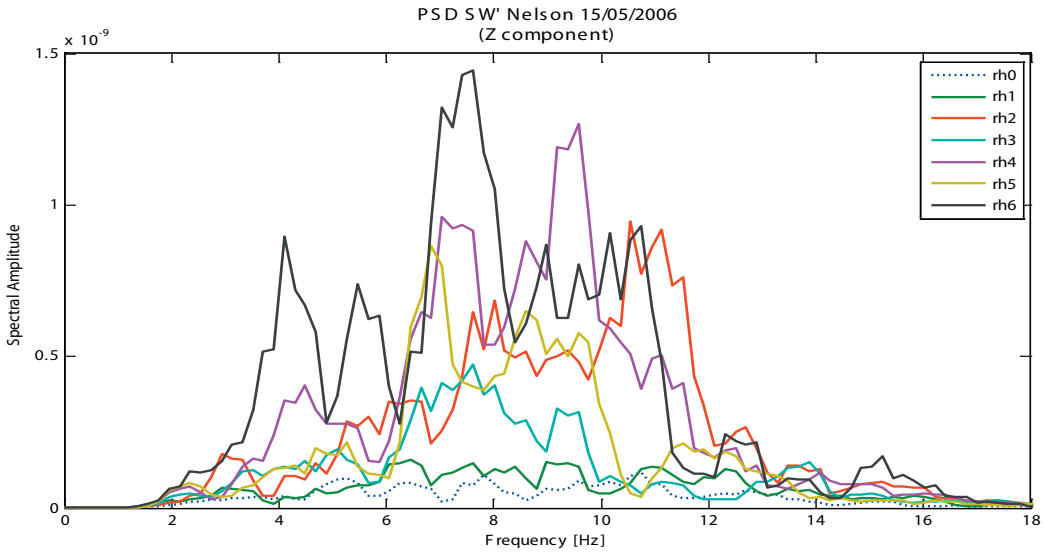
PSD SW' Nelson 15/05/2006
(Z component)
x 10^-9
Spectral Amplitude
Frequency [Hz]
rh0
rh1
rh2
rh3
rh4
rh5
rh6

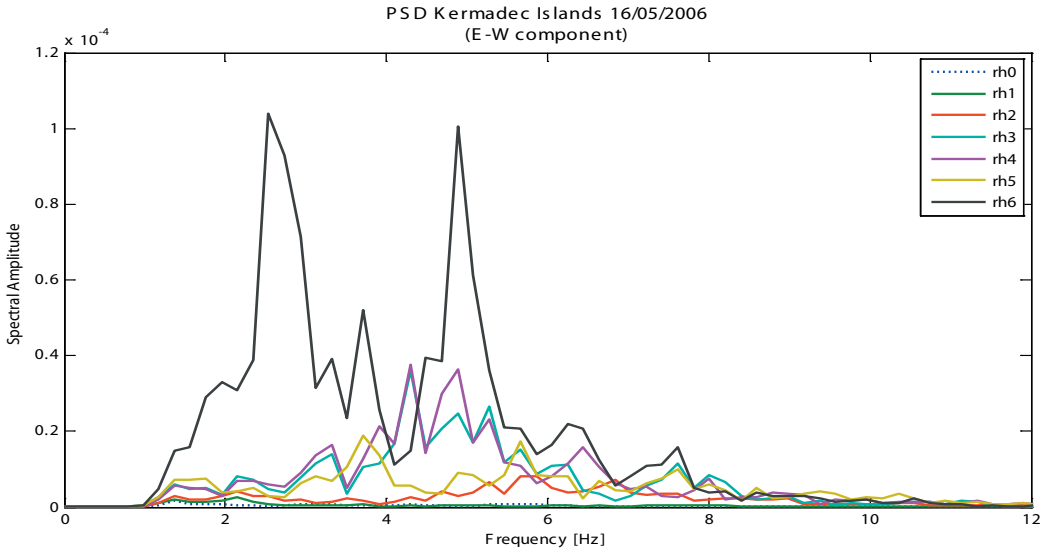
PSD Kermadec Islands 16/05/2006
(E-W component)
x 10^-4
Spectral Amplitude
Frequency [Hz]
rh0
rh1
rh2
rh3
rh4
rh5
rh6

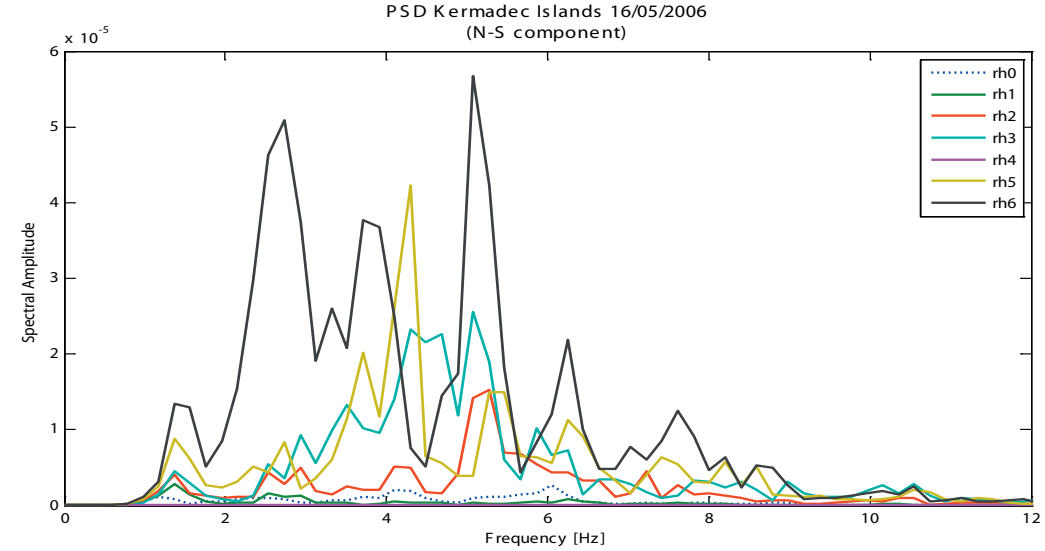
PSD Kermadec Islands 16/05/2006
(N-S component)
x 10^-5
Spectral Amplitude
Frequency [Hz]
rh0
rh1
rh2
rh3
rh4
rh5
rh6

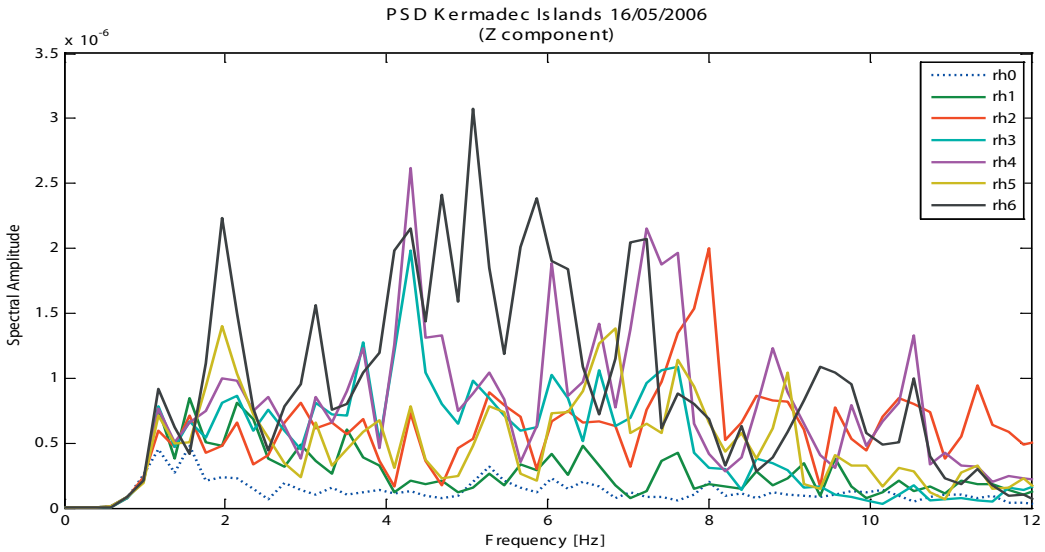
PSD Kermadec Islands 16/05/2006
(Z component)
x 10^-6
Spectral Amplitude
Frequency [Hz]
rh0
rh1
rh2
rh3
rh4
rh5
rh6

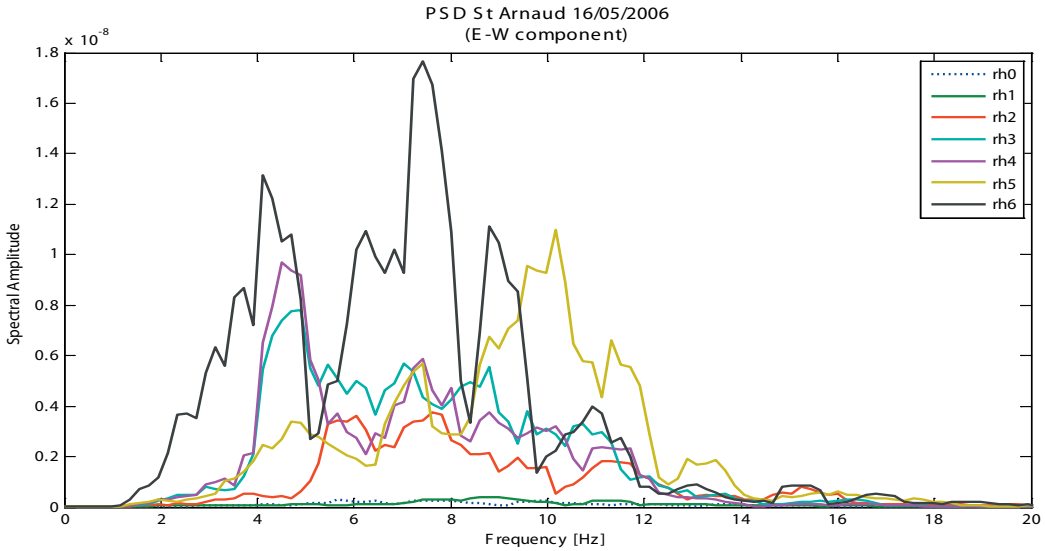
PSD St Arnaud 16/05/2006
(E-W component)
x 10^-8
Spectral Amplitude
Frequency [Hz]
rh0
rh1
rh2
rh3
rh4
rh5
rh6

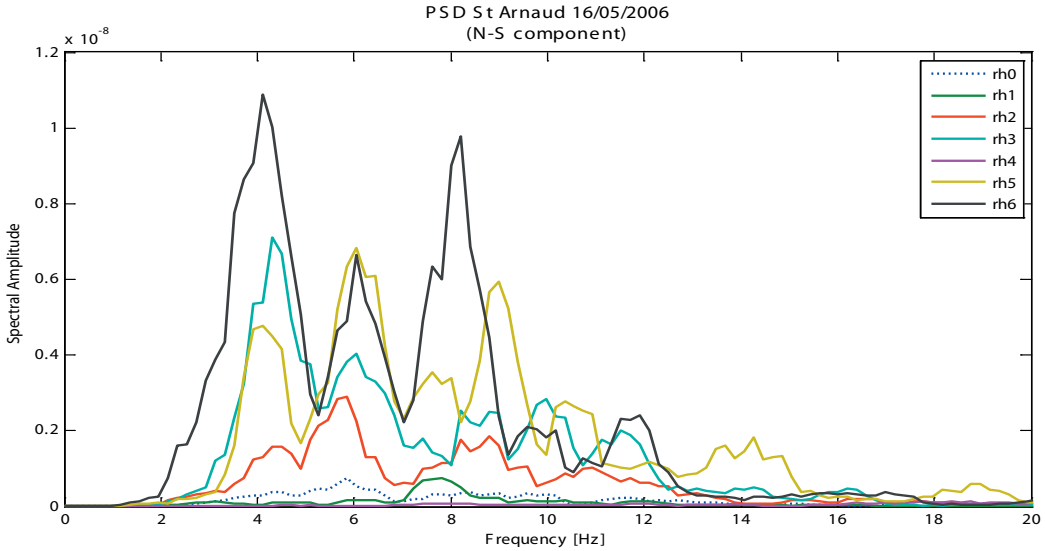
PSD St Arnaud 16/05/2006
(N-S component)
x 10^-8
Spectral Amplitude
Frequency [Hz]
rh0
rh1
rh2
rh3
rh4
rh5
rh6

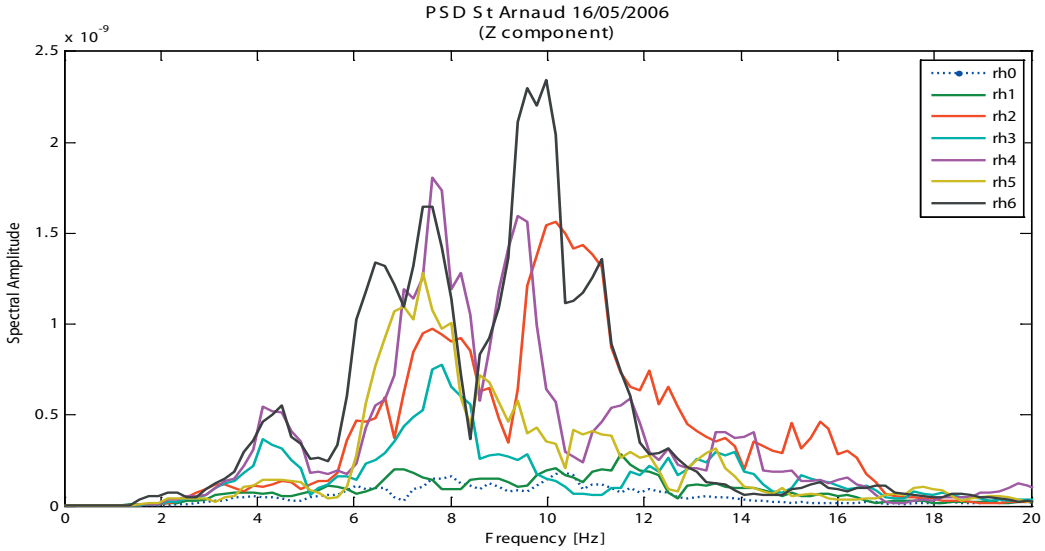
PSD St Arnaud 16/05/2006
(Z component)
x 10^-9
Spectral Amplitude
Frequency [Hz]
rh0
rh1
rh2
rh3
rh4
rh5
rh6

Appendix A.3 Little Red Hill - Pseudo Spectral Density plots

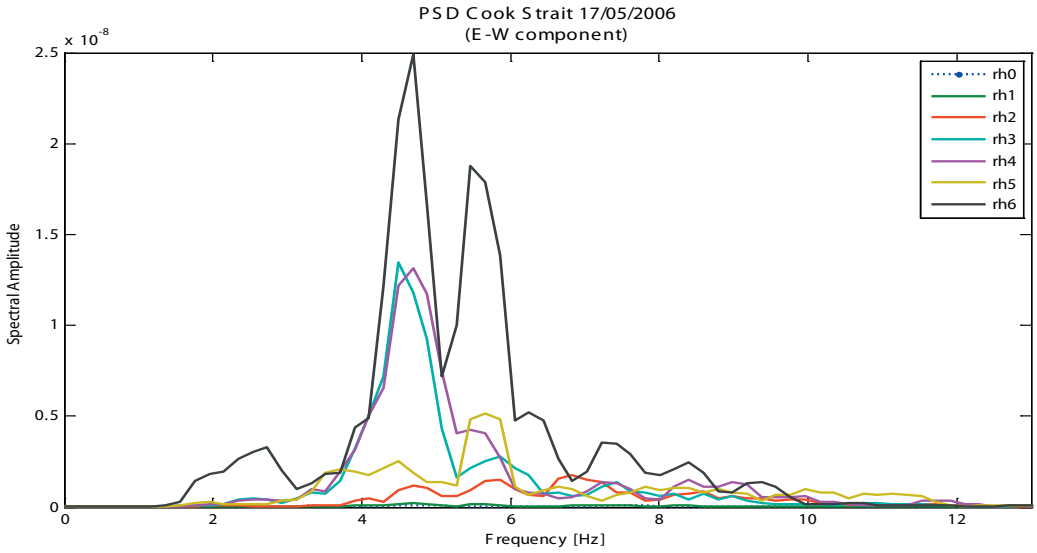

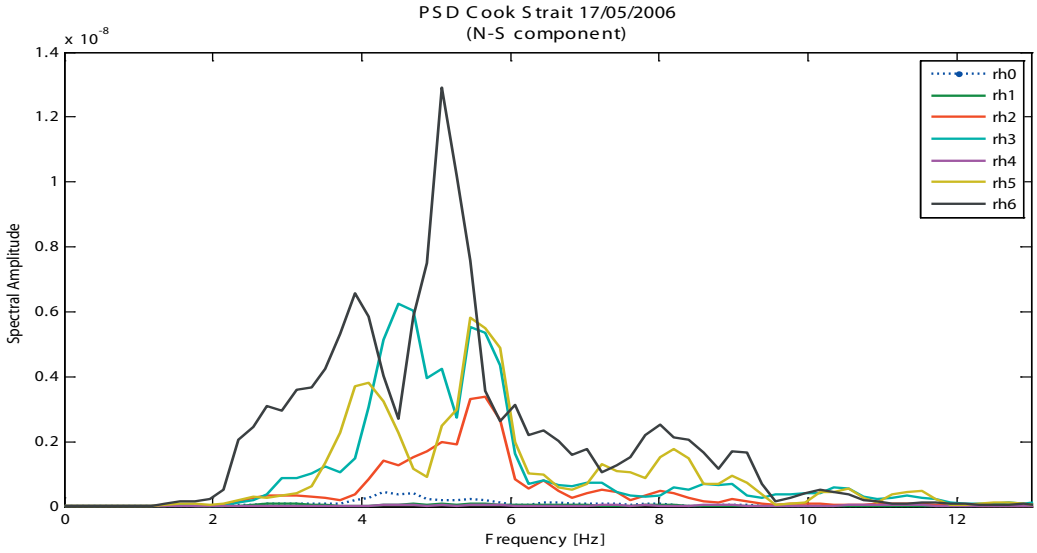

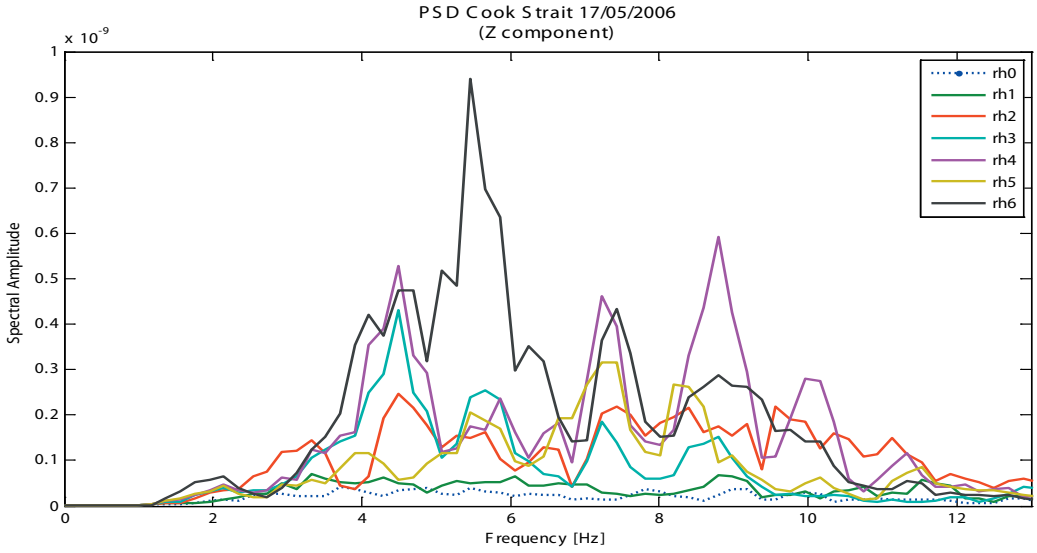

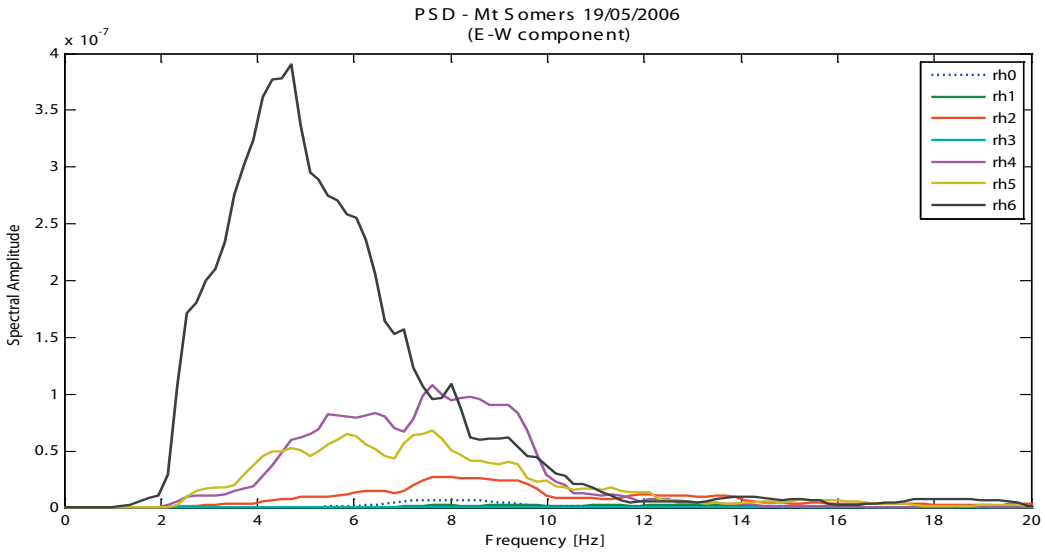
PSD - Mt Somers 19/05/2006
(E-W component)
x 10^-7
Spectral Amplitude
Frequency [Hz]
rh0
rh1
rh2
rh3
rh4
rh5
rh6

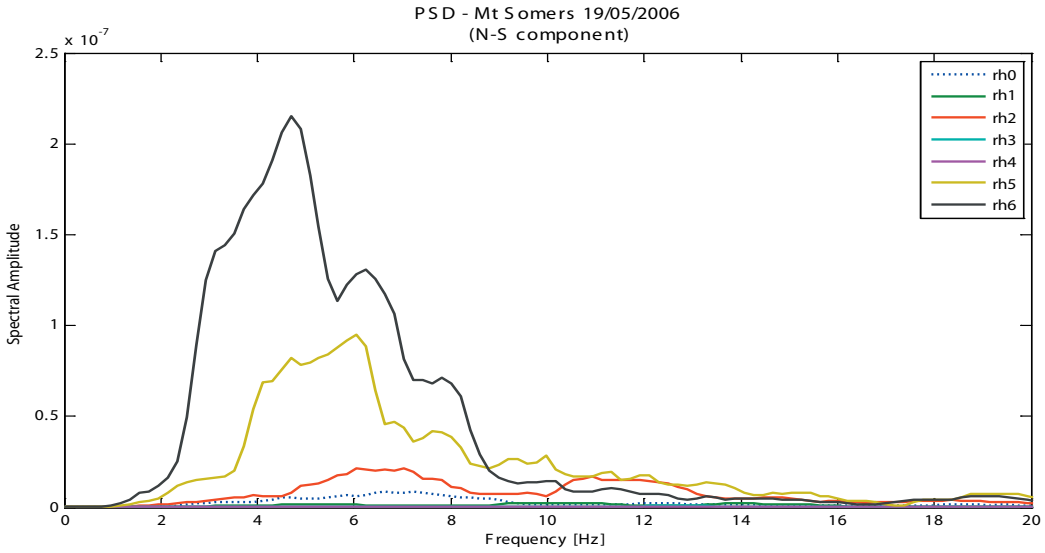
PSD - Mt Somers 19/05/2006
(N-S component)
x 10^-7
Spectral Amplitude
Frequency [Hz]
rh0
rh1
rh2
rh3
rh4
rh5
rh6

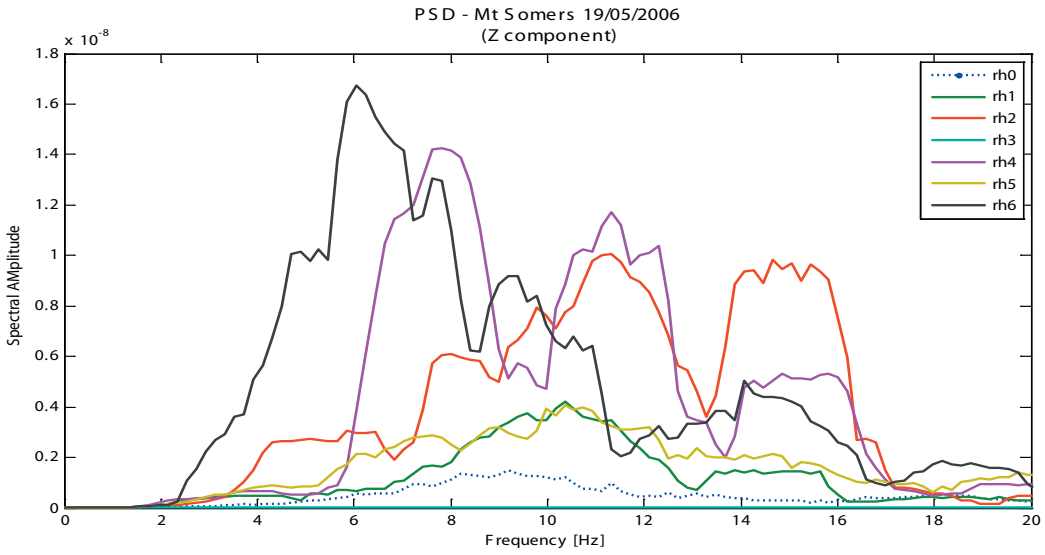
PSD - Mt Somers 19/05/2006
(Z component)
x 10^-8
Spectral AMplitude
Frequency [Hz]
rh0
rh1
rh2
rh3
rh4
rh5
rh6

Appendix A.4

Little Red Hill Field Experiment – Standard Spectral Ratio Plots

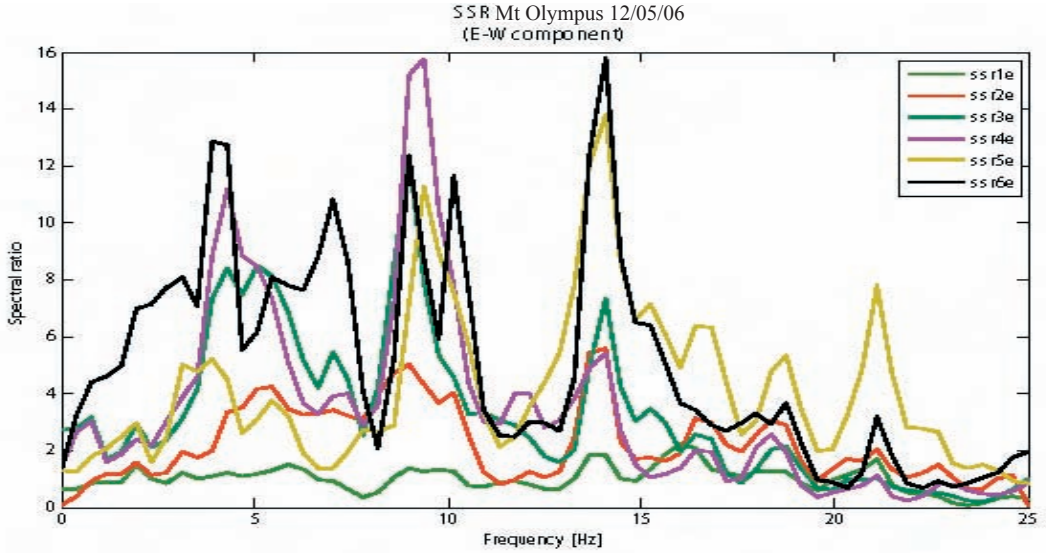
SSR Mt Olympus 12/05/06
(E-W component)
ssr1e
ssr2e
ssr3e
ssr4e
ssr5e
ssr6e
Spectral ratio
Frequency [Hz]

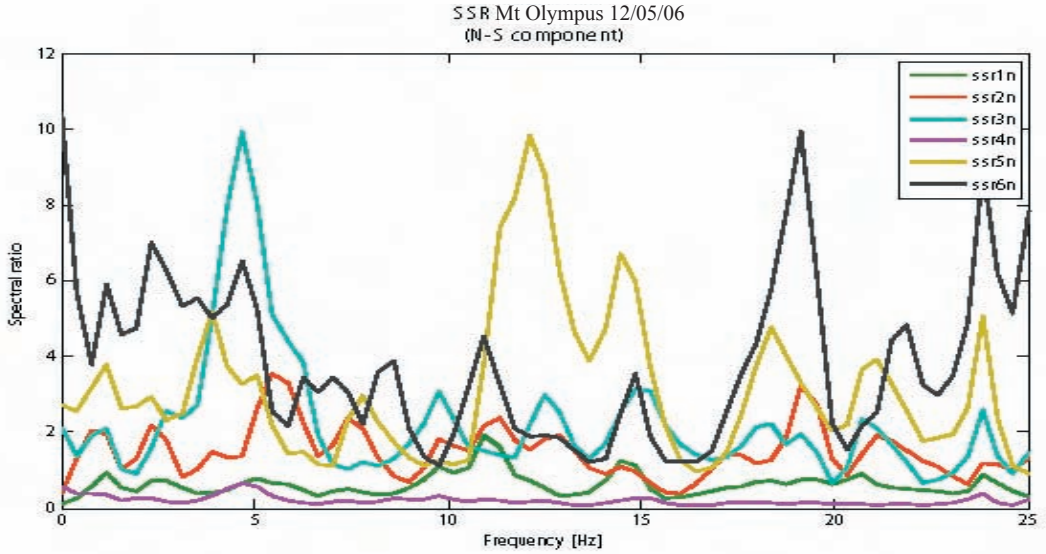
SSR Mt Olympus 12/05/06
(N-S component)
ssr1n
ssr2n
ssr3n
ssr4n
ssr5n
ssr6n
Spectral ratio
Frequency [Hz]

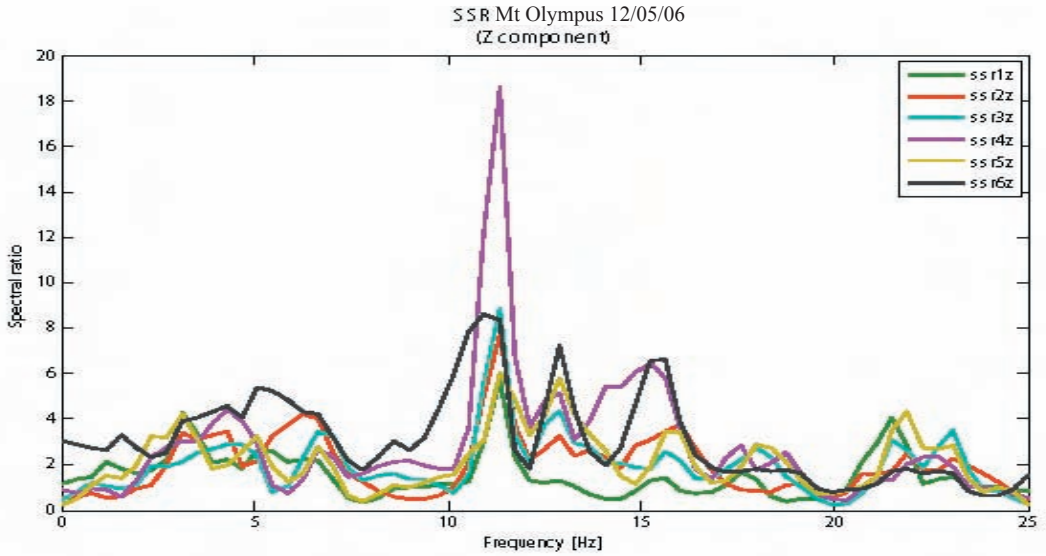
SSR Mt Olympus 12/05/06
(Z component)
ssr1z
ssr2z
ssr3z
ssr4z
ssr5z
ssr6z
Spectral ratio
Frequency [Hz]

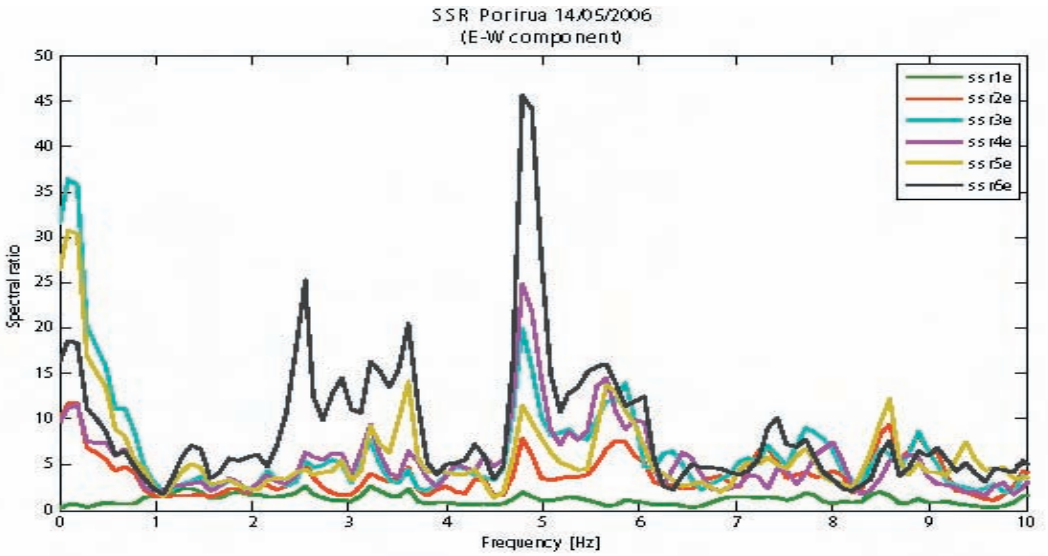
SSR Porirua 14/05/2006
(E-W component)
ssr1e
ssr2e
ssr3e
ssr4e
ssr5e
ssr6e
Spectral ratio
Frequency [Hz]

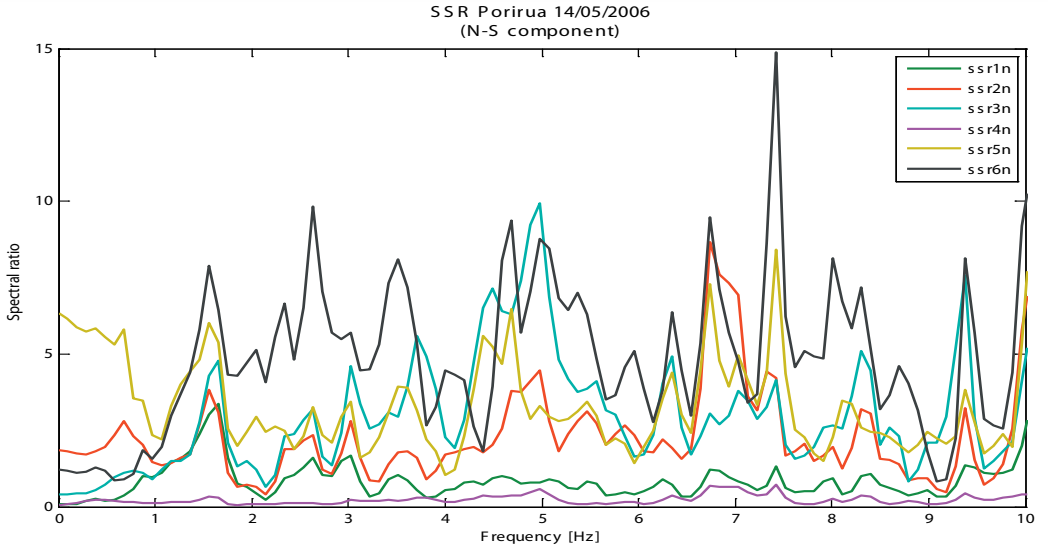
SSR Porirua 14/05/2006
(N-S component)
ssr1n
ssr2n
ssr3n
ssr4n
ssr5n
ssr6n
Spectral ratio
Frequency [Hz]

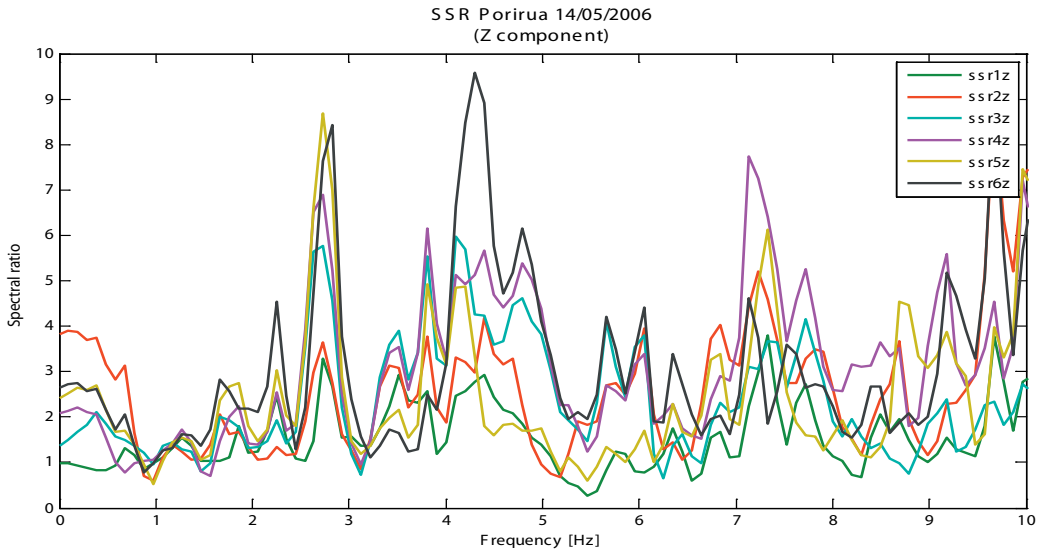
SSR Porirua 14/05/2006
(Z component)
ssr1z
ssr2z
ssr3z
ssr4z
ssr5z
ssr6z
Spectral ratio
Frequency [Hz]

Appendix A.4 Little Red Hill - Standard Spectral Ratio plots

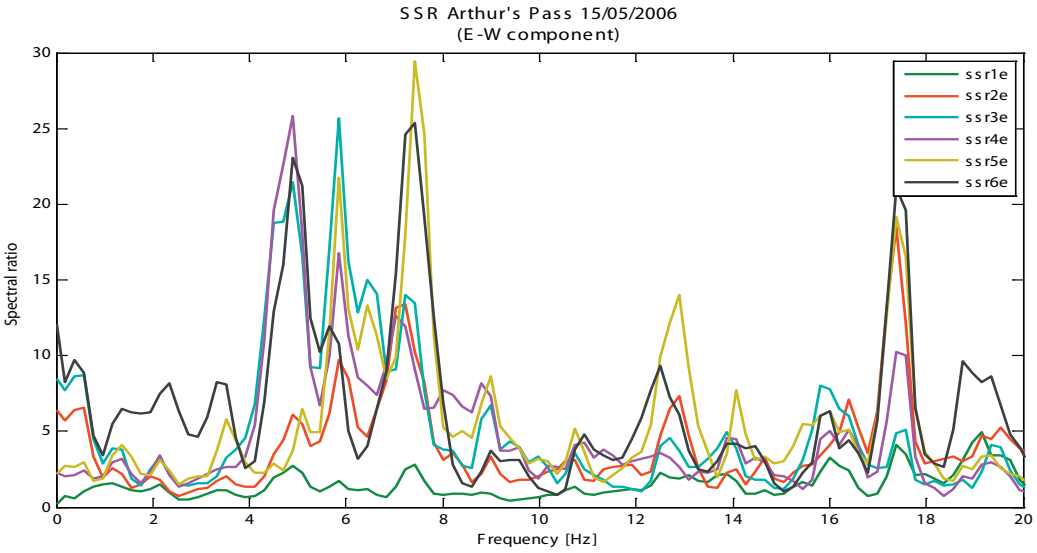

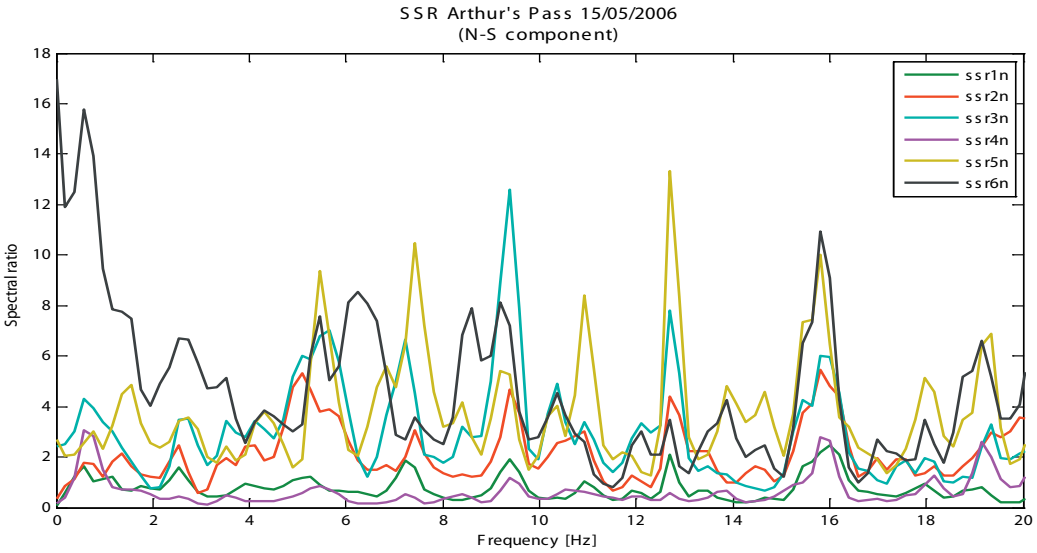

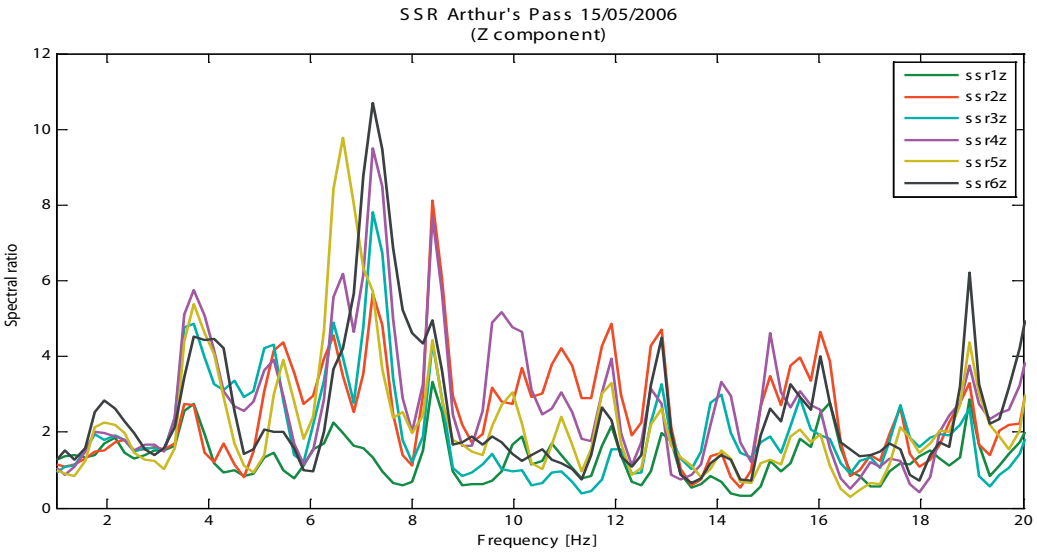

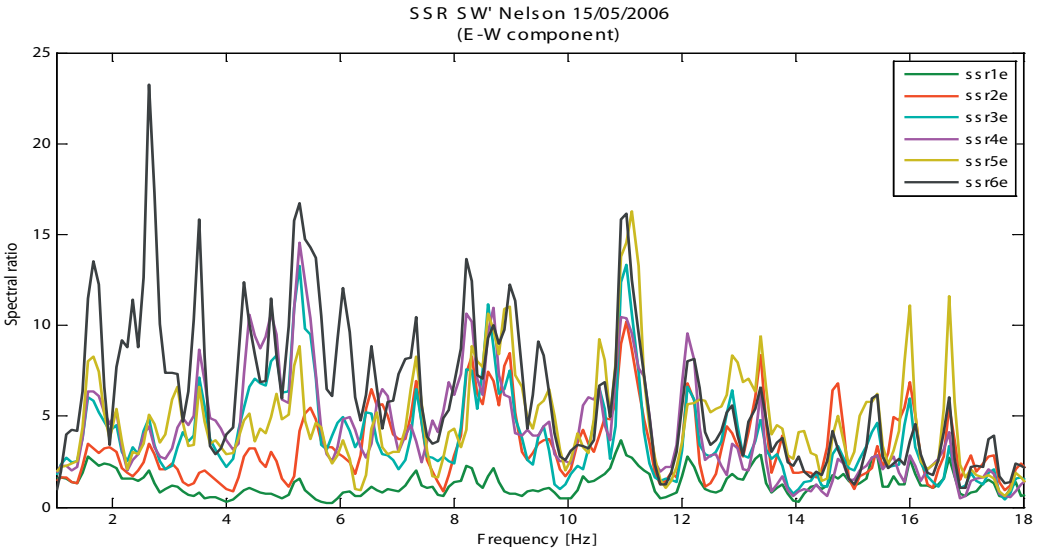
SSR SW' Nelson 15/05/2006
(E-W component)
ssr1e
ssr2e
ssr3e
ssr4e
ssr5e
ssr6e
Spectral ratio
Frequency [Hz]

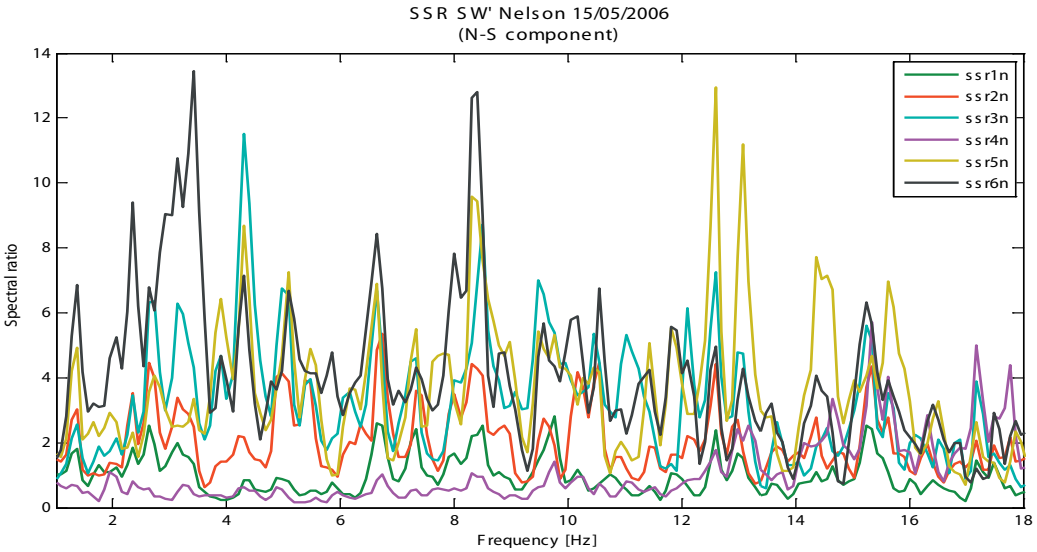
SSR SW' Nelson 15/05/2006
(N-S component)
ssr1n
ssr2n
ssr3n
ssr4n
ssr5n
ssr6n
Spectral ratio
Frequency [Hz]

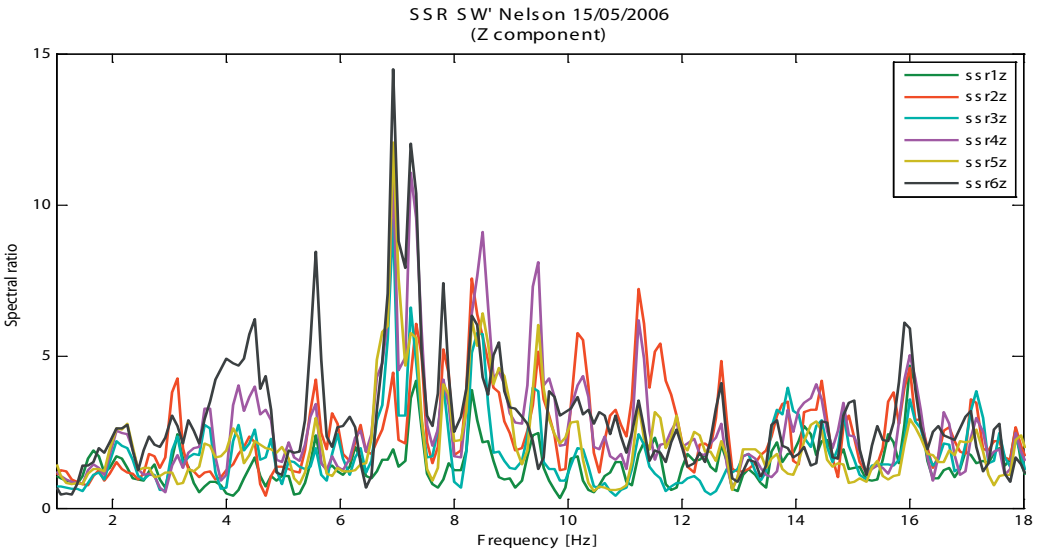
SSR SW' Nelson 15/05/2006
(Z component)
ssr1z
ssr2z
ssr3z
ssr4z
ssr5z
ssr6z
Spectral ratio
Frequency [Hz]

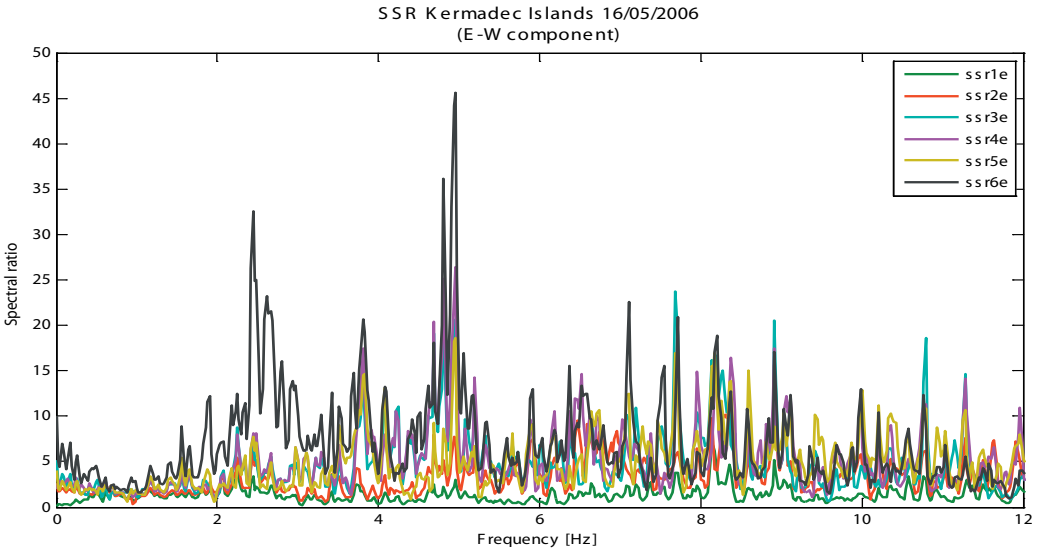
SSR Kermadec Islands 16/05/2006
(E-W component)
ssr1e
ssr2e
ssr3e
ssr4e
ssr5e
ssr6e
Spectral ratio
Frequency [Hz]

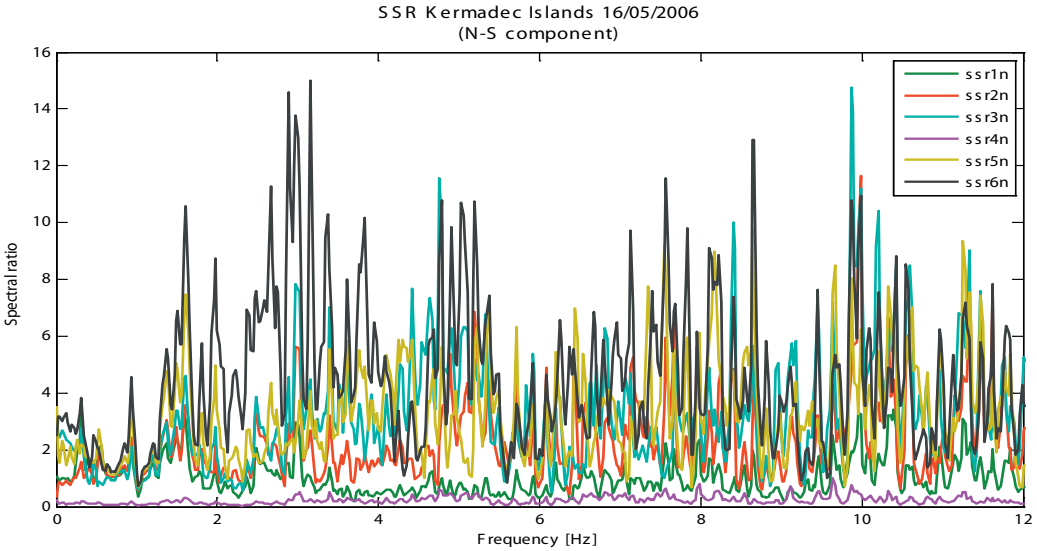
SSR Kermadec Islands 16/05/2006
(N-S component)
ssr1n
ssr2n
ssr3n
ssr4n
ssr5n
ssr6n
Spectral ratio
Frequency [Hz]

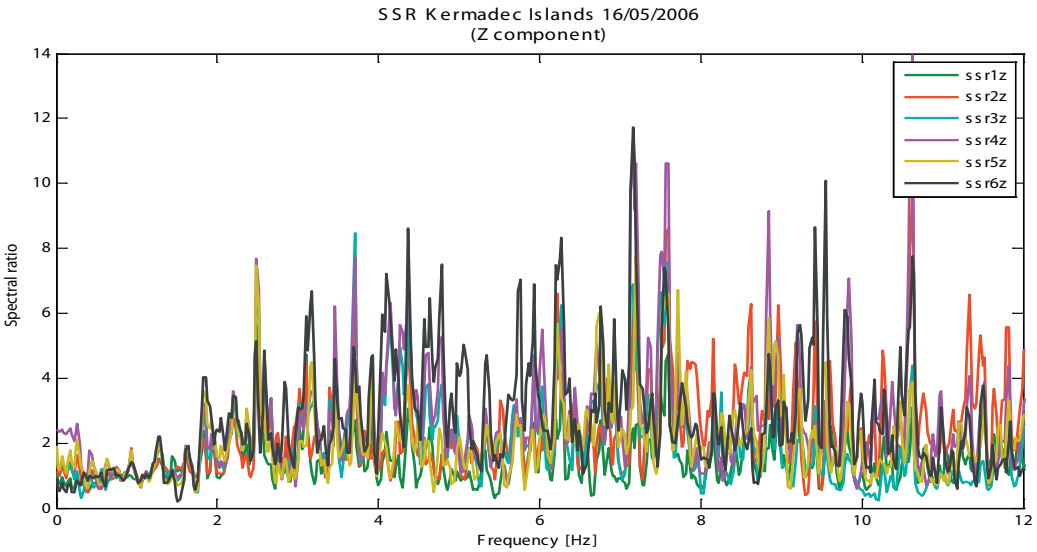
SSR Kermadec Islands 16/05/2006
(Z component)
ssr1z
ssr2z
ssr3z
ssr4z
ssr5z
ssr6z
Spectral ratio
Frequency [Hz]

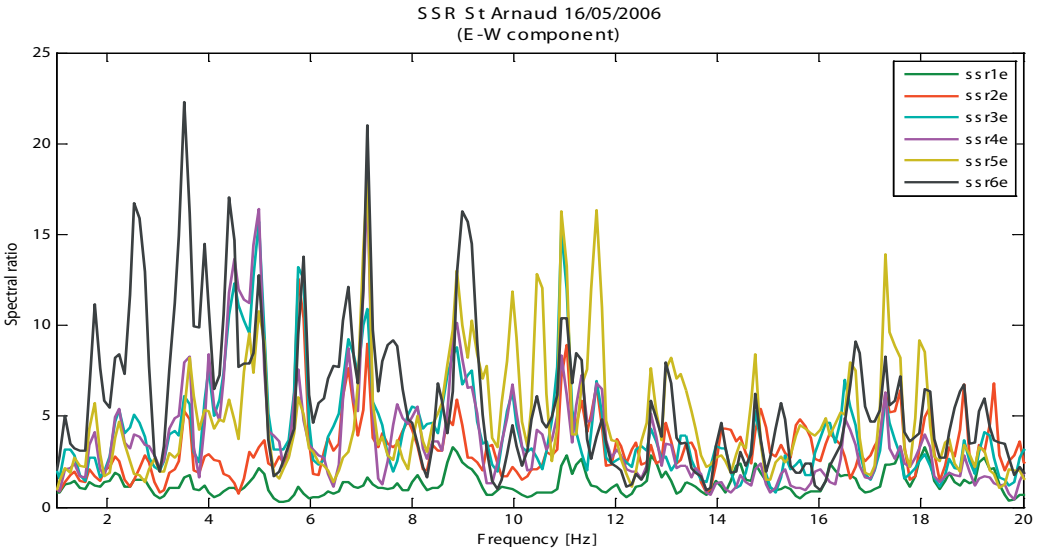
SSR St Arnaud 16/05/2006
(E-W component)
ssr1e
ssr2e
ssr3e
ssr4e
ssr5e
ssr6e
Spectral ratio
Frequency [Hz]

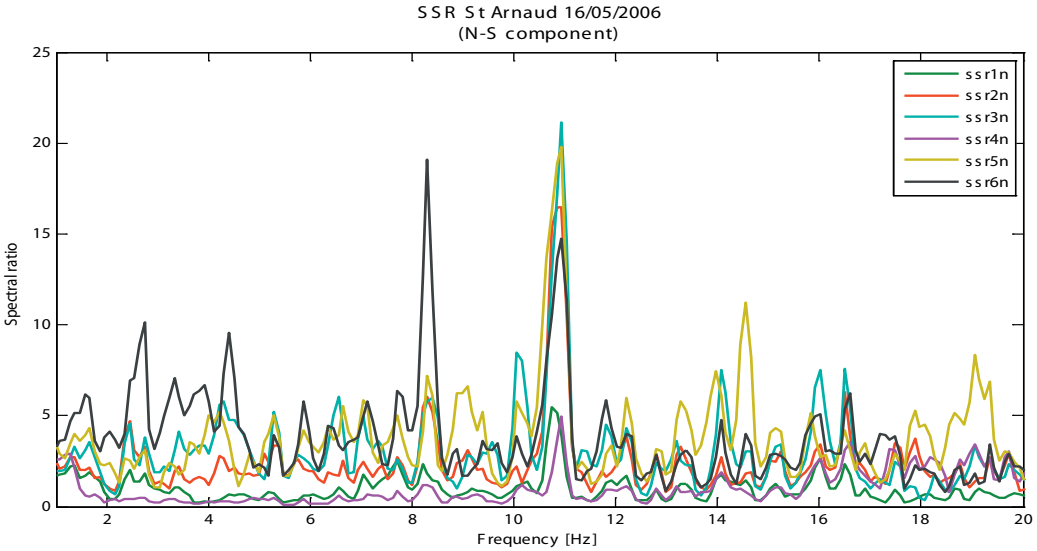
SSR St Arnaud 16/05/2006
(N-S component)
ssr1n
ssr2n
ssr3n
ssr4n
ssr5n
ssr6n
Spectral ratio
Frequency [Hz]

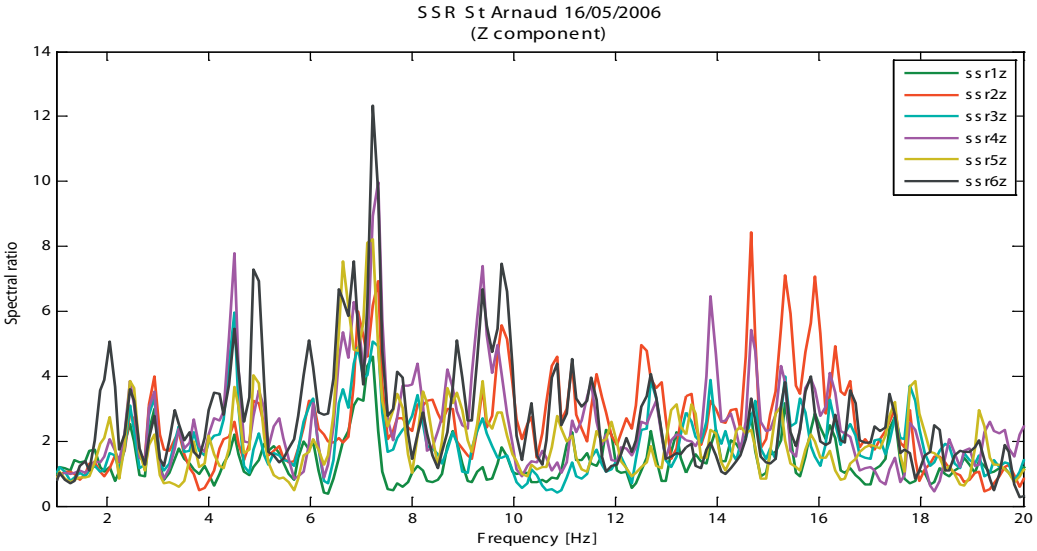
SSR St Arnaud 16/05/2006
(Z component)
ssr1z
ssr2z
ssr3z
ssr4z
ssr5z
ssr6z
Spectral ratio
Frequency [Hz]

Appendix A.4 Little Red Hill - Standard Spectral Ratio plots

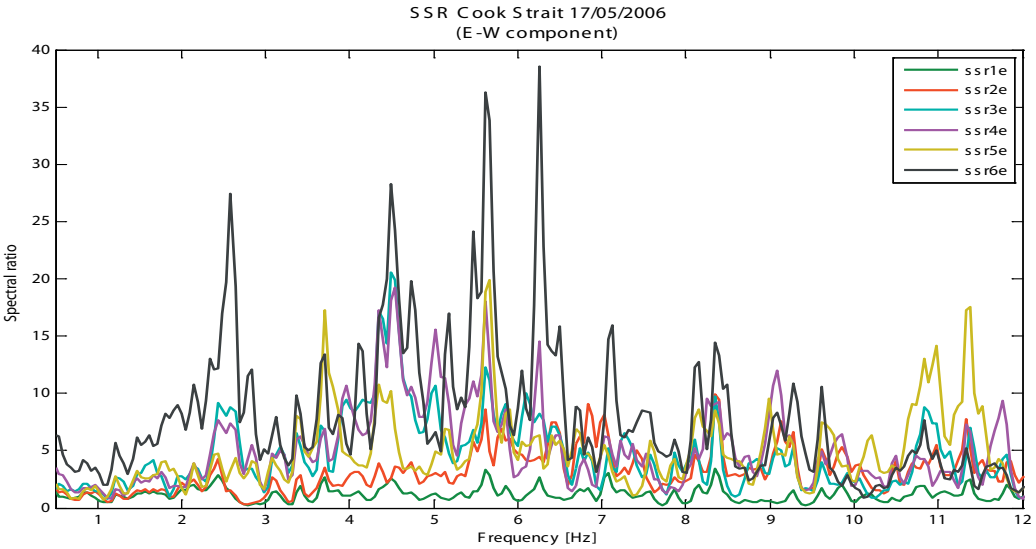

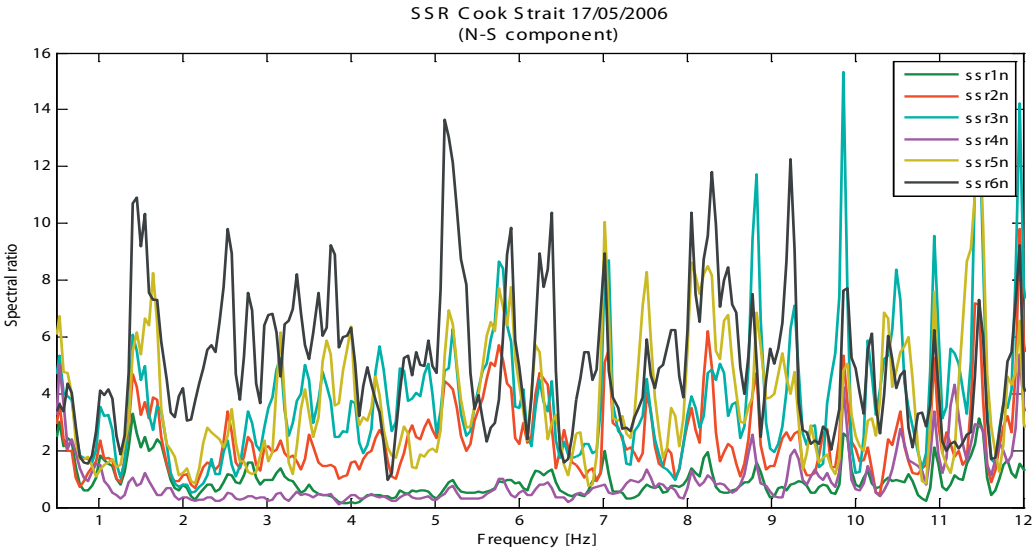

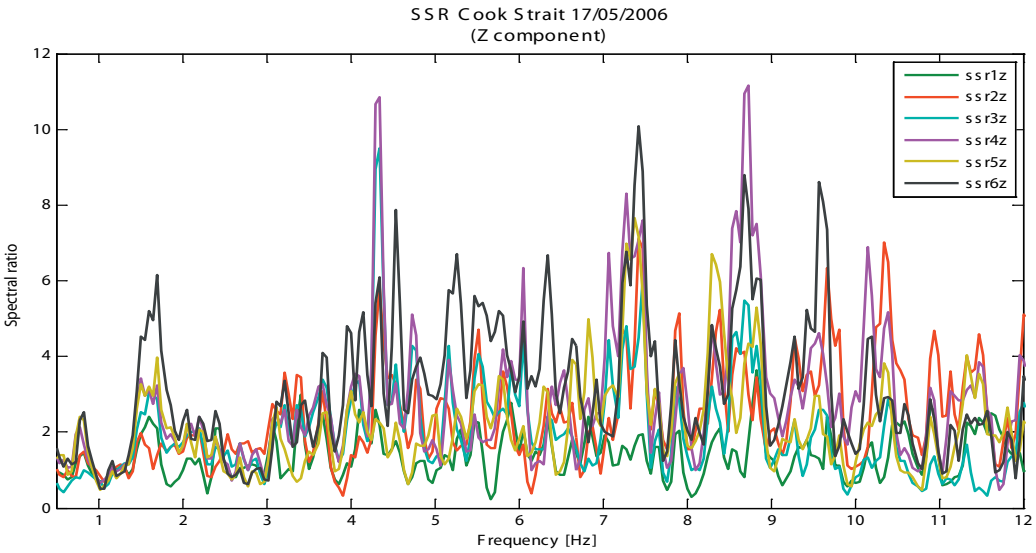

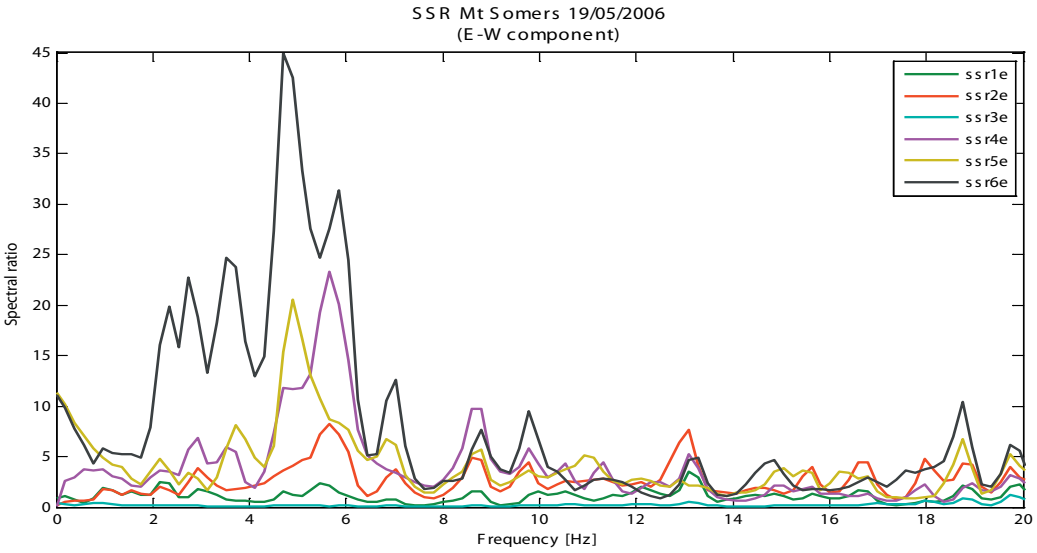
SSR Mt Somers 19/05/2006
(E-W component)
Spectral ratio
Frequency [Hz]
ssr1e
ssr2e
ssr3e
ssr4e
ssr5e
ssr6e

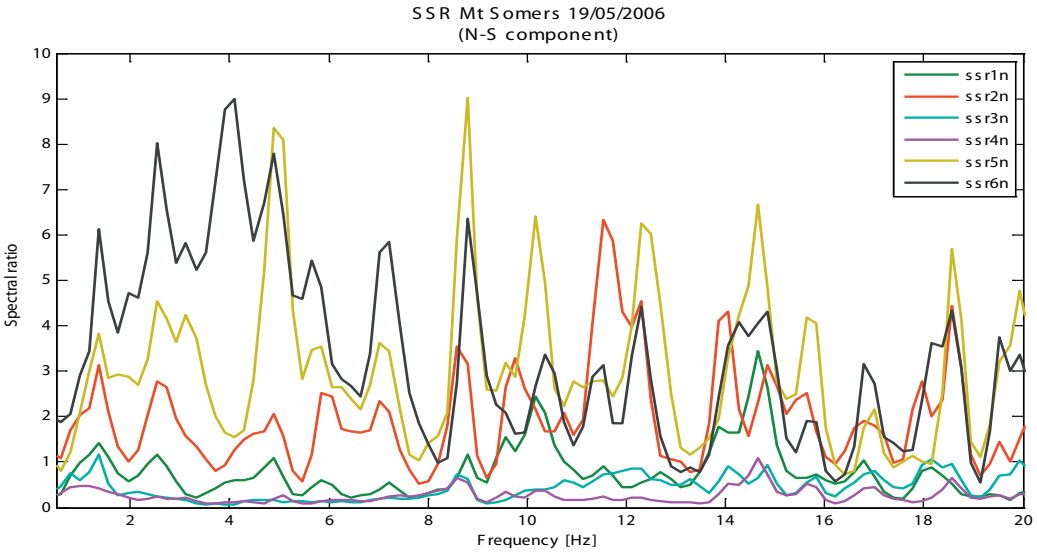
SSR Mt Somers 19/05/2006
(N-S component)
Spectral ratio
Frequency [Hz]
ssr1n
ssr2n
ssr3n
ssr4n
ssr5n
ssr6n

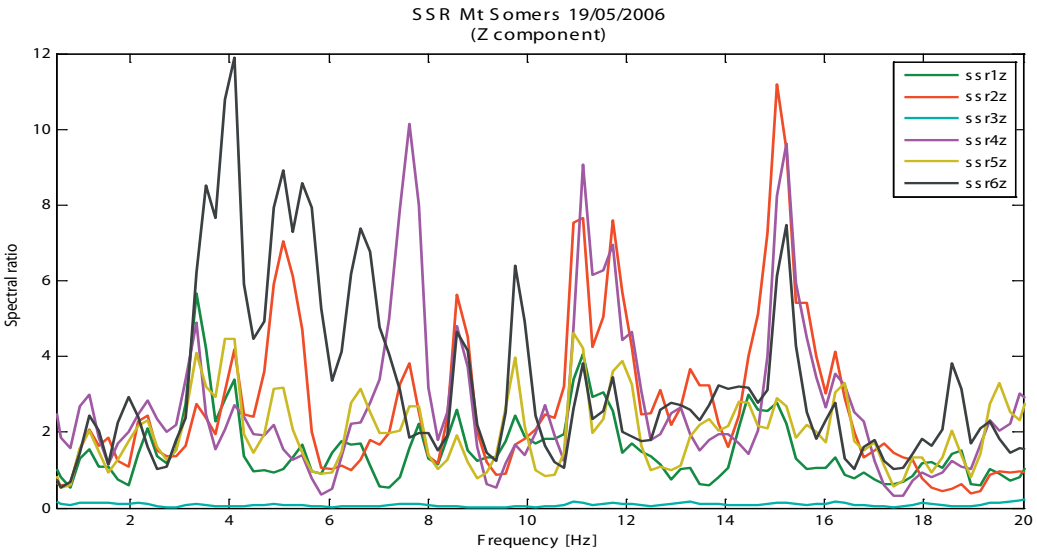
SSR Mt Somers 19/05/2006
(Z component)
Spectral ratio
Frequency [Hz]
ssr1z
ssr2z
ssr3z
ssr4z
ssr5z
ssr6z

Appendix A.5

Little Red Hill Field Experiment – PowerGel™ detonation

POWERGEL DETONATION 20060606.0444

DETONATION SETUP

During a reconnaissance field trip, a site about 1.5 km north of Little Red Hill was chosen to conduct a seismic experiment producing an artificial shock wave. An overview of the test site is shown in figure A.5.2.

At the end of the last phase of the field experiment a detonation of 8 kg of *Powergel*™ provided ground motion data from an artificial source. The explosives were placed in 13 boreholes, each 3.2 m deep, which were drilled into Torlesse bedrock to provide maximum energy transmission towards the test site.

TIME DOMAIN ANALYSIS - PEAK GROUND ACCELERATION (PGA)

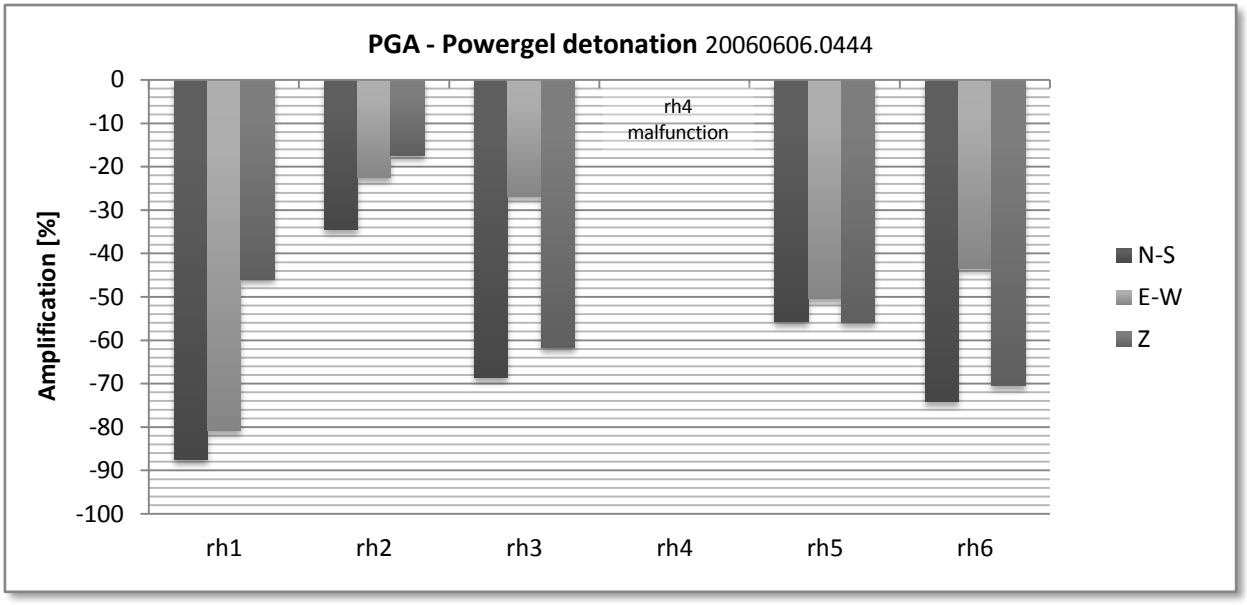

Figure A.5.1: Powergel detonation – Amplification of Peak Ground Accelerations relative to reference station rh0 - Motion component parallel (N-S) to the main axis, transverse (E-W) to the main axis, and in vertical direction (Z)

The recorded ground motions of the detonation were almost opposite to those ground motions observed from natural seismic sources (Fig. A.5.1). De-amplification was recorded at all stations relative to station rh0. The greatest de-amplification occurred in the N-S direction at station rh1 (-88 %), and the least de-amplification occurred at station rh2 (-17) in the vertical direction.

The detonation experiment showed attenuation of the artificial shock waves is dominant. Two factors may contribute to the weak signal response at Little Red Hill during the detonation experiment:

1. The generated wave field, dominated by compressional waves, hit Little Red Hill parallel to the main axis of the edifice resulting in increased energy dissipation due to the higher stiffness of the edifice in that direction.

2. The amount of explosives was insufficient for generating wave motions that would excite the edifice similar to an earthquake input

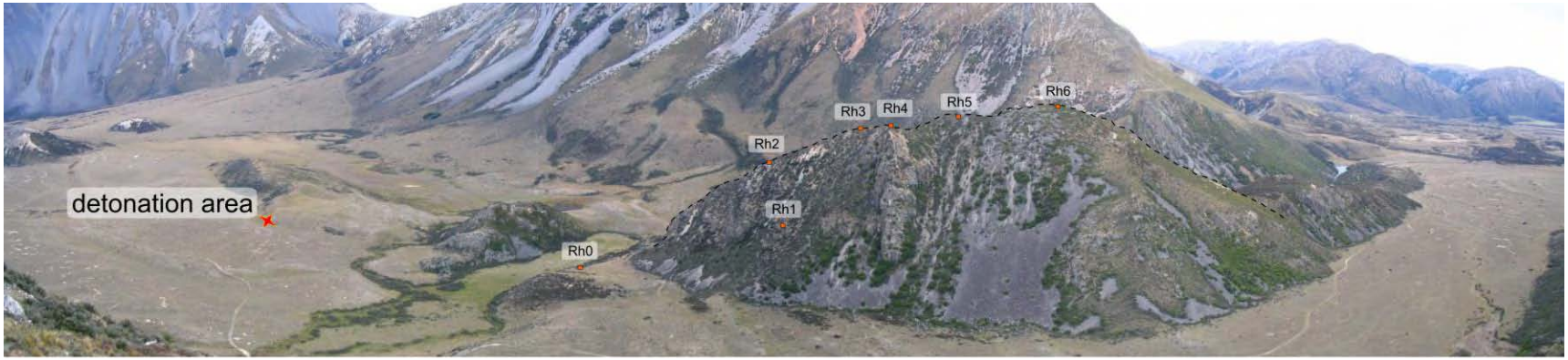

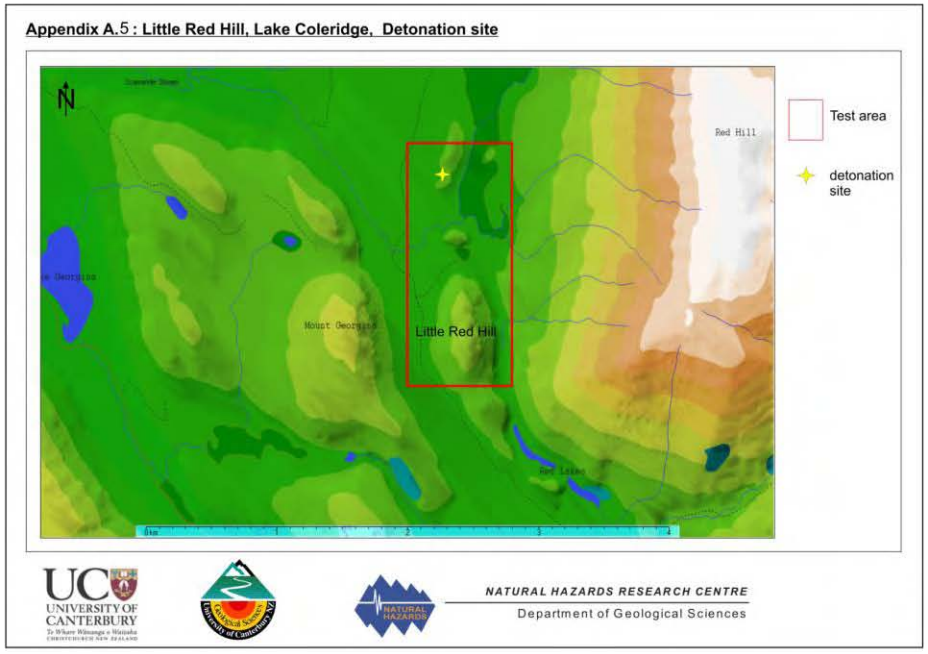

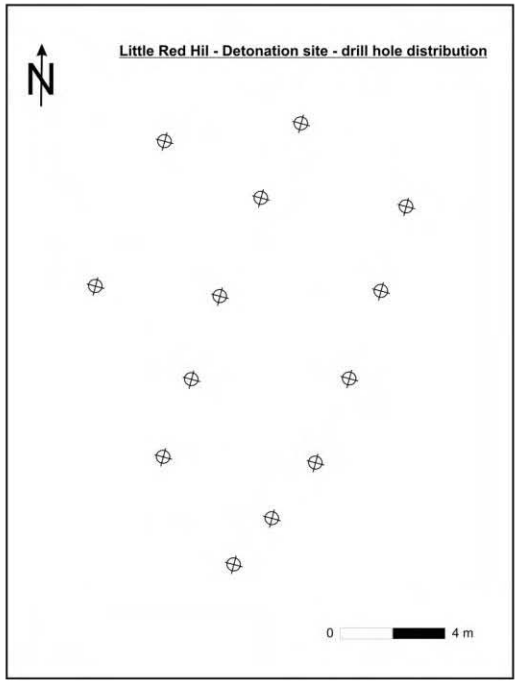

Figure A.5.2: Overview of the detonation test site, showing an oblique photograph of the LRH test site and the location of the detonation site, a topographic overview, and a map of the detonation site with the borehole cluster

Appendix A.6

Little Red Hill Field Experiment – Video Sequences of the horizontal displacements for the selected earthquake events

(For video files, please refer to folder *A6 Appendix Horizontal displ videos* on the attached CD)

A.6.1 Mt Olympus earthquake – horizontal displacement video

A.6.2 Porirua earthquake – horizontal displacement video

A.6.3 Arthurs Pass earthquake – horizontal displacement video

A.6.4 Nelson earthquake – horizontal displacement video

A.6.5 Kermadec Islands earthquake – horizontal displacement video

A.6.6 St Arnaud earthquake – horizontal displacement video

A.6.7 Cook Strait earthquake – horizontal displacement video

A.6.8 Mt Somers earthquake – horizontal displacement video

Appendix B.1

Dimensional Analysis of earthquake triggered landslide initiation

DIMENSIONAL ANALYSIS OF EARTHQUAKE TRIGGERED LANDSLIDE INITIATION

DIMENSIONAL ANALYSIS & SIMILARITY

Small-scale laboratory models are performed when full-scale tests are either impossible to perform or too expensive. Dimensional modeling is used to experiment on a scaled replica (model) of the physical system that has to be modelled (prototype), and then to project the results obtained from the model to the prototype (Szirtes, 2007).

Dimensional analysis is used to establish a relationship between the parameters used in the laboratory model and the prototype situation. It is also a method for reducing the number and complexity of experimental variables which affect a given phenomenon (White, 1994).

The first step in the planning of an experiment is to decide on governing parameters, or variables, that will have an effect on the phenomenon under investigation. The Buckingham Pi Theorem (Buckingham, 1914) is applied to *n* governing dimensional parameters $q_1, q_2, \ldots, q_n$ that are physically relevant for the given problem and inter-related by a dimensionally homogeneous set of equations. It is expressed using a functional relationship of the form

$$q = f(q_1, q_2, \ldots q_n);$$

Each of the governing parameters with their units can then be expressed in terms of basic dimensions (Barenblatt, 1987). In our case each of the parameters can be described by using the three primary dimensions mass, length, and time (M, L, T).

k is the number of primary dimensions required to describe the *n* governing parameters. There will be *m* repeating parameters. In combination with these repeating parameters, the remaining variables can be expressed as a number of ($n - k$) dimensionless and independent Pi-groups π_1, $\pi_2, \ldots \pi_{n-k}$.

The resulting empirical formulas have to be checked to make sure that they are dimensionless. The experiment has to verify the validity of the original assumption and has to show that a condition of similarity exists between the model and the prototype situation (Logan, 1987; Munson, 2002; White, 1994).

The dimensional analysis has been applied to our physical phenomenon as follows:

We specified variables which affect the phenomenon of earthquake triggered landslide initiation:

- Density of the rock material $\boldsymbol{\rho_{rock}}$ [kg/m^3]
- Strength of the rock material $\mathbf{S_{rock}}$ [Pa]
- Elasticity of the rock material **E** [Pa]
- Height of the mountain **h** [m]
- Width of the mountain **w** [m]
- Gravitational acceleration **g** [m/s^2]
- Seismic wave velocity **v** [m/s]
- Seismic wave length **λ** [m]

Parameter	Unit	MLT class
Density of rock material $\boldsymbol{\rho_{rock}}$	[kg/m^3]	ML^{-3}
Strength of rock material $\mathbf{S_{rock}}$	[Pa] = [kg/ms^2]	ML^{-1}T^{-2}
Elasticity of rock material **E**	[Pa] = [kg/ms^2]	ML^{-1}T^{-2}
Height of the mountain **h**	[m]	L
Width of the mountain **w**	[m]	L
Characteristic seismic wave length **λ**	[m]	L
Seismic wave velocity **v**	[m/s]	LT^{-1}
Gravitational acceleration **g**	[m/s^2]	LT^{-2}

Table B.1.0.1: Governing parameters affecting the modelled phenomenon

1. The *n* governing parameters:

   ρ_{rock} , S_{rock} , E, h , w , λ, v, g

   (*n* = 8)

2. *k* primary dimensions:

   M, L, T

   ($k = 3$)

3. Dimensions of all parameters:

Table B.1.2: Governing parameters and dimensions

ρ_{rock}	S_{rock}	E	h	w	λ	v	g
$\frac{M}{L^3}$	$\frac{M}{LT^2}$	$\frac{M}{LT^2}$	L	L	L	$\frac{L}{T}$	$\frac{L}{T^2}$

4. *m* repeating parameters:

The selection of repeating parameters is based on the dimensions of the parameters. All of the governing parameters can be expressed by a combination of the following three parameters.

ρ_{rock},

g,

h

($m = k = 3$)

5. The dimensional equations:

   Combining the repeating parameters with each of the other parameters:

   ($n - k = 5$)

$$\Pi_1 = \rho_r^a \, g^b \, h^c \, S_r$$

$$\Pi_2 = \rho_r^a \, g^b \, h^c \, E$$

$$\Pi_3 = \rho_r^a \, g^b \, h^c \, w$$

$$\Pi_4 = \rho_r^a \, g^b \, h^c \, \lambda$$

$$\Pi_5 = \rho_r^a \, g^b \, h^c \, v$$

6. Solving the equations:

$\Pi_1 = \rho_r^a\, g^b\, h^c\, S_r$

$\Pi_1 = \left(\frac{M}{L^3}\right)^a \left(\frac{L}{T^2}\right)^b (L)^c \left(\frac{M}{LT^2}\right) = M^0\, L^0\, T^0$;

1) M: a + 1 = 0;

   ⇒ a = -1;

2) T: -2b - 2 = 0;

   ⇒ b = -1;

3) L: -3a + b + c – 1 = 0;

1) and 2) in 3): -3 (-1) + (-1) + c -1 = 0;

⇒ c = -1;

$$\Pi_1 = \frac{S_r}{\rho_r\ g\ h}$$

Check to see if the resulting equation is dimensionless:

$$\left[\Pi_1\right] = \left[\frac{\frac{M}{LT^2}}{\frac{M}{L^3}\ \frac{L}{T^2}\ L}\right] = 1;$$

$\Pi_2 = \rho_r^a\, g^b\, h^c\, E$

$\Pi_2 = \left(\frac{M}{L^3}\right)^a \left(\frac{L}{T^2}\right)^b (L)^c \left(\frac{M}{LT^2}\right) = M^0\, L^0\, T^0$;

1) M: a + 1 = 0;

   ⇒ a = -1;

2) T: -2b - 2 = 0;

   ⇒ b = -1;

3) L: -3a + b + c – 1 = 0;

1) and 2) in 3): -3 (-1) + (-1) + c -1 = 0;

⇒ c = -1

$$\Pi_2 = \frac{E}{\rho_r\ g\ h}$$

Check to see if the resulting equation is dimensionless:

$$\left[\Pi_2\right] = \left[\frac{\frac{M}{LT^2}}{\frac{M}{L^3}\frac{L}{T^2}L}\right] = 1;$$

$\Pi_3 = \rho_r^a\, g^b\, h^c\, w$

$$\Pi_3 = \left(\frac{M}{L^3}\right)^a \left(\frac{L}{T^2}\right)^b (L)^c\, (L) = M^0\, L^0\, T^0;$$

1) M: a = 0;
2) T: -2b = 0;

   ⇒ b = 0;

3) L: -3a + b +c + 1 = 0
1) and 2) in 3): c + 1 = 0;

⇒ c = -1;

$$\Pi_3 = \frac{w}{h}$$

Check to see if the resulting equation is dimensionless:

$$\left[\Pi_3\right] = \left[\frac{L}{L}\right] = 1;$$

$\Pi_4 = \rho_r^a\, g^b\, h^c\, \lambda$

$$\Pi_4 = \left(\frac{M}{L^3}\right)^a \left(\frac{L}{T^2}\right)^b (L)^c\, (L) = M^0\, L^0\, T^0;$$

1) M: a = 0;
2) T: -2b = 0;

   ⇒ b = 0;

3) L: -3a + b +c + 1 = 0;
1) and 2) in 3): c + 1 = 0;

⇒ c = -1;

$$\Pi_4 = \frac{\lambda}{h}$$

Check to see if the resulting equation is dimensionless:

$$\left[\Pi_4\right] = \left[\frac{L}{L}\right] = 1;$$

$\Pi_5 = \rho_r^a\, g^b\, h^c\, v$

$\Pi_5 = \left(\frac{M}{L^3}\right)^a \left(\frac{L}{T^2}\right)^b (L)^c \left(\frac{L}{T}\right) = M^0\, L^0\, T^0$;

1) M: a = 0;
2) T: -2b – 1 = 0;

   $\Rightarrow b = -\frac{1}{2}$;

3) L: -3a + b + c + 1 = 0;

1) and 2) in 3): $-\frac{1}{2} + c + 1 = 0$;

$\Rightarrow c = -\frac{1}{2}$;

$$\Pi_5 = \frac{v}{\sqrt{gh}} = \frac{v^2}{gh}$$

Check to see if the resulting equation is dimensionless:

$$\left[\Pi_5\right] = \left[\frac{\left(\frac{L}{T}\right)^2}{\frac{L}{T^2}\,L}\right] = 1;$$

The following dimensionless parameters affecting the small-scale laboratory model have been determined using the above dimensional analysis:

I. Geometry: $\frac{\lambda}{h}$ or $\frac{h}{\lambda}$ or $\frac{\lambda}{w}$ or $\frac{w}{h}$

II. Strength: $\frac{S_r}{\rho_r\ g\ h}$ or $\frac{E}{\rho_r\ g\ h}$ or $\frac{E}{S_r}$

III. Input: $\frac{v^2}{gh}$ or $\frac{v^2}{g\lambda}$ or $\frac{v^2}{gw}$

(or $\frac{v}{hf}$ where f is the frequency of the seismic wave)

SCALE FACTORS

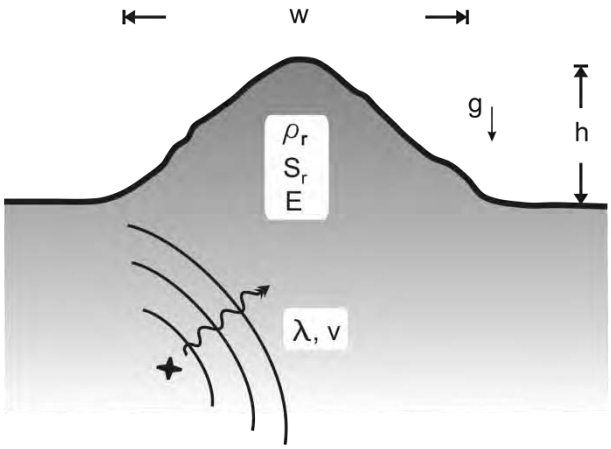

Parameter	Value	Unit
Density of rock material ρ_r	2500	[kg/m^3]
Strength of rock material $\mathbf{S_r}$	200 x 10^6	[Pa] = [kg/ms^2]
Elasticity of rock material **E**	50 x 10^9	[Pa] = [kg/ms^2]
Height of the mountain **h**	210	[m]
Width of the mountain **w**	500	[m]
Characteristic seismic wave length **λ** (S-wave)	500	[m]
Seismic wave velocity **v** (S-wave)	1200	[m/s]
Gravitational acceleration **g**	9.81	[m/s^2]

Figure B.1.1: Prototype parameters affecting the model

Scale factors are used to facilitate and enhance the modeling procedure. They always refer to a particular physical variable and represent the quotient of the magnitudes of that variable for the prototype (Fig. B.1.1) and its model. The capital letter S with the variable as subscript is used as the symbol for the individual scale factors (Szirtes, 2007).

Looking at the geometrical similarity, if the height of the prototype mountain edifice is h_p = 210 m, and the height of the model is h_m = 0.21 m, then the Height Scale Factor S_h for the mountain edifice is

$$S_h = \frac{h_{prototype}}{h_{model}} = \frac{h_p}{h_m} = \frac{210\ m}{0.21\ m} = 1000$$

By using the correlations calculated by dimensional analysis, following scale factors can be derived:

From **I.**:

Modeling at a linear geometric scale of 1000, both the width of the edifice ($S_w = w_p/w_m = 1000$) and the length of the seismic waves in the model have to be 1/1000 of the prototype situation ($S_\lambda = \lambda_p/\lambda_m = 1000$).

From **II.**: $S_{S/\rho} = S_g S_h = 1000$

$(S_r)_p = 2.0 \times 10^8$ and $\rho_p = 2.5 \times 10^3$

$\Rightarrow (S_r/\rho)_p = 80000$

$\Rightarrow (S_r/\rho)_m = (S_r/\rho)_p/1000 = 80$

Therefore, if our model material is based on material with a dry density $(\rho_r)_m = 1200$ kg/m^3, its strength has to be

$(S_r)_m = 1200 \times 80 = 96$ kPa

Thus from $\left(\frac{E}{S_r}\right)_p = \frac{50*10^9}{200*10^6} = 250$

$E_m = 250 \times 96$ kPa $= 24$ MPa

From **III.**:

The required velocity of seismic waves in the model material is given by

$S_v = (S_g S_h)^{0.5} \approx 32,$

$>> v_m \approx 1/32\ v_p$

i.e. $\lambda_m = 1/1000\ \lambda_p$;

$\Rightarrow S_f = S_v / S_\lambda \approx 1/32$

$\Rightarrow$ the model frequency $f_m \approx 32\ f_p$.

REFERENCES

Barenblatt, G.I., 1987. Dimensional Analysis. Gordon and Breach Science Publishers, 135 pp.
Buckingham, E., 1914. On physical similar systems. Physical Reviews, 4(4): 345.
Logan, J.D., 1987. Applied Mathematics: A Contemporary Approach. John Wiley & Sons, Inc., New York, 572 pp.
Munson, B.R., Young, D.F., Okiishi, T.H., 2002. Fundamentals of Fluid Mechanics. John Wiley & Sons, Inc., 840 pp.
Szirtes, T., 2007. Applied Dimensional Analysis and Modeling. Elsevier Inc., 820 pp.
White, F.M., 1994. Fluid Mechanics. McGraw-Hill International, 736 pp.

Appendix B.2

Physical laboratory model construction

Model construction

An initial test tank was constructed to test material properties and technical devices. The test tank was used to cure a test sample block of Rhodorsil® RTV 585 silicone (Figure B.2.1). Thanks to Dr Anekant Wandres for his amazing effort constructing the concrete model and for having brilliant ideas during the process of developing the physical laboratory model (can't hide Swiss precision!).
After the decision was made to use Rhodorsil® RTV 585 silicone as modeling material for the main physical laboratory model, the construction of the base and the mountain model was conducted. The silicone mountain model was cured utilizing an exact negative form of the mountain which was built in casting plaster using a positive wooden mountain model. The circular shaped Rhodorsil® RTV 585 silicone base was cured on a wooden foundation. The mountain model was joined with the silicone base using Rhodorsil® RTV 585 silicone to guaranty maximum wave transmission.
The final Rhodorsil® RTV 585 silicone model has the following dimensions:

Table B.2.1: Dimensions of the small-scale (1:1,000) physical laboratory Rhodorsil® RTV 585 silicone model

Mountain edifice		Base	
Height$_{model}$	0.21 m	**Height$_{base}$**	0.21 m
Length$_{model}$	0.82 m	**Diameter$_{base}$**	1.02 m
Width$_{model}$	0.50 m		
Volume$_{model}$	0.031 m^3	**Volume$_{base}$**	0.17 m^3
Mass$_{model}$	37.4 kg	**Mass$_{base}$**	206 kg

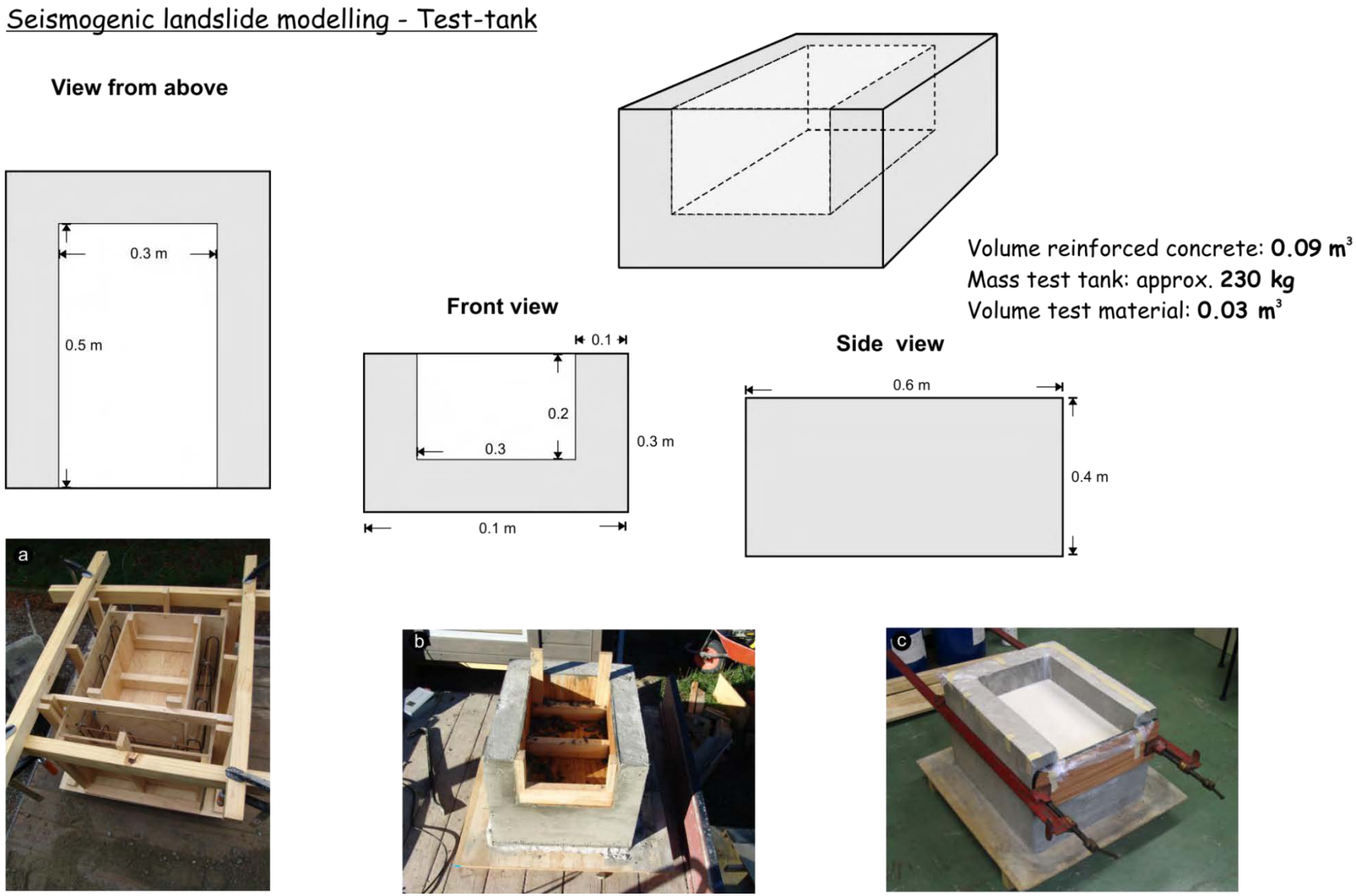

Figure B.2.1: Figure showing the construction plan of the concrete test tank, a) the initial wooden frame, b) the finished concrete test tank , and c) the test tank utilized for the curing process of the Rhodorsil® RTV 585 sample block

Figure B.2.1: Pictures showing the development of the final physical laboratory model; a) wooden mountain model before being utilized to manufacture the negative casting plaster mold; b) finished negative mountain mold, surface was painted with a special coating to prevent the silicone from sticking to the casting plaster; c) work environment showing the mountain and base mold after being filled with the two-component RTV 585 silicone rubber; d) Mountain model – curing finished and recovered; e) oblique and f) top view of the final physical laboratory model

Appendix B.3

Rhodorsil® RTV 585 silicone material tests
&
Input device tests

Ultrasonic tests

Ultrasonic tests with Rhodorsil® RTV 585 silicon samples were conducted to obtain information about material properties. The pulse velocity, v, in a material depends on its density, ρ, and specific elastic properties: $v = \sqrt{\frac{Y}{\rho}}$, where Y represents the Young's modulus (modulus of elasticity).

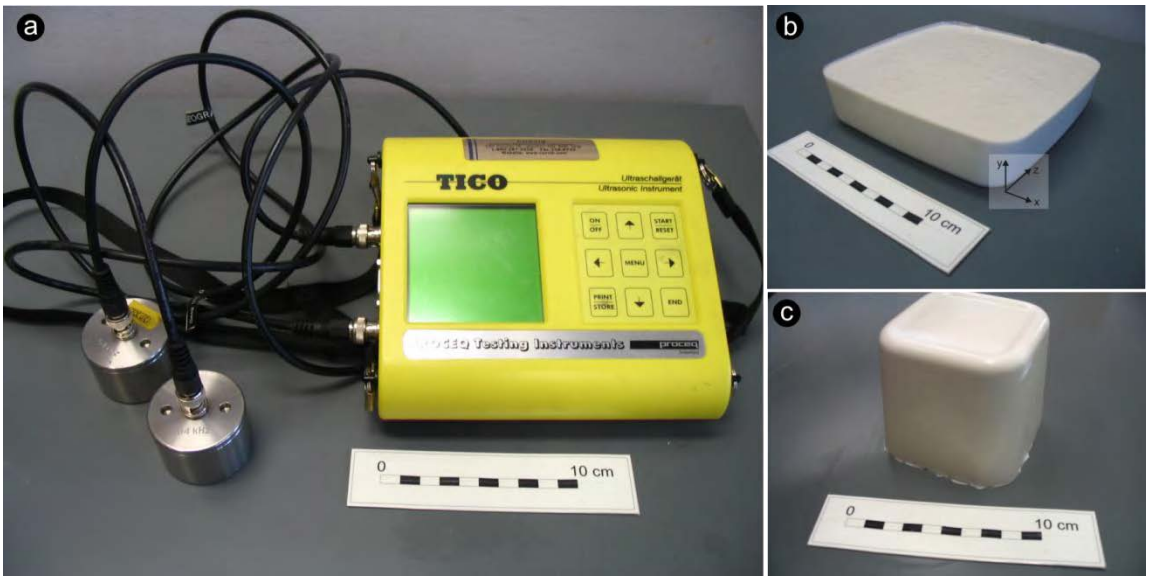

Figure B.3.1: Test setup – Ultrasonic material tests; a) portable TICO Ultrasonic testing instrument including a transmitter and receiver, used on b) a tabular and c) orthorhombic RTV 585 sample

The portable PROCEQ Ultrasonic Testing Instrument (Figure B.3.1; www.proceq.com) was used to measure the transmission time with transducers acting as transmitter and receiver, to calculate the pulse velocity. The transducers are operating with a frequency of 54 kHz.

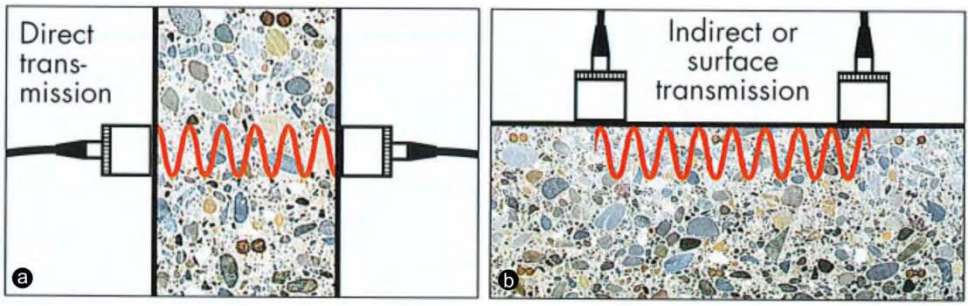

Figure B.3.2: Methods for measuring the transmission time; a) direct transmission, b) indirect transmission

Various test utilizing different transmission techniques (Figure B.3.2) did not result in a conclusive value for the Young's modulus (Figure B.3.3).

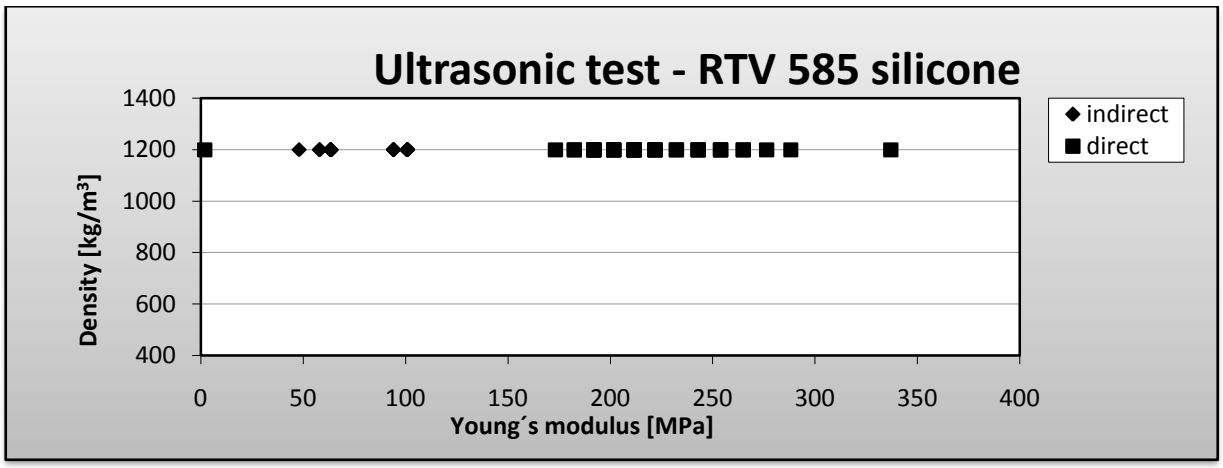

Figure B.3.3: Test results showing calculated values of the Young's modulus for direct and indirect transmission measurement

Further tests utilizing a laboratory ultrasonic test device on cylindrical test samples did not produce conclusive results either. No distinct signal other than high-frequent noise was received. High frequent testing devices in the kHz range turned out to be inadequate for evaluating the material properties of Rhodorsil® RTV 585 silicone rubber.

Voice coil test

A voice coil vibration test on a RTV 585 silicone rubber sample (0.3 m x 0.5 m x 0.2 m) was conducted at the University of Canterbury Mechanical Engineering laboratory facilities. The vibration test was performed under the special direction of Rodney Elliott (scientific officer at the Mechanical Engineering Department).

The test utilized a powerful electromagnetic voice coil activator that produced a sinusoid wave at a frequency of about 200 Hz and maximum amplitude of 1 mm to test the transmission of a sinusoid wave input and to evaluate the applicability of small accelerometers for the proposed test setup. One ADXL 320 accelerometer was used as a receiver. The test setup is shown in figure B.3.4. The data received by the accelerometer indicated good signal transmission for the Rhodorsil® RTV 585 silicone sample block and suitable performance of the ADXL 320 accelerometer.

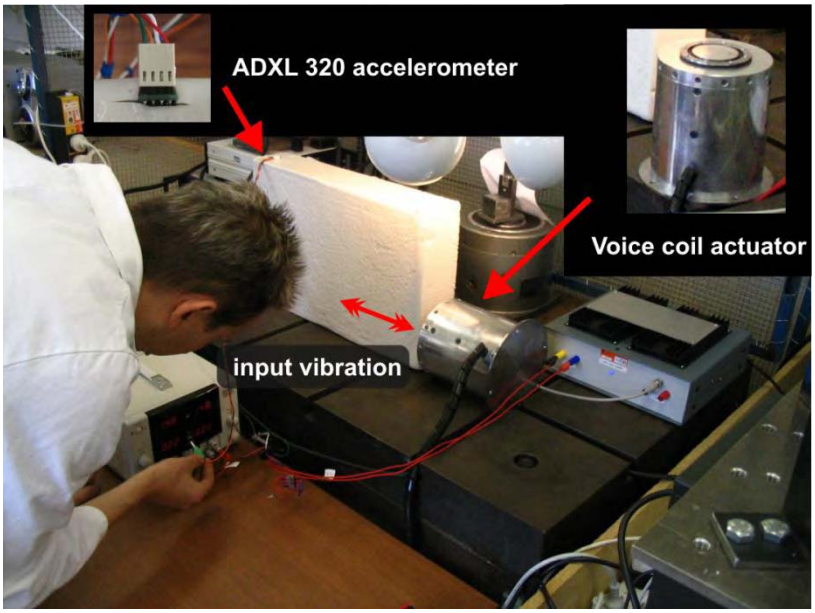

Figure B.3.4: Setup – Sinusoid wave transmission and accelerometer performance test at the Mechanical Engineering laboratory facilities

Uni-axial compression test

A compression test was conducted on a cube of Rhodorsil® RTV 585 silicone. The test took place in the laboratory of the Mechanical Engineering Department (Canterbury University) under the supervision of Mr. Kevin Stabbs (technician).

Adjustments of the testing apparatus:

- max. load limit: 9 kN

- loading rate: 2 mm/min

- plate size: 30 mm x 30 mm (A = 900 mm2)

Sample size: h x w x l = 35 mm x 42 mm x 42 mm

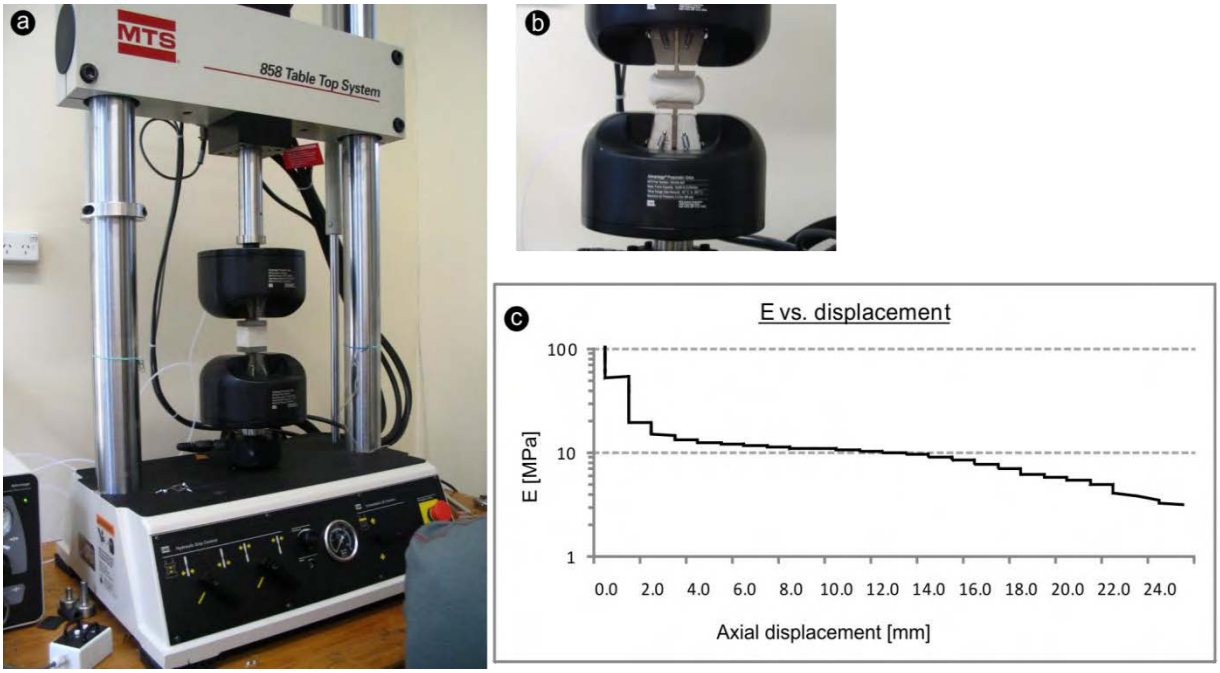

Figure B.3.5: Pictures showing a) test setup of the uni-axial compression test, b) RTV sample bulging under compression, and c) behavior of the Young's modulus, E, during increased compression and deformation of the cubic Rhodorsil® RTV 585 silicone sample

The uni-axial compression test revealed the elastic modulus follows a complex dynamic behavior depending on the amount of compression of the material (Figure B.3.5).

Advanced Compression & Shearing test – micro samples

At a later stage of the project we got the chance to conduct further tests on the Rhodorsil® RTV 585 silicone utilizing a Dynamic Material Analyzer (DMA) at the Mechanical Engineering Department (Canterbury University). Dr Elijah Van Houten and Dr Mark Staiger run compression and shear test on RTV 585 silicone samples on different frequency to evaluate advanced elastic material properties which should provide information for further projects dealing with silicone modeling.

The parameters that were measured during the tests represent the visco-elastic properties of the material. The Storage Modulus E' relates to the elastic behavior of the material (the instantaneous response of the material), while the Loss Modulus E'' relates to the inelastic behavior of the material - the non-instantaneous response, the stress component that is not in phase with the deformation. Tan D represents the ratio of loss over storage: $\tan D = \frac{E''}{E'}$ and gives information

on how viscous the material is behaving. The more viscous the material is behaving, the more energy is being dissipated and therefore tan D gives us information on damping at certain frequencies.

The amplitudes of stress waves in a material attenuate with distance. Two effects, a material effect and the geometry of the wave propagation, influence attenuation in a specific material:

a) Material damping

   Part of the elastic energy of a travelling stress wave is converted to heat. This conversion results in a decrease of specific energy (elastic energy per unit volume) as the stress wave travels through the material. The reduction of specific energy causes the amplitude of the stress wave to decrease with distance.

b) Radiation damping

   Radiation damping (also referred to as geometric attenuation) describes the reduction in amplitude due to spreading of energy over a greater volume of material as the stress wave travels away from its source.

Figure B.3.6 and B.3.7 present results of the advanced compression and the shearing tests that were conducted on the micro-samples. The results for both tests show that with increasing frequency more energy is being dissipated. The increase in the Loss modulus for increasing frequencies is outweighing the increase in the Storage modulus and therefore results in an increase in tan D and an increased damping effect.

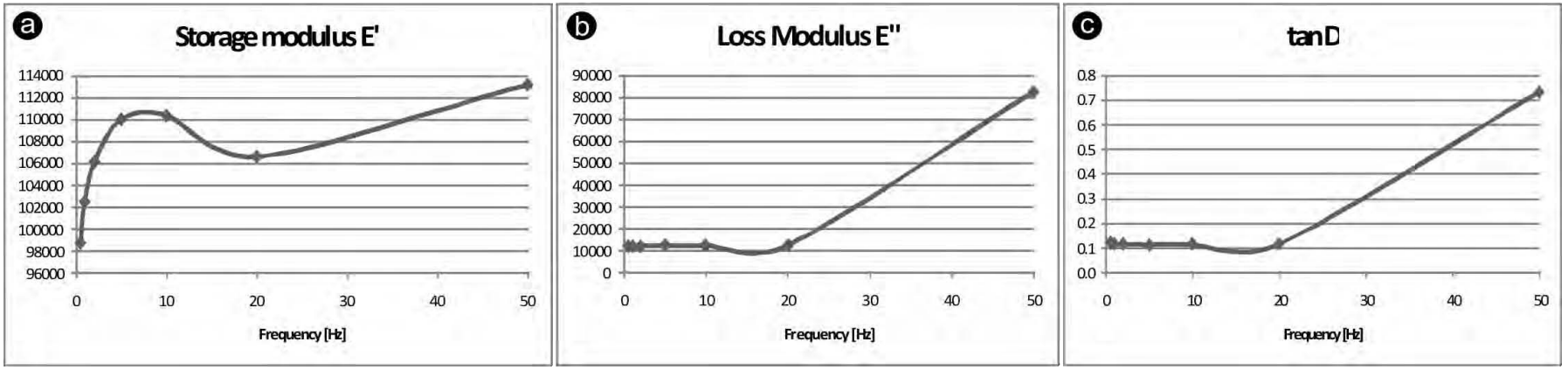

Figure B.3.6: Compression test results (test A) showing a) the Storage modulus E', b) the Loss modulus E'', and c) tan D at a temperature of approximately 17 °C for a set of frequencies

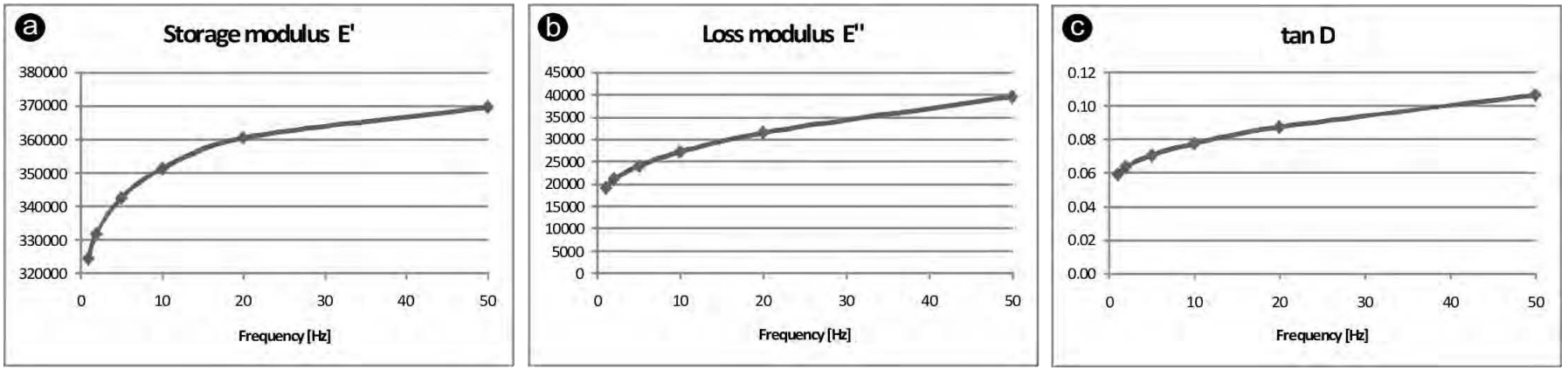

Figure B.3.7: Shearing test results (shear 3) showing a) the Storage modulus E', b) the Loss modulus E'', and c) tan D at a temperature of approximately 18.5 °C for a set of frequencies

Input device & wave propagation tests

Following input devices were tested for the suitability of simulating a seismic wave source under small-scale laboratory conditions (Figure B.3.8):

- Hammer (shear wave input)
- Sledgehammer (shear wave, compressional wave input)
- Electromagnetic actuator (compressional wave input)

a) **Hammer input** device (hammer attached to rack incl. scale and release mechanism)
b) L-shaped metal plate attached to the base of the model used to simulate shear wave input
c) Hammer being released and producing a shear wave actuation
d) **Sledgehammer** (used to produce forceful instantaneous Delta-function input)
e) **Small metal ball** (used to produce high frequency input)
f) **Voice coil actuator** (controlled compressional wave input up to 500 Hz)

Figure B3.8: Display of input devices that were tested for the suitability of simulating a seismic wave source under small-scale laboratory conditions

The use of a hammer device as the seismic input source turned out to be of little use for producing a wave input with appropriate wavelength to simulate amplification and deamplification effects across the mountain model. The physical input caused by the single impulse hammer input load on the material surface results in a forceful instantaneous input. It is mathematically also known as a Dirac Delta Function (Figure B.3.9).

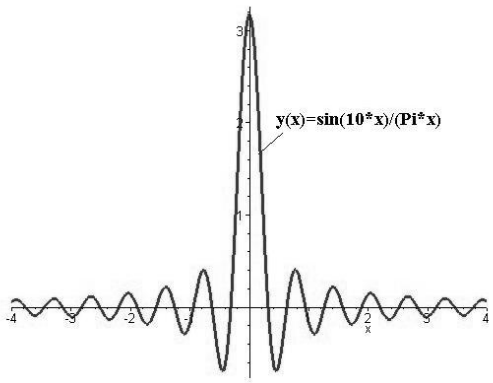

Figure B.3.9: Graph displaying an approximation to the Dirac Delta Function (http://aemes mae.ufl.edu/~uhk/DIRAC.jpg)

Tests using the hammer input device show that the energy imparting into the system seems to be quite low which suggests that most of the high frequency content attenuates within the first few centimeters, leaving only a small amount of low frequency components.

Silicone RTV 585 test block – Signal test

Test 1 outline – compressional wave input:

A signal test was conducted on the RTV 585 silicone test block (51 x 32 x 9.5 cm) using one ADXL 320 (LabVIEW configuration: referenced single ended, 2000 samples to read, rate: 500 Hz). The accelerometer was vertically placed into a cut that was made into the material.

The test was conducted placing the sensor at a distance of 10, 20, 30, and 40 cm away from signal input (Figure B.3.10). Three tests per location.

Compressional wave input signal using the electromagnetic actuator: sine wave form, 50 Hz, duration 4 s signal +- 1 s turn off, amplitude 1.

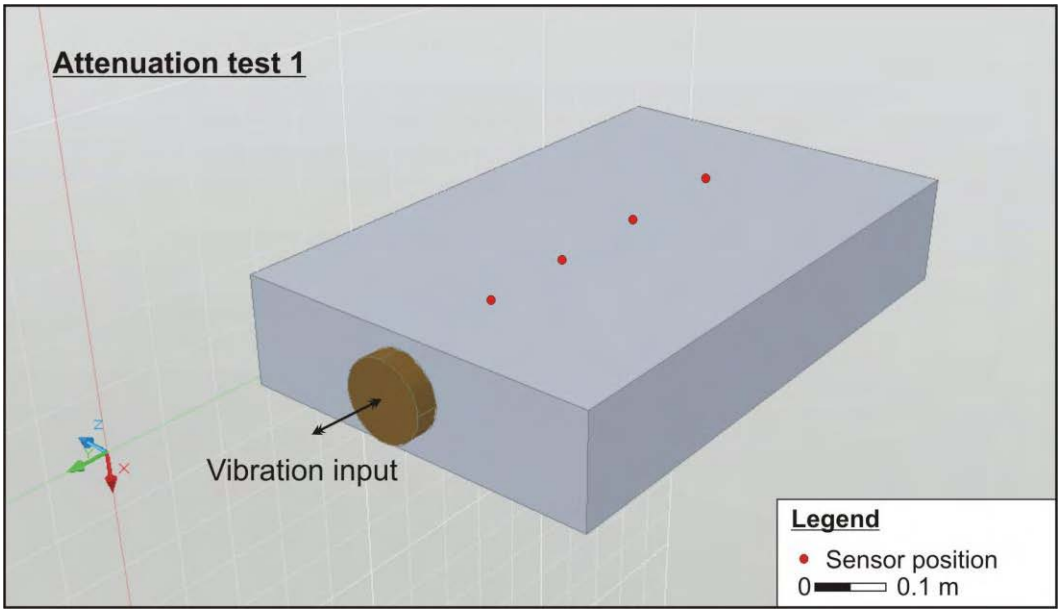

Figure B.3.10: Test configuration showing the distribution of measuring points across the silicone test block to determine the spatial variation of the signal strength

The results are presented in figure B.3.11.

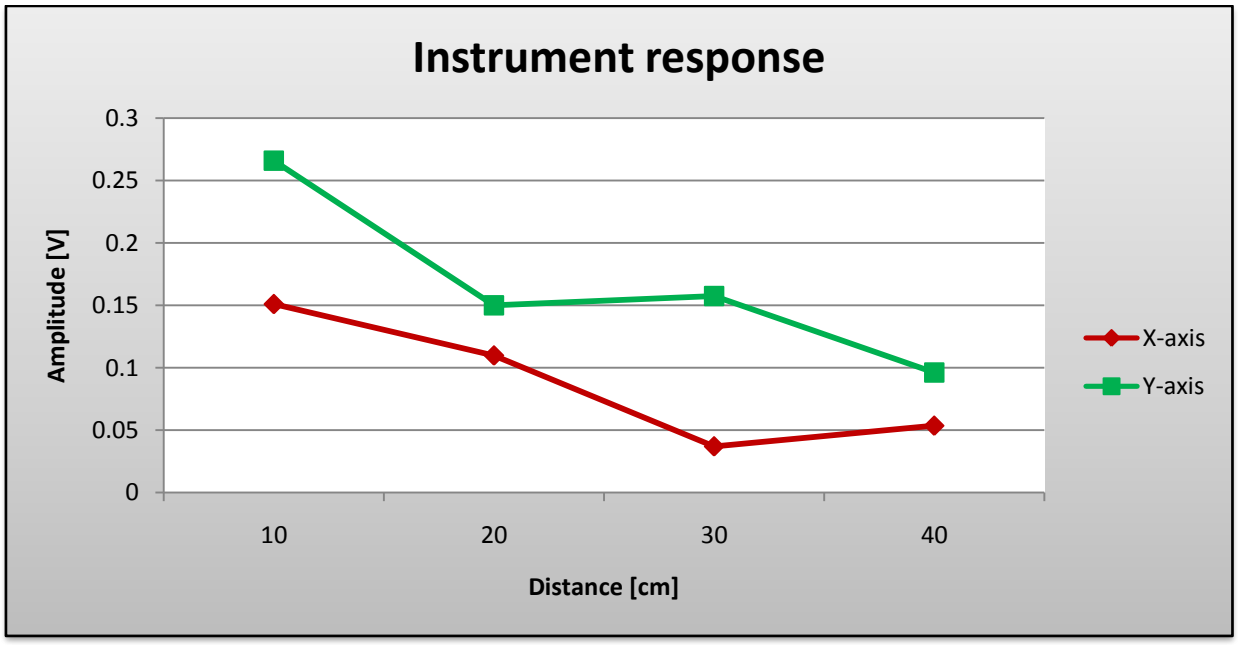

Figure B.3.11: Signal amplitudes computed from the signal test conducted at the RTV 585 silicone test block. Signals are shown for the vertical component (X-axis) and the transverse component (Y-axis) at the measuring points at distances of 10, 20, 30, and 40 cm away from the input

The signal attenuation test across the surface of the silicone test block shows the signal decreases with distance for the measuring points. A signal loss of about 40% is computed for the signal between 10 cm and 40 cm from the input source.

Test 2 outline – shear wave input:

A signal attenuation test was conducted on the RTV 585 silicone test block (51 x 32 x 9.5 cm) using two ADXL 320 (LabVIEW configuration: referenced single ended, 2000 samples to read, rate: 500 Hz). The accelerometers were vertically placed into a cut that was made into the material.

The test was conducted placing one sensor at a distance of 10 cm (base) and the other sensor (hill) at 10, 20, and 30 cm away from the base accelerometer (Figure B.3.12). Three tests per location.

Shear wave input signal was simulated using the hammer input device (Figure B.3.8 a)-c)).

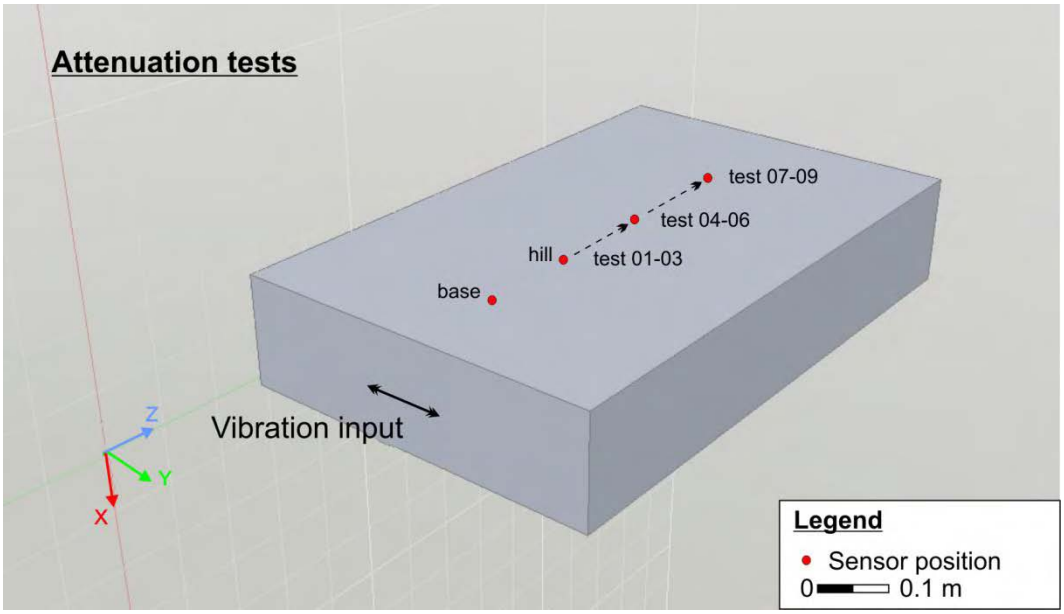

Figure B.3.12: Test configuration showing the distribution of measuring points across the silicone test block to determine the spatial variation of the signal strength. Shear wave input was provided by a hammer device

The results are presented in figure B.3.13.

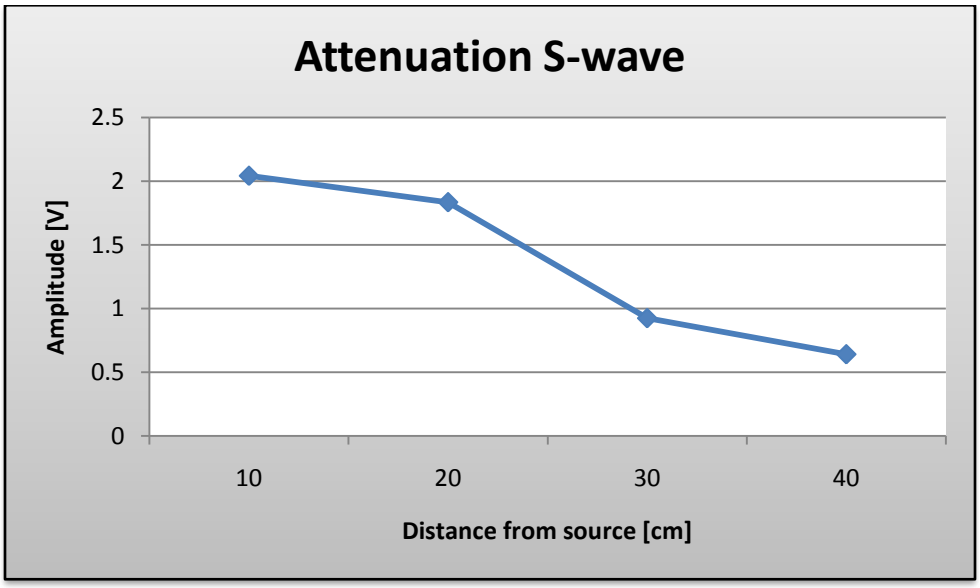

Figure B.3.13: Signal amplitudes computed from the signal test conducted at the RTV 585 silicone test block. Signals are shown for the horizontal component (Y-axis) at measuring points 10, 20, 30, and 40 cm away from the input source

Silicone base – Signal test

Test outline:

A signal test was conducted using one ADXL 320 (LabVIEW configuration: referenced single ended, 100 samples to read, rate: 500 Hz). The accelerometer was mounted flat/horizontally onto the surface of the silicone base.

Compressional wave input signal using the electromagnetic actuator: sine wave form, 50 Hz, duration 3 s signal +- 1 s turn off, amplitude 1.

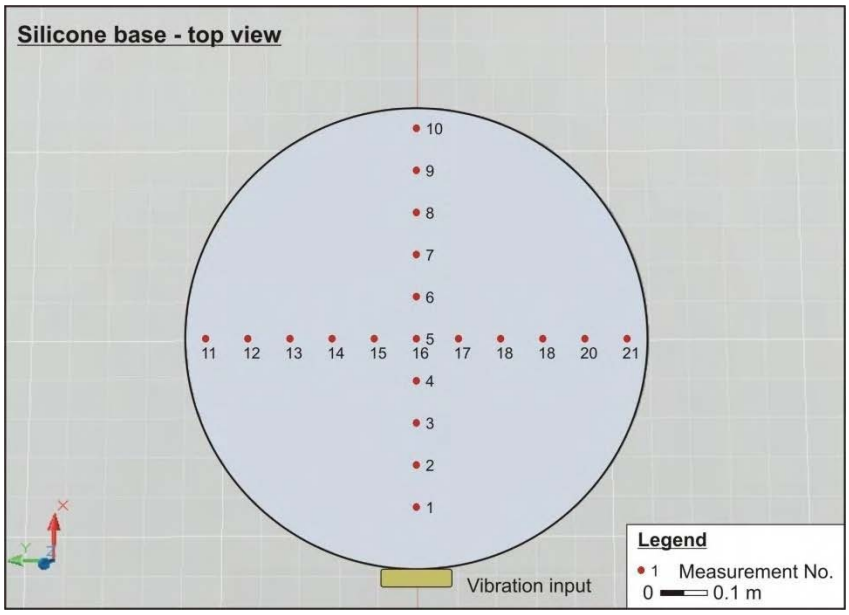

Figure B.3.14: Test configuration showing the distribution of measuring points across the silicone base to determine the spatial variability of the signal strength

Concept (Fig. B.3.14):

I. Collect data by placing ADXL at positions across the model on a path transverse to the wave input (points 1-10)
II. then on a perpendicular trace across the centre of the silicone base (points 11-21)

21 measurements were conducted across the base. First measurement at point 1. Measurement 5 at centre point, 10 at the far end. Then start at the left (point 11). Measurement 16 in the centre again. Last measurement at point 21.

The results are presented in figure B.3.15.

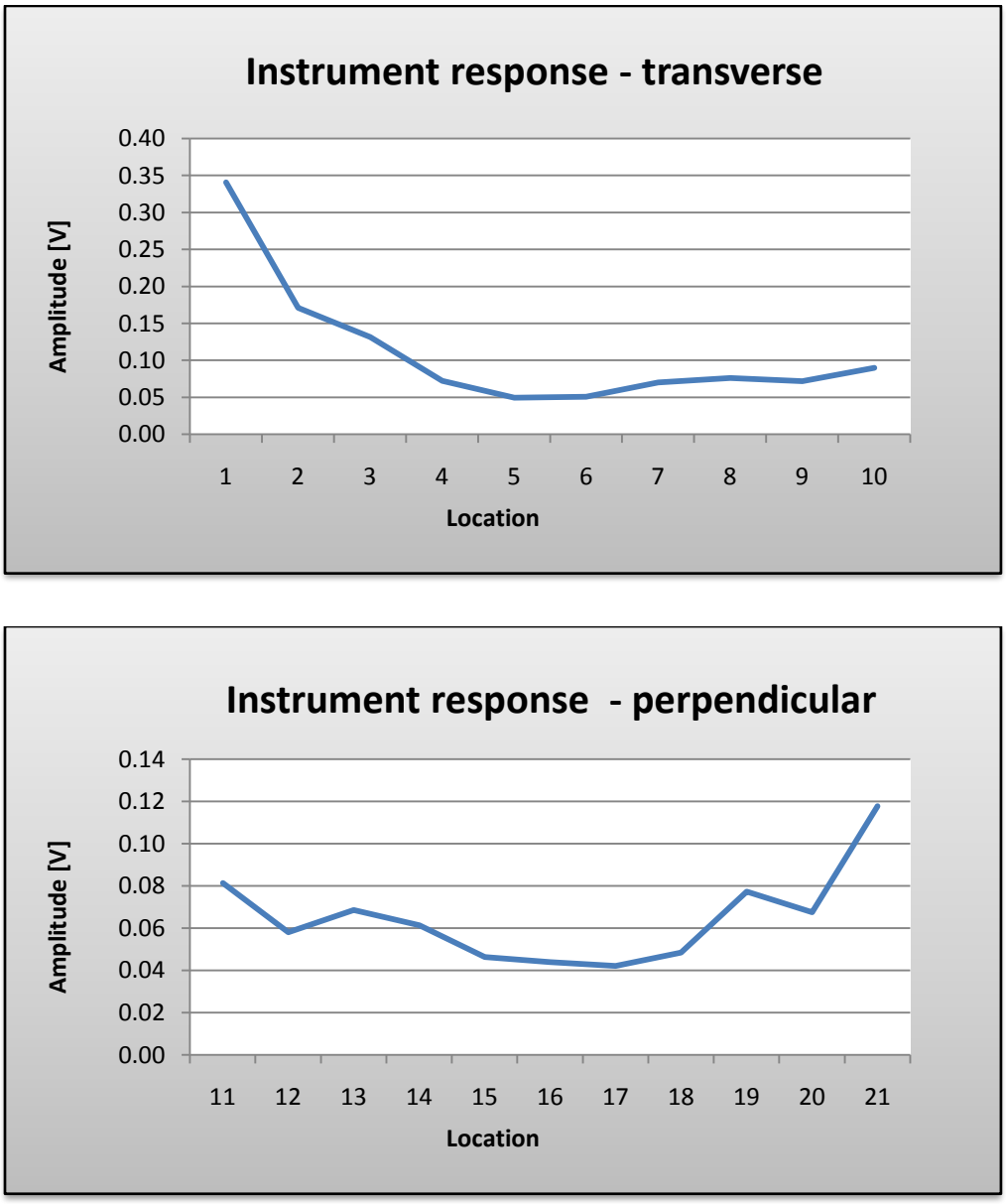

Figure B.3.15: Signal amplitudes computed from the signal test conducted across the silicon base. Signal amplitudes are presented for the measurement points transverse to the wave input (points 1-10) and for the measurement positions perpendicular to the wave input (points 11-21).

The signal test across the surface of the silicone base of the model shows the signal drastically decreases with distance for points 1 to 10. The variation across the centre of the base on a path perpendicular to the wave input shows small signal variation.

Mountain model response tests – hammer device

A signal test was conducted on the RTV 585 silicone laboratory mountain model using two ADXL 320 accelerometers (LabVIEW configuration: referenced single ended, 2000 samples to read, rate: 2000 Hz). The accelerometers were glued horizontally onto the surface of the silicone. One sensor was placed at the base next to the hill (23.5 cm from the input source at 0 degrees) and one at centre of the hill (58.7 cm from the input source at 0 degrees)

The setup is shown in figure B.3.16.

Shear wave input signal was simulated using the hammer input device (Fig. B.3.8 a-c) from different angles towards the main axis of the mountain model. Three tests were conducted at each position. The incident angle was changed at 45 degree increments.

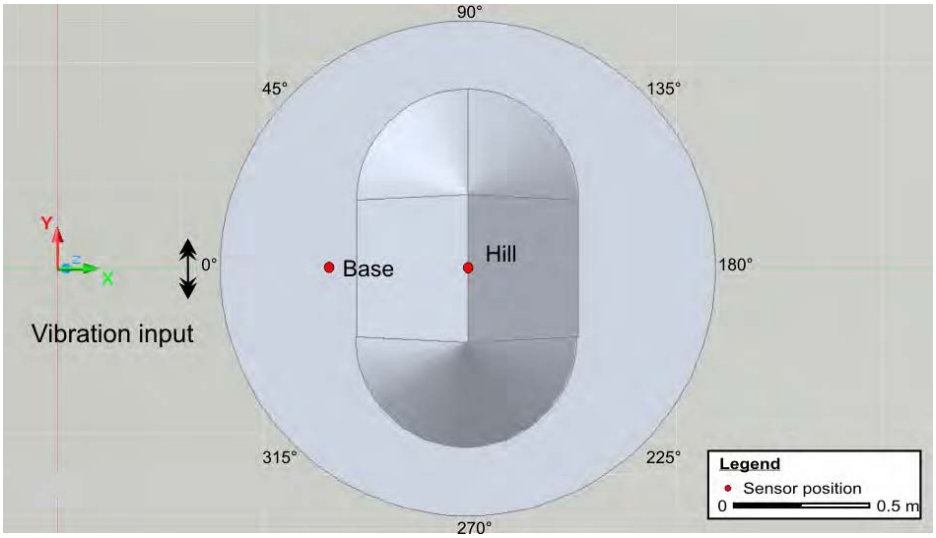

Figure B.3.16: Test configuration showing the distribution of measuring points around the silicone base and the position of the accelerometers to determine the response for different angles of incident for a shear wave input simulated by the hammer input device

The results are presented in figure B.3.17.

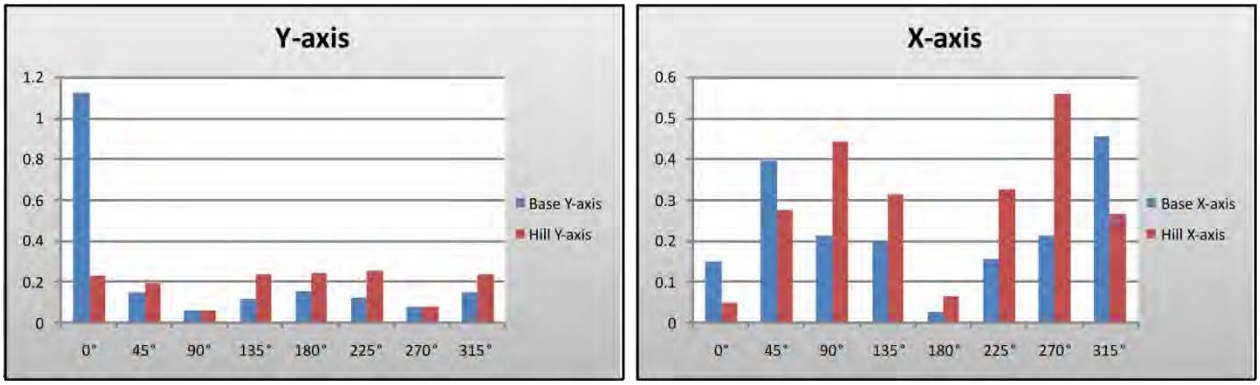

Figure B.3.17: Amplitude response for the accelerometer positions at the base and the centre of the hill and motion components perpendicular (X-axis) and parallel (Y-axis) to the main axis of the mountain edifice

The test using the hammer as a shear wave input device from different angles towards the main axis of the mountain edifice shows strong amplitude decrease for the initial position at 0 degrees for both motion components comparing the response of the base station with the response at the centre of the ridge. The response of the ridge is highest for shear waves polarized perpendicular to the main axis of the edifice. Additional meaningful interpretation was impossible due to the complex visco-elastic behavior of the silicone.

Mountain model response tests – sledgehammer device

A signal test was conducted on the RTV 585 silicone laboratory mountain model using three ADXL 320 accelerometers (LabVIEW configuration: referenced single ended, 2000 samples to read, rate: 2000 Hz). The accelerometers were glued horizontally onto the surface of the silicone. Two sensors were placed at the base on either side next to the hill (*Base 1* at 20 cm from the input source, *Base 2* at 82 cm from the input source) and one at centre of the ridge crest (*Hill* at 58.7 cm from the input source).

The setup is shown in figure B.3.18.

A strong compressional wave input signal was simulated using the sledgehammer as an input device (Fig. B.3.8 d) at an angle of 0 degrees perpendicular towards the main axis of the mountain model. A metal plate was attached to the base and hit by the sledgehammer to increase the high frequency components of the input signal.

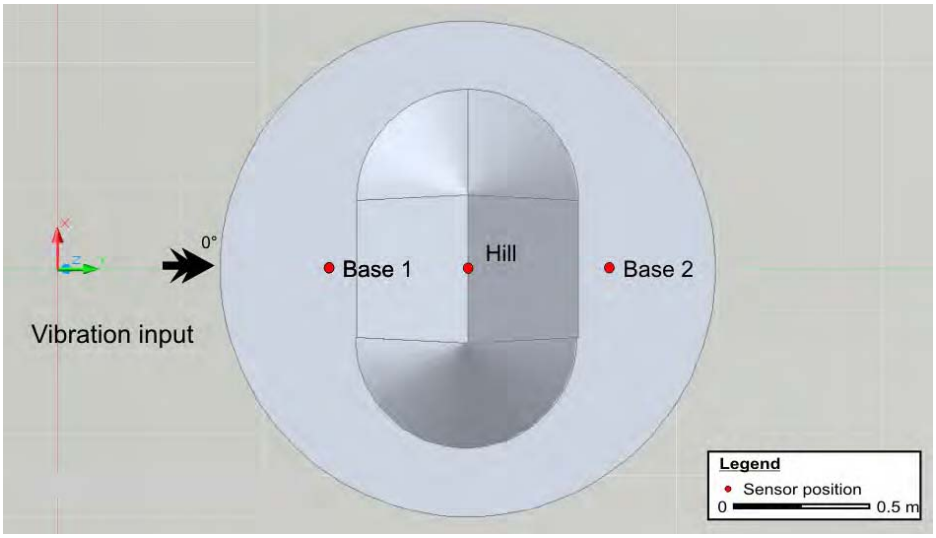

Figure B.3.18: Test configuration showing the position of the accelerometers to determine the response for a strong compressional wave input simulated by the sledgehammer

The results showing the signal response of the instruments for the motion component perpendicular to the main mountain axis (Y-axis) as well as results showing a frequency domain analysis of the received signal are presented in the following paragraph.

The results for the instruments show strong attenuation effects mainly affecting the high frequency components of the input signal. The response is smallest for the site at the ridge crest. The analysis of the Fourier amplitude plots of the signals shows a distinct loss of the high frequency components over distance. The signals transmitting the highest energy are in a frequency range of about 30 Hz. The corresponding wavelengths are too long compared to the base of the mountain and therefore not able to cause amplification effects at the ridge crest. This is shown by the weak response of the crest to the heavy compressional impact signal caused by the sledgehammer.

References

Van Houten, E., 2007. Technical meeting: Silicone - seismic wave actuator.

Sledgehammer Test - Base1 Y-axis

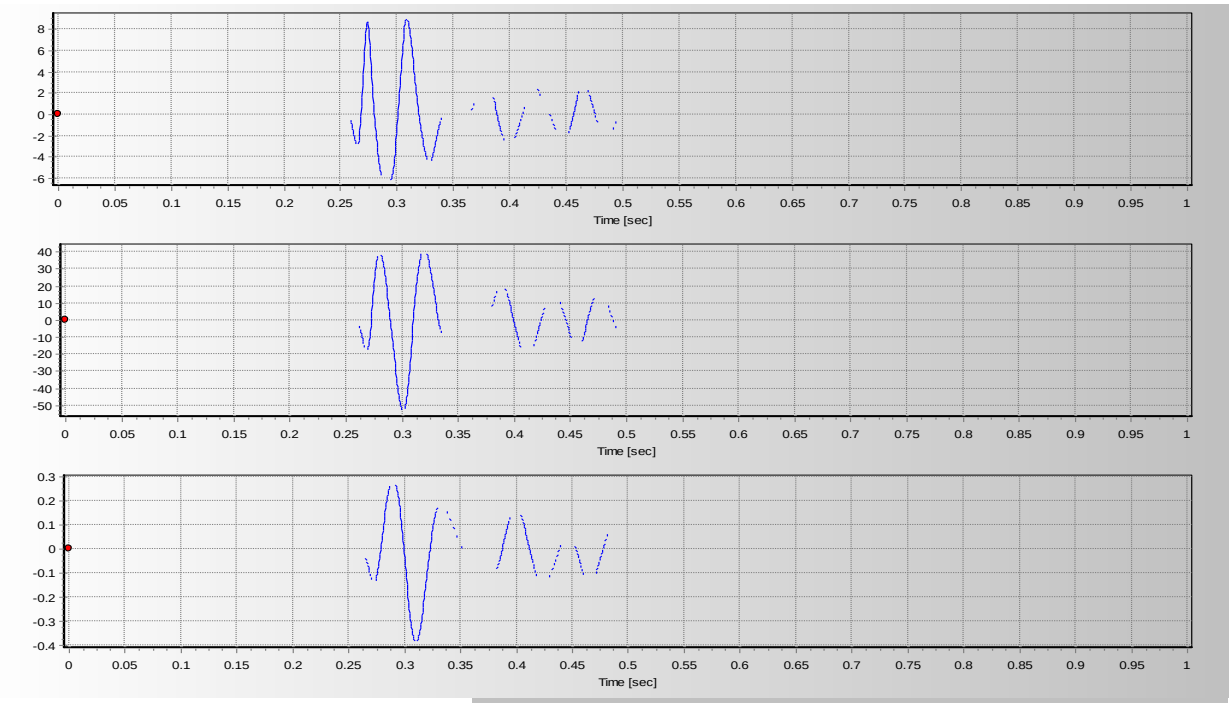

Maximum Acceleration: 9.04945739g
at time t=0.3085sec

Maximum Velocity:
53.64178791cm/sec
at time t=0.3005sec

Maximum Displacement:
0.38862082cm
at time t=0.31sec

Predominant Period (Tp): 0.04sec

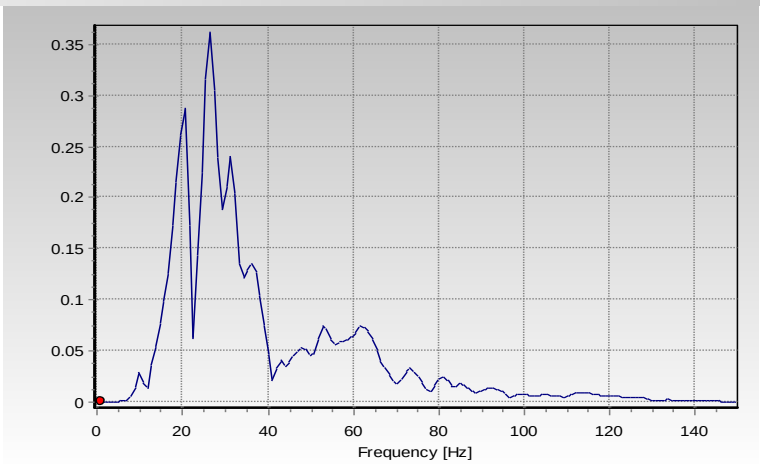

Sledgehammer Test - Hill Y-axis

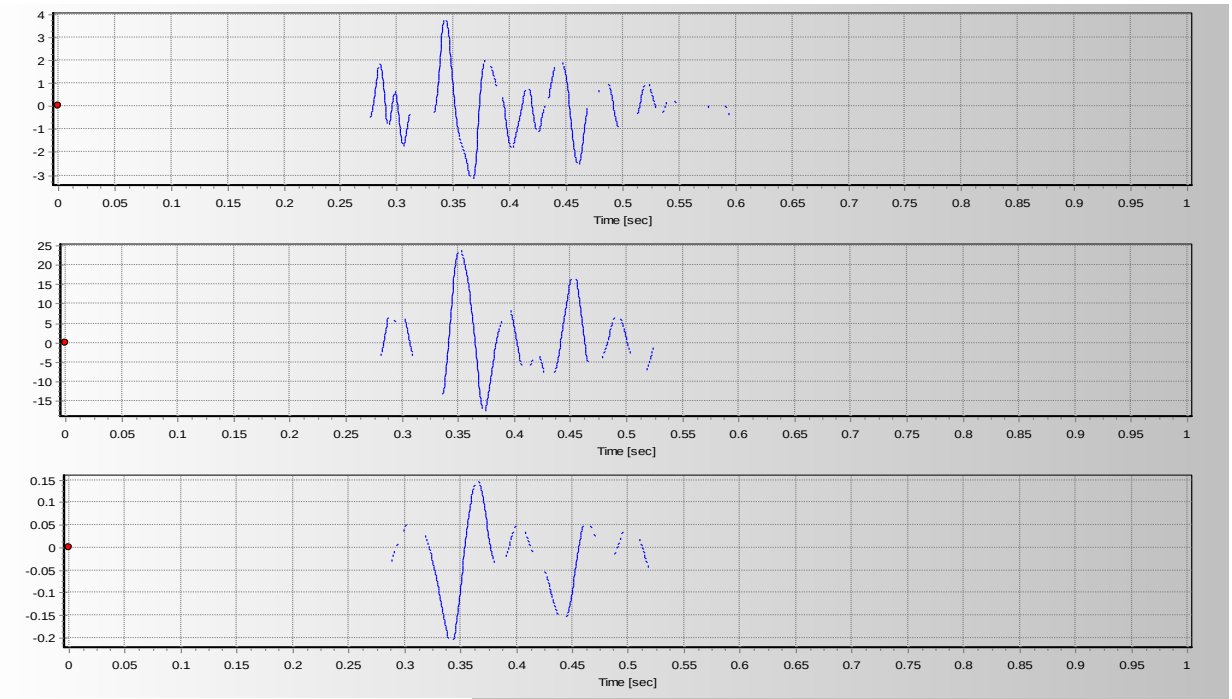

Maximum Acceleration: 3.86140141g
at time t=0.3425sec

Maximum Velocity:
24.08613247cm/sec
at time t=0.351sec

Maximum Displacement:
0.21150093cm
at time t=0.3415sec

Predominant Period (Tp): 0.04sec

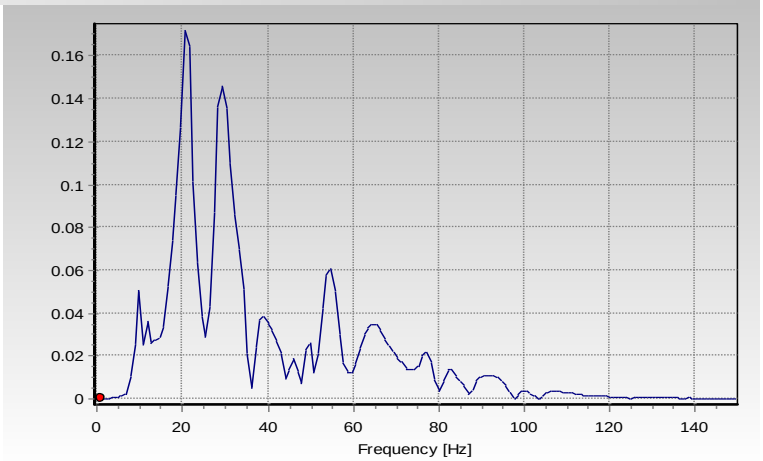

Sledgehammer Test – Base 2 Y-axis

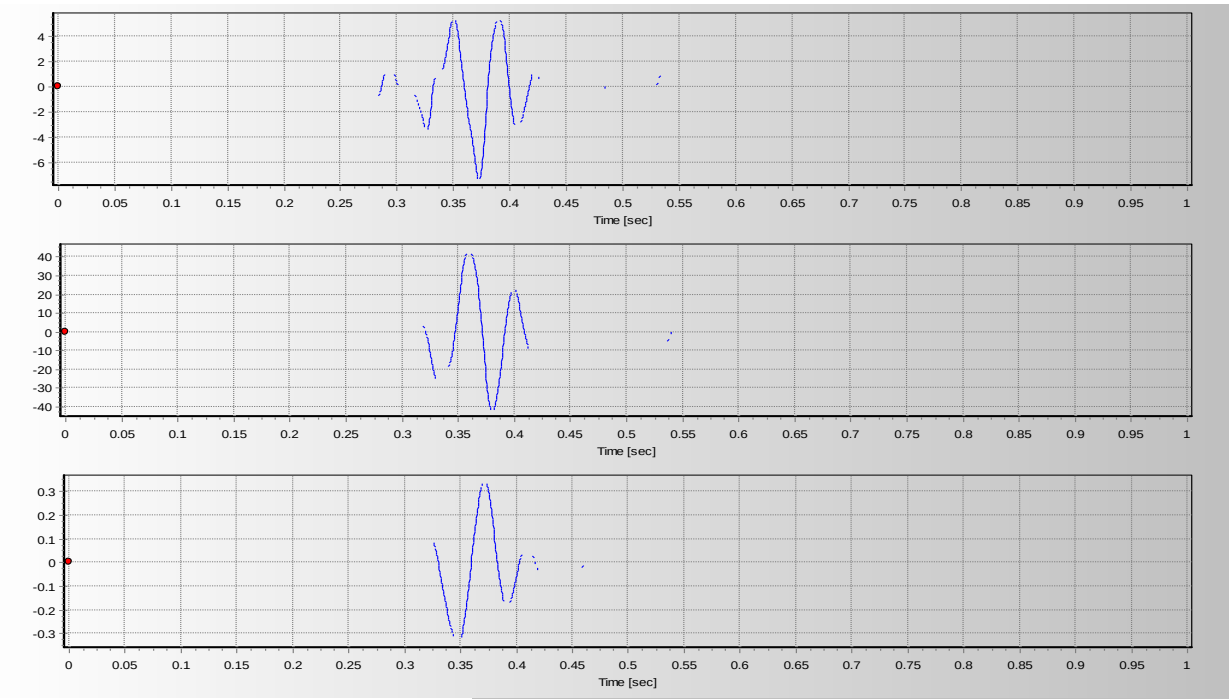

Maximum Acceleration: 7.47187536g
at time t=0.3725sec

Maximum Velocity:
44.17398406cm/sec
at time t=0.3595sec

Maximum Displacement:
0.34647619cm
at time t=0.3715sec

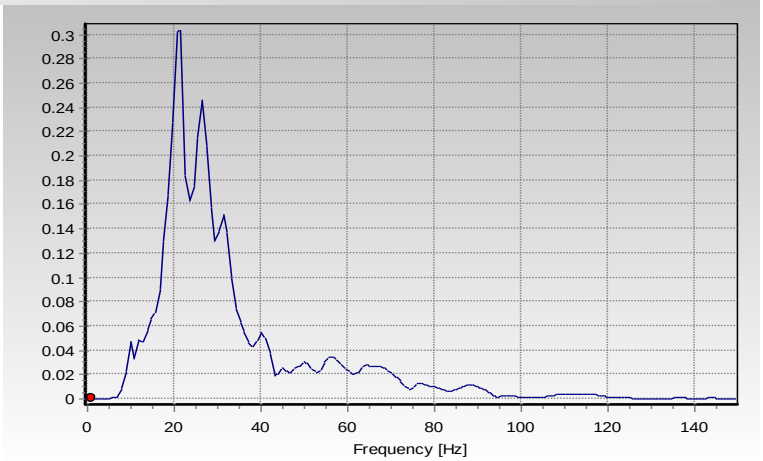

Predominant Period (Tp): 0.04sec

Module	DMS							
Channel	1							
Data Name	Eli 15-10-07							
Measurement Time	16/10/2007 2:25:06 p.m.							
Sample Name	silicone							
Sample Shape	Geometry Factor	0.02618	m					
	Length	3	mm					
	Diameter	10	mm					
Temperature Program		Cel		Cel		Cel/min	min	
	1	15		15		2	10	
	Sampling	1	s					
	Temperature Program Mode	Ramp						
Measurement Mode	Compression							
Meas. Frequency Information								
	Meas. Frequency	7	Frequency					
		0.5	Hz					
		1	Hz					
		2	Hz					
		5	Hz					
		10	Hz					
		20	Hz					
		50	Hz					
Operator Name	PYRIS							
Organization Name	University of Canterbury							
Comment	Operator: PYRIS							
	Gas1: N2							

Freq.	Temp.	E'(G')	E"(G")	dL	tanD	Ft	Time
Hz	Cel	Pa	Pa	um		mN	min
50	17.17035866	100118.1	98092.72	-575.672	0.97977	-72.6283	0.15
20	17.15267181	131441.9	15300.76	-575.672	0.116407	-80.4625	0.25
10	17.17288589	130277.8	13686.45	-575.672	0.105056	-80.4625	0.366667
5	17.15488243	126797.4	13053.88	-575.672	0.102951	-80.4625	0.483333
2	17.17067528	121244.7	12974.77	-575.672	0.107013	-80.4625	0.616667

1	17.16530609	116605.3	13300.27	-575.672	0.114062	-80.4625	0.8
0.5	17.16751671	112353.8	13355.39	-575.672	0.118869	-80.4625	1.016667
50	17.15519905	111674.1	82190.76	-563.172	0.735987	-40.326	1.133333
20	17.16246223	111890.6	13636.59	-565.255	0.121874	-57.8612	1.233333
10	17.15235519	114980.5	13314.89	-568.033	0.115801	-64.4233	1.35
5	17.14793396	116111.2	12599.61	-570.116	0.108513	-64.9899	1.466667
2	17.15646172	115139.8	12643.91	-570.81	0.109814	-74.0811	1.616667
1	17.14540672	111361	12019.64	-570.81	0.107934	-72.4289	1.8
0.5	17.14003754	107776.1	11704.42	-570.81	0.108599	-70.9358	2.016667
50	17.14130211	117499.1	87045.14	-562.477	0.740815	-38.9915	2.116667
20	17.14288139	109318.9	12985.73	-562.477	0.118788	-53.0453	2.216667
10	17.1356163	113439.6	12831.78	-564.561	0.113116	-61.2095	2.333333
5	17.14351273	112165	12713.94	-565.949	0.11335	-63.2934	2.45
2	17.13972282	108593	12825.04	-566.644	0.118102	-63.4696	2.6
1	17.11982346	104394.1	12617.8	-566.644	0.120867	-62.2916	2.783333
0.5	17.13056183	100538.8	12470.64	-566.644	0.124038	-61.1571	2.983333
50	17.11034966	115614.2	79701.33	-560.394	0.689373	-36.1633	3.1
20	17.11856079	105505.1	12899.41	-561.088	0.122263	-52.2818	3.2
10	17.11287498	111291.8	12714.78	-563.866	0.114247	-60.6722	3.316667
5	17.09960938	110722.1	12527.32	-565.949	0.113142	-62.0462	3.433333
2	17.1094017	106149.9	12283.78	-565.949	0.115721	-61.3749	3.566667
1	17.1018219	102221.3	11954.22	-565.949	0.116944	-60.0831	3.75
0.5	17.08855629	97990.03	12216.69	-565.949	0.124673	-58.8432	3.966667
50	17.08602905	116408.2	80184.45	-559.699	0.688821	-33.8607	4.083333
20	17.08792305	104110.2	11910.7	-560.394	0.114405	-51.0137	4.183333
10	17.07465935	109317.6	12613.26	-563.172	0.115382	-60.0589	4.3
5	17.06929016	109689.8	12540.13	-565.949	0.114324	-61.562	4.416667
2	17.06423569	104873.3	12255.82	-565.949	0.116863	-60.5831	4.55
1	17.05539131	101200.2	11992.25	-565.949	0.1185	-59.3431	4.733333
0.5	17.04086304	97212.44	12257.62	-565.949	0.126091	-58.0261	4.95
50	17.03581047	115756.6	80678.99	-559.699	0.696971	-33.987	5.066667
20	17.03612518	103333.9	11963.11	-560.394	0.115771	-50.7743	5.166667
10	17.03170395	108953.7	12864.43	-563.172	0.118072	-59.3733	5.283333
5	17.03170395	109153.6	12541.79	-565.949	0.1149	-61.2439	5.4
2	17.02064896	104479.4	12098.26	-565.949	0.115796	-60.1618	5.533333
1	17.02254486	101004.4	12019.13	-565.949	0.118996	-59.0611	5.716667

0.5	17.02917671	96899.77	12215.66	-565.949	0.126065	-57.7637	5.933333
50	17.02349281	115252.7	81834.52	-559.699	0.710044	-34.1587	6.05
20	17.01843834	103472.8	11879.55	-560.394	0.114808	-50.424	6.15
10	17.01496506	108140	12452.74	-563.172	0.115154	-59.1486	6.266667
5	17.01275444	109334.8	12500.88	-565.949	0.114336	-61.0758	6.383333
2	17.00359344	104305.9	11915.86	-565.949	0.11424	-60.0208	6.533333
1	17.00106812	100567.5	11768.48	-565.949	0.117021	-59.0173	6.716667
0.5	16.99790955	97046.41	12022.64	-565.949	0.123885	-57.6919	6.933333
50	16.99127579	114774.1	79277.66	-552.061	0.690728	-34.5151	7.1
20	16.98748589	100307.8	11267.96	-552.755	0.112334	-44.2696	7.2
10	16.98116875	103208.7	11337.57	-555.533	0.109851	-51.6965	7.316667
5	16.9745369	102799.4	11885.3	-557.616	0.115616	-53.5117	7.433333
2	16.96600914	98415.35	11211.68	-557.616	0.113922	-52.5118	7.566667
1	16.9634819	95419.6	10848.46	-557.616	0.113692	-51.4714	7.75
0.5	16.95369148	91939.21	10750.18	-557.616	0.116927	-50.5808	7.966667
50	16.9521122	110526.6	73132.3	-549.283	0.661671	-29.9298	8.083333
20	16.94010925	96849.39	11192.44	-551.366	0.115565	-42.7162	8.183333
10	16.93947792	100857.4	11107.83	-554.838	0.110134	-49.4788	8.3
5	16.93663597	100333.9	11257.89	-556.922	0.112204	-50.8767	8.416667
2	16.92526436	98688.03	11403.23	-558.311	0.115548	-54.8105	8.566667
1	16.91515923	95507.4	10887.18	-558.311	0.113993	-53.962	8.75
0.5	16.9053669	92553.2	10586.17	-558.311	0.114379	-52.9196	8.95
50	16.89589119	114185.8	78742.75	-552.061	0.689602	-30.3118	9.066667
20	16.89525986	99867.22	11150.66	-552.755	0.111655	-45.6396	9.166667
10	16.89210129	103262.4	11400.67	-556.227	0.110405	-53.4751	9.283333
5	16.89336586	102775.7	11455.31	-558.311	0.111459	-54.9779	9.4
2	16.88389015	98751.86	10892.58	-558.311	0.110303	-54.9169	9.55
1	16.88925934	95818.64	10472.05	-558.311	0.10929	-54.0043	9.716667
0.5	16.87946892	92852.64	10340.8	-558.311	0.111368	-53.1226	9.933333

Module	DMS							
Channel	1							
Data Name	Eli 15-10-08 - b							
Measurement Time	16/10/2007 3:15:23 p.m.							
Sample Name	silicone							
Sample Shape	Geometry Factor		0.02618	m				
	Length		3	mm				
	Diameter		10	mm				
Temperature Program		Cel		Cel		Cel/min	min	
	1		15		15		2	10
	Sampling		1	s				
	Temperature Program Mode	Ramp						
Measurement Mode	Compression							
Meas. Frequency Information								
	Meas. Frequency		7	Frequency				
			0.5	Hz				
			1	Hz				
			2	Hz				
			5	Hz				
			10	Hz				
			20	Hz				
			50	Hz				
Operator Name	PYRIS							
Organization Name	University of Canterbury							
Comment	Operator: PYRIS							
	Gas1: N2							

Freq.	Temp.	E'(G')	E"(G")	dL	tanD	Ft	Time
Hz	Cel	Pa	Pa	um		mN	min
50	16.8042984	101308.618	95246.85698	-577.755	0.940165	-88.4323	0.15
20	16.80113983	142341.8802	16363.30138	-574.977	0.114958	-88.4323	0.266667
10	16.80113983	136312.4226	14904.50178	-571.505	0.109341	-82.1863	0.366667
5	16.80461311	133156.464	14069.73566	-571.505	0.105663	-87.164	0.483333
2	16.80492973	127528.4406	13539.06194	-571.505	0.106165	-87.164	0.633333

1	16.81093025	122998.6143	13635.70427	-571.505	0.110861	-87.164	0.816667
0.5	16.82040596	118272.2254	13839.38102	-571.505	0.117013	-87.164	1.033333
50	16.81472015	113771.6717	100973.0591	-555.533	0.887506	-42.3256	1.2
20	16.80935097	119675.86	14146.04843	-556.227	0.118203	-61.9759	1.3
10	16.81724739	121638.4457	13346.43705	-558.311	0.109722	-66.941	1.416667
5	16.81693077	119230.7733	12747.31894	-559.699	0.106913	-67.6727	1.533333
2	16.81819534	114481.1639	12219.06869	-559.699	0.106734	-66.3445	1.666667
1	16.81566811	110455.6318	12071.05925	-559.699	0.109284	-64.9797	1.85
0.5	16.82608986	105916.564	12021.20987	-559.005	0.113497	-63.5267	2.066667
50	16.82956505	115133.0806	94778.62438	-551.366	0.823209	-40.0302	2.183333
20	16.83146095	108654.6382	13136.85611	-552.061	0.120905	-50.7454	2.283333
10	16.83493423	112908.8965	13028.33427	-554.144	0.115388	-57.7155	2.4
5	16.8267231	111310.3965	12860.34965	-555.533	0.115536	-58.6127	2.516667
2	16.82608986	106516.0528	12877.4013	-555.533	0.120896	-57.55	2.65
1	16.83777618	102087.7436	13156.9875	-555.533	0.128879	-56.4754	2.833333
0.5	16.84156799	97679.65219	13044.44405	-555.533	0.133543	-55.1466	3.05
50	16.84156799	116260.5317	85881.11392	-547.894	0.738695	-35.3664	3.166667
20	16.84377861	102661.0278	11845.67044	-548.588	0.115386	-45.031	3.266667
10	16.84693718	105302.6207	12017.27569	-551.366	0.114121	-52.127	3.383333
5	16.84314537	106399.4096	12567.83949	-553.449	0.118119	-53.162	3.5
2	16.84693718	101744.5751	12002.97855	-552.061	0.117972	-52.2411	3.633333
1	16.85198975	97343.89743	11530.16015	-550.672	0.118448	-51.1015	3.816667
0.5	16.84819984	93679.84912	11182.66693	-549.977	0.119371	-49.9153	4.05
50	16.84630394	113241.1169	77606.26142	-541.644	0.685319	-31.1875	4.15
20	16.84535789	99619.08262	11719.84634	-544.422	0.117647	-44.7926	4.266667
10	16.84283066	104759.8774	11788.43411	-548.588	0.112528	-51.6388	4.366667
5	16.84851646	104546.1839	12128.54387	-550.672	0.116011	-55.1123	4.483333
2	16.84346199	102088.07	12002.52277	-552.061	0.11757	-58.119	4.633333
1	16.85420036	99114.34075	11801.26598	-552.061	0.119067	-56.7574	4.816667
0.5	16.84977913	95694.55486	11473.86569	-552.061	0.119901	-55.6199	5.033333
50	16.84788322	116393.336	92164.33658	-536.089	0.791835	-32.7001	5.2
20	16.85167313	101983.3915	11474.28067	-534.7	0.112511	-41.9086	5.3
10	16.84693718	103991.187	11040.98367	-536.089	0.106172	-49.1762	5.416667
5	16.85420036	102496.8993	10875.62301	-537.477	0.106107	-50.5496	5.533333
2	16.85767555	98920.6784	10419.72336	-538.172	0.105334	-50.2997	5.683333
1	16.86272812	95926.69416	10191.84115	-538.172	0.106246	-49.5369	5.866667

0.5	16.85925484	92413.97982	10238.67373	-538.172	0.110791	-48.638	6.083333
50	16.87125587	113583.8191	77975.16361	-532.616	0.686499	-32.2091	6.183333
20	16.86967659	99860.63133	11383.06577	-533.311	0.11399	-42.4687	6.283333
10	16.87283516	102762.1161	10999.91424	-536.089	0.107042	-48.8716	6.4
5	16.86651802	102201.5892	10848.37394	-538.172	0.106147	-49.9668	6.516667
2	16.86683464	98500.8171	10221.47055	-538.172	0.10377	-49.3918	6.666667
1	16.86872864	95116.25357	9904.863338	-538.172	0.104134	-48.6227	6.833333
0.5	16.86778259	91618.59988	10027.17523	-537.477	0.109445	-47.6953	7.066667
50	16.86936188	112391.9382	76599.43077	-529.144	0.681538	-28.6093	7.166667
20	16.86557198	97542.51161	11695.87052	-531.922	0.119905	-42.1326	7.266667
10	16.8567276	102129.8016	10937.78669	-536.089	0.107097	-48.9385	7.383333
5	16.85420036	102123.6001	10901.07459	-538.172	0.106744	-51.156	7.5
2	16.85420036	99163.11304	10367.31647	-538.866	0.104548	-53.4971	7.65
1	16.85988617	96213.34092	10022.07536	-538.866	0.104165	-52.5581	7.833333
0.5	16.84409332	93302.18563	10128.52927	-538.866	0.108556	-51.5493	8.05
50	16.83651352	115725.3515	85599.0553	-534.005	0.739674	-30.6902	8.15
20	16.83367157	101646.9466	11266.70704	-534.7	0.110842	-44.8115	8.266667
10	16.83556557	104577.6575	11193.37608	-537.477	0.107034	-52.5989	8.366667
5	16.83556557	103970.0648	10883.3993	-539.561	0.104678	-54.1583	8.483333
2	16.83367157	100153.1904	10430.08747	-539.561	0.104141	-53.7253	8.633333
1	16.82956505	97459.28166	10210.21935	-539.561	0.104764	-52.8976	8.816667
0.5	16.82988167	94075.5481	10119.84724	-538.866	0.107571	-52.0691	9.033333
50	16.83082771	115171.1659	83043.49008	-532.616	0.721044	-33.1925	9.133333
20	16.82640648	100466.8438	11304.74919	-533.311	0.112522	-42.5463	9.25
10	16.83209229	103296.6622	10882.57632	-536.783	0.105353	-49.3649	9.35
5	16.82451248	102570.7385	10684.19761	-538.172	0.104164	-50.6475	9.466667
2	16.82514381	98335.54153	9893.183168	-538.172	0.100606	-49.9789	9.616667
1	16.8267231	95856.09091	9803.235369	-538.172	0.10227	-49.3449	9.8

Module	DMS							
Channel	1							
Data Name	shear 1							
Measurement Time	26/10/2007 10:27:01 a.m.							
Sample Name	silicone							
Sample Shape	Geometry Factor		0.05405	m				
	Length		3.7	mm				
	Width		10	mm				
	Thickness		10	mm				
Temperature Program		Cel		Cel		Cel/min	min	
	1		16		16		2	10
	Sampling		1	s				
	Temperature Program Mode	Ramp						
Measurement Mode	Shear							
Meas. Frequency Information								
	Meas. Frequency		6	Frequency				
			1	Hz				
			2	Hz				
			5	Hz				
			10	Hz				
			20	Hz				
			50	Hz				
Operator Name	PYRIS							
Organization Name	University of Canterbury							
Comment	Operator: PYRIS							
	Gas1: N2							

Freq.	Temp.	E'(G')	E"(G")	dL	tanD	Ft	Time
Hz	Cel	Pa	Pa	um		mN	min
1	16.81819534	356794.4	22446.05	119.5461	0.06291	0	0.583333
1	16.84283066	358081.5	21829.76	124.4072	0.060963	0	9.483333
1	16.84314537	357810.2	21784.09	124.4072	0.060882	0	8.933333
1	16.84693718	357732.3	22006.78	123.0183	0.061517	0	4.483333
1	16.84883118	357801.3	21974.36	124.4072	0.061415	0	7.266667

1	16.84946251	357619.1	22362.3	119.5461	0.062531	0	1.133333
1	16.84977913	357970.9	21919.49	124.4072	0.061233	0	7.816667
1	16.85009575	357862.8	21913.68	124.4072	0.061235	0	8.383333
1	16.85830688	357636.4	22082.46	123.0183	0.061746	0	5.6
1	16.85956955	357688.8	22017.57	123.7127	0.061555	0	6.15
1	16.85988617	357680.8	21980.14	123.0183	0.061452	0	5.033333
1	16.86146545	357817.8	22002.04	123.7127	0.061489	0	6.716667
1	16.86209679	357820.5	22185.68	123.0183	0.062002	0	3.933333
1	16.86841393	357418.1	22150.42	121.6294	0.061973	0	2.25
1	16.86999321	357683.2	22419.64	120.2405	0.06268	0	1.683333
1	16.87094116	357391.1	22052.72	122.3238	0.061705	0	3.366667
1	16.8753624	357601	22026.88	121.6294	0.061596	0	2.816667
2	16.81787872	365292.4	24675.22	119.5461	0.067549	0	0.433333
2	16.830513	365913.6	24398.55	119.5461	0.066678	0	0.983333
2	16.83556557	366188	24016.18	124.4072	0.065584	0	9.883333
2	16.84188271	366228.8	24051.13	124.4072	0.065672	0	9.333333
2	16.84883118	366273.8	24062.22	124.4072	0.065695	0	8.783333
2	16.8491478	366255.3	24173.05	123.0183	0.066001	0	4.883333
2	16.85135841	366133.3	24054.56	124.4072	0.065699	0	8.233333
2	16.85198975	366164.5	24061.66	124.4072	0.065713	0	7.666667
2	16.85356903	365965.2	24106.23	123.0183	0.06587	0	4.333333
2	16.8567276	366092.9	24103.31	123.0183	0.065839	0	5.45
2	16.85925484	366196.3	24085.66	123.7127	0.065773	0	7.116667
2	16.86020088	366384.7	24346.9	123.0183	0.066452	0	3.783333
2	16.86114883	366086.3	24303.24	120.935	0.066387	0	2.1
2	16.86367607	366233.7	24135.7	123.7127	0.065902	0	6
2	16.86525536	366080.1	24292.39	121.6294	0.066358	0	2.666667
2	16.86557198	365931.8	24341.65	122.3238	0.06652	0	3.216667
2	16.86714935	366068.8	24074.16	123.7127	0.065764	0	6.566667
2	16.86841393	365850.1	24337.71	120.2405	0.066524	0	1.533333
5	16.81914139	377624.5	28100.94	119.5461	0.074415	0	0.316667
5	16.83304024	378141.5	27859.56	119.5461	0.073675	0	0.883333
5	16.8343029	378510.3	27555.36	124.4072	0.0728	0	9.783333
5	16.84504128	378539.5	27577.27	124.4072	0.072852	0	8.683333
5	16.84725189	378454	27554.54	124.4072	0.072808	0	8.116667
5	16.84788322	378284.6	27520.26	124.4072	0.07275	0	9.233333

5	16.84883118	378473.5	27576.66	124.4072	0.072863	0	7.566667
5	16.8529377	378158.6	27637.14	123.0183	0.073083	0	4.233333
5	16.85420036	378294.1	27593.43	123.0183	0.072942	0	4.783333
5	16.85893822	378417.9	27580.04	123.7127	0.072883	0	5.9
5	16.85956955	378288.3	27673.19	122.3238	0.073154	0	3.666667
5	16.86304474	378466.1	27583.22	123.7127	0.072882	0	7.016667
5	16.86399269	378188.1	27708	121.6294	0.073265	0	2.55
5	16.86399269	378260.5	27635.09	123.7127	0.073058	0	6.45
5	16.86557198	378103.7	27825.68	120.2405	0.073593	0	1.433333
5	16.86651802	378229.2	27724.67	122.3238	0.073301	0	3.116667
5	16.86683464	378294.9	27623.7	123.0183	0.073022	0	5.333333
5	16.87030792	378203.5	27749.47	120.935	0.073372	0	2
10	16.80461311	387884.2	31622.77	119.5461	0.081526	0	0.233333
10	16.82924843	388256.7	31456.35	119.5461	0.081019	0	0.8
10	16.83461761	388707	31269.14	124.4072	0.080444	0	9.7
10	16.84030342	388498.5	31210.47	124.4072	0.080336	0	8.6
10	16.8491478	388485.1	31228.41	124.4072	0.080385	0	8.033333
10	16.84946251	388398.1	31454.46	123.0183	0.080985	0	4.15
10	16.85041046	388543.5	31232.19	123.0183	0.080383	0	4.7
10	16.85230637	388647.1	31262.14	124.4072	0.080438	0	9.15
10	16.85388565	388498.9	31225.2	124.4072	0.080374	0	7.483333
10	16.85641098	388474.5	31292.45	123.0183	0.080552	0	5.25
10	16.8605175	388474.3	31275.12	123.7127	0.080508	0	5.816667
10	16.86146545	388458.5	31236.75	123.7127	0.080412	0	6.933333
10	16.86241341	388345.4	31218.17	122.3238	0.080388	0	3.583333
10	16.86335945	388440.2	31338.58	120.935	0.080678	0	1.916667
10	16.86683464	388344.1	31336.86	121.6294	0.080694	0	2.466667
10	16.86714935	388300.9	31354.83	120.2405	0.080749	0	1.35
10	16.86746597	388400.5	31251.95	123.7127	0.080463	0	6.366667
10	16.87062454	388365.9	31296.2	122.3238	0.080584	0	3.033333
20	16.80745697	398551.1	36541.4	119.5461	0.091686	0	0.166667
20	16.83304024	399054.6	36305.42	119.5461	0.090979	0	0.716667
20	16.83651352	399544.9	36038.76	124.4072	0.0902	0	9.616667
20	16.83872414	399394.2	36139.19	124.4072	0.090485	0	9.066667
20	16.84377861	399258.8	36170.68	124.4072	0.090595	0	8.516667
20	16.84598923	399294.4	36116.24	124.4072	0.09045	0	7.416667

20	16.84756851	399441.2	36157.48	124.4072	0.09052	0	7.966667
20	16.85135841	399355.6	36176.73	123.0183	0.090588	0	4.633333
20	16.85325241	399090.9	36293.13	120.2405	0.09094	0	1.283333
20	16.85451698	399319.2	36235.39	123.0183	0.090743	0	4.066667
20	16.8567276	399126.3	36035.95	123.0183	0.090287	0	5.183333
20	16.85988617	399198.3	36141.34	122.3238	0.090535	0	3.516667
20	16.86020088	399402.8	36205.07	123.7127	0.090648	0	5.733333
20	16.86146545	399445.7	36093.4	123.7127	0.090359	0	6.85
20	16.86683464	399146.1	36235.37	121.6294	0.090782	0	2.4
20	16.86778259	399347.8	36227.01	123.7127	0.090715	0	6.3
20	16.86809731	399271.4	36276.12	120.935	0.090856	0	1.833333
20	16.86841393	399154.4	36233.21	121.6294	0.090775	0	2.95
50	16.80714035	408502.1	45877.08	119.5461	0.112306	0	0.1
50	16.82735443	410929.1	45262.31	119.5461	0.110146	0	0.65
50	16.83872414	411150	44920.17	124.4072	0.109255	0	9.55
50	16.84377861	410907.3	45225.93	120.2405	0.110064	0	1.2
50	16.84662056	411050.5	44924.32	124.4072	0.109291	0	7.9
50	16.84788322	411277.8	44797.89	124.4072	0.108924	0	9
50	16.84819984	410862.2	44903.02	124.4072	0.10929	0	7.333333
50	16.84851646	411098.4	45065.67	124.4072	0.109623	0	8.45
50	16.85356903	411079.2	45041.01	123.7127	0.109568	0	5.666667
50	16.85767555	411322.4	44922.38	123.0183	0.109215	0	5.116667
50	16.8586216	411025.5	45102.12	123.0183	0.109731	0	4
50	16.85893822	410999.4	44847.66	123.0183	0.109119	0	4.55
50	16.86304474	410970.6	44964.76	123.7127	0.109411	0	6.216667
50	16.86683464	410693.3	45061.3	122.3238	0.10972	0	3.433333
50	16.86714935	411175.9	45050.38	123.7127	0.109565	0	6.783333
50	16.86999321	410708.3	45066.78	120.935	0.109729	0	1.766667
50	16.87252045	410829.2	45039.11	121.6294	0.10963	0	2.333333
50	16.88136292	410890.4	45098.78	121.6294	0.109759	0	2.883333

Module	DMS							
Channel	1							
Data Name	shear 2							
Measurement Time	26/10/2007 11:51:05 a.m.							
Sample Name	silicone							
Sample Shape	Geometry Factor	0.05405	m					
	Length	3.7	mm					
	Width	10	mm					
	Thickness	10	mm					
Temperature Program		Cel		Cel		Cel/min	min	
	1	16		16		2	10	
	Sampling	1	s					
	Temperature Program Mode	Ramp						
Measurement Mode	Shear							
Meas. Frequency Information								
	Meas. Frequency	6	Frequency					
		1	Hz					
		2	Hz					
		5	Hz					
		10	Hz					
		20	Hz					
		50	Hz					
Operator Name	PYRIS							
Organization Name	University of Canterbury							
Comment	Operator: PYRIS							
	Gas1: N2							

Freq.	Temp.	E'(G')	E"(G")	dL	tanD	Ft	Time
Hz	Cel	Pa	Pa	um		mN	min
1	18.44257164	282905.4	15437.48	-217.952	0.054568	0	9.466667
1	18.4457283	282855.7	15417.52	-217.952	0.054507	0	7.816667
1	18.4457283	282895.1	15385.33	-217.952	0.054385	0	8.366667
1	18.44604492	282703.8	15419.04	-217.952	0.054541	0	8.916667
1	18.48268318	282591.3	15436.49	-217.952	0.054625	0	7.25

1	18.49373627	282627.1	15436.36	-217.952	0.054617	0	6.7
1	18.51995277	282590	15428.73	-217.952	0.054598	0	6.15
1	18.52974319	282505.7	15472.19	-217.257	0.054768	0	5.583333
1	18.54774666	282305.5	15504.74	-217.257	0.054922	0	5.033333
1	18.5673275	280447.7	15879.7	-216.563	0.056623	0	0.583333
1	18.5692234	282231.8	15488.21	-217.257	0.054878	0	4.466667
1	18.57490921	281256.9	15703.56	-217.257	0.055834	0	1.15
1	18.57838249	282052	15533.32	-217.257	0.055073	0	3.916667
1	18.59828186	281961.4	15549.46	-217.257	0.055147	0	3.366667
1	18.60175514	281800.4	15555.18	-217.257	0.055199	0	2.8
1	18.60207176	281703.6	15620.99	-217.257	0.055452	0	2.25
1	18.60301781	281480.1	15684.59	-217.257	0.055722	0	1.7
2	18.42109299	288945.1	16835.73	-217.952	0.058266	0	9.883333
2	18.44730759	288588.2	16871.39	-217.952	0.058462	0	8.766667
2	18.44825554	288718.1	16870.35	-217.952	0.058432	0	9.316667
2	18.44920349	288572.3	16871.5	-217.952	0.058465	0	7.666667
2	18.45204544	288533.5	16852.22	-217.952	0.058406	0	8.216667
2	18.48773575	288629.3	16856.83	-217.952	0.058403	0	7.1
2	18.50573921	288547.2	16897.19	-217.952	0.05856	0	6.55
2	18.51995277	288463.6	16916.82	-217.952	0.058645	0	6
2	18.53479576	288202.3	16918.52	-217.257	0.058704	0	5.433333
2	18.55248451	288100.2	16929.41	-217.257	0.058762	0	4.883333
2	18.55658913	286226.5	17255.3	-216.563	0.060285	0	0.433333
2	18.57238197	288107.3	16934.16	-217.257	0.058777	0	4.316667
2	18.57585526	286939.2	17054.88	-217.257	0.059437	0	1
2	18.59196472	287819.5	16948.63	-217.257	0.058886	0	3.766667
2	18.59417534	287663.7	16929	-217.257	0.05885	0	3.216667
2	18.59670258	287594.2	17015.47	-217.257	0.059165	0	2.65
2	18.60080719	287329.8	17110.94	-217.257	0.059552	0	1.55
2	18.60175514	287359.2	16983.92	-217.257	0.059103	0	2.1
5	18.42646217	297263.6	19190.83	-217.952	0.064558	0	9.766667
5	18.44288635	297199.2	19175.2	-217.952	0.06452	0	9.216667
5	18.44667625	297040.2	19239.09	-217.952	0.064769	0	8.116667
5	18.44888687	297091.8	19164.92	-217.952	0.064508	0	8.666667
5	18.45615196	297014.2	19153.33	-217.952	0.064486	0	7.55
5	18.48268318	296785.5	19199.34	-217.952	0.064691	0	7

5	18.50763512	296788.3	19195.41	-217.952	0.064677	0	6.433333
5	18.52058411	296677.1	19226.6	-217.952	0.064806	0	5.883333
5	18.53795433	296680.4	19240.2	-217.257	0.064852	0	5.333333
5	18.54869461	296341	19217.66	-217.257	0.06485	0	4.766667
5	18.56890678	294687.5	19529.33	-216.563	0.066271	0	0.333333
5	18.57332993	295314.4	19349.1	-217.257	0.06552	0	0.883333
5	18.57901382	296345	19242.21	-217.257	0.064932	0	4.216667
5	18.58943748	296009.1	19229.22	-217.257	0.064962	0	3.1
5	18.5897541	295496	19345.47	-217.257	0.065468	0	1.45
5	18.59101677	296110.7	19309.06	-217.257	0.065209	0	2.55
5	18.59733391	296234	19254.08	-217.257	0.064996	0	3.666667
5	18.60270309	295813	19306.78	-217.257	0.065267	0	2
10	18.43277931	303953.2	21683.87	-217.952	0.071339	0	9.683333
10	18.44130707	303670.1	21635.11	-217.952	0.071245	0	8.033333
10	18.44509697	303790.2	21648.38	-217.952	0.071261	0	9.133333
10	18.44636154	303848.3	21644.15	-217.952	0.071233	0	8.583333
10	18.46341705	303799.9	21654.51	-217.952	0.071279	0	7.466667
10	18.47794533	303544.5	21688.31	-217.952	0.07145	0	6.916667
10	18.52026749	303577.2	21632.42	-217.952	0.071258	0	6.366667
10	18.53037453	303464.6	21702.81	-217.952	0.071517	0	5.8
10	18.54616737	303420.1	21650.2	-217.257	0.071354	0	5.25
10	18.55879974	303329.5	21779.63	-217.257	0.071802	0	4.683333
10	18.55911636	301413	21924.94	-216.563	0.072741	0	0.25
10	18.57364464	303284.7	21690.97	-217.257	0.07152	0	4.133333
10	18.57933044	302211.5	21779.31	-217.257	0.072066	0	0.8
10	18.5878582	302697.9	21869.53	-217.257	0.072249	0	2.466667
10	18.58817482	302443.6	21724.37	-217.257	0.071829	0	1.366667
10	18.59322739	302999.3	21661.25	-217.257	0.071489	0	3.583333
10	18.60049248	302854.4	21602.45	-217.257	0.071329	0	3.016667
10	18.60112381	302674.4	21737.93	-217.257	0.07182	0	1.916667
20	18.43656921	310879.4	25052.88	-217.952	0.080587	0	9.616667
20	18.44541359	310903.4	25092.58	-217.952	0.080709	0	7.95
20	18.44983482	310745.5	25037.39	-217.952	0.080572	0	8.516667
20	18.45078278	310751.4	25021.15	-217.952	0.080518	0	9.066667
20	18.4643631	310717.4	24994.73	-217.952	0.080442	0	7.4
20	18.48520851	310739.9	25085.02	-217.952	0.080727	0	6.833333

20	18.51774025	310403.2	25087.48	-217.952	0.080822	0	6.283333
20	18.53321838	310473.8	25000.25	-217.952	0.080523	0	5.733333
20	18.54237747	310263.4	25005.73	-217.257	0.080595	0	5.166667
20	18.55911636	308226.5	25168.56	-216.563	0.081656	0	0.166667
20	18.56006432	310139.9	25130.7	-217.257	0.08103	0	4.616667
20	18.57554054	308880.1	25086.9	-217.257	0.081219	0	0.733333
20	18.57711983	310060	25022.43	-217.257	0.080702	0	4.05
20	18.58343697	309294.1	25032.46	-217.257	0.080934	0	1.283333
20	18.5878582	309667.5	25080.86	-217.257	0.080993	0	2.4
20	18.59417534	310068.4	25143.71	-217.257	0.081091	0	3.5
20	18.59891319	309470.1	25094.42	-217.257	0.081088	0	1.833333
20	18.60112381	309687.5	25028.65	-217.257	0.080819	0	2.95
50	18.4400444	315444.4	30792.08	-217.952	0.097615	0	9.55
50	18.44446564	315283.5	30815.36	-217.952	0.097739	0	7.883333
50	18.44888687	315357.8	31061.29	-217.952	0.098495	0	8.983333
50	18.45046616	315489.5	30971.96	-217.952	0.098171	0	8.433333
50	18.47826004	315309.4	30920.05	-217.952	0.098063	0	7.333333
50	18.49089432	315152.2	30970.75	-217.952	0.098272	0	6.766667
50	18.52658463	315196.8	30764.36	-217.952	0.097604	0	6.216667
50	18.5316391	314945.9	30746.11	-217.257	0.097623	0	5.65
50	18.5411129	314958.4	30900.72	-217.257	0.09811	0	5.1
50	18.55690575	311277.2	31568.87	-215.174	0.101417	0	0.1
50	18.56606483	314827.2	30662.93	-217.257	0.097396	0	4.533333
50	18.56954002	313540.5	31063.24	-216.563	0.099073	0	0.65
50	18.57711983	314880.6	30924.1	-217.257	0.098209	0	3.983333
50	18.57775116	313869.3	31049.21	-217.257	0.098924	0	1.216667
50	18.59006882	314450.5	30970.4	-217.257	0.098491	0	3.433333
50	18.59417534	313979.6	30923.49	-217.257	0.098489	0	1.766667
50	18.59417534	314317.6	30846.3	-217.257	0.098137	0	2.316667
50	18.60396576	314600.1	30816.11	-217.257	0.097953	0	2.883333

Module	DMS							
Channel	1							
Data Name	shear 3							
Measurement Time	26/10/2007 12:07:46 p.m.							
Sample Name	silicone							
Sample Shape	Geometry Factor	0.05405	m					
	Length	3.7	mm					
	Width	10	mm					
	Thickness	10	mm					
Temperature Program		Cel		Cel		Cel/min	min	
	1	16		16		2	10	
	Sampling	1	s					
	Temperature Program Mode	Ramp						
Measurement Mode	Shear							
Meas. Frequency Information								
	Meas. Frequency	6	Frequency					
		1	Hz					
		2	Hz					
		5	Hz					
		10	Hz					
		20	Hz					
		50	Hz					
Operator Name	PYRIS							
Organization Name	University of Canterbury							
Comment	Operator: PYRIS							
	Gas1: N2							

Freq.	Temp.	E'(G')	E"(G")	dL	tanD	Ft	Time
Hz	Cel	Pa	Pa	um		mN	min
1	18.38824654	325037.9	18987.37	-8.23088	0.058416	0	9.466667
1	18.39298439	324918.1	19007.87	-8.23088	0.0585	0	8.916667
1	18.41351318	324669.4	18982.04	-8.23088	0.058466	0	8.35
1	18.42804146	324687.6	18993.65	-8.23088	0.058498	0	7.8
1	18.46373177	324752.9	19044.02	-8.23088	0.058642	0	7.25

1	18.48236656	324612.7	19015.92	-8.23088	0.05858	0	6.683333
1	18.48900032	324640.2	19086.11	-8.23088	0.058792	0	6.133333
1	18.51931953	324408.8	19033.8	-8.23088	0.058672	0	5.583333
1	18.52184677	322363.4	19430.99	-7.53644	0.060277	0	0.583333
1	18.54237747	324274.7	19065.95	-8.23088	0.058796	0	5.016667
1	18.56037903	324238.1	19057.96	-8.23088	0.058778	0	4.466667
1	18.57269859	324265.2	19057.84	-8.23088	0.058772	0	3.916667
1	18.57522392	323182.5	19239.17	-7.53644	0.05953	0	1.133333
1	18.57775116	323716.6	19132.9	-8.23088	0.059104	0	2.25
1	18.57869911	324122.5	19094.24	-8.23088	0.058911	0	3.366667
1	18.58122635	323560.3	19188.95	-8.23088	0.059306	0	1.683333
1	18.59859657	323965.5	19125.42	-8.23088	0.059035	0	2.8
2	18.36266327	332425.8	20835.86	-8.23088	0.062678	0	9.866667
2	18.38445663	332233.1	20850.87	-8.23088	0.06276	0	9.316667
2	18.39614105	332343.9	20858.39	-8.23088	0.062761	0	8.766667
2	18.41635513	332208.4	20880.38	-8.23088	0.062853	0	8.2
2	18.44257164	332168.5	20886.35	-8.23088	0.062879	0	7.65
2	18.46499634	332210.6	20900.72	-8.23088	0.062914	0	7.1
2	18.48994637	332080.7	20866.92	-8.23088	0.062837	0	6.533333
2	18.49784279	332018.5	20920.74	-8.23088	0.063011	0	5.983333
2	18.50258064	329772.6	21265.62	-7.53644	0.064486	0	0.433333
2	18.51900482	331773.3	20883.6	-8.23088	0.062945	0	5.433333
2	18.5449028	331669.3	20902.62	-8.23088	0.063022	0	4.866667
2	18.56069565	331773.3	20920.27	-8.23088	0.063056	0	4.316667
2	18.5616436	330521.1	21091.91	-7.53644	0.063814	0	0.983333
2	18.57238197	330971.8	21049.04	-8.23088	0.063598	0	1.55
2	18.57869911	331695.1	20942.38	-8.23088	0.063137	0	3.766667
2	18.58501625	331121.7	20983.89	-8.23088	0.063372	0	2.1
2	18.58912086	331551.3	20937.53	-8.23088	0.06315	0	3.216667
2	18.60238647	331232.9	20944.15	-8.23088	0.063231	0	2.65
5	18.36676788	343118.2	23903.51	-8.23088	0.069666	0	9.766667
5	18.38508797	342931.7	23848.37	-8.23088	0.069543	0	9.216667
5	18.39993286	342997.4	23897.12	-8.23088	0.069671	0	8.65
5	18.42014503	342710.4	23882.2	-8.23088	0.069686	0	8.1
5	18.44857216	342741.5	23887.3	-8.23088	0.069695	0	7.533333
5	18.4700489	342807.1	23885.62	-8.23088	0.069677	0	6.983333

5	18.48742104	342640.6	23934.46	-8.23088	0.069853	0	6.433333
5	18.48773575	340513.5	24036.73	-7.53644	0.07059	0	0.316667
5	18.51016045	342664.4	23895.74	-8.23088	0.069735	0	5.883333
5	18.52658463	342417	23886.09	-8.23088	0.069757	0	5.316667
5	18.55027199	342328.6	23887.2	-8.23088	0.069779	0	4.766667
5	18.55185127	341191.7	24099	-7.53644	0.070632	0	0.883333
5	18.55943298	342267.9	23920.6	-8.23088	0.069889	0	4.216667
5	18.57522392	342238.3	23944.93	-8.23088	0.069966	0	3.666667
5	18.57648849	341660.3	24018.81	-8.23088	0.0703	0	1.433333
5	18.58343697	341841.3	24021.64	-8.23088	0.070271	0	1.983333
5	18.58691025	341972.5	23941.46	-8.23088	0.07001	0	2.55
5	18.59259605	342081.5	23953.24	-8.23088	0.070022	0	3.1
10	18.37624359	351841.4	27038.53	-8.23088	0.076849	0	9.683333
10	18.3876133	351847.5	27044.1	-8.23088	0.076863	0	9.133333
10	18.40466881	351626.8	27018.5	-8.23088	0.076839	0	8.566667
10	18.42204094	351675	27081.75	-8.23088	0.077008	0	8.016667
10	18.46215248	351537.7	27075.32	-8.23088	0.07702	0	7.466667
10	18.46910095	351440.2	27053.32	-8.23088	0.076978	0	6.9
10	18.48268318	349256.2	27372.74	-7.53644	0.078374	0	0.233333
10	18.4867878	351382.5	27054.41	-8.23088	0.076994	0	6.35
10	18.50826645	351353.4	27080.89	-8.23088	0.077076	0	5.8
10	18.52848053	351288	27104.34	-8.23088	0.077157	0	5.233333
10	18.54711533	350071.6	27243.18	-7.53644	0.077822	0	0.8
10	18.55374718	351160.9	27056.22	-8.23088	0.077048	0	4.683333
10	18.56827545	351021.1	27110.25	-8.23088	0.077233	0	4.133333
10	18.57111931	350410.2	27119.34	-8.23088	0.077393	0	1.35
10	18.57585526	351183.7	27067.88	-8.23088	0.077076	0	3.583333
10	18.58248901	350673	27123.4	-8.23088	0.077347	0	1.916667
10	18.58880615	350811.2	27122.19	-8.23088	0.077313	0	2.466667
10	18.58880615	350981.9	27089.02	-8.23088	0.077181	0	3.016667
20	18.3819294	361242.7	31442.85	-8.23088	0.087041	0	9.616667
20	18.38729858	361057	31498.44	-8.23088	0.08724	0	9.05
20	18.40846062	361115.4	31472.64	-8.23088	0.087154	0	8.5
20	18.42267227	360952.9	31468.8	-8.23088	0.087183	0	7.95
20	18.46467972	360909.7	31451.76	-8.23088	0.087146	0	7.383333
20	18.46910095	358437.1	31633.84	-7.53644	0.088255	0	0.166667

20	18.47762871	360643	31453.91	-8.23088	0.087216	0	6.833333
20	18.48710442	360850.4	31480.48	-8.23088	0.08724	0	6.283333
20	18.51363564	360656.6	31425.34	-8.23088	0.087134	0	5.716667
20	18.53005981	360699.3	31462.25	-8.23088	0.087226	0	5.166667
20	18.53132248	359298.8	31574.48	-7.53644	0.087878	0	0.716667
20	18.55627441	360490.9	31460	-8.23088	0.08727	0	4.616667
20	18.56606483	360258.4	31418.17	-8.23088	0.08721	0	4.05
20	18.57680321	360448.4	31488.4	-8.23088	0.087359	0	3.5
20	18.57743454	359797.3	31472.53	-8.23088	0.087473	0	1.283333
20	18.58280373	360200.4	31383.74	-8.23088	0.087129	0	2.383333
20	18.58564758	359734.3	31398.01	-8.23088	0.087281	0	1.833333
20	18.59101677	360318.8	31501.48	-8.23088	0.087427	0	2.95
50	18.38224411	370363.6	39228.27	-8.23088	0.105918	0	9.533333
50	18.39235115	370220.9	39295.14	-8.23088	0.10614	0	8.983333
50	18.40688133	370239.7	39186.48	-8.23088	0.105841	0	8.416667
50	18.42772675	370161.8	39556.13	-8.23088	0.106862	0	7.866667
50	18.45899391	366076.3	39769.18	-7.53644	0.108636	0	0.083333
50	18.46215248	370036.6	39470.47	-8.23088	0.106666	0	7.316667
50	18.47952461	370224.9	39372.12	-8.23088	0.106347	0	6.766667
50	18.48584175	369991.4	39176.13	-8.23088	0.105884	0	6.2
50	18.51805687	369756.4	39344	-8.23088	0.106405	0	5.65
50	18.52626801	368232.2	39354.44	-7.53644	0.106874	0	0.65
50	18.5316391	369987.8	39414.9	-8.23088	0.10653	0	5.1
50	18.55722237	369753.1	39269.06	-8.23088	0.106203	0	4.533333
50	18.57111931	369675.6	39174.83	-8.23088	0.105971	0	3.983333
50	18.57269859	368883.3	39408.64	-7.53644	0.106832	0	1.2
50	18.58090973	369244.6	39392.43	-8.23088	0.106684	0	2.316667
50	18.58185768	369040.2	39340.88	-8.23088	0.106603	0	1.766667
50	18.58217239	369511	39308.89	-8.23088	0.106381	0	3.433333
50	18.59828186	369371.6	39226.16	-8.23088	0.106197	0	2.883333

Appendix B.4

Physical laboratory model - LabVIEW™ environment

NATIONAL INSTRUMENTS LABVIEW™ ENVIRONMENT

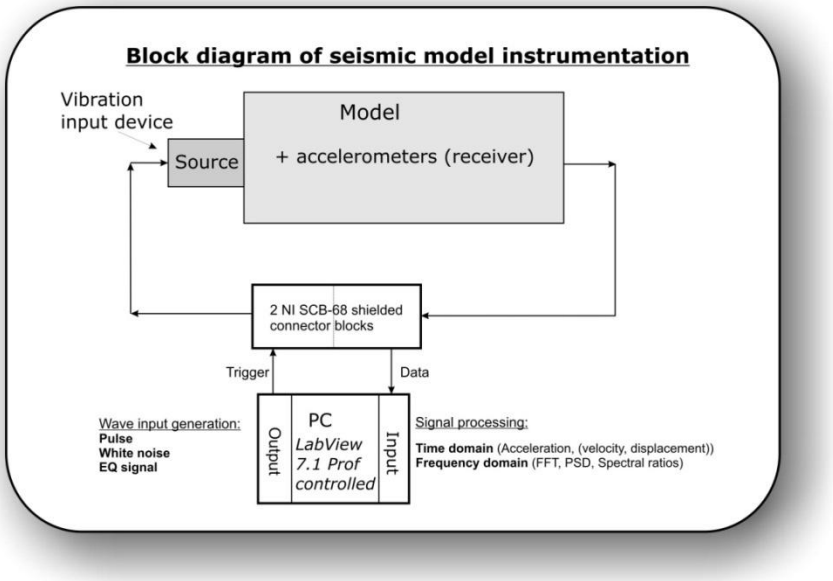

Figure B.4.1: Block diagram showing the schematic technical setup of the physical modeling of topographic effects on seismic ground motions

To generate and measure physical signals, the LabVIEW™ data acquisition system (NI-DAQ™) was applied to the physical laboratory model. LabVIEW™ 7.1 Professional Edition, a graphical programming software for measurement and instrumentation, was used to program a user interface to manage the model data output and input. Combined with the LabVIEW™ software package, NATIONAL INSTRUMENTS hardware devices controlled the electronic devices. The input and output was controlled by two internal computer boards, a NI PCI-6711 12-bit high-speed analog output board, a NI PCI-6220 data acquisition device, and two external NI SCB-68 connector blocks (Figure B.4.1).

A LabVIEW™ data acquisition environment was designed, consisting of a user interface and a virtual instrument environment, to communicate with hardware devices such as motion input devices (electromagnetic actuator) and data acquisition devices (ADXL accelerometers). In LabVIEW programs are called virtual instruments because their appearance and operation imitates physical instruments. The user is able to build a user interface with controls and indicators to operate hardware devices and to display data that were acquired. The user interface, or front panel (Figure B.4.3), is connected to a block diagram in the background (Figure B.4.2). The user

develops a code using virtual instruments and structures to control the front panel objects (National_Instruments_Corporation, 2003).

LabVIEW was used for the physical laboratory modeling to setup and control the electromagnetic input device and the accelerometers. It was also used to process and analyze the acquired data (PSD, signal properties etc.). Typical configurations used for the LabVIEW physical laboratory environment are shown in figure B.4.2 (block diagram) and figure B.4.3 (user interface/front panel).

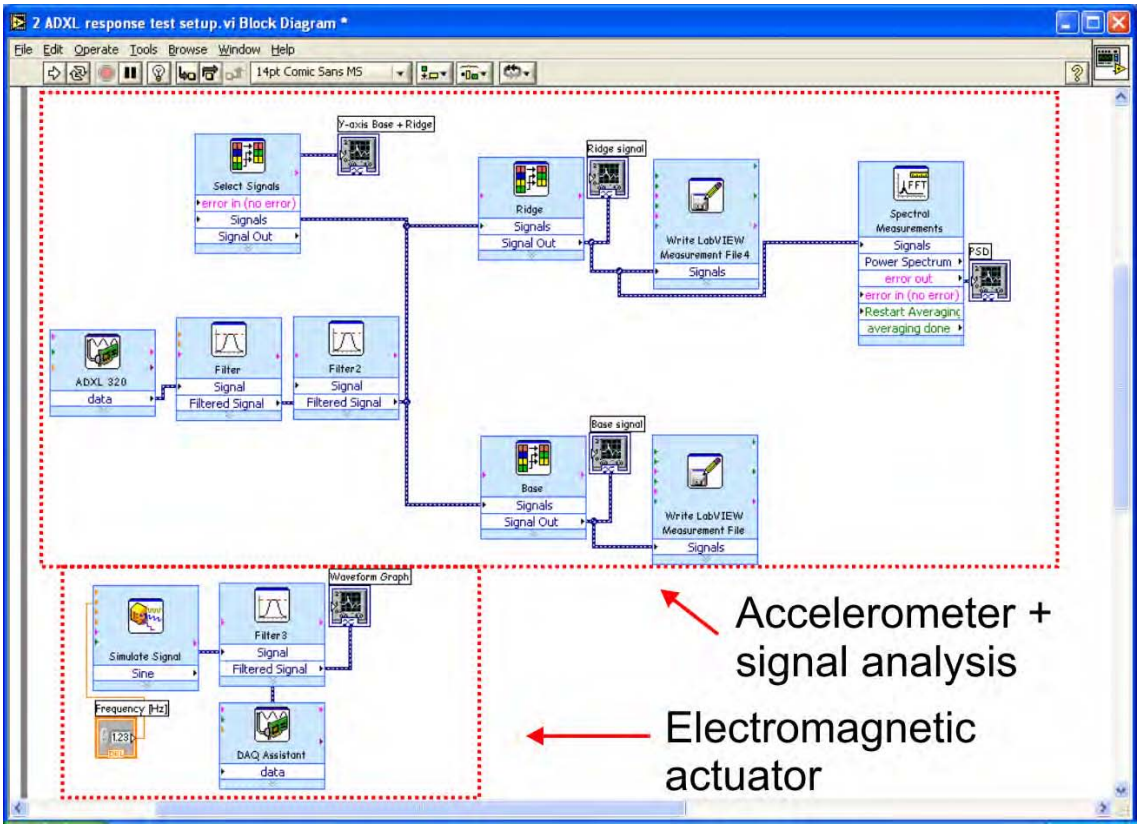

Figure B.4.2: Screen shot showing a LabVIEW block diagram of one test configurations for the physical laboratory model. The configurations for both the electromagnetic actuator and the accelerometers are highlighted by the red rectangles. Different virtual instruments are presented allowing the user to configure and control hardware components, to filter, analyze, and display data.

Figure B.4.3: Screen shot showing a LabVIEW user interface / front panel of one test configurations for the physical laboratory model. The front panel displays a) the frequency input control, b) a graph showing the real-time input signal display, and c) different graphs showing the real-time signal display of the received ADXL accelerometer signal components as well as a PSD output.

LabVIEW is equipped with a special data acquisition assistant that allows the user to configure the hardware devices in detail (Figure B.4.4).

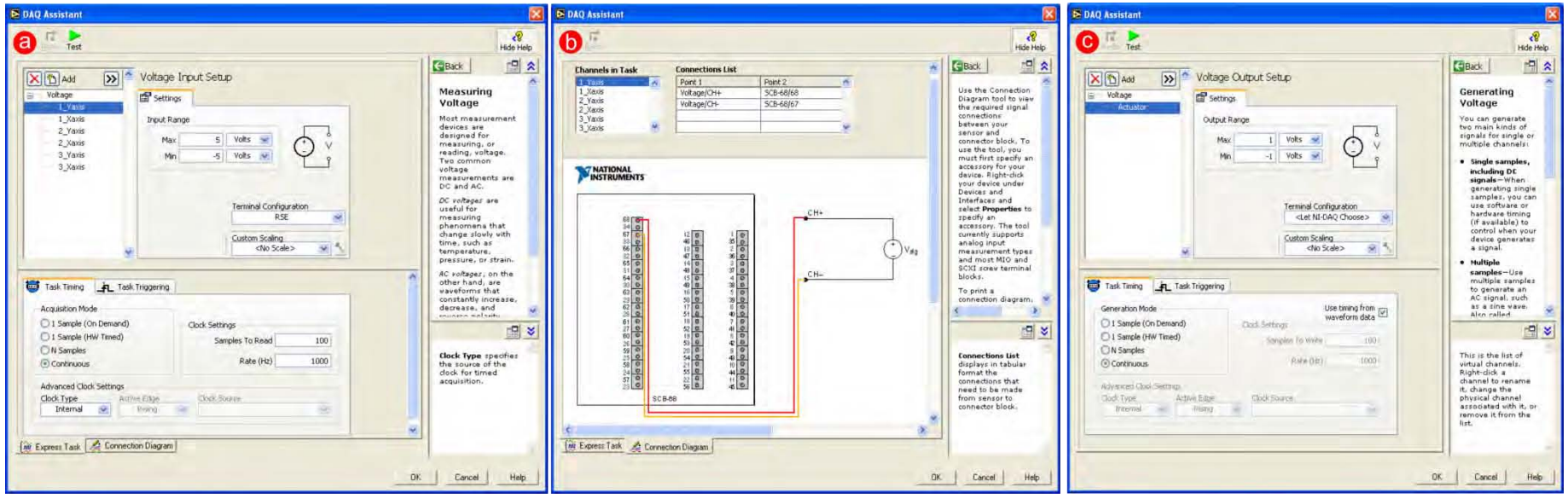

Figure B.4.4: Screenshots showing examples of the LabVIEW Data Acquisition Assistant. a) detailed configuration of the dual-axis ADXL 320 accelerometers , b) the connection diagram to the external NI connector blocks and c) a typical setup configuration for the electromagnetic actuator

REFERENCES

National_Instruments_Corporation, 2003. LabView 7 Express - User Manual. National Instruments Corporation.

Appendix B.5

Rhodorsil® RTV 585 silicone – Technical specifications

Material Safety Data Sheet

Infosafe No. 2RHPB Issue Date: June 2003 ISSUED by RHODIA

Product Name: **RHODORSIL RTV 585**

Not Classified as Hazardous according to criteria of NOHSC

COMPANY DETAILS

Company Name	Rhodia Australia Pty Ltd (ABN 24050029000)
Address	352 Ferntree Gully Road, NOTTINGHILL VIC 3168
Emergency Tel.	1800 033 111
Tel/Fax	Ph: (03) 9541 1000 Fax: (03) 9548 8648
Other Information	

IDENTIFICATION

Product Name	RHODORSIL RTV 585
Proper Shipping Name	None Allocated
UN Number	None Allocated
DG Class	None Allocated
Packing Group	None Allocated
Hazchem Code	None Allocated
Poisons Schedule	Not Scheduled
Product Use	Rhodorsil RTV 585 is a Silicone compound which vulcanizes to an elastomer after the addition of a catalyst. It is used in moulding, reproduction, encapsulation and other applications.

Physical Data

Appearance	Opaque, viscous liquid.
Specific Gravity	1.2 (Water = 1)
Flamm. Limit LEL	Non-flammable

Other Properties

Volatile Component	Less than 10%
Form	Liquid
Decomposition Temp.	>200°C
Formula	Compounded silicone elastomer base.

Ingredients

Ingredients	Name	CAS	Proportion
	POLYDIMETHYLSILOXANE COMPOUNDS	63148-62-9	60-100%
	AMORPHOUS SILICA	55599-33-2	30-60%
	PIGMENTS	1309-37-1	0-10%

HEALTH HAZARD INFORMATION

Health Effects

Acute - Swallowed	May cause irritation to mouth, throat and stomach.
Acute - Eye	May cause mild irritation.
Acute - Skin	None known.
Acute - Inhaled	Low hazard. Viscous liquid of low volatility.

Material Safety Data Sheet

Infosafe No. 2RHPB Issue Date: June 2003 ISSUED by RHODIA

Product Name: **RHODORSIL RTV 585**

Not Classified as Hazardous according to criteria of NOHSC

Chronic Health Hazard	Low risk. Liquid of low volatility.

First Aid

Swallowed	Give water or milk to drink. DO NOT induce vomiting. Seek immediate medical assistance.
Eye	Irrigate with copious quantity of water for 15 minutes. Seek medical assistance if irritation persists.
Skin	Wash with plenty of soap and water.
Inhaled	If affected remove to fresh air.

Advice to Doctor

Advice to Doctor	All treatments should be based on observed signs and symptoms of distress of the patient. Consideration should be given to the possibility that overexposure to materials other than this product may have occurred. Treat symptomatically. No specific antidote available.

Other Health Hazard Information

PRECAUTIONS FOR USE

Other Exposure Info.	No exposure limit is assigned to this compound.
Eng. Controls	No special ventilation is required when handling this compound.

Personal Protection

Protective Equip.	General safe work practice should be observed. When using the catalysed mixture avoid skin and eye contact. Wear appropriate clothing to prevent repeated or prolonged skin contact. Wear eye protection to prevent any reasonable probability of eye contact. When mixing with the separately supplied catalyst the followng is appropriate: Avoid all skin contact with the catalyst, and the catalysed RTV until curing is complete.
Work/Hygienic Practices	Personal hygiene is an important work practice exposure control measure and the **following general measures should be undertaken when working with or handling this** material: (1) Do not store, use, and/or consume foods, beverages, tobacco products, or cosmetics in areas where this material is stored. (2) Wash hands and face carefully before eating, drinking, using tobacco, applying cosmetics, or using the toilet. (3) Wash exposed skin promptly to remove accidental splashes of contact with this material.

Flammability

Fire Hazards	Non-flammable. Combustible. Will burn if involved in a fire but not considered to be a signifiant fire risk. The main combustion products are silica, carbon dioxide and carbon monoxide.
Other Precautions	Safe working practice and good hygiene should be observed.

Rhodia

Material Safety Data Sheet

Infosafe No. 2RHPB Issue Date: June 2003 ISSUED by RHODIA

Product Name: **RHODORSIL RTV 585**

Not Classified as Hazardous according to criteria of NOHSC

SAFE HANDLING INFORMATION

Storage and Transport

Storage Precautions	Store in clearly labeled, and sealed containers. Avoid spillage.
Other Storage Info.	The foregoing data applies to the uncured uncatalysed base compound. The hazards **associated with the catalyst are due mainly to the organic tin compounds. When** curing is complete, the resulting product is an inert, non-toxic, silicone elastomer.
Proper Shipping Name	None Allocated
EPG Number	
IERG Number	

Spills and Disposal

Spills & Disposal	Consult local regulations. Non-biodegradable, inert material.

Fire/Explosion Hazard

Fire/Explos. Hazard	Low hazard. Non-flammable liquid. Forms essentially amorphous silica, carbon **dioxide and carbon monoxide on combustion. Fire can be extinguished by carbon** dioxide, powder or water type extinguisher.
Hazardous Reaction	The product is considered stable under normal handling conditions. May reactupon **contact with strong oxidisers.**
Hazchem Code	None Allocated

OTHER INFORMATION

Toxicology	Silica and other fine powder ingredients are bound in the paste mixture and do not present any risk of toxicity under normal conditions of use and handling. Important: The data and information in this MSDS relate to the silicone compound only. For specific risks connected with the use of the catalyst, please refer to the corresponding data sheet.
Environ. Protection	Non-biodegradable. No negative ecological effects are known.
Pkg. & Labelling	Keep in original airtight container to prevent degradation.
Regulatory Information	All ingredients are listed in the Australian Inventory of Chemical Substances.
Technical Data	A Technical Data sheet for this product is available upon request.
References	1. Australian Health Minister's Advisory Council, 'Standard for the uniform scheduling of drugs and poisons,' No 11., AGPS, Canberra, 1996.

2. National Occupational Health and Safety Commission, 'National Code of Practice for the Preparation of Material Safety Data Sheets' [NOHSC:2011(1994)], AGPS, Canberra, 1994.

3. National Occupational Health and Safety Commission, 'List of Designated Hazardous Substances' [NOHSC:10005(1994)], AGPS, Canberra,1994.

4. National Occupational Health and Safety Commission, 'Exposure Standards for

Rhodia

Material Safety Data Sheet

Infosafe No. 2RHPB Issue Date: June 2003 ISSUED by RHODIA

Product Name: **RHODORSIL RTV 585**

Not Classified as Hazardous according to criteria of NOHSC

Atmospheric Contaminants in the Occupational Environment' [NOHSC:1003(1995)], AGPS, Canberra,1995.

5. National Occupational Health and Safety Commission, 'Approved Criteria for Classifying Hazardous Substancest' [NOHSC:1008(1994)], AGPS, Canberra,1994.

6. Commonwealth of Australia, 'Australian Code for the Transport of Dangerous Goods by Road and Rail,' 5th Ed., AGPS, Canberra, 1992.

7. Rhodia internal data.

CONTACT POINT

Contact

National Sales Manager
Rhodia Australia Pty Ltd. Telephone (03) 9541 1000 Fax (03) 9548 8648
EMERGENCY TELEPHONE: 1800 033 111 (ALL HOURS)

ADVICE TO THE USER:
This Material Safety Data Sheet should be used in conjunction with the Technical Data Sheets. It does not replace them. The information given is based on our knowledge of the health and safety data of this product, at the time of publication. It is given in good faith. The attention of the user is drawn to the possible risks incurred by using the product for any purpose other than that for which it was intended. If clarification or further information is needed to enable appropriate risk assessment, the user should contact Rhodia Australia. Our responsibility for products sold is subject to our standard terms and conditions sent to customers. No liability whatsoever can be accepted with regard to the handling, processing or use of the product concerned which, in all cases, shall be in accordance with the appropriate regulations and/or legislation.

...End of Report...

Appendix B.6

Analog Devices ADXL 320 – Technical specifications

Small and Thin ±5 *g* Accelerometer

ADXL320

FEATURES

Small and thin
4 mm × 4 mm × 1.45 mm LFCSP package
2 m*g* resolution at 60 Hz
Wide supply voltage range: 2.4 V to 5.25 V
Low power: 350 µA at V_S = 2.4 V (typ)
Good zero *g* bias stability
Good sensitivity accuracy
X-axis and Y-axis aligned to within 0.1° (typ)
BW adjustment with a single capacitor
Single-supply operation
10,000 *g* shock survival
Compatible with Sn/Pb and Pb-free solder processes

APPLICATIONS

Cost-sensitive motion- and tilt-sensing applications
Smart hand-held devices
Mobile phones
Sports and health-related devices
PC security and PC peripherals

GENERAL DESCRIPTION

The ADXL320 is a low cost, low power, complete dual-axis accelerometer with signal conditioned voltage outputs, which is all on a single monolithic IC. The product measures acceleration with a full-scale range of ±5 *g* (typical). It can also measure both dynamic acceleration (vibration) and static acceleration (gravity).

The ADXL320's typical noise floor is 250 µ*g*/√Hz, allowing signals below 2 m*g* to be resolved in tilt-sensing applications using narrow bandwidths (<60 Hz).

The user selects the bandwidth of the accelerometer using capacitors C_X and C_Y at the X_{OUT} and Y_{OUT} pins. Bandwidths of 0.5 Hz to 2.5 kHz may be selected to suit the application.

The ADXL320 is available in a very thin 4 mm × 4 mm × 1.45 mm, 16-lead, plastic LFCSP.

FUNCTIONAL BLOCK DIAGRAM

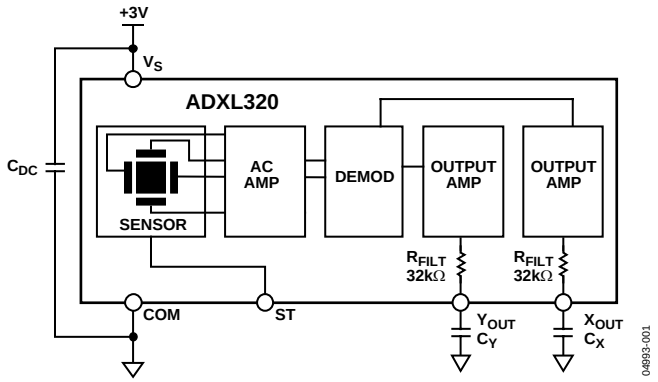

Figure 1.

One Technology Way, P.O. Box 9106, Norwood, MA 02062-9106, U.S.A.
Tel: 781.329.4700 **www.analog.com**
Fax: 781.326.8703

TABLE OF CONTENTS

REVISION HISTORY

9/04—Revision 0: Initial Version

SPECIFICATIONS[1]

T_A = 25°C, V_S = 3 V, C_X = C_Y = 0.1 µF, Acceleration = 0 *g*, unless otherwise noted.

Table 1.

Parameter	Conditions	Min	Typ	Max	Unit
SENSOR INPUT	Each axis				
Measurement Range			±5		*g*
Nonlinearity	% of full scale		±0.2		%
Package Alignment Error			±1		Degrees
Alignment Error	X sensor to Y sensor		±0.1		Degrees
Cross Axis Sensitivity			±2		%
SENSITIVITY (RATIOMETRIC)[2]	Each axis				
Sensitivity at X_{OUT}, Y_{OUT}	V_S = 3 V	156	174	192	mV/*g*
Sensitivity Change due to Temperature[3]	V_S = 3 V		0.01		%/°C
ZERO *g* BIAS LEVEL (RATIOMETRIC)	Each axis				
0 *g* Voltage at X_{OUT}, Y_{OUT}	V_S = 3 V	1 3	1 5	1.7	V
0 *g* Offset Versus Temperature			±0.6		m*g*/°C
NOISE PERFORMANCE					
Noise Density	@ 25°C		250		µ*g*/√Hz rms
FREQUENCY RESPONSE[4]					
C_X, C_Y Range[5]		0.002		10	µF
R_{FILT} Tolerance			32 ± 15%		kΩ
Sensor Resonant Frequency			5 5		kHz
SELF-TEST[6]					
Logic Input Low			0.6		V
Logic Input High			2.4		V
ST Input Resistance to Ground			50		kΩ
Output Change at X_{OUT}, Y_{OUT}	Self-test 0 to 1		55		mV
OUTPUT AMPLIFIER					
Output Swing Low	No load		0 3		V
Output Swing High	No load		2 5		V
POWER SUPPLY					
Operating Voltage Range		2.4		5 25	V
Quiescent Supply Current			0.48		mA
Turn-On Time[7]			20		ms
TEMPERATURE					
Operating Temperature Range		–20		70	°C

[1] All minimum and maximum specifications are guaranteed. Typical specifications are not guaranteed.
[2] Sensitivity is essentially ratiometric to V_S. For V_S = 2.7 V to 3.3 V, sensitivity is 154 mV/V/*g* to 194 mV/V/*g* typical.
[3] Defined as the output change from ambient-to-maximum temperature or ambient-to-minimum temperature.
[4] Actual frequency response controlled by user-supplied external capacitor (C_X, C_Y).
[5] Bandwidth = 1/(2 × π × 32 kΩ × C). For C_X, C_Y = 0.002 µF, bandwidth = 2500 Hz. For C_X, C_Y = 10 µF, bandwidth = 0.5 Hz. Minimum/maximum values are not tested.
[6] Self-test response changes cubically with V_S.
[7] Larger values of C_X, C_Y increase turn-on time. Turn-on time is approximately 160 × C_X or C_Y + 4 ms, where C_X, C_Y are in µF.

ABSOLUTE MAXIMUM RATINGS

Table 2.

Parameter	Rating
Acceleration (Any Axis, Unpowered)	10,000 *g*
Acceleration (Any Axis, Powered)	10,000 *g*
V_S	−0.3 V to +7.0 V
All Other Pins	(COM − 0.3 V) to (V_S + 0.3 V)
Output Short-Circuit Duration (Any Pin to Common)	Indefinite
Operating Temperature Range	−55°C to +125°C
Storage Temperature	−65°C to +150°C

Stresses above those listed under Absolute Maximum Ratings may cause permanent damage to the device. This is a stress rating only; functional operation of the device at these or any other conditions above those indicated in the operational section of this specification is not implied. Exposure to absolute maximum rating conditions for extended periods may affect device reliability.

ESD CAUTION

ESD (electrostatic discharge) sensitive device. Electrostatic charges as high as 4000 V readily accumulate on the human body and test equipment and can discharge without detection. Although this product features proprietary ESD protection circuitry, permanent damage may occur on devices subjected to high energy electrostatic discharges. Therefore, proper ESD precautions are recommended to avoid performance degradation or loss of functionality.

PIN CONFIGURATION AND FUNCTION DESCRIPTIONS

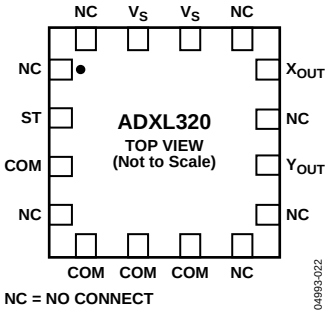

Figure 2. Pin Configuration

Table 3. Pin Function Descriptions

Pin No.	Mnemonic	Description
1	NC	Do Not Connect
2	ST	Self-Test
3	COM	Common
4	NC	Do Not Connect
5	COM	Common
6	COM	Common
7	COM	Common
8	NC	Do Not Connect
9	NC	Do Not Connect
10	Y_{OUT}	Y Channel Output
11	NC	Do Not Connect
12	X_{OUT}	X Channel Output
13	NC	Do Not Connect
14	V_S	2.4 V to 5 25 V
15	V_S	2.4 V to 5 25 V
16	NC	Do Not Connect

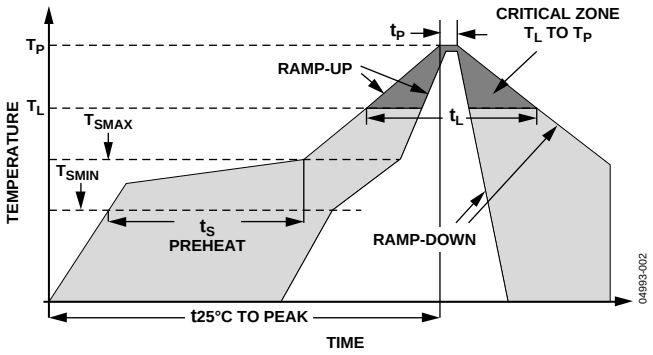

Figure 3. Recommended Soldering Profile

Table 4. Recommended Soldering Profile

Profile Feature	Sn63/Pb37	Pb-Free
Average Ramp Rate (T_L to T_P)	3°C/s max	3°C/s max
Preheat		
Minimum Temperature (T_{SMIN})	100°C	150°C
Minimum Temperature (T_{SMAX})	150°C	200°C
Time (T_{SMIN} to T_{SMAX}), t_S	60 s – 120 s	60 s – 150 s
T_{SMAX} to T_L		
Ramp-Up Rate	3°C/s	3°C/s
Time Maintained Above Liquidous (T_L)		
Liquidous Temperature (T_L)	183°C	217°C
Time (t_L)	60 s – 150 s	60 s – 150 s
Peak Temperature (T_P)	240°C + 0°C/−5°C	260°C + 0°C/−5°C
Time within 5°C of Actual Peak Temperature (t_P)	10 s – 30 s	20 s – 40 s
Ramp-Down Rate	6°C/s max	6°C/s max
Time 25°C to Peak Temperature	6 min max	8 min max

TYPICAL PERFORMANCE CHARACTERISTICS (V_S = 3.0 V)

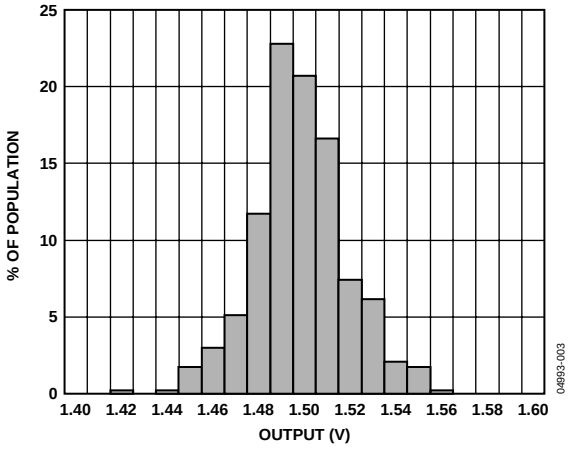

Figure 4. X-Axis Zero g Bias Deviation from Ideal at 25°C

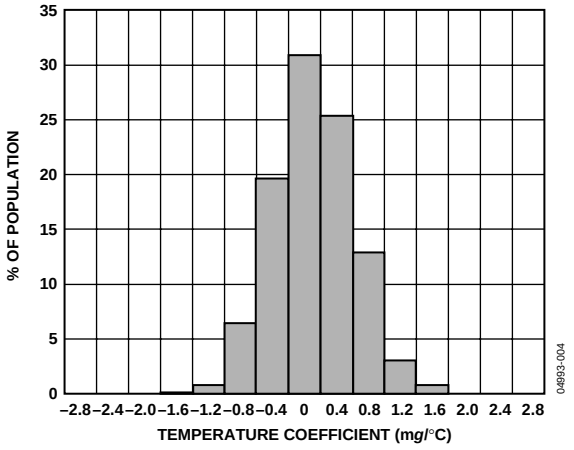

Figure 5. X-Axis Zero g Bias Temperature Coefficient

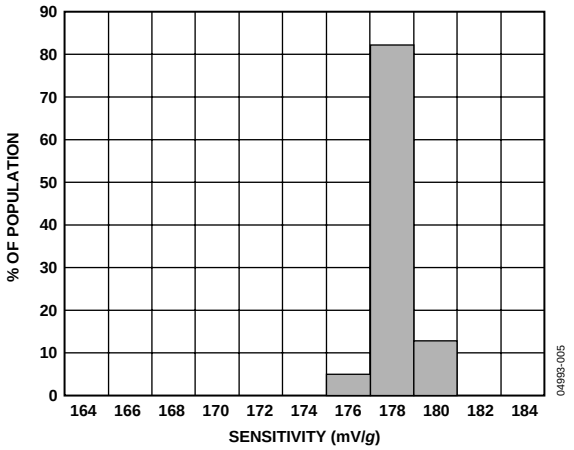

Figure 6. X-Axis Sensitivity at 25°C

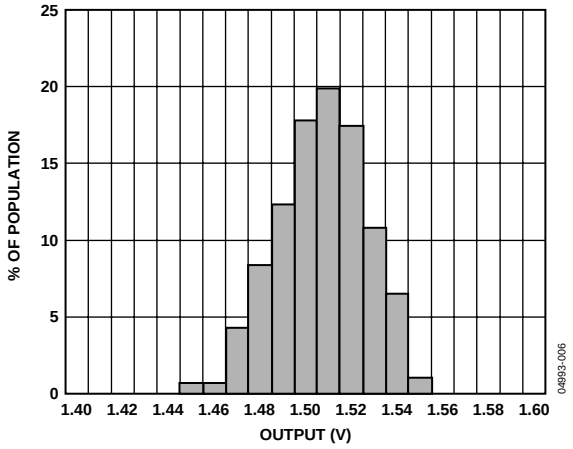

Figure 7. Y-Axis Zero g Bias Deviation from Ideal at 25°C

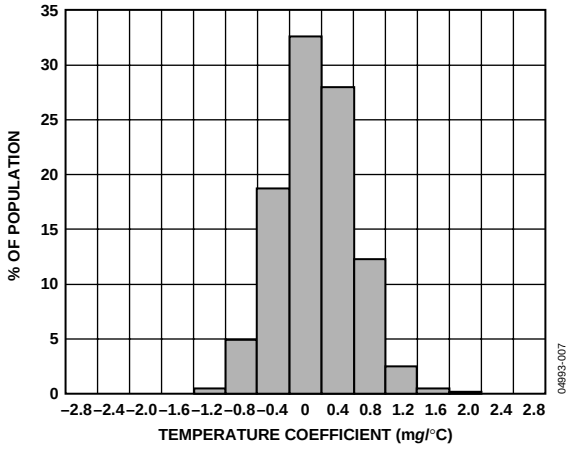

Figure 8. Y-Axis Zero g Bias Temperature Coefficient

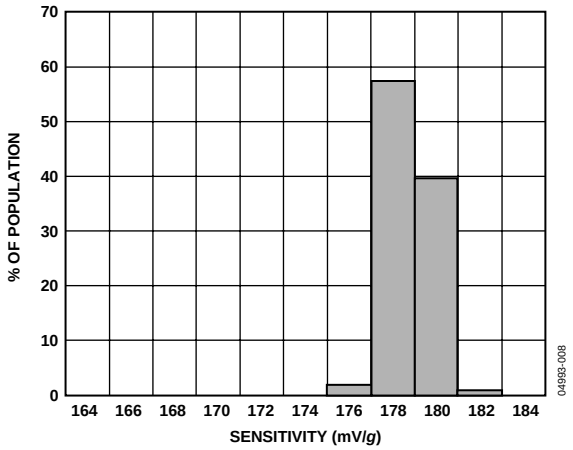

Figure 9. Y-Axis Sensitivity at 25°C

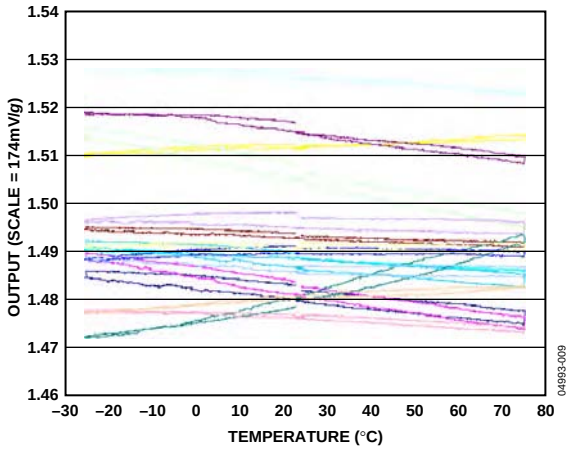

Figure 10. Zero g Bias vs. Temperature—Parts Soldered to PCB

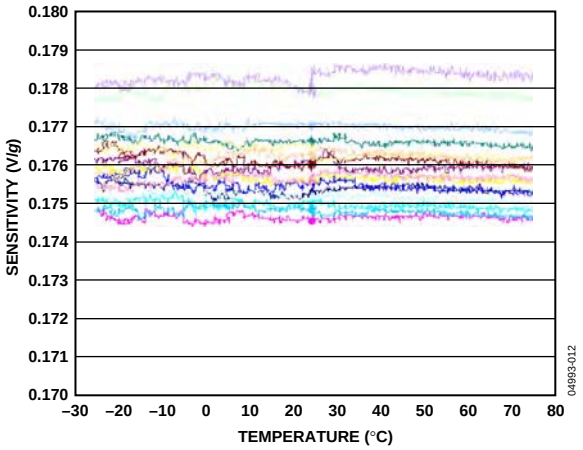

Figure 13. Sensitivity vs. Temperature—Parts Soldered to PCB

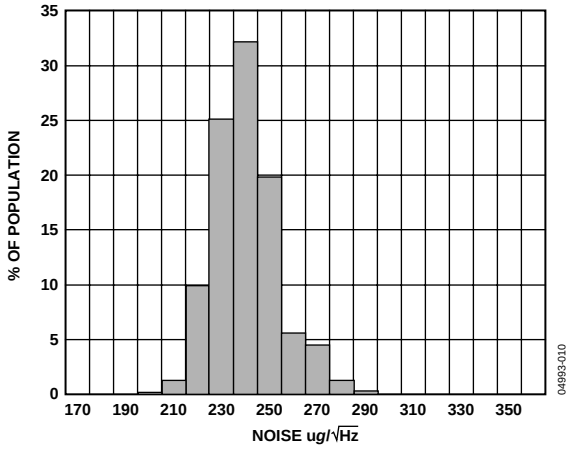

Figure 11. X-Axis Noise Density at 25°C

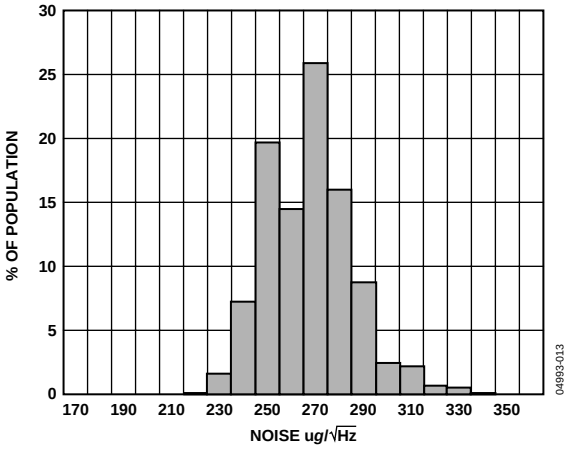

Figure 14. Y-Axis Noise Density at 25°C

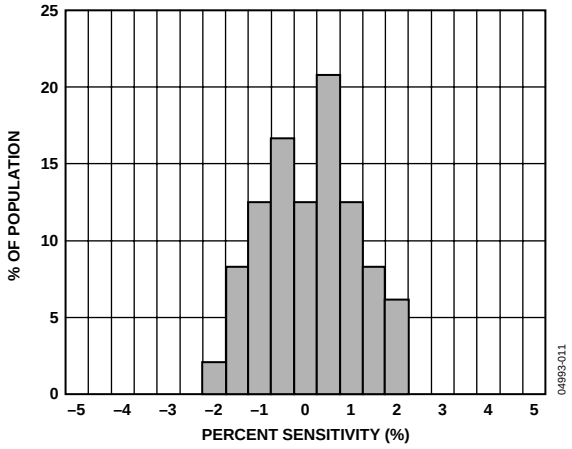

Figure 12. Z vs. X Cross-Axis Sensitivity

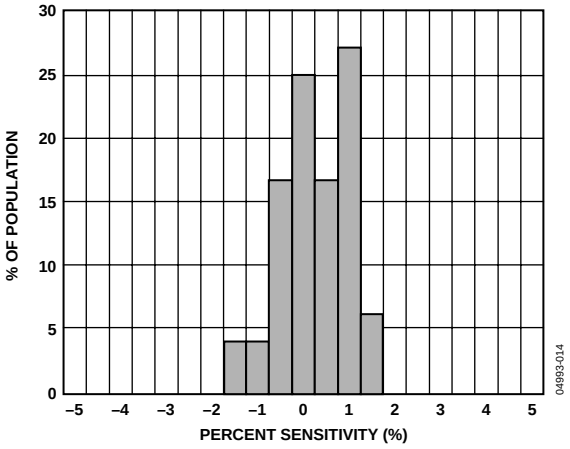

Figure 15. Z vs. Y Cross-Axis Sensitivity

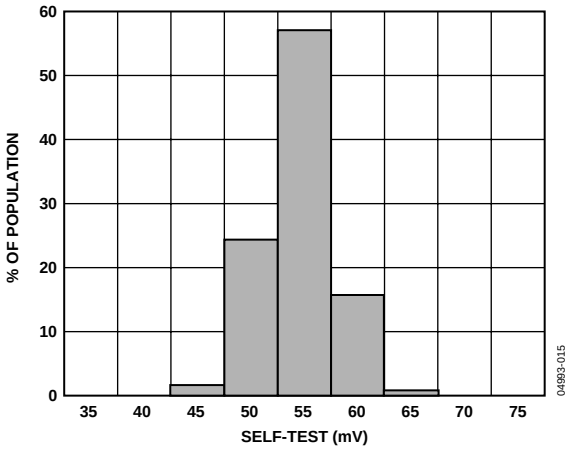

Figure 16. X-Axis Self-Test Response at 25°C

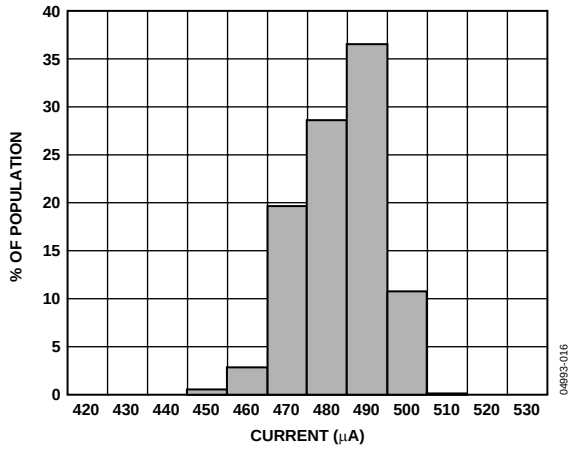

Figure 17. Supply Current at 25°C

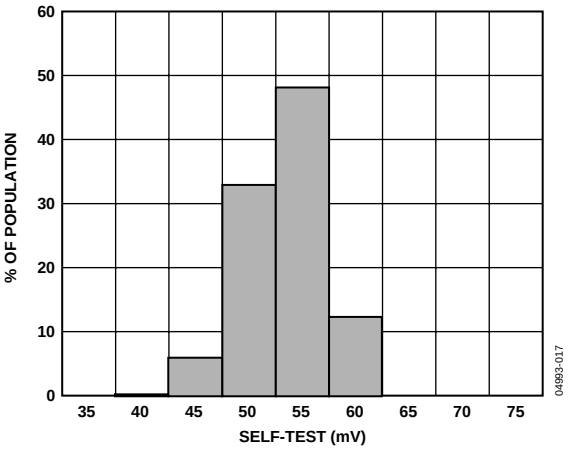

Figure 18. Y-Axis Self-Test Response at 25°C

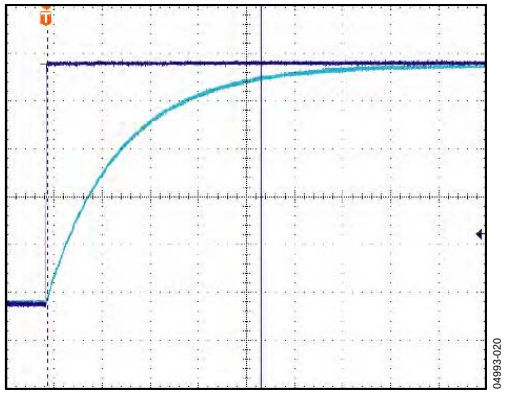

Figure 19. Turn-On Time—C_X, C_Y = 0.1 µF, Time Scale = 2 ms/DIV

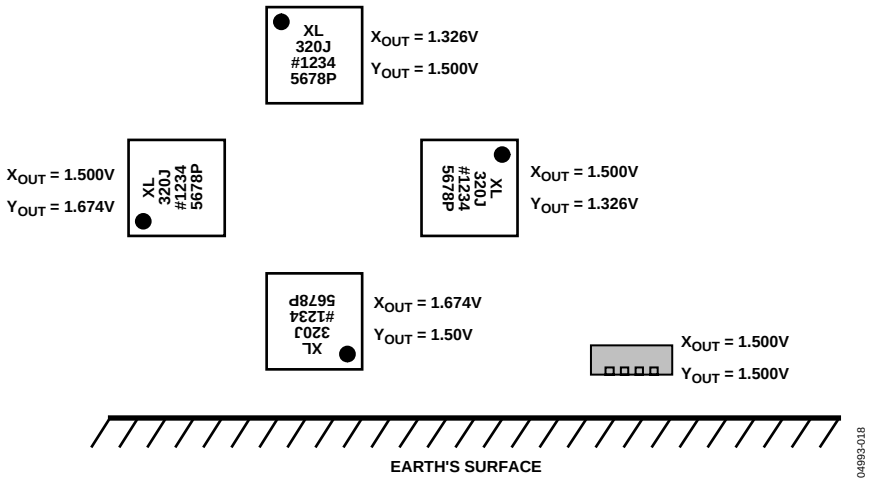

Figure 20. Output Response vs. Orientation

THEORY OF OPERATION

The ADXL320 is a complete acceleration measurement system on a single monolithic IC. The ADXL320 has a measurement range of ±5 *g*. It contains a polysilicon surface-micromachined sensor and signal conditioning circuitry to implement an open-loop acceleration measurement architecture. The output signals are analog voltages that are proportional to acceleration. The accelerometer measures static acceleration forces, such as gravity, which allows it to be used as a tilt sensor.

The sensor is a polysilicon surface-micromachined structure built on top of a silicon wafer. Polysilicon springs suspend the structure over the surface of the wafer and provide a resistance against acceleration forces. Deflection of the structure is measured using a differential capacitor that consists of independent fixed plates and plates attached to the moving mass. The fixed plates are driven by 180° out-of-phase square waves. Acceleration deflects the beam and unbalances the differential capacitor, resulting in an output square wave whose amplitude is proportional to acceleration. Phase-sensitive demodulation techniques are then used to rectify the signal and determine the direction of the acceleration.

The demodulator's output is amplified and brought off-chip through a 32 kΩ resistor. The user then sets the signal bandwidth of the device by adding a capacitor. This filtering improves measurement resolution and helps prevent aliasing.

PERFORMANCE

Rather than using additional temperature compensation circuitry, innovative design techniques have been used to ensure high performance is built-in. As a result, there is neither quantization error nor nonmonotonic behavior, and temperature hysteresis is very low (typically less than 3 m*g* over the −20°C to +70°C temperature range).

Figure 10 shows the zero *g* output performance of eight parts (X- and Y-axis) over a −20°C to +70°C temperature range.

Figure 13 demonstrates the typical sensitivity shift over temperature for supply voltages of 3 V. This is typically better than ±1% over the −20°C to +70°C temperature range.

APPLICATIONS

POWER SUPPLY DECOUPLING

For most applications, a single 0.1 µF capacitor, C_{DC}, adequately decouples the accelerometer from noise on the power supply. However, in some cases, particularly where noise is present at the 140 kHz internal clock frequency (or any harmonic thereof), noise on the supply may cause interference on the ADXL320 output. If additional decoupling is needed, a 100 Ω (or smaller) resistor or ferrite bead may be inserted in the supply line. Additionally, a larger bulk bypass capacitor (in the 1 µF to 4.7 µF range) may be added in parallel to C_{DC}.

SETTING THE BANDWIDTH USING C_X AND C_Y

The ADXL320 has provisions for band-limiting the X_{OUT} and Y_{OUT} pins. Capacitors must be added at these pins to implement low-pass filtering for antialiasing and noise reduction. The equation for the 3 dB bandwidth is

$$F_{-3\,dB} = 1/(2\pi(32\ k\Omega) \times C_{(X,Y)})$$

or more simply,

$$F_{-3\,dB} = 5\ \mu F/C_{(X,Y)}$$

The tolerance of the internal resistor (R_{FILT}) typically varies as much as ±15% of its nominal value (32 kΩ), and the bandwidth varies accordingly. A minimum capacitance of 2000 pF for C_X and C_Y is required in all cases.

Table 5. Filter Capacitor Selection, C_X and C_Y

Bandwidth (Hz)	Capacitor (µF)
1	4.7
10	0.47
50	0.10
100	0.05
200	0.027
500	0.01

SELF-TEST

The ST pin controls the self-test feature. When this pin is set to V_S, an electrostatic force is exerted on the accelerometer beam. The resulting movement of the beam allows the user to test if the accelerometer is functional. The typical change in output is 315 m*g* (corresponding to 55 mV). This pin may be left open-circuit or connected to common (COM) in normal use.

The ST pin should never be exposed to voltages greater than V_S + 0.3 V. If this cannot be guaranteed due to the system design (for instance, if there are multiple supply voltages), then a low V_F clamping diode between ST and V_S is recommended.

DESIGN TRADE-OFFS FOR SELECTING FILTER CHARACTERISTICS: THE NOISE/BW TRADE-OFF

The accelerometer bandwidth selected ultimately determines the measurement resolution (smallest detectable acceleration). Filtering can be used to lower the noise floor, which improves the resolution of the accelerometer. Resolution is dependent on the analog filter bandwidth at X_{OUT} and Y_{OUT}.

The output of the ADXL320 has a typical bandwidth of 2.5 kHz. The user must filter the signal at this point to limit aliasing errors. The analog bandwidth must be no more than half the A/D sampling frequency to minimize aliasing. The analog bandwidth may be further decreased to reduce noise and improve resolution.

The ADXL320 noise has the characteristics of white Gaussian noise, which contributes equally at all frequencies and is described in terms of µg/√Hz (the noise is proportional to the square root of the accelerometer's bandwidth). The user should limit bandwidth to the lowest frequency needed by the application in order to maximize the resolution and dynamic range of the accelerometer.

With the single-pole, roll-off characteristic, the typical noise of the ADXL320 is determined by

$$rmsNoise = (250\ \mu g/\sqrt{Hz}) \times (\sqrt{BW \times 1.6})$$

At 100 Hz bandwidth the noise will be

$$rmsNoise = (250\ \mu g/\sqrt{Hz}) \times (\sqrt{100 \times 1.6}) = 3.2\ mg$$

Often, the peak value of the noise is desired. Peak-to-peak noise can only be estimated by statistical methods. Table 6 is useful for estimating the probabilities of exceeding various peak values, given the rms value.

Table 6. Estimation of Peak-to-Peak Noise

Peak-to-Peak Value	% of Time That Noise Exceeds Nominal Peak-to-Peak Value
2 × rms	32
4 × rms	4.6
6 × rms	0.27
8 × rms	0.006

Peak-to-peak noise values give the best estimate of the uncertainty in a single measurement. Table 7 gives the typical noise output of the ADXL320 for various C_X and C_Y values.

Table 7. Filter Capacitor Selection (C_X, C_Y)

Bandwidth (Hz)	C_X, C_Y (µF)	RMS Noise (*mg*)	Peak-to-Peak Noise Estimate (*mg*)
10	0.47	1.0	6
50	0.1	2.25	13.5
100	0.047	3.2	18.9
500	0.01	7.1	42.8

USE WITH OPERATING VOLTAGES OTHER THAN 3 V

The ADXL320 is tested and specified at V_S = 3 V; however, it can be powered with V_S as low as 2.4 V or as high as 5.25 V. Note that some performance parameters change as the supply voltage is varied.

The ADXL320 output is ratiometric, so the output sensitivity (or scale factor) varies proportionally to supply voltage. At V_S = 5 V, the output sensitivity is typically 312 mV/*g*. At V_S = 2.4 V, the output sensitivity is typically 135 mV/*g*.

The zero *g* bias output is also ratiometric, so the zero *g* output is nominally equal to V_S/2 at all supply voltages.

The output noise is not ratiometric but is absolute in volts; therefore, the noise density decreases as the supply voltage increases. This is because the scale factor (mV/*g*) increases while the noise voltage remains constant. At V_S = 5 V, the noise density is typically 150 µ*g*/√Hz, while at V_S = 2.4 V, the noise density is typically 300 µ*g*/√Hz,

Self-test response in *g* is roughly proportional to the square of the supply voltage. However, when ratiometricity of sensitivity is factored in with supply voltage, the self-test response in volts is roughly proportional to the cube of the supply voltage. For example, at V_S = 5 V, the self-test response for the ADXL320 is approximately 250 mV. At V_S = 2.4 V, the self-test response is approximately 25 mV.

The supply current decreases as the supply voltage decreases. Typical current consumption at V_S = 5 V is 750 µA, and typical current consumption at V_S = 2.4 V is 350 µA.

USE AS A DUAL-AXIS TILT SENSOR

Tilt measurement is one of the ADXL320's most popular applications. An accelerometer uses the force of gravity as an input vector to determine the orientation of an object in space.

An accelerometer is most sensitive to tilt when its sensitive axis is perpendicular to the force of gravity (that is, when it is parallel to the earth's surface). At this orientation, its sensitivity to changes in tilt is highest. When the accelerometer is oriented on axis to gravity (near its +1 *g* or −1 *g* reading), the change in output acceleration per degree of tilt is negligible. When the accelerometer is perpendicular to gravity, its output changes nearly 17.5 m*g* per degree of tilt. At 45°, its output changes at only 12.2 m*g* per degree of tilt, and resolution declines.

Converting Acceleration to Tilt

When the accelerometer is oriented so both its X-axis and Y-axis are parallel to the earth's surface, it can be used as a 2-axis tilt sensor with both a roll axis and pitch axis. Once the output signal from the accelerometer has been converted to an acceleration that varies between −1 *g* and +1 *g*, the output tilt in degrees is calculated as

$$PITCH = ASIN(A_X/1\ g)$$

$$ROLL = ASIN(A_Y/1\ g)$$

Be sure to account for overranges. It is possible for the accelerometers to output a signal greater than ±1 *g* due to vibration, shock, or other accelerations.

OUTLINE DIMENSIONS

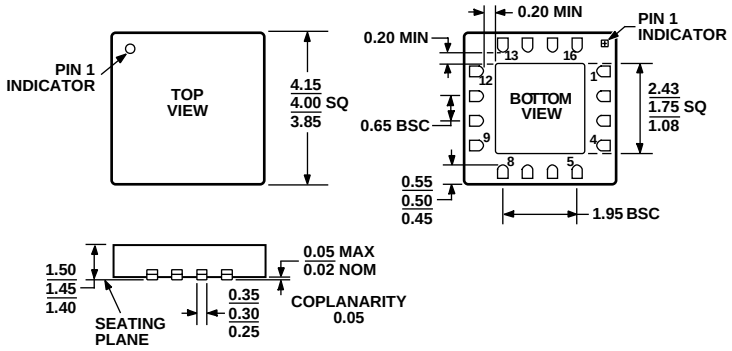

Figure 21. 16-Lead Lead Frame Chip Scale Package [LFCSP]
4 mm × 4 mm Body (CP-16-5)
Dimensions shown in millimeters

ORDERING GUIDE

Model	Measurement Range	Specified Voltage (V)	Temperature Range	Package Description	Package Option
ADXL320JCP[1]	±5 *g*	3	−20°C to +70°C	16-Lead LFCSP	CP-16-5
ADXL320JCP–REEL[1]	±5 *g*	3	−20°C to +70°C	16-Lead LFCSP	CP-16-5
ADXL320JCP–REEL7[1]	±5 *g*	3	−20°C to +70°C	16-Lead LFCSP	CP-16-5
ADXL320EB				Evaluation Board	

[1] Lead finish—Matte tin.